

**PROPERTIES OF CALCIUM PHOSPHATE BIO-CERAMIC
PREPARED BY SOLID STATE AND CHEMICAL ROUTE**

NATASHA BINTI AHMAD NAWAWI

**FACULTY OF ENGINEERING
UNIVERSITY OF MALAYA
KUALA LUMPUR**

2017

**PROPERTIES OF CALCIUM PHOSPHATE
BIOCERAMIC PREPARED BY SOLID STATE
AND CHEMICAL ROUTE**

NATASHA BINTI AHMAD NAWAWI

**THESIS SUBMITTED IN FULFILMENT OF THE
REQUIREMENTS FOR THE DEGREE OF
DOCTOR OF PHILOSOPHY**

**FACULTY OF ENGINEERING
UNIVERSITY OF MALAYA
KUALA LUMPUR**

2017

UNIVERSITY OF MALAYA
ORIGINAL LITERARY WORK DECLARATION

Name of Candidate: _____ (I.C/Passport No: _____)

Matric No: _____

Name of Degree: _____

Title of Project Paper/Research Report/Dissertation/Thesis (“this Work”): _____

Field of Study: _____

I do solemnly and sincerely declare that:

- (1) I am the sole author/writer of this Work;
- (2) This Work is original;
- (3) Any use of any work in which copyright exists was done by way of fair dealing and for permitted purposes and any excerpt or extract from, or reference to or reproduction of any copyright work has been disclosed expressly and sufficiently and the title of the Work and its authorship have been acknowledged in this Work;
- (4) I do not have any actual knowledge nor do I ought reasonably to know that the making of this work constitutes an infringement of any copyright work;
- (5) I hereby assign all and every rights in the copyright to this Work to the University of Malaya (“UM”), who henceforth shall be owner of the copyright in this Work and that any reproduction or use in any form or by any means whatsoever is prohibited without the written consent of UM having been first had and obtained;
- (6) I am fully aware that if in the course of making this Work I have infringed any copyright whether intentionally or otherwise, I may be subject to legal action or any other action as may be determined by UM.

Candidate’s Signature _____

Date: _____

Subscribed and solemnly declared before,

Witness’s Signature _____

Date: _____

Name: _____

Designation: _____

ABSTRACT

In this research, a simple solid state sintering was successfully employed to synthesize highly crystalline, high purity and single phase nanostructured hydroxyapatite powder using waste eggshells (HA-Es). The process involved mixing calcined eggshell powder and dicalcium hydrogen phosphate di-hydrate followed by a heat treatment at 800 °C. The resultant flower-like morphology of HA-Es powder exhibited excellent sintering characteristics. Besides that, pure HA was also synthesized using commercial chemical as Ca precursors through two chemical methods that are wet chemical precipitation (HA-Wp) and sol-gel (HA-Sg) for comparison study.

In conventional pressureless sintering, HA-Es was able to retain the single HA phase stability until 1250 °C. The optimum sintering temperature for HA-Es was 1250 °C with the overall best combination of properties being recorded: relative bulk density of 97.7 %, Vickers hardness of 5.62 GPa, excellent fracture toughness of 1.51 MPam^{1/2} and average grain size was below 1 µm (0.950 µm). In contrast, the optimum sintering temperature of HA-Wp was 1200 °C with a bulk density of 97.9 %, Vickers hardness of 4.8 GPa, fracture toughness of 1.29 MPam^{1/2} and average grain size of 1.62 µm. In addition, the overall structural characterization and relative density of HA-Wp were significantly better than that of the HA-Sg.

In microwave sintering, HA-Es was able to retain the HA phase stability up to 1200 °C and this is regarded as the optimum sintering temperature with the following properties: relative bulk density of 96.0 %, Vickers hardness of 3.65 GPa, fracture toughness of 1.05 MPam^{1/2} and average grain size of 2.08 µm. Meanwhile for HA-Wp, the optimum sintering temperature was 1100 °C with a bulk density of 96.9 %, Vickers hardness of 3.82 GPa, fracture toughness of 0.86 MPam^{1/2} and average grain size of 0.85 µm.

Overall, these results revealed that the sinterability and mechanical properties of the HA-Es produced by the conventional sintering method were significantly better than HA-Es produced by the microwave sintering method. Basically, the hardness and fracture toughness of all HA samples were initially influenced by the increase in relative density with sintering temperature until they reached a maximum value at a critical grain size limit (d_c). Above this critical limit, grain growth acts as the controlling parameter. Therefore, the properties then decreased with increasing grain size despite exhibiting high bulk density.

Both in vitro dissolution study in PBS and cell culture investigations confirmed that conventionally sintered eggshell derived HA exhibited excellent biological performance. In this work, sintered HA-Es at 1250 °C was found to have the best cell response and also improved mechanical properties.

It can be suggested that the mechanical properties and the efficiency of HA in cell response are grain size dependent activities. Smaller grain size will induce an increase in grain boundary at the surface and therefore facilitates the cells to proliferate. Thus, this research proved that HA synthesized from waste eggshell through solid state method could be a potential bioceramic for use in the clinical application.

ABSTRAK

Di dalam penyelidikan ini, satu kaedah persinteran keadaan pepejal yang mudah telah berjaya digunakan dalam mensintesis serbuk nano-kristal hidroksiapatit dengan menggunakan sisa kulit telur (HA-Es). Proses ini melibatkan percampuran antara sisa kulit telur yang telah dikalsin dan dikalsium hidrogen fosfat dihidrat diikuti dengan perawatan haba pada suhu 800 °C. Struktur nano seperti bentuk bunga yang terhasil dari serbuk HA-Es ini juga menunjukkan sifat-sifat persinteran yang sangat baik. Sebagai perbandingan dalam kajian, fasa tulen HA juga telah disintesis dengan menggunakan bahan kimia komersial sebagai sumber Ca melalui dua kaedah kimia iaitu pemendakan kimia basah (HA-Wp) dan sol-gel (HA-Sg) .

Melalui persinteran konvensional tanpa tekanan dalam udara, HA-Es telah berupaya mengekalkan kestabilan satu fasa HA sehingga suhu 1250 °C. Didapati suhu optimum untuk persinteran serbuk HA-Es ialah pada suhu 1250°C dan ini membawa kepada kombinasi ciri-ciri yang baik: ketumpatan relatif 97.7 % dengan kekerasan Vickers sebanyak 5.62 GPa, ketahanan patah yang sangat baik pada bacaan 1.51 MPam^{1/2} dan purata saiz butiran didapati lebih kecil dari 1 µm (0.950 µm). Secara kontranya, suhu optimum untuk persinteran serbuk HA-Wp pula ialah 1200 °C dan ini membawa kepada kombinasi ciri-ciri yang baik: ketumpatan relatif 97.9 %, kekerasan Vickers sebanyak 4.80 GPa, ketahanan patah pada 1.29 MPam^{1/2} dan saiz butiran 1.62 µm. Tambahan lagi, didapati bahawa keseluruhan percirian struktur dan ketumpatan relatif HA-Wp adalah jauh lebih baik daripada HA-Sg.

Melalui persinteran gelombang mikro, HA-Es telah berupaya mengekalkan kestabilan fasa HA sehingga suhu 1200 °C dan ini merupakan suhu optimum dengan kombinasi ciri-ciri: ketumpatan relatif 96.0 %, kekerasan Vickers 3.65 GPa, ketahanan patah pada bacaan 1.05 MPam^{1/2} dan purata saiz butiran pada 2.08 µm. Sementara itu,

suhu optimum untuk persinteran serbuk HA-Wp pula ialah 1100 °C dengan ketumpatan relatif 96.9 %, kekerasan Vickers setinggi 3.82 GPa, ketahanan patah pada 0.86 MPam^{1/2} dan purata saiz butiran sebesar 0.85 µm.

Secara keseluruhannya, keupayaan persinteran dan ciri-ciri mekanikal yang ditunjukkan oleh HA-Es yang dihasilkan melalui persinteran konvensional tanpa tekanan adalah jauh lebih baik daripada HA-Es yang dihasilkan melalui persinteran gelombang mikro. Pada dasarnya, kekerasan Vickers dan juga ketahanan patah semua sampel HA dipengaruhi oleh peningkatan ketumpatan relatif seiring dengan suhu persinteran sehingga had kritikal maksimum saiz butiran (d_c) dicapai. Melebihi had kritikal ini, ia dikawal oleh pertumbuhan saiz butiran. Dengan itu, peredaran mekanikal menurun dengan peningkatan saiz butiran walaupun menunjukkan ketumpatan pukal yang tinggi.

Keputusan kajian pembubaran secara in vitro dalam larutan garam penampat fosfat (PBS) dan pengkulturan sel mengesahkan persinteran HA dari kulit telur memaparkan prestasi biologi yang baik. Dalam penyelidikan ini, HA-Es yang disinter pada 1250 °C telah menunjukkan tindak balas sel yang terbaik selain mempunyai sifat-sifat mekanikal yang lebih baik.

Dapat dicadangkan bahawa peredaran mekanikal dan kecekapan HA dalam tindak balas sel bergantung pada saiz butiran. Saiz butiran yang lebih kecil akan mendorong peningkatan kawasan sempadan butiran dan sekaligus memudahkan percambahan sel. Dengan ini, dapat dibuktikan bahawa HA yang disintesis daripada sisa kulit telur melalui kaedah persinteran keadaan pepejal mempunyai potensi untuk digunakan sebagai biosemen dalam aplikasi klinikal.

ACKNOWLEDGEMENTS

Foremost, I would like to express my sincerest gratitude and appreciation to my research supervisors Prof. Ir. Dr. Ramesh Singh and Assoc. Prof. Dr. Tan Chou Yong, for their valuable guidance, advice, discussion, comments, enthusiasm and encouragement throughout this project and thesis. Special thanks goes to Prof. Ir. Dr. Ramesh as he has not only shared his vast technical knowledge in the area of engineering ceramics but more importantly have moulded me to be a competent researcher. Special appreciation also goes to Dr. Le Thi Bang, for her continuous assistance, guidance and valuable insights through the entire journey of the research work and thesis preparation as well. I would also like to take this opportunity to thank all the technicians and members of the Advanced Materials Laboratory, University Malaya for their assistance and teamwork that have made the laboratory a pleasant place to work.

I would like to acknowledge the University of Malaya for providing the necessary facilities and resources for this research. This research was supported by the HIR Grant no. UM.C/ HIR/MOHE/ENG/33, PPP Grant no. PG079-2013A and UMRG Grant no. RP011D-13AET. I would also like to acknowledge the Ministry of Higher Education and Universiti Teknologi Mara for the scholarship provided under the ‘Tenaga Pengajar Muda’ scheme.

I would also like to express my utmost gratitude to my beloved husband, Fairul Ifnee bin Othman, my beloved parents, daughter and all family members for their endless support, patience, strength and encouragement throughout my candidature.

Last but not least, I would like to thank everyone who have directly or indirectly assisted and contributed to the knowledge of the study. Thank you.

TABLE OF CONTENTS

Abstract.....	iii
Abstrak.....	v
Acknowledgements.....	vii
Table of Contents.....	viii
List of Figures.....	xiii
List of Tables.....	xix
List of Symbols and Abbreviations.....	xx
List of Appendices.....	xxii
CHAPTER 1: INTRODUCTION.....	1
1.1 Background.....	1
1.2 Problem Statement.....	4
1.3 Objectives.....	8
1.4 Structure of the Thesis.....	9
CHAPTER 2: LITERATURE REVIEW.....	11
2.1 Introduction.....	11
2.2 Biological Apatite.....	12
2.3 Biomaterial.....	15
2.3.1 Calcium Phosphate Ceramics.....	17
2.3.2 Hydroxyapatite.....	20
2.4 Fabrication of Calcium Phosphate Nanoceramics.....	22
2.5 Synthesis of Hydroxyapatite.....	25
2.5.1 Development of HA from Natural Organic Sources.....	26

2.5.2	Development of HA from Inorganic Sources.....	32
2.5.3	Dry Methods.....	33
2.5.3.1	Solid state reaction.....	33
2.5.4	Wet Methods.....	36
2.5.4.1	Wet chemical precipitation.....	37
2.5.4.2	Sol-gel.....	39
2.6	Sintering of Hydroxyapatite (HA).....	41
2.7	Sintering Techniques.....	47
2.7.1	Conventional Pressureless Sintering.....	48
2.7.2	Microwave Sintering.....	50
2.7.3	High Pressure-Assisted Sintering.....	52
2.8	Bioactivity and Biological Performance Evaluation of Calcium Phosphate	54
2.8.1	In vitro Evaluation using Phosphate Buffered Saline (PBS).....	55
2.8.2	In vitro Evaluation using Cell Culture.....	55
2.9	Summary.....	56
CHAPTER 3: MATERIALS AND METHODS.....		58
3.1	Introduction.....	58
3.2	Powder Preparation.....	58
3.2.1	Direct Conversion of Waste Eggshells as a Natural Source of Calcium Precursor to HA through Solid State Method.....	58
3.2.2	Preparation of HA Powder through Wet Chemical Precipitation.....	60
3.2.3	Preparation of HA Powder through Sol-Gel Method.....	62
3.2.4	Calcination of HA Powder.....	63
3.3	Preparation of HA Green Compacts from Different Synthesis Methods.....	64

3.4	Sintering of HA Green Compacts.....	64
3.4.1	Conventional Pressureless Sintering (CS).....	64
3.4.2	Microwave Sintering (MW).....	65
3.5	Characterization of HA Powders and Compacts.....	66
3.5.1	Phase stability and Crystallite Size.....	66
3.5.2	Differential Thermal Analysis.....	67
3.5.3	Fourier Transform Infrared (FTIR).....	68
3.5.4	Specific Surface Area.....	68
3.5.5	Microstructural Examination.....	68
3.5.6	Transmission Electron Microscopic Analysis.....	70
3.5.7	Bulk Density Measurement.....	70
3.5.8	Vickers Microhardness Testing.....	71
3.5.9	Indentation Fracture Toughness Measurements.....	73
3.6	In vitro Evaluation on the Bioactivity of Heat Treated HA-Es: Phosphate Buffered Saline (PBS).....	74
3.7	In vitro Evaluation on the Biocompatibility of Heat Treated HA-Es: Cell Study.....	75
3.7.1	Sample Preparation.....	75
3.7.2	MC3T3-E1 Osteoblast-like Cell.....	76
3.7.3	Rat Bone Marrow Cell (RBMC) Isolation.....	77
3.7.4	Cell Detachment and Cell Counting Prior to Seeding on the Sample.....	77
3.7.5	Cell Morphology.....	78
3.7.6	Cell Proliferation.....	78
3.7.7	Cell Differentiation: Alkaline phosphatase activity.....	79
3.7.8	Mineralization Assay.....	80

CHAPTER 4: RESULTS AND DISCUSSION (PART 1)	82
4.1 Introduction.....	81
4.2 Development and Characterization of Eggshell Based Hydroxyapatite (HA-Es) Based on A Solid State Reaction.....	82
4.3 Characterization of HA Powders Synthesized via Wet Chemical Precipitation (HA-Wp) and Sol-Gel Method (HA-Sg) Using Commercial Chemicals as Ca-precursor.....	91
 CHAPTER 5: RESULTS AND DISCUSSION (PART 2)	107
5.1 Introduction.....	107
5.2 Consolidation of HA Powder through Conventional Pressureless Sintering.....	108
5.2.1 HA Phase Stability.....	108
5.2.2 Linear Shrinkage.....	114
5.2.3 Bulk Density Analysis.....	117
5.2.4 Microstructural Evolution and Grain Size Analysis.....	120
5.2.5 Vickers Hardness Analysis.....	125
5.2.6 Fracture Toughness.....	128
5.3 Consolidation of HA Powder through Microwave Sintering.....	130
5.3.1 HA Phase Stability.....	131
5.3.2 Linear Shrinkage.....	135
5.3.3 Microstructural Evolution and Grain Size Analysis.....	136
5.3.4 Bulk Density Analysis.....	141
5.3.5 Vickers Hardness Analysis.....	143
5.3.6 Fracture Toughness Analysis.....	144
5.4 Conventional Pressureless Sintering vs Microwave Sintering.....	150

5.5	Biocompatibility of Eggshell Derived Hydroxyapatite.....	157
5.5.1	In vitro Biodegradation Studies.....	158
5.5.2	Cell Study In vitro: MC3T3-E1 Osteoblast-like cell.....	162
5.5.2.1	Cell morphology and adherence.....	162
5.5.2.2	Cell proliferation.....	164
5.5.3	Cell Study In vitro: Rat Bone Marrow Cells (RBMC).....	166
5.5.3.1	Cell morphology and adherence.....	166
5.5.3.2	Cell proliferation.....	168
5.5.3.3	Cell differentiation.....	170
5.5.2.4	Cell mineralization: Alizarin red S staining.....	171
CHAPTER 6: CONCLUSION AND FUTURE WORKS.....		175
6.1	Conclusion.....	175
6.2	Recommendation for Future Work.....	180
	References.....	182
	List of Publications and Papers Presented.....	206
	Appendix.....	207

LIST OF FIGURES

Figure 1.1: Flow chart of dense sample preparation and characterization.....	9
Figure 2.1: Structure of a long bone in longitudinal section.....	14
Figure 2.2: SEM micrographs of (a) attrition and (b) ball milled, samples after heat treatment at 900 °C (Gergely et al., 2012).....	35
Figure 2.3: Optical micrographs of HAp ceramics; AD sintered at (a) 1100, (b) 1200, (c) 1300 and (d) 1400 °C; CP (calcined only) sintered at (e) 1100, (f) 1200, (g) 1300 and (h) 1400 °C; CM (calcined and milled) sintered at (i) 1100, (j) 1200, (k) 1300 and (l) 1400 °C (Thangamani et al., 2002).....	43
Figure 2.4: SEM image of the polished and thermally etched surface of the HA sample sintered at 900 °C for 2 h, and b) SEM image of the HA sample sintered at 850 °C for 24 h (Wang & Shaw, 2007).....	50
Figure 2.5: The microwave-sintered BCP ceramics under various sintering conditions. The sintering temperature, heating rate, and holding time are; (a) 1200 °C, 80 °C/min, and 1 min; (b) 1000 °C, 80 °C/min, and 3 min, (c) 1000 °C, 30 °C/min, and 1 min; (d) and 950 °C, 80 °C/min, and 1 min, respectively (Hong et al., 2010).....	51
Figure 2.6: Assembly of the LTUHP sintering experiments (Tan et al., 2011).....	53
Figure 2.7: The time course of osteoblast function on a newly implanted Biomaterial (Liu & Webster, 2007).....	56
Figure 3.1: Flow chart of preparation of HA powder from waste eggshell via solid state reaction (HA-Es).....	60
Figure 3.2: Flow chart of preparation of HA powder via wet chemical precipitation (HA-Wp).....	62

Figure 3.3: Flow chart of preparation of HA powder via sol-gel method (HA-Sg).....	63
Figure 3.4: Pressureless sintering regime of synthesized HA green compacts.....	65
Figure 3.5: Microwave sintering regime of synthesized HA green compacts.....	66
Figure 3.6: Diagram showing the score given for the type of intersections.....	70
Figure 3.7: The Vickers Hardness Test (a) Vickers indentation and (b) measurement of impression diagonals.....	72
Figure 3.8: Vickers indentation showing cracks emanating from the four corner of the indent.....	74
Figure 4.1: The XRD of crushed and heat treated eggshells.....	83
Figure 4.2: TGA analysis of eggshells powder and DCPD mixture after attrition milling.....	84
Figure 4.3: XRD patterns of as-milled and calcined at (a) 700 °C, (b) 800 °C, (c) 900 °C and (d) 1000 °C, powder mixture.....	86
Figure 4.4: XRD patterns of HA-Es powder pre-heated at 800 °C.....	87
Figure 4.5: FTIR spectra of HA-Es powder pre-heated at 800 °C.....	89
Figure 4.6: SEM of HA-Es powder pre-heated at 800 °C.....	90
Figure 4.7: XRD patterns of as-synthesized HA powders obtained from: (a) wet chemical (HA-Wp) and (b) sol-gel (HA-Sg). All peaks corresponded to the HA phase.....	93
Figure 4.8: XRD patterns of calcined HA-Wp and HA-Sg powders at respective temperatures: (a) 800 °C, (b) 900 °C and (c) 1000 °C.....	95
Figure 4.9: FTIR spectra of as-synthesized HA powders obtained from (a) wet chemical precipitation (HA-Wp) and (b) sol-gel (HA-Sg) methods.....	98

Figure 4.10: TG/DTA analysis of as-synthesized HA powders: (a) wet chemical precipitation (HA-Wp) and (b) sol-gel (HA-Sg) (before heat treatment)	99
Figure 4.11: FESEM images of as-synthesized HA powders from (a) wet chemical precipitation (HA-Wp) and (b) sol-gel (HA-Sg) synthesis.....	102
Figure 4.12: TEM images of synthesized nano-HA powder derived from (a) wet chemical precipitation (HA-Wp) and (b) sol-gel (HA-Sg) method.....	105
Figure 5.1: XRD patterns of HA-Es samples sintered at various temperatures.....	110
Figure 5.2: XRD patterns of HA-Wp samples sintered at various temperatures. All the peaks corresponded to that of stoichiometric HA.....	112
Figure 5.3: XRD patterns of HA-Sg samples sintered at various temperatures.....	113
Figure 5.4: Linear shrinkage of HA-Es samples at various sintering Temperatures.....	116
Figure 5.5: Linear shrinkage of HA-Wp and HA-Sg samples at various sintering temperatures.....	116
Figure 5.6: The variation in relative density of conventional sintered HA-Es as a function of sintering temperature.....	118
Figure 5.7: The variation in relative density of conventional sintered HA-Wp and HA-Sg as a function of sintering temperature.....	119
Figure 5.8: Microstructural evolution of HA-Es sintered at (a)1000 °C, (b)1050 °C, (c)1100 °C, (d)1150 °C, (e)1200 °C, (f)1250°C, (g)1300°C and (h)1350°C.....	122

Figure 5.9: Microstructural evolution of HA-Wp sintered at (a)1000 °C, (b)1050 °C, (c)1100 °C, (d)1150 °C, (e)1200 °C, (f)1250°C, (g)1300°C and (h)1350°C.....	124
Figure 5.10: Average grain size variation of HA-Es and HA-Wp sintered at various temperatures.....	125
Figure 5.11: The variation in Vickers hardness of conventional sintered HA-Es and HA-Wp as a function of sintering temperature.....	127
Figure 5.12: The variation in fracture toughness of conventional sintered HA-Es and HA-Wp as a function of sintering temperature.....	130
Figure 5.13: XRD patterns of HA-Es(M) samples microwave-sintered at various temperatures.....	132
Figure 5.14: XRD patterns of HA-Wp(M) samples microwave-sintered at various temperatures.....	133
Figure 5.15: Linear shrinkage of HA-Es(M) and HA-Wp(M) samples microwave-sintered at various sintering temperatures.....	135
Figure 5.16: Microstructural evolution of HA-Es(M) samples microwave-sintered at (a)950 °C, (b)1000 °C, (c)1050 °C, (d)1100 °C, (e)1150 °C, (f)1200 °C and (g)1250 °C.....	137
Figure 5.17: Microstructural evolution of HA-Wp(M) samples microwave-sintered at (a) 950 °C, (b)1000 °C, (c)1050 °C, (d)1100 °C, (e)1150 °C, (f)1200 °C and (g)1250 °C.....	139
Figure 5.18: Average grain size variation of HA-Es(M) and HA-Wp(M) samples microwave-sintered at various temperatures.....	140
Figure 5.19: The variation in relative density of microwave sintered HA-Es(M) and HA-Wp(M) as a function of sintering temperature.....	142

Figure 5.20: The variation in Vickers hardness of microwave sintered HA-Es(M) and HA-Wp(M) as a function of sintering temperature.....	144
Figure 5.21: The variation in fracture toughness of microwave sintered HA-Es(M) and HA-Wp(M) as a function of sintering temperature.....	146
Figure 5.22: The effect of relative density on the Vickers hardness of sintered HA.....	147
Figure 5.23: The effect of relative density on the fracture toughness of sintered HA.....	148
Figure 5.24: Vickers hardness dependence on the grain size of HA in microwave sintering.....	149
Figure 5.25: Fracture toughness dependence on the grain size of hydroxyapatite.....	150
Figure 5.26: Comparison of XRD patterns between conventional and microwave sintered HA-Es at various temperatures.....	151
Figure 5.27: Relative density of HA-Es sintered at various temperatures by the conventional and microwave method.....	152
Figure 5.28: Average grain size of HA-Es sintered at various temperatures by the conventional and microwave methods.....	154
Figure 5.29: Vickers hardness of HA-Es sintered at various temperatures by the conventional and microwave methods.....	155
Figure 5.30: Fracture toughness of HA-Es sintered at various temperatures by the conventional and microwave methods.....	156
Figure 5.31: Typical SEM micrographs of the eggshell derived HA compacts before and after immersion in PBS: (a) HA-Es(800),(b) HA-Es(1200) and (c) HA-Es(1250).....	159
Figure 5.32: The changes of PBS solution pH with respect to the number of immersion days of HA-Es samples.....	160

Figure 5.33: Mass loss (in miligrams) of as-prepared and sintered HA-Es samples with respect to immersion periods in PBS solution.....	161
Figure 5.34: Cell morphology on the surface of HA-Es samples after 4 hours of incubation at different magnification. The white arrows indicate the adhered cell.....	163
Figure 5.35: SEM images of osteoblast cell attachment on the surface of HA-Es samples at different sintering conditions. The white arrows indicate the adhered cell.....	164
Figure 5.36: MC3T3-E1 cell proliferation on the different HA-Es samples.....	166
Figure 5.37: SEM images of bone marrow cell morphology on: (a) HA-Es(800), (b) HA-Es(1200) and (c) HA-Es(1250), after 4 hours culture. The white arrows indicate the adhered cell.....	167
Figure 5.38: RBMC cell proliferation on the different HA-Es samples.....	169
Figure 5.39: ALP activity of RBMC on different HA-Es samples.....	171
Figure 5.40: Bone nodule formation on HA-Es at (a) 800 °C, (b) 1200 °C and (c) 1250 °C.....	172
Figure 5.41: Calcium quantification detected on HA-Es samples after 14 and 21 days of culture.....	173

LIST OF TABLES

Table 2.1: Foreign ions in the HA lattice of human bone (Milovac et al., 2014; Siddharthan et al., 2009).....	13
Table 2.2: Mechanical properties of skeletal tissues (LeGeros & LeGeros, 1993).....	15
Table 2.3: Typical physical properties of different biomaterials (Carter and Norton, 2007).....	17
Table 2.4: Various forms of calcium phosphate.....	19
Table 2.5: Comparison of mechanical properties of sintered HA with hard tissue (Hench, 1998).....	21
Table 3.1: JCPDS data reference.....	67
Table 3.2: Amount of working reagents used for ALP measurement.....	80
Table 4.1: Crystallite size of calcined HA-Es powder at various temperatures.....	86
Table 4.2: The elemental composition (wt %) of HA-Es. Data are presented in mean \pm standard deviation.....	91
Table 4.3: Crystallite size of calcined HA-Wp and HA-Sg powders at various temperatures.....	96
Table 4.4: Relative intensity ratio of β -TCP presented in HA-Wp and HA-Sg powders upon calcinations.....	96
Table 4.5: The elemental composition (wt %) of HA-Wp and HA-Sg samples. Data are presented in mean \pm standard deviation.....	104
Table 4.6: Summary of the average size and morphology of wet chemical (HA-Wp) and sol-gel (HA-Sg) powders as observed by SEM and TEM.....	106
Table 5.1: Total sintering time for two different sintering methods.....	153

LIST OF SYMBOLS AND ABBREVIATIONS

ALP	: Alkaline Phosphatase
Ca/P	: Calcium to phosphorus molar ratio
CaP	: Calcium Phosphate
CS	: Conventional sintering
DCPD	: Dicalcium phosphate dihydrate
h	: Hour
HA	: Hydroxyapatite
HA-Es	: Hydroxyapatite derived from eggshell by solid-state reaction
HA-Wp	: Hydroxyapatite prepared by wet chemical precipitation
HA-Sg	: Hydroxyapatite prepared by sol-gel method
HA-Es(M)	: Microwave sintered eggshell derived HA
HA-Wp(M)	: Microwave sintered wet chemical precipitation derived HA
H ₃ PO ₄	: Orthophosphoric Acid
JCPDS	: Joint Committee on Powder Diffraction Standards
KBr	: Potassium Bromide
MSCs	: Mesenchymal stem cells
MW	: Microwave sintering
NH ₄ OH	: Ammonia
PBS	: Phosphate Buffer Saline
RBMC	: Rat Bone Marrow Cell
SEM	: Scanning Electron Microscope
TCP	: Tricalcium Phosphate
TG/DTA	: Thermogravimetric/Differential Thermal Analyzer
TTCP	: Tetracalcium Phosphate

α -TCP : Alpha-Tricalcium Phosphate

β -TCP : Bbeta-Tricalcium Phosphate

T.D : Theoretical density

U/mg protein : $\mu\text{mol}/\text{min}/\text{mg}$ protein

wt % : Weight percent

University of Malaya

LIST OF APPENDICES

Appendix A: Calculations

- A-1 : Calculation for the synthesis of Eggshell derived Hydroxyapatite through solid-state reaction (HA-Es).....207
- A-2 : Calculation for the synthesis of Hydroxyapatite through wet chemical precipitation (HA-Wp).....207

Appendix B: Laboratory Apparatus and Equipment

- Figure B-1 : Attritor Mill (Akron Electric Inc., USA).....208
- Figure B-2 : Conventional Furnace208
- Figure B-3 : Microwave Furnace (Shenzen BduVo, Delta, China).....209
- Figure B-4 : Preparation of sample for sintering regime.....209

Appendix C: Apparatus and Results of Biocompatibility Test

- Figure C-1 : Calcium Hydrogenphosphate Dihydrate (Nacalai Tesque, Japan).....210
- Figure C-2 : Phosphate Buffer Saline (PBS) buffer pouch (Sigma Aldrich, USA).....210
- Figure C-3 : Surface of HA-Es(1250) compact after 21 days of PBS immersion....211
- Figure C-4 : Rat bone marrow cell proliferation on different HA-Es samples after 5 days.....211
- Figure C-5 : Bio-Rad Protein Assay (Bio-Rad Laboratories Inc., USA).....212
- Figure C-6 : Calcium quantification of HA-Es(800)-Sp1, HA-Es(1200)-Sp2 and HA-Es(1250)-Sp3 after 21 days as compared to the standard solution of 10,5, 0.5 and blank.....212

CHAPTER 1: INTRODUCTION

1.1 Background

During the last several decades, Hydroxyapatite [HA, $\text{Ca}_{10}(\text{PO}_4)_6(\text{OH})_2$] has attracted considerable attention for use in orthopedics and dentistry because of its structural and compositional similarity with natural bone. HA has been primarily used to form sintered body and polymer composites (Thein-Han & Misra, 2009) as replacements for bone and periodontal defects (Ajdukovic et al., 2007; Ye & Wang, 2007), dental materials (Ye & Wang, 2007; Veljovic et al., 2010), and maxillofacial implants (Ajdukovic et al., 2007). In fact, its biocompatibility and ability to bond with surrounding tissues of HA have been experimentally proven to be superior to any other biomaterial (Sadat-Shojai et al., 2013). However, most synthetic apatites are formed via high temperature processes, resulting in a well-crystallized structure, which presents little or no activity toward bioresorption (Zakaria et al., 2013). This is because HA solubility increases from crystalline to amorphous and reduces crystal size (Martinez-Castanon et al., 2012).

It has been reported that nano-size bone mineral crystals have a very large surface area. Meanwhile, synthetic HA which conventionally in micron size presents a low surface area and regularly highly agglomerated. As a result, the resorption process of synthetic HA is equally different from that of bone mineral where synthetic HA present a lower bioactivity (Kim et al., 2014). Therefore, producing HA at nano-level would be functionally significant due to the similarity of ultra-fine structure with large surface area to volume ratio to biological apatite (Driessens et al., 2002; Fathi et al., 2008). Besides that, resorbability of HA can be developed by improving its degree of crystallinity similar to biological HA (Driessens et al., 2002). Note that, bone mineral crystals has 60-70% crystalline phase. This, in turn, would result in great impact on implant-cell interaction in body environment (LeGeros, 1991).

In general, the raw materials used to synthesize HA originate from commercial chemicals and natural sources. Naturally sourced HA involve extraction via heat treatment of animal cortical bones (bovine, pig, etc.) and natural waste (egg shell, clamshell) (Lau et al., 2012), as well as conversion from marine coral derivatives (Kusmanto et al., 2013) to natural HA with acceptable porosity. Over the years, various HA preparation methods have been developed and this can technically be categorized into four groups, namely, dry methods (e.g. solid state synthesis, mechanochemical method), wet chemical methods (e.g. wet chemical precipitation, hydrolysis method, sol-gel, hydrothermal, emulsion method, sonochemical method), high-temperature processes (e.g. combustion, pyrolysis), and combination procedures (e.g. hydrothermal-mechanochemical, hydrothermal-hydrolysis). These methods vary in terms of the precursors used and processing cost and HA powders with various morphologies, stoichiometry, and level of crystallinity can be obtained depending on the method of synthesis (Sadat-Shojai et al., 2013). Among these routes, wet chemical methods, e.g. precipitation and sol-gel, present advantages of precise control over the morphology and size of the particles. Thus, these methods are the most promising for the synthesis of nanosized HA with expected morphology (Sadat-Shojai et al., 2013). Sol-gel synthesis method involves the formation of a colloidal sol, which will subsequently turn into a gel (Alexandra & Raul, 2011). This method requires no special energy conditions for the formation of the desired compound; thus, the synthesis of ceramic materials could be carried out at room temperature (Alexandra & Raul, 2011). However, sol-gel synthesis requires a strict control of process parameters and an intimate contact mixing at the molecular level (because of the slow reaction between Ca and P precursors in the sol phase) to obtain highly pure, nanosized powder with homogeneous composition. Meanwhile, wet chemical precipitation requires a special pH value control condition for precipitation to occur because the degree of neutralization of phosphoric acid is pH

dependent (Sadat-Shojai et al., 2013). Moreover, the morphology (shape and size) of nanoparticles obtained via this method is highly sensitive to reactant addition rate in which a lower addition rate of acid could result in a large particle size (Paz et al., 2012). However, HA derived from these method are normally lack in the presence of trace ions in its lattice structure.

As for bone mineral, it is considered as a non-stoichiometric HA with the presence of trace ions in its HA lattice (Siddharthan et al., 2009). Meanwhile, HA derived from natural resources and biowastes are non-stoichiometric due to the various ionic substitutions in its crystal structure for the OH^- , PO_4^{3-} , and Ca^{2+} groups, making its usage in the development of bone-like implants highly desirable (Milovac et al., 2014).

According to Best et al. (2008), interest in dense HA for its use in implantation has emerged in the past 20-38 years. Dense HA is described as a ceramic that has a microporosity less than 5 volume percent with micropores size diameter less than $1\mu\text{m}$ and grain size bigger than $0.2\mu\text{m}$ (LeGeros & LeGeros, 1993). The microporosity is unintentionally introduced and is dependent on the temperature and duration of sintering (Raynaud et al., 2002). However, the lacks in mechanical strength of HA restrict its capability to succeed in long-term load-bearing applications (Banerjee et al., 2007). Moreover, sufficient mechanical properties (e.g. hardness, bend strength and fracture toughness) is also necessary even for the nonload-bearing applications. As a consequence, the mechanical properties of HA have been studied extensively.

Thus, in recent years interest in the dense bioceramics with average grain size below 100 nm has increased because of its high surface activity (Wang & Shaw, 2009; Lukic et al., 2012), improved sinterability at lower temperature and resulting in a high dense body coupled with enhanced mechanical properties (Evis & Webster, 2011; Martinez-Castanon et al., 2012; Zakaria et al., 2013; Champion, 2013). Moreover, this ultrafine

structure is similar to the mineral found in hard tissues and can readily promote osteointegration and subsequent bone tissue formation. Thus, HA with nanograin size is more desirable in clinical applications due to its improved properties over micron size grains.

Generally, nanostructured ceramic is obtained by compacting the HA nanopowders followed by the conventional pressureless sintering at different temperatures and holding time in air atmosphere. Nevertheless, sintering of HA is regarded as a complex process since many parameters influence the densification process such as properties of the synthesized powders (e.g. Ca/P molar ratio, crystallinity and particles size), sintering parameters and atmospheres (Veljovic et al., 2009). In general, consolidation of ceramic through conventional method requires high sintering temperatures and long sintering times that often result in decomposition of the HA phase and grain coarsening. This, in turn results in deterioration of the mechanical properties of ceramic (Gu et al., 2004; Tang et al., 2009). For example, sintering above 1300 °C was reported to introduce secondary phases of calcium phosphates such as CaO and α -TCP (Tadic et al., 2004). Consequently, microwave sintering of ceramics has gained much attention during the last decade. This is because, as heat is generated within the material, rapid and uniform heating are achievable followed by enhanced densification rate, improved microstructure and potential for energy and cost savings when compared to conventional sintering (Harabi et al., 2011). Therefore, selection of suitable sintering method is a critical controlling parameter in order to produce HA with desired structure and properties.

1.2 Problem Statement

In the last 50 years, the number of bioceramics used in clinical applications has increased progressively. To date, the direction of bioceramic research is focused on the

improvement of the mechanical performance and biological properties of existing bioactive ceramics particularly HA. It is known that major drawback of HA ceramic is its low fracture toughness ($< 1 \text{ MPam}^{1/2}$) than those of cortical bone (Kokubo et al., 2003) which hinder its use to repair bone defects in the load bearing clinical application. This, in turn calls for the development of dense nanostructured HA with improved bone-like mechanical properties and the major concern is to enhance densification while limiting its grain growth. In HA synthesis, precise control of crystal growth presents the ultimate challenge because it directly relates to the characteristics of the final particles (grain size, material crystallinity and geometric shape and distribution). These primary characteristics are widely documented to majorly affect mechanical properties (Kokubo et al., 2003; Sadat-Shojai, 2013; Ramesh et al., 2015), biocompatibility and bioactivity (Webster et al., 2001; Sadat-Shojai, 2013). Therefore, many attempts of powder processing have been carried out to synthesize bioactive HA with the aim of obtaining the most effective synthesis method and conditions to produce distinct particle morphology (Kokubo et al., 2003).

The most popular sintering technique used is the conventional pressureless sintering. However, the long sintering hours usually result in coarse-grained microstructure and low mechanical properties. In order to overcome the problem of grain growth, unconventional sintering (e.g. microwave sintering and hot isostatic pressing) has been introduced in which provides fine microstructure, improved mechanical properties of the material and reduced manufacturing costs due to energy savings, lower temperature of sintering and shorter processing times (Khalil, 2007).

HA can be converted from natural bio-sources such as bovine bones, fish bones, cuttlefish shells, oyster shells and coralline via solid-state processing. These biological compounds are generally denoted as calcium-deficient and containing a wide variety of relatively small amounts of substitute atoms or groups such as carbonate, Na, Mg and Sr

ions (Ho et al., 2013; Wu et al., 2015). The primary advantage of using bones from the animal species is the similarity of its inherent morphology and pore structure to human bone. However, problems do arise due to the variable nature of the bone's physical and chemical properties and unlike eggshells, the continuous use of some of these resources may lead to their extinction, for example in the case of corals as they have a slow growth rate (Wu et al., 2013).

Concurrently, waste eggshell which composed predominantly of CaCO_3 (~ 94 %) has been used as a raw material or direct source of calcium precursor to synthesize HA. In addition, the remnants of several trace elements from the natural biological origin of the eggshells e.g. K, Na, Mg, Si and Sr, in the crystalline structure of synthesized HA make its composition similar to human bone. On the other hand, synthetic HA requires laborious processes in order to incorporate these ions into its lattice structure which potentially increases the cost of production on top of its high cost in acquiring these precursors (Landi et al., 2003; Pietak et al., 2007). Thus, these drawbacks justify the usage of natural resources as precursors in the synthesis of HA, as it is both sustainable and cost effective. Besides that, the HA synthesized from eggshell demonstrated superior sinterability and better morphology when compared with HA synthesized from other sources (Kumar et al., 2012; Abdulrahman et al., 2014). In terms of cell culture, HA synthesized from eggshell showed a better cell response because the other elements inherent in eggshell could induce a better guide signal for the cells to adhere and migrate (Landi et al., 2010; Bang et al., 2015).

HA derived from eggshell can be synthesized by microwave irradiation (Krishna et al., 2007; Kumar et al., 2012), precipitation (Habib et al., 2012; Kamalanathan et al., 2014), ball milling and attrition milling processes (Gergely, et al., 2010) and solid state reactions (Ho et al., 2013; Wu et al., 2013). The milling process is carried out for homogenization whilst structural transition takes place during sintering. However, it is

reported that this milling process induced the risk of contamination that affects the purity of the end product (Rhee, 2002; Evis & Webster, 2011). As a result, the dry method particularly solid-state method has received the least attention probably because of the difficulty in obtaining homogeneous HA composition and small diffusion of ions within the solid phase (Evis & Webster, 2011; Sadat-Shojai et al., 2013). However, this method is known to be suitable for mass production of highly crystalline HA (Rhee, 2002) powders with good mechanical properties (Pramanik et al., 2007) as it does not require precise control condition. By modifying the milling process to minimize contamination, the eggshell derived HA powders was fabricated using solid-state reaction recently (Ho et al., 2013). Based on these studies, homogeneous mixing of the starting materials is utmost important whilst proper heat treatment of eggshells is necessary before carry out further heat treatment or sintering process for the solid-state reaction to take place.

Thus, in this research pure HA was synthesized using waste eggshell as calcium precursor based on a novel and simple solid-state reaction and also by using inorganic Ca precursors through two wet methods (wet chemical precipitation and sol-gel method), in order to compare the behavior of each powder upon sintering. Wet chemical precipitation and sol-gel methods have been classified as simple routes employed in producing HA (Nayak, 2010; Harabi et al., 2011) and are able to produce high-purity HA (Sanosh et al., 2010). Moreover, the sol-gel method employed in this work is economically attractive, using nitrates compounds as raw materials which are cheaper and easily obtained (Sanosh et al., 2010; Seema, et al., 2012), compared to a conventional sol-gel method which usually uses expensive alkoxide compounds. However, for both methods, the reaction media involves no foreign elements and most importantly, they produces only water as the by-product.

For the preparation of dense HA ceramics, the prepared green compacts were subjected to two types of sintering process, e.g. the conventional pressureless and microwave sintering. This step is employed to evaluate the effect of different sintering method on the densification and mechanical properties of synthesized HA. In addition, previous research works on eggshell-derived HA (HA-Es) through solid state synthesis have only be focusing on the synthesis and characterization on the synthesized HA-Es powder. Therefore, a thorough mechanical property and biological performance (in vitro) evaluation on the sintered HA-Es samples are necessary to evaluate its viability for biomedical applications.

1.3 Objectives

The present research aims at producing phase pure HA from natural sources by using waste eggshells as a calcium precursor based on solid state sintering method. In this work, phase pure HA was also synthesized via wet chemical synthesis route as proposed by Ramesh (2004) and sol-gel synthesis as proposed by Sopyan et al. (2008). Sintering studies via a conventional pressureless sintering and microwave sintering were performed on compacted HA ceramics prepared from each method to evaluate its mechanical properties.

The main objectives of the research are:

1. To develop a process to produce eggshell-derive pure HA using solid state sintering method.
2. To synthesis a well-defined, crystalline, pure HA phase powder using two techniques; wet precipitation technique and sol-gel method.
3. To investigate the sinterability and properties of synthesized HA and compare to the eggshell-derived HA powder.

4. To investigate the biocompatibility nature of the eggshell-derived HA for biomedical application.

The process flow of the work is shown in Figure 1.1.

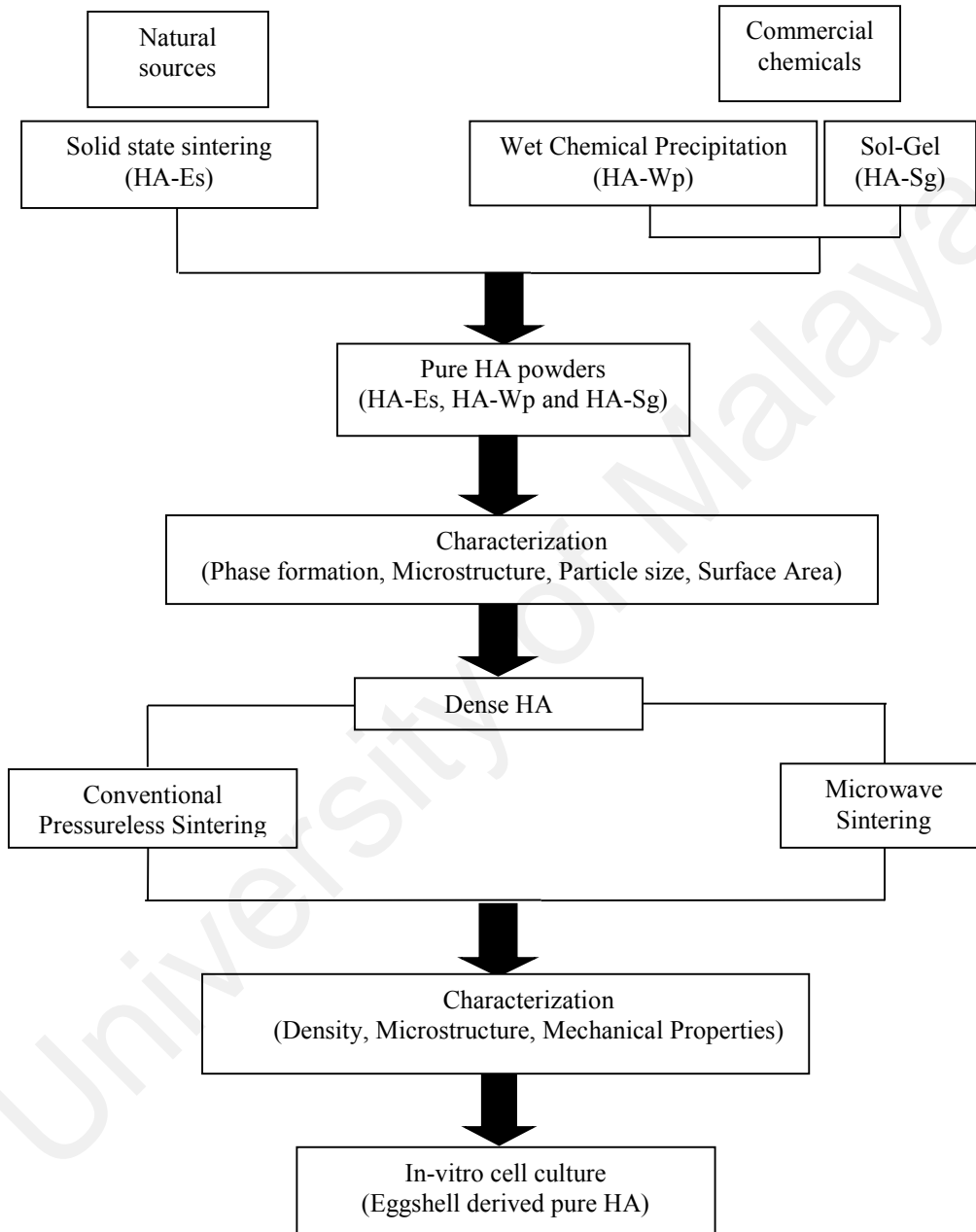


Figure 1.1: Flow chart of dense sample preparation and characterization

1.4 Structure of the Thesis

Chapter 2 provides a brief overview on the bioceramics particularly HA, the origin of available Ca precursors and various processing techniques to produce HA together with previous studies that have been performed to synthesis HA powder. This chapter also reviews the literature related to the type of sintering methods and parameters and theories that governed the mechanical and biological properties of dense HA ceramics.

Chapter 3 describes the experimental procedure and synthesis technique employed to manufacture the starting HA powder and its dense ceramic from natural sources and commercial chemical Ca precursors. The various characterization methods and equipment used in this research are also presented in this chapter.

The results and discussion are presented in two chapters. Chapter 4 focuses on the results obtained for the three different HA powders, e.g. HA prepared from waste eggshell through solid state sintering (HA-Es) and also HA prepared through wet chemical precipitation (HA-Wp) and sol-gel method (HA-Sg) in terms of powder characteristic.

Meanwhile, the second part of the result and discussion as presented in Chapter 5 deliberates on the effects of different sintering methods that are conventional pressureless sintering and microwave sintering on the sinterability and mechanical properties of HA. The outcome of the bioactivity and biocompatibility studies of HA cell response at selected sintering temperature is also discussed in this chapter.

Finally, Chapter 6 presents the conclusion of the current research and provides some suggestions for future work.

Other relevant details pertaining to the research work and thesis are included in the various appendices.

CHAPTER 2: LITERATURE REVIEW

2.1 Introduction

Naturally derived bone grafts have been used for years as the primary source in the reconstruction of human bone defects. Harvesting autografts have the osteogenic capacity and no adverse immunological response. However, the supply is limited by the physiological conditions of the donor site to precisely duplicate the replaced bone. Moreover, it caused additional cost and pain for the patient due to the following surgery for harvesting. Although allografts are available in considerable quantity but they have main constraints of transplantation due to immunogenic effects.

Thus, with such critical arguments, a contrast approach to naturally derived bone graft was taken for the reconstruction of bone defect. Implantation method was generated which involves the use of implants made or modified from the man-made material into artificial bone substitute materials (He, et al., 2012). In general, this artificial bone substitute material is termed as a biomaterial. Implant has prominent benefits in terms of availability, reproducibility and reliability over transplant. These implants were then developed which anticipate interaction with the host tissues without posing a viral or bacterial risk to patients and does not damage healthy tissue (Eshtiagh-Hosseini, et al., 2007). Therefore, development of artificial bone substitution materials appears to be of great importance for clinical applications

2.2 Biological Apatite

Bone is a living composite material composed of cells and a blood supply encased in a strong, interwoven composite structure (LeGeros & LeGeros, 1993). It is build up by the organic constituents of collagen (30 wt %) and the inorganic mineral of an apatite phase in the chemical arrangement termed calcium hydroxyapatite (70 wt %). Besides

that, this non-stoichiometric apatite exhibits the same crystal structure as stoichiometric HA (Lee & Oh, 2003). The reported size of biological apatite crystals generally lies within the nanometric level of 30-50 nm (length), 15-30 nm (width) and 2-10 nm (thickness) (Dorozkhin, 2010). However, the values reported in the literature slightly vary due to the different treatment methods and analysis techniques used.

It should be mentioned that calcium phosphate in bone is similar, but not identical to mineral HA. This is because bone mineral composed of non-stoichiometric HA with significant amounts of carbonate ions and traces of other ions are substituted into its structure (Siddharthan et al., 2009). The presence of a small quantity of these ions has been known to be beneficial to the bone as well as calcium phosphate based implants as it enhances the compressive strength of bone (Pietak et al., 2007). Bone is essentially brittle due to poor tensile strength, nevertheless, it does have a degree of significant elasticity contributed by its organic components (collagen) (Dorozkhin, 2010). Table 2.1 shows list of the trace amounts of ions in the bone mineral lattice structure. For instance, the presence of sodium and magnesium ions is essential in bone development. A decrease in its ionic content results in a decrease in osteoblast cell activity, which causes bones loss and fragility (Akram et. al, 2014). Besides that, sodium ions are beneficial in terms of bone metabolism (Siddharthan et al., 2009).

Table 2.1: Foreign ions in the HA lattice of human bone

(Milovac et al., 2014; Siddharthan et al., 2009)

Cations		Anions	
Barium	Ba ²⁺	Carbonate	CO ₃ ²⁻
Calcium	Ca ²⁺	Chloride	Cl ⁻
Iron	Fe ²⁺	Fluoride	F ⁻
Magnesium	Mg ²⁺	Phosphate	PO ₄ ³⁻
Potassium	K ⁺	Hydroxyl	OH ⁻
Silicon	Si ²⁺		
Sodium	Na ⁺		
Strontium	Si ²⁺		

Although the shape of bone varies in different parts of the body, similar physicochemical structure of bone was observed for these bones (Yuan & Groot, 2004). The major constituents of human bones is shown in Figure 2.1. Basically, bone is comprised of a dense outer layer of cortical or compact bone with the density of ~1.80 g/cm³ and wrapping the cancellous or also known as trabecular bone. This cancellous bone has a porosity of 75-95 % (density ~0.2 g/cm³) (Vallet-Regi & Gonzalez, 2004; Dorozhkin, 2009) as shown in the figure below. In terms of mechanical properties, the porosity of the cancellous bone has reduced both the strength and weight of the bones. Porosity, cortical bone thickness and solid matrix organization which is derived from the organic phase of bone influenced its mechanical properties and subsequently its load bearing ability (Dorozhkin, 2009).

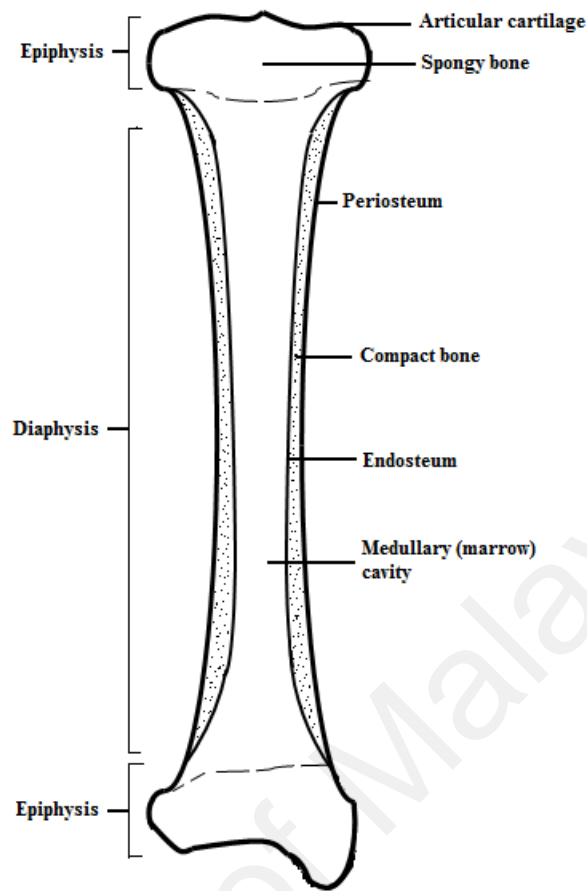


Figure 2.1: Structure of a long bone in longitudinal section

Mechanical properties of bone is governing by two factors that are the compartment of bone (cortical vs. cancellous) and the bone orientation. Cortical bone is basically high in strength and fracture toughness (Dorozhkin, 2009) and this is attributed to the layered microstructure of the HA matrix in the cortical bone (Orlovskii et al., 2002). Nevertheless, cortical bone has lower strain to failure than cancellous bone with higher modulus of elasticity (Hench & Thompson, 2010). This fact conform to the function of cancellous bone that is to direct stresses to the denser cortical bone (Ruppel et. al, 2008). Table 2.2 lists the primary mechanical properties of the human bone tissues.

Table 2.2: Mechanical properties of skeletal tissues (LeGeros & LeGeros, 1993)

Properties	Cortical Bone	Cancellous Bone
Compressive Strength (MPa)	100-230	2-12
Flexural, Tensile Strength (MPa)	50-150	10-20
Strain to Failure	1-3	5-7
Young's (Tensile) Modulus (GPa)	7-30	0.5-0.05
Fracture Toughness (K_{Ic}) (MPam ^{1/2})	2-12	-

2.3 Biomaterial

Biomaterial is defined as any synthetic material that constitutes parts of medical implants that can be used in implantation or incorporation with a living system in order to supplement or replace the functions of living tissue or organs (Li et al., 2003; Park & Lakes, 2007). Artificial materials such as hearing aids and wearable artificial limbs are not regarded as biomaterials as they are only in contact with the skin. However, biomaterials is unique due to its special biocompatibility with the living system which fulfil the biological prerequisite (Dee, et al., 2003).

In a consideration for implantation, a biomaterial's tissue response is highly important. This is because the reconstruction of a normal tissue could be completed without inflammation if the biomaterial is bioactive and bioresorbable. Besides that, it has to be steadily resorbed over a period of time to in order to avoid hindering further tissue growth (Kim & Mooney, 1998). This criterion is important as it permits the organism to replace the foreign material by a fully functional bone in expected time schedule (Ignatius et al., 2001). Besides that, the selected biomaterial should also allow the engineered tissue to maintain sufficient mechanical integrity to support itself in early development. Additionally, biomaterials for implant should also have sufficient physical

and mechanical properties (i.e. strength, stiffness and fatigue) to endure in vivo forces exerted by the neighboring tissue (Kim et al., 2000). However, this requirement depends on the tissue sites as well as the applications.

Note that, it is advantageous to have the ability to tailor the mechanical properties of the biomaterial to match those of the body component which it is replacing. The workability of a biomaterial as an implant in the body rest on the materials properties (composition and morphology), design and biocompatibility (Li et al., 2003). Researchers have classified synthetic biomaterials into several categories that are polymers, metals, ceramics and composites. Each of these biomaterials has different properties which give each material unique capabilities and advantages as showed in Table 2.3. Among these biomaterials, bioceramics was found to be most bioactive as it can be bonded directly to the bone. Therefore, in order to efficiently perform its intended function, biomaterials must exhibit several general requirements such as biocompatibility, degradability, osteoconductivity and mechanical integrity. Besides these, the material also should be reproducible, reliable and also easily available for practical usage as an implant (Hench, 2000).

Table 2.3: Typical physical properties of different biomaterials

(Carter and Norton, 2007)

Material	Density (g/cm ³)	Ultimate Tensile Strength (MPa)	Compressive Strength (MPa)	Young's Modulus (GPa)	Fracture Toughness (MPam ^{1/2})
HA	3.1	40-300	300-900	80-120	0.6-1.0
Tri-calcium phosphate	3.14	40-120	450-650	90-120	1.20
Bioglasses	1.8-2.9	20-350	800-1200	40-140	-2
Apatite and Wollastonite (A-W) glass ceramic	3.07	215	1080	118	2
Silica glass	2.2	70-120	-	70	0.7-0.8
Aluminum Oxide	3.85-3.99	270-500	3000-5000	380-410	3-6
Partially Stabilized Zirconia	5.6-5.89	500-650	1850	195-210	5-8
Polyethylene	0.9-1.0	0.5-65	-	0.1-1.0	0.4-4.0
Titanium (Ti)	4.52	345	250-600	117	60
Ti/Aluminum/Vanadium alloy	4.4	780-1050	450-1850	110	40-70
Ti/Aluminum/Niobium/Tantalum alloys	4.4-4.8	840-1010	-	105	50-80

2.3.1 Calcium Phosphate Ceramics

Apatite [Ca₁₀(PO₄)₆X₂] is a type of calcium phosphate with exceptional biocompatibility and it is the main inorganic component of human hard tissues such in tooth and bone. The "X" in the apatite formula represents hydroxyl (OH⁻) group for

hydroxyapatite (HA), fluoride (F⁻) group for fluoroapatite and chloride (Cl⁻) group for chloroapatite (Pramanik et al, 2007). These minerals show excellent tissue response with good osteoconductivity (Ishikawa et al., 2003) and osteointegration (Jaramillo et al, 2010).

Based on this fact, calcium phosphates based bioceramics have been the topic of interest for over half a century and have been the substitute material of choice in both dentistry and medicine field due to its chemical similarity to the dominant mineral phase (Jillavenkatesa, et al., 1999; Nakano, et al., 2002; Yuan and Groot, 2005; Ramesh, et al., 2007b; Lukic, et al., 2012). Another primary consideration in the clinical application of calcium phosphates is the biological performance or response. It is known that calcium phosphate ceramics are bioactive and bioresorbable in nature, besides showing no foreign body response during implantation. It has been used since the 1980s in coating of orthopedic (total hip and knee surgery) and dental implants, maxillofacial surgery and scaffolds for bone growth (Hench, 1998).

Despite that, the existence of different forms and phases of calcium phosphate is subjected to the reaction temperature, partial pressure of water and the presence of impurities (Hench, 1998; Kalita et al., 2007). The stability of this bioceramic in solution normally increases with increasing Ca/P ratio (Best et al., 2008; Juhasz & Best, 2012) whilst rate of dissolution increases as the Ca/P ratio decreases. There are mono-, di-, tri-, and tetra-calcium phosphates, in addition to the commercially available hydroxyapatite, β -tricalcium phosphate and α -tricalcium phosphate. In this case, the usage depends on the requirement (e.g. degradable or bioactive) for the intended application. In addition, the phase stability of calcium phosphate ceramics depend on temperature and the presence of water. This is because the Ca²⁺, PO₄³⁻ and OH⁻ ions can be replaced by other ions (Hench, 1998). For instance, in a series of sintering of calcium phosphate ceramics at various temperatures, the final product of calcium phosphate can

be hydroxyapatite or β -TCP or the mixture of both (HA+ β -TCP). However, the most thermodynamically stable calcium phosphate phase at physiological pH ($\text{pH} \geq 4.3$) is apatite (Correia, et al., 1996; Pattanayak et al., 2011). Table 2.4 summarizes the various forms of calcium phosphates.

Table 2.4: Various forms of calcium phosphates

Compound	Chemical Formula	Abbreviation	Ca/P ratio	Usage
Tetracalcium phosphate	$\text{Ca}_4(\text{PO}_4)_2\text{O}$	TTCP	2.0	Cement
Hydroxyapatite	$\text{Ca}_{10}(\text{PO}_4)_6(\text{OH})_2$	HA	1.67	Bulk material, Cement
Fluoroapatite	$\text{Ca}_{10}(\text{PO}_4)_6\text{F}_2$	FA	1.67	
Calcium deficient apatite	$\text{C}_{10-x}(\text{PO}_4)_{6-x}(\text{HPO}_4)_x(\text{OH})_{2-x}$	CDHA	<1.67	
Biphasic calcium phosphate	$\text{Ca}_{10}(\text{PO}_4)_6(\text{OH})_2 + \text{Ca}_3(\text{PO}_4)_2$	BCP	1.55-1.66	
β -tricalcium phosphate	$\beta\text{-Ca}_3(\text{PO}_4)_2$	β -TCP	1.5	Bulk material, Cement
α -tricalcium phosphate	$\alpha\text{-Ca}_3(\text{PO}_4)_2$	α -TCP	1.5	Cement
Octacalcium phosphate	$\text{Ca}_8(\text{PO}_4)_4(\text{HPO}_4)_2 \cdot 5\text{H}_2\text{O}$	OCP	1.33	
Dicalcium phosphate dehydrate	$\text{CaHPO}_4 \cdot 2\text{H}_2\text{O}$	DCPD	1.0	Cement
Anhydrous dicalcium phosphate	CaHPO_4	DCPA	1.0	Cement

It is reported that the usage of synthetic apatites for repairing damaged hard tissues are expected to result in close resemblance to composition and structure to those of biological apatite (Han et al., 2002). However, the limitations in ceramic is the brittle nature of the material, which constraints its usage to non-load bearing applications (Siva Krishna et al., 2007). Hence, continuous attempts have been directed to overcome this weakness by means of improving the synthesis methods to produce ceramics with enhanced mechanical properties. As a consequence, the field of bioceramics research is progressing at a fast pace (Ishikawa et al., 2003).

2.3.2 Hydroxyapatite

Hydroxyapatite (HA) with the chemical composition of $\text{Ca}_{10}(\text{PO}_4)_6(\text{OH})_2$, is the most significant among the calcium phosphate compounds as its composition is found close to the dominant inorganic component of human body hard tissues such as bone, dentin and enamel. Literally, mineral component of bone is composed of nanostructured non-stoichiometric HA of dimensions 20 nm in diameter and 50 nm long with trace amounts of ions such as Na^+ , Mg^{2+} , K^+ , F^- and CO_3^{2-} (Siva Krishna et al., 2007). Besides being non-toxic, one of the outstanding hydroxyapatite properties as a biomaterial is its excellent biocompatibility which originated from its similarity in chemical composition to hard tissue. It also appears to promote and form a direct chemical bonding with bone (bioactive) (Ishikawa, 2009, Ashley, et al., 2007). This behaviour also leads to an intimate physic-chemical bound between the implants and bone (osteointegration) (Dorozkhin, 2010). This criterion meets the requirement of any material designed for bone repair and augmentation. In addition, HA acts as reinforcement in hard tissues and is responsible for the stiffness of bone, dentine and enamel. Park and Lakes (2007) reported that the mineral part of bone and teeth is made of a crystalline form of calcium phosphate that is similar to HA. Due to the high bioactivity, hence HA in the

nanocrystalline form is usually applied for implant coatings and dental cements (Goloshchapov et. al, 2013).

With respect to clinical applications, synthetic HA powder has been used in surgery since 1920 to promote osteoblast adhesion and proliferation in surgery (Anselme, 2000; Palin et al., 2005). Since then, HA has been used in a variety of physical forms over the last four decades such as a sintered ceramic in granular block or porous form (Slosarczyk & Bioloskorski, 1999; Gibson, et al., 2002; Nakano, et al., 2002; Kokubo et al., 2003; Tadic, et al., 2004; Zhang & Vecchio, 2006), as a deposited coating on implants to promote bone in-growth (Durucan & Brown, 2000; Kim, et al., 2005; Zhang and Vecchio, 2006; Suzuki, et al., 2010; Ryu, et al., 2002; Trommer, et al., 2007) or as a filler (Gibson, et al., 2002) to replace damaged bone (Goloshchapov et al., 2013). Typical mechanical properties of dense HA as compared to hard tissues are shown in Table 2.5.

Table 2.5: Comparison of mechanical properties of sintered HA with hard tissue (Hench, 1998)

Properties	Cortical	Cancellous	Dense HA
Compressive Strength (MPa)	250-400	140-300	270-900
Young's Modulus (GPa)	40-80	10-22	35-120
Fracture Toughness (MPam ^{1/2})	3.4-3.7	2.2-4.6	0.7-1.2
Vickers Hardness (GPa)	0.5-1	0.4-0.7	3.0-7.0

However, the inherent brittleness and low mechanical strength, i.e. lower toughness (0.8-1.2 MPam^{1/2}) and flexural strength (< 140 MPa) than those of human cortical bone (Hench, 1991; Suchanek & Yoshimura, 1998; Ramesh, 2001; Dorozkhin, 2010) limits

its application to the non-load bearing areas. Moreover, the poor mechanical behaviour is more obvious for highly porous ceramics and scaffolds due to the conflicting requirements of porosity and strength (Ratner et al., 2004). In general, porosity ($> 100 \mu\text{m}$) is considered as a requirement for proper vascularization and bone cell colonization (Hing et al., 1999). As a result, HA is mostly used as fillers and coatings (Dorozkhin, 2010).

Although application of pure HA ceramics is restricted due to the brittle nature of HA, its preparation with superior mechanical properties is possible if the starting HA powder is stoichiometry, i.e. has Ca/P molar ratio of 1.67. Moreover, mechanical strength and bioactivity of HA depend strongly upon its microstructure such as grain size and distribution, porosity and its shape and distribution, and material crystallinity (Ishikawa et al., 2003). Therefore, with proper designing and processing, HA with improved and desired properties could be prepared depending on the needs of application. This will improve the mechanical properties of HA and later enhance the applicability of HA as an implant material in load bearing application.

2.4 Fabrication of Calcium Phosphate Nanoceramics

Traditionally, nanostructured ceramics are usually processed via three main steps that start with powder synthesis, shaping and sintering process. In this case, dense or porous HA ceramics are processed by compacting HA nanopowders at high pressures followed by sintering at a temperature lower than the melting point in various atmospheres (Tas, 2000; Veljovic et al., 2009). Sintering temperature, duration of sintering and composition of the ceramic materials used are among the factors that controlled the mechanical properties of HA (Veljovic, 2009).

In the last 15 years, numerous studies have been carried out and showed that HA derived from natural resources and biowaste such as bovine bone, porcine bone, fish

bone, cuttlefish bone, and coral are capable of producing calcium deficient HA which makes it an attractive alternative in the production of biomedical implants (Ben-Nissan, 2003; Prabakaran et al., 2005; Boutinguiza et al., 2012; Milovac et al., 2014). But these attempts possible success is connected with issues of impaired biological properties (Lukic et al., 2012).

Hence, a promising way to obtain materials with mechanical properties matching that of natural bone tissue could be a fabrication of fully dense nanostructured materials through sintering process. It is known that fully dense bioceramics with average grain size below 100 nm result in improved mechanical properties (Wang, 2007; Wang & Shaw, 2009). Besides, surface properties, like wettability, attachment of important macromolecules, and cell adhesion, proliferation and differentiation would be enhanced because of the presence of high volume fraction of energetically rich grain boundary areas (Bose, 2010).

A lot of emphasis is now being placed on nanomaterials or nanostructured materials, which brings specific difficulties because of the nanometric size of particles and their growth during high temperature treatment (Champion, 2013). Various sizes of biological apatite crystals have been reported which depends on different treatment methods and analysis techniques and the values ranging from 30-50 nm (length), 15-30 nm (width) and 2-10 nm (thickness) (Dorozkhin, 2010). In general, nanostructured biomaterials are described as any biomaterials whose structure or morphology can be engineered to get features with nanometer-scale dimensions (Thomas et al., 2006). The nanometer-scale of particle size is needed to accommodate large surface to volume ratio as greater surface area allows higher sinter ability that leads to the use of lower densification temperature (Ramesh et al., 2007b) and maintain HA phase stability. Hence, nanostructured ceramics can be sintered at a lower temperature.

Moreover, nanoscale materials have unique surface properties such as increased number of grain boundaries and defects at the surface compared to conventional micron-sized materials. The increasing number of grain boundaries has proven to contribute in trivial ductility before failure (Dorozkhin, 2010). As for actual clinical application, a higher amount of nanoscale defects (i.e. pores) influences the type and amount of adsorption of selective proteins which could enhance specific osteoblast adhesion. Despite that, obtaining nanosized HA crystals is utmost important in biomedical applications due to its structural biomimicry and increased osteoconductivity, bioactivity and osseointegration than HA with coarser crystals (Wu et al., 2013).

In a study of investigating the influence of crystallinity, the same 20 nm nanoparticle size of amorphous HA and crystalline HA films have been prepared (Xu et al., 2001). In that research, more cells were adsorbed and proliferated on the well-crystallized HA films than those on the amorphous films. This new view of the relationship between the crystallinity of calcium orthophosphates and the responses of MSCs emphasizes the importance of size and phase control in the application of biomedical materials (Xu et al., 2001; Walsh et al., 2008). For this, a high degree of crystallinity and chemical stability have been included in the desirable properties of an ideal nanostructured HA.

The characteristics of synthesized biomaterials in laboratory conditions depend on their synthesis parameters, which later reflect their applicability. Mechanical strength of HA mainly depends on grain size, grain size distribution, porosity and other micro structural defects (Sinha, et al., 2001). For example, the presence of hard agglomerates tends to disrupt the densification process resulting in the formation of defects such as porosity, grain growth and micro cracks (Tan, et al., 2007).

Hence, the fabrication of such a densely sintered ceramic almost always starts with the synthesis of a hydroxyapatite powder of desirable particle characteristics,

characterized by fine and uniform particle size, preferably in the nanometer range, homogeneity in phase and chemical composition together with a minimized degree of particle agglomeration (Yeong et al., 2001).

2.5 Synthesis of Hydroxyapatite

Over the years there are various techniques developed to prepare HA. In general, the raw materials used to synthesize HA originate from inorganic based precursor or from the natural organic based resources which include conversion from marine coral derivatives to natural HA with acceptable porosity (Abdulrahman et al., 2014). Nevertheless, both types of biomaterials are equally bioactive and biocompatible in nature. For the synthesis using inorganic component, the synthesis methods are divided into two types that are wet chemical methods (precipitation, sol-gel and hydrothermal) and dry processes (solid-state reactions). These methods vary in terms of the precursors used, processing cost, the morphology of the HA powder produced, Ca/P ratio, as well as the particle size produced (Sadat-Shojai et al., 2013). Moreover, the conventional methods involve no trace of beneficial elements in the synthesis of HA. In addition, the HA crystals synthesized using the synthetic precursors are different from the apatite crystals since the apatite crystals grown in the living system bear smaller crystallite size thus have a large surface area which further allows them to absorb the extra amount of ions (Verdelis et al., 2007; Abdulrahman et al., 2014). Moreover, this processing method of using synthetic precursors is associated with the relatively high cost due to the use of high purity reagents.

2.5.1 Development of HA from Natural Organic Sources

The continuous research attempts in producing biocompatible biomaterial from natural organic waste have added a valuable aspect of its recovery. This is because some of this waste contains active compounds that have value in medical applications. Moreover, the waste is readily available and cheap as compared to the cost of the whole biomaterial production.

HA extracted from natural resources and bio-wastes is a non-stoichiometric with presence of trace ions which considered as a potential material for bone graft purposes, making its usage in the development of bone-like implants highly desirable (Goller et al., 2006; Best et al., 2008; Abdulrahman et al., 2014; Akram et al., 2014; Milovac et al., 2014). Presence of beneficial cations like Na^+ , K^+ , Mg^{2+} , Sr^{2+} , Zn^{2+} and Al^{3+} or anions like F^- , Cl^- , SO_4^{2-} and CO_3^{2-} or the presence of both is proven to be better for different medical application (Palmer et al., 2008). Meanwhile, synthetic HA is a stoichiometric material with Ca/P ratio of 1.67 which requires strict control over process parameters to produce high-quality stoichiometric HA. Hence, the incorporation of these trace ions into its stoichiometric lattice structure is a laborious process which potentially increases the cost of production on top of its high cost in procuring these precursors (Landi et al., 2003; Li et al., 2007; Pietak et al., 2007, Akram et al., 2014). These drawbacks justify the further efforts in utilizing natural resources and biowastes as precursors in the synthesis of HA. Despite the superior characteristics of the extracted material, this method is also economical and contributes to the environmental benefits of waste recovery (Sadat-Shojai, 2013).

Generally, HA and its precursors can be converted from biological resources and these resources can be grouped into 3 types that are bone, plants and biogenic. In this case, bones present mammalian (bovine, sheep, pig), chicken and fish bones, whilst biogenic sources are eggshells, seashells and conversion from marine coral derivatives to

natural HA with acceptable porosity. These biological compounds that denoted as calcium-deficient contain a wide variety of relative small amounts of other substitute atoms or groups such as carbonate, Na, Mg and Sr ions (Ho et al., 2013; Wu et al., 2015). It was reported that the biomolecules amount of these waste materials influenced the latter product shape, size and its crystal morphology which reflected their applications.

The nature of a bovine bone which is composed of HA nanocrystals and collagen fibers have drawn the attention to its feasible extraction of natural HA. Moreover, these mammalian bones especially the bovine bones are a rich source of ion-doped HA. It was reported that a complete conversion of bovine bone from 1.6 kg of compact bone can furnish as much as 1 kg of HA (Bahrololoom et al., 2009). In short, process of HA extraction from natural sources (i.e. bovine bone) via various techniques (simple thermal treatment, enzymatic hydrolysis, plasma processing, subcritical water processing and alkaline hydrothermal analysis) start off with the removal process of unwanted organic matter that inherent in the bone. The animal bones are thoroughly washed, boiled with distilled water, followed by washing with NaOH or hypochlorite to remove dirt from the surface of the bones (Abdulrahman et al., 2014). As for calcinations regime, bones are heated in a furnace at temperatures between 500 and 1400 °C in order to completely remove the organic materials from the bone while leaving pure HA as residue (Sadat-Shojai, 2013) and to enhance the crystallinity of HA while avoiding thermal decomposition of the final HA product (Abdulrahman et al., 2014). However, it was reported that calcinations treatment above 850 °C destroys the pathogens and could solve the problem of probable transmission of disease from the cattle to the patient (Krishna et al., 2007). Subsequently, bones are either directly cut into small pieces or ball milled. These steps will latter determine the morphology and particle size of the final product as the milling duration influence the size of the particle.

For example, the Vibro milling method has been employed on deproteinized bovine bone after calcination at 800 °C for 3 hours where the longer vibro-milling time resulted in the break-down of HA needles into fine powder (Ruksudjarit et al., 2008).

After all, the primary advantage of using bones from the animal species is the similarity of its inherent morphology and pore structure to human bone. However, problems do arise due to the variable nature of the bone's physical and chemical properties, calcinations temperature, and the extraction technique (Abdulrahman et al., 2014; Bang et al., 2015). Any of these conditions can affect the properties, efficiency, phase purity and size distribution of HA. Furthermore, certain ethical issues will always be an issue to the HA produced from animal bones and will no doubt limit the use of such HA (Akram, 2014). In a research of pure HA extraction from bovine bone biowaste by Barakat et al. (2009), three extraction techniques was employed i.e. conventional thermal decomposition (750 °C), subcritical water extraction (275 °C) and alkaline hydrothermal method (250 °C), respectively, decompose, dissolve and hydrolyze the organic compounds of bovine bone. The results showed that all three methods were capable of producing phase pure HA with an average yield of 65 % but with different morphology and particle size which were influenced by the extraction process employed. Following this development, HA products from the bovine origin are already commercially available (Tadic & Epple, 2004; Dorozkhin, 2010). Examples of these products are Endobon[®], Cerabon[®], and Pep-Gen P-15[®] (Piccirillo et al., 2013).

Following this, exploitation of the presence of calcium carbonate in biogenic sources, i.e. skeleton of various marine species (fish bones, fish scales, algae, cuttlefish bones, corals, seashells) have arisen in the synthesis of HA from natural resources. The first investigation of the fish bones as natural materials for HA was done by Ozawa and Suzuki (2002) through thermal treatment process. In that study, it was found that single HA phase was detected via XRD analysis up to < 1300 °C following the complete

removal of organic matter at ~ 600 °C. In an experiment reported on the extraction of HA from fish scales by Mondal et al. (2010), it was found after proper organic removal treatment and calcinations, single phase HA appeared at 800 °C until it decomposed to secondary phases of β -TCP and TTCP at 1000 °C and 1400 °C, respectively. Further study on the same natural sources but through enzymatic method by Huang et al. (2011) concluded that the cell activity of HA derived from fish scale on the MG63 osteoblast-like was comparable to that of commercial HA samples (Piccirillo et al., 2013). Fish bones and scales are also a good starting source to develop nano-to micron-sized calcium deficient HA with good biocompatibility. Other than fish bones and scales, seashells also a by-product of the fishing industry, have been used and converted into valuable HA powder.

Besides these species, it is well noticed that the calcium carbonate originated from marine species exhibits similar characteristics of porosity and interconnectivity found in human bone which favors cellular growth and osteointegration (Walsh et al., 2008; Piccirillo et al., 2013; Shadat-Shojai, 2013). For example, corals have a 3D skeleton structure, highly porous with high level of interconnectivity and contain calcium carbonate in the form of calcite as its main component (Piccirillo et al., 2013). Hence, appropriate conversion of the carbonate based corals into phosphate whilst maintaining its natural interconnected porous structure is necessary.

HA-based products based on the conversion from marine skeleton has been made available in the market such as ProOsten[®] and Interpore200[®] made from *Goniopora*, one of coral species (Dorozkhin, 2010). Several studies were performed to assess their effectiveness as bone substitutes. However, the continuous large consumption of these corals may lead to their extinction as they have a slow growth rate (Wu et al., 2013). Moreover, corals are not available widely but only in some coastal water region. With that, cuttlefish bones later have become the main attention since they have similar

carbonated porous interconnected structure as found in corals. For example, an obvious advantage is seen in the development of scaffolds. Interconnected porous networks are required in the development of scaffolds, as it plays a significant role in the transport of metabolic waste, nutrients as well as cell attachment (Milovac et al., 2014). Polymer sponge replication (Ramay & Zhang, 2003; Tripathi & Basu, 2012), gel casting (Ramay & Zhang, 2003; Kim et al., 2011) and freeze casting (Deville et al., 2006; Tang et al., 2013) are some of the methods in which scaffolds are developed from synthetic HA. These methods require various processing routes and conditions, making it a tedious development process. Instead, a simple hydrothermal conversion of natural aragonite from cuttlefish bone at 200 °C has shown to result in a highly interconnected porous structure (Milovac et al., 2014). Moreover, the cuttlefish bone also contains minor trace elements as its mineral components besides calcium carbonate which originates its biocompatibility. This has further justified the advantages of naturally derived HA. However, the availability of cuttlefish bone is also constraint to certain coastal water region.

Further study on the marine species was carried out on Algae. In a research by Walsh et al. (2008), HA was successfully synthesized by reacting the extracted calcium carbonate from red Algae with $(\text{NH}_4\text{OH})\text{H}_2\text{PO}_4$ at 100 °C for 12 hours. Besides that, SEM images showed that the original micro-porous of granular shaped structure with a rough external surface of red Algae remain intact. The same result was also reported in another research on red Algae conversion to HA through hydrothermal treatment (Kusmanto et al., 2008). In this research, HA produced from red Algae was found to be non-cytotoxic and biocompatible with good cell attachment interactions with MG63 cells. Apparently, HA product derived from Algae is also readily available in the market that is Algipore[®]. It has been produced using *Corallina officinalis* and *Amphiroa ephedra* algae through a high-pressure hydrothermal synthesis.

Although some porous structures with good degree of porosity and interconnected pores have already been obtained, however it still lack proper bio-physical response, which can only be shown by scaffolds endowed with a high degree of hierarchy (Studart et al., 2006; Bang et al., 2015). Hence, natural resources from plant with hierarchically structures are further studied in order to improve the bio-response. Tampieri et al. (2009) reported a sequence of thermal and hydrothermal processes which consist of a novel multi-step process (pyrolysis, carburization, oxidation, carbonation and phosphatization) in converting native wood into porous HA while maintaining a highly anisotropic microstructure for bone tissue engineering. The production of HA took place during the last stage of phosphatization process through the hydrothermal treatment. XRD and FTIR results revealed the formation of pure HA phase and the presence of carbonate groups substituted in the HA lattice, respectively. Significant efforts have also been made to synthesize HA using fruits peel extracts of pomelo, grape and sweet potato through hydrothermal method (Wu et al., 2013). In that research, HA derived from pomelo peelings exhibited good aspect ratios, similar morphology to crystalline HA structures of natural bone. It was also reported that HA has been extracted from leaves and stalks of *Catha Edulis* (Khat), basil, mint, green tea and trifolium (Shaltout et al., 2011). HA was found to be the main phase together with minor amount of $\text{Ca}(\text{OH})_2$ in the leaves of Khat and basil plants after subjected to calcinations at 800 °C.

Another source of biogenic sources that have significant impact on the development of biomaterial is chicken eggshells. This waste eggshell has big potential in its usage as a raw material for the synthesis of HA due to its wide availability as waste product in food industries, beauty industries and personal consumption as in home cooking. These eggshells are basically discarded as a waste material. However, the protein-rich membrane which adheres to the shell favours microbial growth. In addition, the expensive cost of eggshells disposal in scarce landfills space indirectly lead to

environmental pollution (Wu et al., 2015). Therefore, the recycle of waste eggshell will reduce the need for waste management and contribute to cleaner environment with improved ecosphere. Despite its wide availability, the remnants of several trace elements from the natural biological origin of the eggshells in the crystalline structure of synthesized HA make their composition similar to human bone. It was also reported that the HA synthesized from eggshell demonstrates superior sinterability and better morphology when compared with HA synthesized from other sources (Kumar et al., 2012; Abdulrahman et al., 2014). Moreover, biocompatibility of eggshell derived HA has been well established in number of research (Krishna et al., 2007). In cell culture, HA synthesized from eggshell showed a better cell response because the other elements inherent in eggshell could induce a better guide signal for the cells to adhere and migrate (Landi et al., 2010; Bang et al., 2015).

2.5.2 Development of HA from Inorganic Sources

There are many methods employed in producing HA powders and they can be categorized into four groups, namely, dry methods, e.g. solid state synthesis and mechanochemical method (Rao, et al., 1997; Pramanik, et al., 2005), wet chemistry methods, e.g. wet chemical precipitation, hydrolysis method, sol–gel, hydrothermal, emulsion method and sonochemical method (Slosarczyk and Bialoskorski, 1999; Kweh, et al., 1999; Jillavenkatesa, et al., 1999; Liu, 2002; Silva, et al., 2003; Feng, et al., 2005; Pattanayak, et al., 2005; Seema, 2012) high-temperature processes, e.g. combustion and pyrolysis (Paz et al., 2012) and combination procedures, e.g. hydrothermal–mechanochemical and hydrothermal–hydrolysis. Based on these techniques, HA powders with various morphology, stoichiometry and level of crystallinity can be prepared. However, there are several disadvantages in these techniques such as expensive raw materials and equipment and low purity of the final HA product. The

other main drawback lies in the impracticable for large scale production due to the complex processes involved.

The subsequent section provides a brief overview of two types of synthesis techniques that have been used by researchers in the production of HA powders and that are dry (particularly solid state reaction) and wet methods (chemical precipitation and sol-gel). The purpose of these processes is to produce HA powders which demonstrate desired characteristics such as high specific surface area and fine grain size.

2.5.3 Dry Methods

Dry methods are defined by the absence of solvent in the HA preparation. This method is known to be suitable for mass production of highly crystalline HA as it does not require precise control condition. In another word, the characteristic of the synthesized HA does not highly influenced by the processing parameters (Sadat-Shojai, 2013). The well-known and simple method is solid state method. Besides that, mechanochemical processing is another successful method to produce nanostructured HA in a dry state (Dorozkhin, 2010). Both methods have the advantages of being straightforward and highly reproducible. However, the mechanical alloying has been greatly used by researchers compared to solid state synthesis because it offers well-defined HA structure (Sadat-Shojai, 2013).

2.5.3.1 Solid state reactions

Traditionally, solid state consists of stoichiometric reaction of powders that requires relatively high temperature in the environment (air, vacuum, or in inert or reactive gasses). However, solid state method has received the least attention in the preparation of HA due to the resultant of heterogeneous HA particles with irregular shape, risk of contamination during milling and long heat treatment times. Moreover, sinterability of

such irregular powders has been reported to be low (Suchanek et al., 2002). However, it is improper to dismiss the usage of solid-state synthesis in the synthesis of HA particles because with proper processing, nanostructured HA powder with regular shape can be achieved.

In this method, solids are not raised to their melting point which means reactions take place in the solid state (subsolidus) hence small diffusion of ions within the solid phase (Evis & Webster, 2011). As a result, increasing the temperatures is generally required to speed up the reaction since it increases the diffusion rate. Generally, the standard ceramic processing through solid state method involves the process of grinding or mixing the solid starting materials using agate mortar and pestle or ball milling for a certain period. Thorough grinding is important to achieve a homogenous mixture of reactants. The dried ground mixture is pressed into a pellet and then subjected to heat treatment. With respect to these steps, there is a risk of contamination during the mixing process and the desired compound may decompose at high temperatures. In addition, high calcination temperature leads to many disadvantages such as large particle size and wide size distribution. Hence, proper and modified mixing process has been introduced and carried out by researchers to minimize the contamination and lower the calcinations temperature (Stojanovic et al., 2005). The calcinations temperature can be lowered by using mechanically activated powders and this could be achieved by subjecting the powder mixture to milling prior calcinations which lead to the decrease in apparent activation energy of the reactants. The advantages of this simple and highly reproducible technique are melting is not essential, inexpensive (less number of raw materials), environmentally friendly and that the products have nanostructure characteristics.

In a research by Gergely et al. (2010), HA has been prepared via solid state prior to heat treatment. Raw eggshell has been treated at 900 °C for 3 hours to obtain CaO

before mixing with H_3PO_4 . The mixture is then milled at 4000 rpm for 5 hours (attritor milling) and at 350 rpm for 10 hours (ball milling) followed by heat treatment at 900 °C for 2 h in air atmosphere. It was reported that nanosize particle of 100 nm was achieved with attritor milling (Figure 2.2 (a)) compared to coagulated samples with smooth surfaces obtained through ball milling as in Figure 2.2 (b).

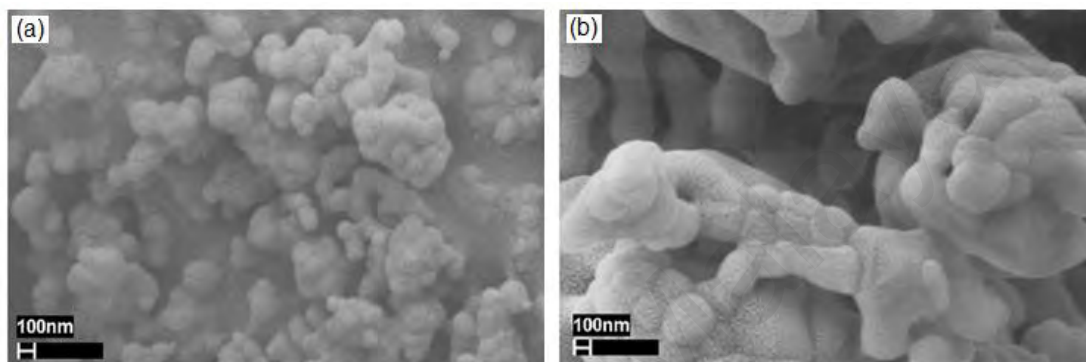


Figure 2.2: SEM micrographs of (a) attrition and (b) ball milled, samples after heat treatment at 900 °C (Gergely et al., 2012)

By modifying the milling process to minimize contamination, the eggshell derived HA powders was fabricated using solid-state reaction recently (Ho et al., 2013). The two types of Ca precursor used were uncalcined eggshell (raw eggshell, CaCO_3) and calcined eggshell (CaO). Meanwhile, dicalcium phosphate di-hydrate (DCPD) was used as phosphorus precursor. Homogeneous conventional mixing with deionized water was carried out. Pure HA was only obtained after heat treated the mixture of calcined eggshell of CaO and DCPD at 1150 °C for 3 hours. Meanwhile, a mixture of HA and β -TCP was obtained after sintering at 1100 °C when using uncalcined eggshell of CaCO_3 . It was thought that the conventional mixing of the precursors was not effective, and therefore, mixing by planetary ball milling for a short time was carried out (1 hour) (Wu et al., 2015). However, the formation of biphasic calcium phosphate (HA+ β -TCP) was reported for the samples sintered at 900 °C to 1100 °C with the gradual disappearance

of β -TCP phase with higher sintering temperature. As a result, highly crystalline phase pure HA having the particle size of 2.54 μm only formed upon sintering at 1200 $^{\circ}\text{C}$. Based on these studies, homogeneous mixing of the starting materials is utmost important whilst proper heat treatment of eggshells is necessary before subjecting to further calcination or sintering process.

2.5.4 Wet Methods

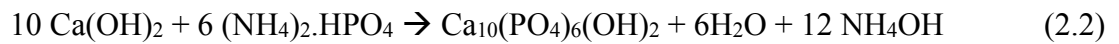
The wet technique can be divided into three main groups that are precipitation, hydrothermal method and hydrolysis of other calcium phosphates. Each method has its own advantages over the others. Among these routes, wet chemistry methods are the most popular, i.e., precipitation and sol–gel, as it presents advantages of precise control over the morphology and size of the particles. Moreover, the wet process produces only water as a by-product (Raynaud et al., 2002; Saeri et al., 2003) and has a low probability of contamination during processing. However, the disadvantage is the composition of the resulting product is greatly affected even by a slight difference in the reaction conditions. In addition, the powder properties such as surface area and morphology also vary when the powder is calcined at different temperatures (Patel, 2001). Meanwhile, hydrothermal process deals with the application of high temperatures to aqueous solutions to facilitate the precipitation of crystals of dimensions larger than those attainable using ordinary wet methods. Although it is able to produce single phase HA, this process is very time consuming and requires equipment that must be corrosion resistant, able to withstand high pressures and high temperatures (LeGeros & LeGeros, 1993).

2.5.4.1 Wet chemical precipitation

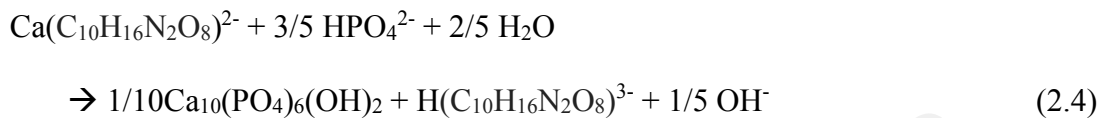
Wet chemical precipitation or chemical precipitation is known as one of the easiest method in preparing HA powder owing to its ease in experiment operations and low working temperatures. Besides that, large amount of HA can be produced in the absence of organic solvents at a reasonable cost (Santos et al., 2004; Monmaturapoj, 2008; Nayak, 2010). This method was originally reported by Jarcho and co-worker in 1976, as indicated by Monmaturapoj (2008). Calcium hydroxide, $\text{Ca}(\text{OH})_2$ and orthophosphoric acid (H_3PO_4) were starting materials of this reaction (equation 2.1). The only by-product of this reaction was water and the reaction involved no foreign elements.



In this synthesis, orthophosphoric acid addition rate and the reaction temperature directly influence the size, shape and surface area of the HA particles, which the orthophosphoric acid addition rate is strongly linked to the pH obtained at the end of the synthesis. Meanwhile, the reaction temperature determines the crystalline type (monocrystalline or polycrystalline) of the synthetic HA crystals. It was reported that HA particles synthesized at low temperature ($< 60\text{ }^\circ\text{C}$) are monocrystalline (Bouyer et al., 2000). Santos et al. (2004) have stated another two reactions for the synthesis of HA by precipitation technique. In the first reaction, ammonium phosphate, $(\text{NH}_4)_2\text{HPO}_4$ and $\text{Ca}(\text{OH})_2$ were starting materials (equation 2.2). Meanwhile in the second reaction, calcium hydrogen phosphate, $\text{Ca}(\text{H}_2\text{PO}_4)_2 \cdot \text{H}_2\text{O}$ and $\text{Ca}(\text{OH})_2$ were used as the starting materials (equation 2.3). In the first reaction, the temperature of HA synthesis was maintained at $40\text{ }^\circ\text{C}$ and in the second, synthesis was done at room temperature.



Janackovic et al. (2001) modified the process based on the homogeneous precipitation technique using the following reaction (equation 2.4):



The modification involved the addition of urea for precipitation as a substitute for NaOH. This has led to more homogeneous precipitation and subsequent transformation to HA due to pH changes for urea hydrolysis. The reaction temperature varied between 125 °C and 160 °C.

In addition, HA products synthesized using precipitation methods are commercially available starting in 2002. The first one is Ostim® (Osartis GmbH & Co. KG, Obernburg, Germany) which has been prepared by a wet chemical reaction with ~35% HA content of average crystal dimension of 100 x 20 x 3 nm³ (Dorozkhin et al, 2010). It is a readily use injectable bone matrix in paste form that received Conformite Europeenne (CE) approval in 2002 (Dorozkhin, 2010). Its viscosity enables it to form close contact with bone and formation of new bone is visible after only 3 months (Huber et al., 2006; Dorozkhin et al., 2010). Another commercial HA product derived from wet precipitation method is NanOss™, a bone void filler from Angstrom Medica, Inc. which received clearance by the US Food and Drug Administration (FDA) in 2005 (Dorozkhin, 2010). The synthesized HA powder is being compressed and heated to form a dense, transparent and nanocrystalline material that mimics the microstructure, composition and performance of human bone. Moreover, it is mechanically strong and

osteoconductive like human bone, hence it has been used in the sports medicine, trauma, spine and general orthopaedics markets (Paul & Sharma, 2006).

2.5.4.2 Sol-gel

Sol-gel synthesis method involves the formation of a colloidal sol, which will subsequently turn into a gel (Paz et al., 2012). This method requires no special energy conditions for the formation of the desired compound; thus, the synthesis of ceramic materials could be carried out at room temperature (Paz et al., 2012). However, sol-gel synthesis requires a strict control of process parameters and an intimate contact mixing at molecular level due to the slow reaction between Ca and P precursors in the sol phase to obtain highly pure, nanosized powder with homogeneous composition. However, a long period of the sol preparation time, e.g. 24 h or longer, is commonly reported in literature as required to form a desirable HA morphology (Layrolle et al., 1998). For instance, Gross et al. (2004) reported that 24 hours is needed for the highly active phosphorus alkoxide (triethyl phosphite) to interact with calcium alkoxide in order to obtain HA. Regardless the long duration employed, HA synthesized by sol-gel process are reported to be efficient in improving the contact and stability of both artificial and natural bone interfaces in both in vitro and in vivo environment (Seema, 2012).

Note that, chemical activity and the temperature required to form the apatite structure depends largely on the chemical nature of the precursors. $\text{Ca}(\text{NO}_3)_2 \cdot 4\text{H}_2\text{O}$ and triethyl phosphate were used as calcium and phosphorous precursor respectively, when the stoichiometric Ca/P ratio 1.67 was maintained. The synthesized HA powders were dried and calcined at different temperatures up to 900 °C. Brendel et al (1992) has synthesized HA at low temperature (400 °C) using $\text{Ca}(\text{NO}_3)_2 \cdot 4\text{H}_2\text{O}$ and phenyl dichlorophosphite ($\text{C}_6\text{H}_5\text{PCl}_2$) as precursors. But, the resulting HA had low purity and poor crystallinity. Further increase in temperature up to 900 °C resulted in a pure, well-

crystallized HA phase. Takahashi et al. (1995) has developed a sol-gel route for synthesis of HA using $\text{Ca}(\text{NO}_3)_2 \cdot 4\text{H}_2\text{O}$ and phosphonoacetic acid, $\text{HOOCCH}_2\text{PO}(\text{OH})_2$ in an aqueous solution at 700 °C. The crystallinity was improved with increasing temperature up to 1100 °C. Following this development, Haddow et al (1998) used calcium acetate together with various phosphorous precursors, i.e. phosphoric acid (H_3PO_4), phosphorous pentoxide (P_2O_5) and triethyl phosphate for HA coating. Meanwhile, Vijayalakshmi et al. (2008) have successfully synthesized microcrystalline HA powders from calcium acetate and triethyl phosphate in water and ethanol medium at a temperature of 600 °C. On the another note, it was also reported that formation of sol-gel derived HA is frequently accompanied by secondary phase of calcium oxide (CaO) due to the chemistry of the sol-gel routes (Zanotto et al., 2012).

Therefore, although wet chemical precipitation and sol-gel methods have been classified as the simple wet routes employed in producing HA (Kusmanto et al., 2009; Lau et al., 2012) and are able to produce high-purity HA (Alexandra & Raul, 2011), the production of HA nanoparticle with expected morphology via these method remain challenging mainly because of the raw materials used for synthesis.

2.6 Sintering of Hydroxyapatite (HA)

Sintering of HA is the final step in preparation of calcium phosphate ceramic bodies after compacting the powders at high pressure. This last step consists of elimination of pores and induces consolidation and densification of the compacted body through thermal treatment at high temperature that is lower than the melting point (Champion, 2013). It is a critical controlling parameter in order to obtain a high density HA bodies and is actually the most significant step since the final properties of the ceramics bodies strongly depends on it. It provides the final chemical compositions and microstructural design (grain size and shape, porosity ratio) of dense ceramics that directly governs the mechanical performance as well as the biological behavior (Champion, 2013). However, it is regarded as a complex process since experimental and physicochemical parameters such as powders' properties (e.g. chemical composition, crystallinity, particle size and specific surface area), compaction pressure, green density of the samples, sintering parameters (temperature, time, heating rate, atmosphere and technique) influence the sintering ability and the resultant mechanical properties of dense HA.

Theoretically, nanosized particles are characterized by a high surface area which increases the driving force of sintering due to the higher surface free energy and thus sintering at lower temperatures could be made possible (Gibson et al., 2000; Chaudhry et al., 2011; Champion, 2013). However, these powders are regularly highly agglomerated with respect to the high surface energy and this characteristic is responsible for poor sintering behavior (Veljovic et al., 2009). Moreover, it is important that the HA powder are in soft agglomerates form because agglomerates with different bulk densities which persist during powder consolidation will contribute to different shrinkage rates relative to the surrounding powder compact during densification. This in turn led to the formation of crack-like voids (Thangamani et al., 2002). Hence,

deagglomerated particles with high surface area that leads to homogeneous and high packing density are favorable in order to enhance sintering rates and densification (Champion, 2013).

In addition, it was also reported that Ca/P molar ratio has to be very close to the stoichiometric ratio of 1.67 in order to avoid chemical substitutions that affect its densification behavior. This is because densification (% of T.D) increased with increase in powders initial Ca/P molar ratio (Landi et al., 2000; Pattanayak, 2007). Moreover, when the Ca/P molar ratio exceeds the stoichiometric value, CaO forms during sintering and decreased strength meanwhile if the Ca/P molar ratio is lower than 1.67, decomposition of HA to secondary phases (β - or α -TCP) may take place at temperature less than 1350 °C which will hinder sintering and causes decreased in the density (Landi et al., 2000; Muralithran & Ramesh, 2000; Tadic et al., 2004). The presence of these extra phases may adversely affect the biological response to the implant in-vivo (Best et al., 2008). Besides that, it has been proven that the mechanical properties of stoichiometric HA (Ca/P=1.67) was found to be more superior than the non-stoichiometric HA (Slosarczyk & Piekarczyk, 1999; Raynaud et al., 2002).

Besides that, sinterability of HA powder compacts also depends on the crystallinity of the powder. In order to increase the crystallinity of the HA particles, calcination was introduced during various powder processing. Besides that, the calcinations have extensively reduced the particle size and resulting in narrow particle size distribution (Gibson et al., 2000; Thangamani et al., 2002). Narrow particle size distribution contributes to better powder packing during shape forming hence better densification, homogeneous grain structure and improved mechanical properties are achievable. This was proven in a research by Thangamani et al. (2002) where HA powder was prepared by precipitation method and the as dried powder (AD) was further calcined at 800 °C (3 hours) (CP) and ball milled (CM) before uniaxially pressed at 65 MPa into pellets

and sintered at temperature ranging from 1000 to 1400 °C in air. In their findings, the as dried powder compacts (AD) revealed a non-uniform microstructure and abnormal growth with increasing sintering temperatures meanwhile, calcined only (CP) and calcined and milled powder compact (CM) revealed more uniform microstructures as shown in Figure 2.3.

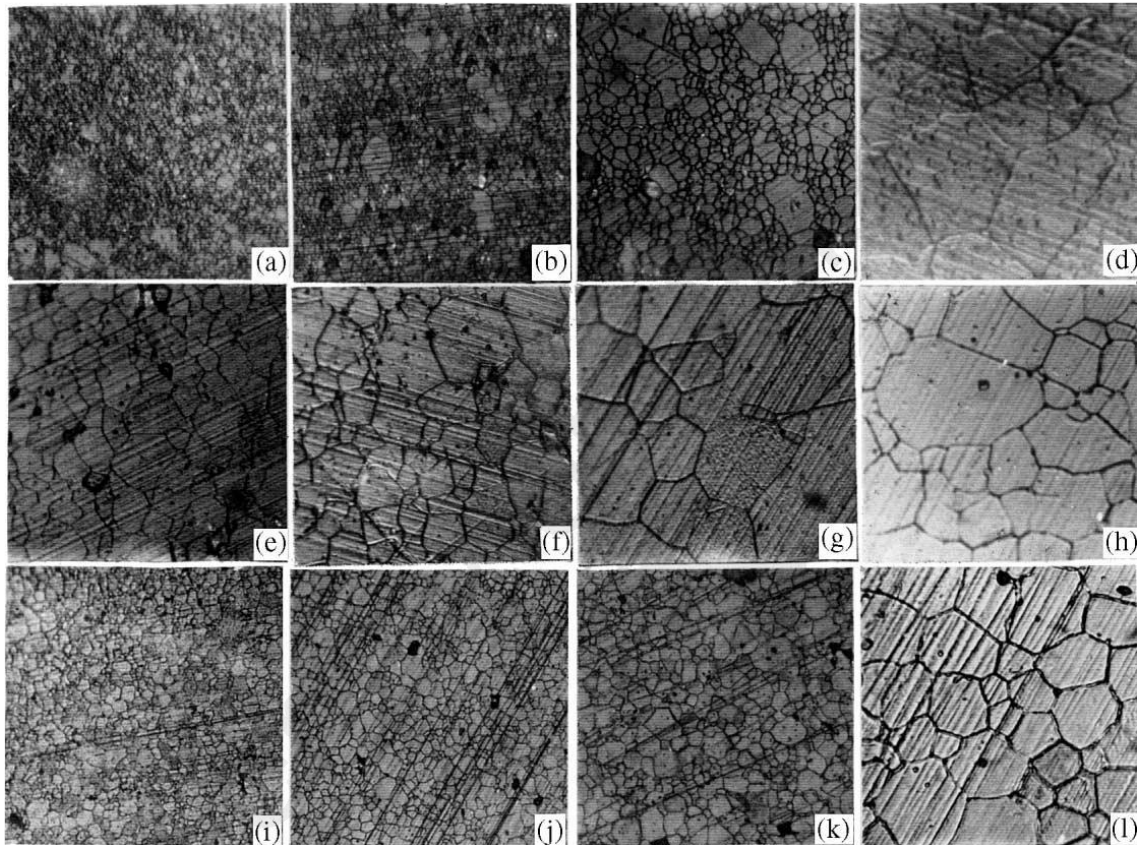


Figure 2.3: Optical micrographs of HAp ceramics; AD sintered at (a)1100, (b)1200, (c)1300 and (d)1400 °C; CP (calcined only) sintered at (e)1100, (f)1200, (g)1300 and (h)1400 °C; CM (calcined and milled) sintered at (i)1100, (j)1200, (k)1300 and (l)1400 °C (Thangamani et al., 2002)

In that research, the wide particle size distribution of the starting powder causes poor packing and generates forces on the grain boundaries which results in exaggerated grain growth during sintering. However, additional step of powder milling has further reduces

the particle size ($d_{ave} = 1.0\mu\text{m}$) and narrows the size distribution of CM powders, hence greater packing of powder compacts and as a result gradual grain growth were observed with increasing temperature when compared to CP compact. Moreover, maximum densification was achieved at lower temperature of 1100 °C (97 % of T.D) compared to CP at 1200 °C. Hence, calcined powders together with additional step of milling process were found to exhibit better densification, uniform microstructure and improved mechanical properties.

Meanwhile, Pattanayak et al. (2007) found that HA powders that have been prepared by solution route and subsequently calcined at a temperature of 600 °C showed more sharpen spectra in the XRD analysis due to well-crystallized phases. However, dehydroxylation of HA started to occur above this temperature and leading to phase transformation of HA to TCP. In addition, Patel et al. (2001) reported that the sintered densities of compacts made from powders calcined between 400-1000 °C were similar as that obtained from compacts made from uncalcined HA powders. Hence, calcination process had negligible effect on the sintered densities of the compacts. It was further documented that sintering of dense compacts prepared from calcined HA powders resulted in linear shrinkage that is associated merely with densification on sintering whilst for uncalcined powders it involved both loss of weight (water and volatile species) on sintering and the densification process. The primary concern is heat treating the powders to a certain temperature can be detrimental since it leads to coarsening of the crystallites within an individual particle and as a result, decrease in specific surface area (SSA). Hence, the calcinations has a subjective influence on the sintering ability as it depends on the powder processing employed by the researchers.

Usually, densification of HA is achieved via uniaxial pressing at particular compaction pressure and sintering at high temperature. Unfortunately, the sintered body normally tends to lose its uniformity and develop cracks after sintering (Muralithran &

Ramesh, 2000) Thus, slightly high compaction pressure can be applied in attempt to obtain dense HA with limited grain growth at slightly lower temperature, as for example by subjecting the samples to Cold Isostatic Press (CIP) before sintering (Dejong, 1926; Muralithran and Ramesh, 2000; Ramesh, 2001; Tadic and Epple, 2003; Tadic, et al., 2004; Ramesh, et al., 2007a, 2007b). This will help to enhance the densification process due to decrease in pore volume with increasing compaction pressure. Pramanik et al. (2007) in their study revealed that as the cold compaction pressure increases, so does the mechanical properties of HA prepared through solid state route and subjected to sintering at 1250 °C.

Sintering temperature, holding time and heating rate are also important parameters in the consolidation process to determine the structures and morphologies of the sintered products. The sintering temperature for dense HA bioceramic highly depends on the starting powder properties and powder packing (Thangamani et al., 2002) where good powder packing before sintering can lead to low temperature sintering (Wang & Shaw, 2007). Generally, relative density and grain size of sintered compacts increase with sintering temperature, holding time and heating rate. Note that, these two properties later determine the mechanical properties (e.g. hardness, fracture toughness and flexural strength) of the sintered HA. However, sintering at high sintering rate (above 10 °C/min) subsequently lead to partial dehydroxylation of HA which results in decomposition of HA to TCP. This phenomenon would also possible to happen in which tendency of functional group HA elimination in the matrix is increased if sintering of HA is carried out at high temperature. As a result, decomposition of HA phase to other secondary phases (i.e. α -TCP, β -TCP and TTCP) (Muralithran & Ramesh, 2000; Pattanayak et al., 2007). Hence, optimization of the mechanical properties requires that full density is reached while keeping the grain size as small as possible and this has also been emphasized by Ramesh (2001).

Besides the above mentioned sintering parameters, the sintering atmosphere, i.e. in pressureless sintering or in vacuum or inert gas environment, which related to the effect of moisture presence, does play a role in the sinterability of HA powder compacts. Generally, moisture was introduced in the sintering environment to prevent dehydroxylation of HA which in turn will slow down the decomposition rate. This is because sintering is actually be enhanced by the creation of lattice vacancies resulting from the dehydroxylation of HA (Wang & Chaki, 1993; Champion, 2013).

The sintering of a powder compact can be precisely divided into three stages that are (Champion, 2013):

- (I) Initial stage: Superficial diffusion
- (II) Intermediate stage: Densification and volume or grain boundary diffusion
- (III) Final stage: Reduction of residual closed pores

Generally, grain growth takes place in parallel with densification process, but often densification dominates over grain growth in the initial stages of sintering while grain growth active during the last stage of sintering (Hoepfner & Case, 2003) and it is boosted by high temperatures (Champion, 2013). According to Sanosh et al., (2010), during the sintering process, atoms migrate from the grain boundaries between the particles to the neck area, while the vacancies travel in the opposite direction to the material and are discharged at the surface of the material. As a result, the finer the particle size, the faster is the motion of the atoms, hence increases the density of the material during sintering. In the last stage of sintering, the weight loss due to the dehydration stops when the residual pores are closed and resulting in maximum densification (Champion, 2013). Liu & Shen (2012) showed that when water vapor is trapped inside the closed pores at the last stage of sintering, further densification is restricted by water vapor diffusion through the bulk material near the surface and this

phenomenon is defined as ‘anti-densification processes’. In another word, maximum densification is generally achieved at the temperature which pores become closed.

Besides that, many works have been directed towards enhancing HA densification kinetics while limiting its grain growth in order to obtain HA ceramics bodies with good mechanical properties. This is because poor mechanical properties such as low fracture toughness with respect to their grain growth during high temperature heat treatment are still a critical limitation for load bearing applications. Following this, significant works have been carried out through the control of density and microstructure characteristics.

As pointed out by Veljovic et al. (2009), an increase in fracture toughness is obtained with decreasing grain size, that greater energy is absorbed through the grained boundaries during crack propagation. Thus, lower sintering temperatures should be applied to preserve the morphology of initial particles and develop microstructures made of nanosized grains (Champion, 2013). Note that, normal grain growth is associated with monomodal grain size distribution meanwhile abnormal growth is associated with bi-or multimodal grain size distributions which was induced by prolong sintering. Hence, in this case, selection of the sintering method is proven to be a very crucial parameter in the preparation of HA ceramics.

2.7 Sintering Techniques

Sintering of dense HA bodies normally carried out at a temperature of 1100 °C and higher. It was clearly documented that sintering at higher temperatures do not improve the densification process but resulted in exaggerated grain growth and decomposition of HA coupled with a deterioration in the mechanical properties (Muralithran & Ramesh, 2000). With that, many alternative techniques have been developed which make it possible to attain a fully dense body at a much lower temperature with better thermal stability and mechanical properties. The subsequent section provides a brief overview of

the types of sintering techniques that have been used by researchers in the production of HA powders.

2.7.1 Conventional Pressureless Sintering

Literally, conventional pressureless sintering (CS) in air atmosphere has been widely used in preparation of HA considering the cost, simplicity and practicality. Sintering of dense HA bodies normally carried out at a temperature of 1100 °C and higher. Thangamani et al. (2012) stated that synthetic HA nanoparticles can be pressureless sintered close to the theoretical density (3.156 gcm^{-3}) at a temperature as low as 1000 °C. Varma et al. (2002) used the uncalcined nanometer-sized powder particles and sintered to 1000 °C for 2 hours and the outcome of the sintering is transparent ceramic (> 99 % of T.D) that had a uniform grain size of 250 μm and Vickers hardness of 6.57 GPa. The most common problem with high sintering temperatures is HA powders typically decompose into secondary phases such as TTCP and CaO at this temperature (Wang & Chaki, 1993; Gergely, 2010) together with exaggerated grain growth which leads to deterioration in the mechanical properties (Muralithran and Ramesh, 2000). In addition, Prokopiev & Sevostianov (2006) state that the ramp rate employed must be or less than 5 °C/min to avoid the generation of thermal and residual stress. Besides, the requirement of the long holding time also often encourages grain growth phenomena (Mazaheri et al., 2009). In addition, lowering the sintering temperature in the processing of bulk ceramics is also necessary because of preservation of surface hydrated layer and ceramics bioactivity (Grossin et al., 2010).

However, it is improper to dismiss the usage of conventional pressureless sintering (CS) in the preparation of dense HA nanoceramics because with proper starting powder processing and properties alongside control of sintering parameters, nanostructured HA

ceramics with good mechanical properties can be prepared. For example, it was proven in the work by Wang & Shaw (2007) where conventional sintering with reduced sintering temperature was successfully applied on HA nanorods that have been synthesized through wet precipitation method. The as dried HA nanorods were subjected to ball milling first to further break down the particles size and the milled nanorods HA was then calcined at 300 °C for 2 h before subjected to sintering in air following uniaxially pressing into green samples at 300 MPa. In that study, when the density of the green compacts was 49 % and 55 % of the theoretical density (T.D=3.16 gcm⁻³), densification of 93.2 % and 99.4 % of the T.D, respectively were achieved after being sintered at 900 °C for 2 hours. The influence of green density to the sintered density of dense HA ceramic has also been reported in another research by Gibson et al. (2001). This observation implies that highly powder packing in green bodies before sintering is crucial in order to achieve low-temperature sintering. Besides sintering temperature of 900 °C, another sintering attempt was also carried out at lower temperature of 850 °C for 24 hours and the image analysis reveals that 900 °C and 850 °C sintered HA compacts have an average grain diameter of ~83.1 nm (Figure 2.4(a)) and ~67.1 nm (Figure 2.4 (b)), respectively. Therefore, the nanorod morphology has reduced the densification temperature of HA from 1000 °C to 850 °C (Wang & Shaw, 2009) and this temperature is the lowest temperature ever reported in the literature for obtaining densified hydroxyapatite bioceramics through conventional sintering. In a subsequent study by the same authors, it was observed that hardness decreases as the load increases and the hardness (Knoop's indentation) of the HA dense samples at 850 °C was found to be 7.2 GPa and 5.5 GPa at 50 g and 200 g load, respectively (Wang & Shaw, 2010). This sintering temperature is comparative to the temperature of HPS sintering employed by Veljovic et al. (2009).

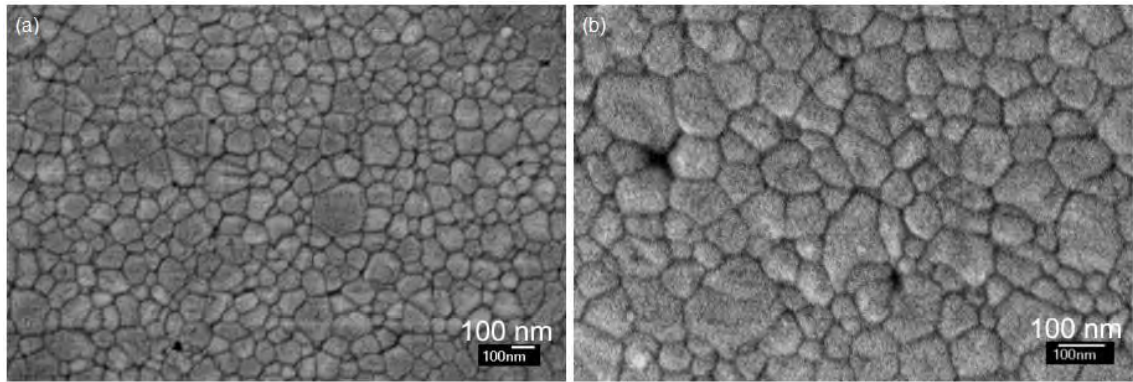


Figure 2.4: SEM image of the (a) polished and thermally etched surface of the HA sample sintered at 900 °C for 2 h, and b) SEM image of the HA sample sintered at 850 °C for 24 h (Wang & Shaw, 2007)

2.7.2 Microwave Sintering

Microwave sintering (MW) was introduced because the heating in MW is very fast and rapid. The heat generated by the electromagnetic energy (Das et al., 2008) is from within the material instead of being transferred from outer to inside the material (Agrawal, 1998; Ramesh et al., 2007a). MW offers a shorter time of processing, uniform heating, enhanced material properties and suppressed grain coarsening that normally occurred in conventional pressureless sintering. The MW technique has many advantages over other mentioned sintering methods, such as reduce sintering time, energy saving, rapid heating rates, enhanced densification rate and restrain excessive grain growth due possible lower temperature sintering.

In a microwave sintering process, there are 3 vital parameters that need to be controlled that are sintering temperature, heating rate and holding time. Hong et al. (2010) affirms that too high sintering temperature (Figure 2.5 (a), 1200 °C), long holding time (Figure. 2.5 (b), 3 min) or slow heating rate (Figure 2.5 (c), 30 °C/min) directed the growth of HA nanoparticles into the microscale grains. Contrary to this, at a lower sintering temperature (i.e. 950 °C) it was found that the nanoparticles grains did

not fuse completely and formed a rougher surface in the microscale region (Figure 2.5 (d)).

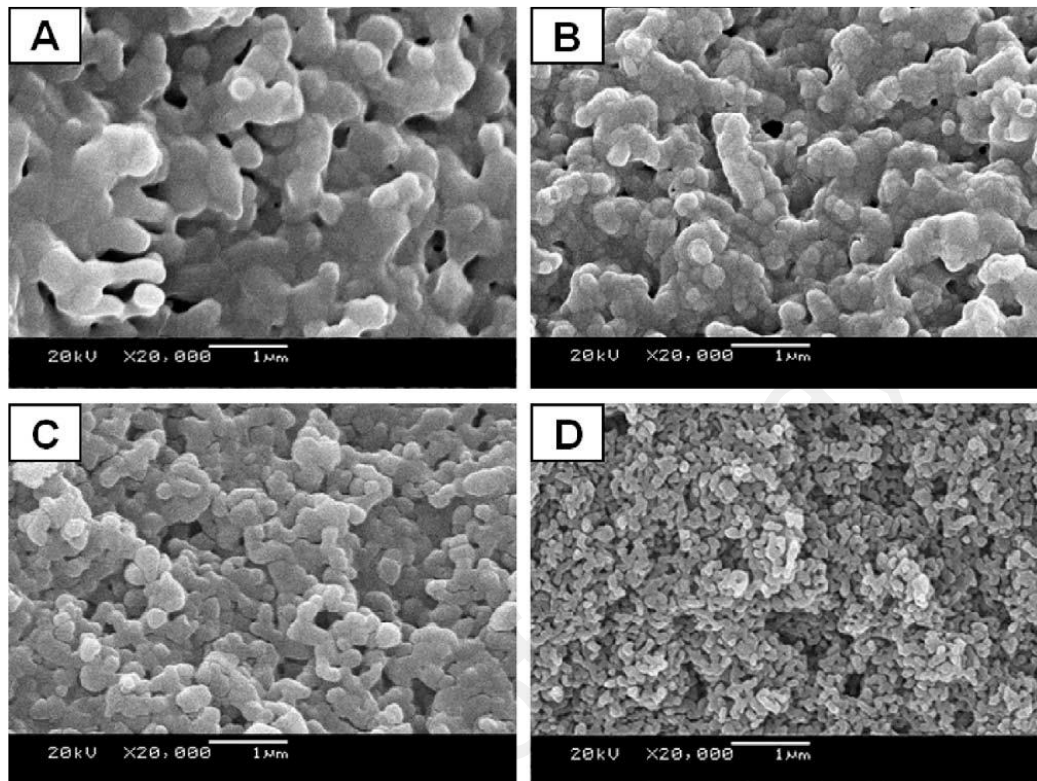


Figure 2.5: The microwave-sintered BCP ceramics under various sintering conditions.

The sintering temperature, heating rate, and holding time are; (a) 1200 °C, 80 °C/min, and 1 min; (b) 1000 °C, 80 °C/min, and 3 min, (c) 1000 °C, 30 °C/min, and 1 min; and (d) 950 °C, 80 °C/min, and 1 min, respectively (Hong et al., 2010)

Yang et al. (2002) performed a research based on the effect of microwave and conventional sintering on HA. The authors reported that the density of MW-HA sintered samples were in the range ~95.6 – 98.8 % of theoretical density. However, CS-HA samples attained densification in the range of ~93.8 – 97.9 % of theoretical density. Furthermore, the authors found that MW-HA samples have finer grain size than CS-HA samples.

2.7.3 High Pressure-assisted Sintering

Some of the alternative techniques that have also been used to sinter the HA ceramics are hot pressing sintering (HPS), hot isostatic pressing (HIP) and spark plasma sintering (SPS). These techniques offer extra driving forces (pressure, electric/magnetic field) which render the sintering process to take place at lower temperature hence shorter sintering time. This phenomenon is expected to enhance densification and prevent grain growth (Champion, 2013). Nevertheless, each stated method has its own advantages over the others.

This pressure assisted methods such as hot pressing (HPS) and hot isostatic pressing (HIP) are proven to be an effective technique in preparing dense HA. It involves mechanical uniaxial compressive stress application and high relative densities are attainable with limited grain growth due to the lower sintering temperature and time (Kang, et al., 2004; Rapacz-Kmita, et al., 2005; Fang, et al., 2008; Veljovic et al., 2009, Champion, 2013). It has been proven that HPS produce transparent HA ceramics and this phenomenon is characterized by a pore-free material with very small grain size (Barralet et al., 2004; Tan et al., 2011; Lukic et al., 2012; Champion, 2013). In a study by Veljovic et al. (2009), it was discovered that translucent dense HA samples were obtained when subjected to HPS at 950 °C and 1000 °C for 1 hour. The attained grain size at 950 °C was 50 nm whilst the fracture toughness and microhardness were at 1.52 MPam^{1/2} and 4.30 GPa, respectively. This finding is comparatively higher than those achieved on the second set of green samples through conventional sintering at 1200 °C for 2 hours whereby the grain size, fracture toughness and microhardness attained was 3 µm, 0.28 MPam^{1/2} and 2.39 GPa, respectively. However, this conventional sintering applied at 1200 °C did not cause HA decomposition.

Concurrently, a novel low temperature ultra-high pressure (LTUHP) (ranging from 325–450 °C and 2.0–5.0 GPa) sintering method was employed by Tan et al. (2011)

(Figure 2.6). Transparent dense and nanostructured HA bioceramic with uniform grain size at ~ 200 nm was successfully achieved when the sample was sintered with a pressure of 3.0 GPa at 435 °C. In that work, the HA powder was first synthesized using the sol-gel method and the samples were initially compressed and then heated to the preset value with a heating rate of 65 °C/min for 20 minutes. The temperature was quenched to room temperature following a rapid reduced to ambient pressure. By reducing the pressure first, the phenomenon of cooling before decompression was avoided hence dense HA samples with no apparent cracks has been obtained (Lu et al., 2006). It was observed that the sintering temperature was inversely proportional to the sintering pressure where the higher the sintering pressure, the lower the sintering temperature. When the sample was sintered with a pressure of 3.0 GPa at 435 °C the best result of uniform grain size at ~ 200 nm, hardness value of 7.9 ± 0.3 MPa and relative density above 96 % was achieved. It was proven that LTUHP method has successfully produce transparent dense HA bioceramics while inhibit its grain growth and improve the mechanical properties.

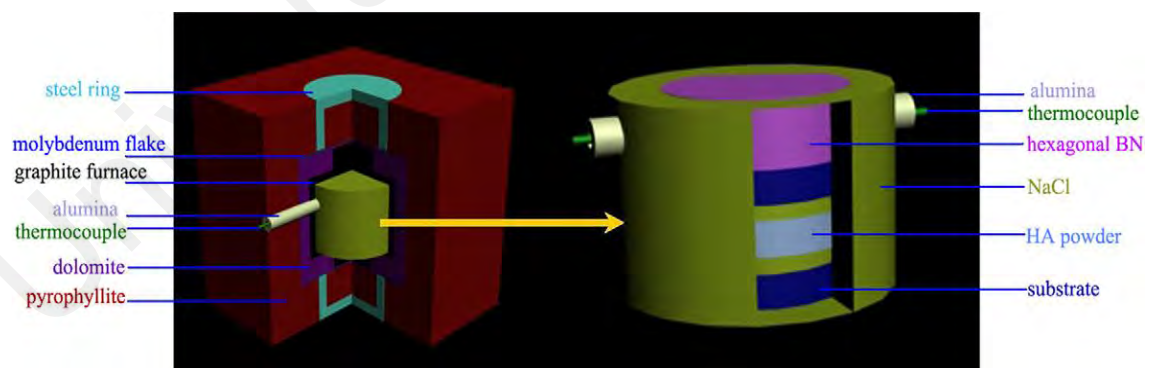


Figure 2.6: Assembly of the LTUHP sintering experiments (Tan et al., 2011)

Another available method used in sintering of HA ceramics is the spark plasma sintering (SPS) method. It is a rapid sintering method that uses self-heating phenomena of the ceramic powders in which sintering is made possible at lower temperatures. By using SPS, Gu et al. (2002) attained samples with maximum densification (~99.6 %), hardness (~5.2 GPa) and fracture toughness (~1.26 MPam^{1/2}) at a relatively low sintering temperature of 950 °C. Hence, it can be concluded that SPS can produce dense HA at a significantly shorter time and temperature due to the activation of the powder particle by the high current input of SPS.

However, pressure assisted sintering (HPS, HIP, SPS) regularly comes with expensive and complicated equipment and also unreliable for application in the industry due to the difficulties in the processing of samples with special shape.

2.8 Biological Performance Evaluation of Calcium Phosphate

The biological performance of a biomaterial is conventionally measured by its biocompatibility for example in the preparation of scaffold for tissue engineering. A biomaterial would be regarded as an ideal biomaterial if it have appropriate surface chemistry and microstructures to facilitate cellular attachment, proliferation and differentiation (Liu et al., 2007). Besides that, the good indicators of cell response is collectively represented by the adhesion, proliferation, differentiation and mineralization processes of the HA ceramics. Moreover, this attributes is later expected when the biomaterial is used in vivo (Bang et al., 2015). Besides that, the biomaterial should result in a trivial immune reaction to avoid body rejection after implantation (Bang et al., 2014).

2.8.1 In vitro Evaluation Using Phosphate Buffered Saline (PBS)

The bioactivity evaluation was carried out by immersing the sintered disc samples in phosphate buffered saline (PBS) which imitate the in vitro environment as solute and ion concentration match to human blood plasma at 37 °C. PBS has been used biological research as it is non-toxic to most cells and being isotonic in nature (Asgary et al., 2009). Immersion in PBS normally resulted in deposition of apatite layer on the surface of the bioactive material after certain time. Together with this, the change of ion concentration and pH of the PBS was measured to evaluate the solubility of bioactive materials (Combes & Rey, 2002). Extension of ionic substitutions is believed to be the one of the primary factors that affect the solubility of material. It was claimed that ionic substitution disrupts the structure of lattice. This has led to the variations in dissolution properties of the material (Fulmer et al, 2002, Pan et al., 2010). This properties has also indirectly influenced the thickness of deposited apatite layer (Combes & Rey, 2002).

2.8.2 In vitro Evaluation Using Cell Culture

The primary method used in order to study the biocompatibility of the synthetic implant is cell culture. Besides that, it can be also used to study the effects of toxic compounds on the cells. This method involves the removal of cells from an animal or plant and their subsequent growth in a favourable artificial environment. There are 3 types of bone cell that are osteoblast, osteocytes and osteoclasts. These bone cells cooperate in the bone remodelling process (Crockett et al., 2011). While bone tissue is maintained by the balance of bone formation and bone resorption, while osteoblasts and osteoclasts are involved in bone formation and bone resorption, respectively (Nakamura, 2007).

Figure 2.7 shows the summary of the time course of osteoblast function on a newly implanted biomaterial. When the proliferation and extracellular matrix synthesis start,

osteoblast cells will synthesize type I collagen, vitronectin and fibronectin. The proliferation process period takes place from the beginning of implant to about 10-12 days for the extracellular matrix development. After 12 days to 1 month, the osteoblast cells will differentiate when the extracellular matrix matures and the mineralization is obtained. The time course of osteoblast function varies from 30 days onwards depending upon the material implant.

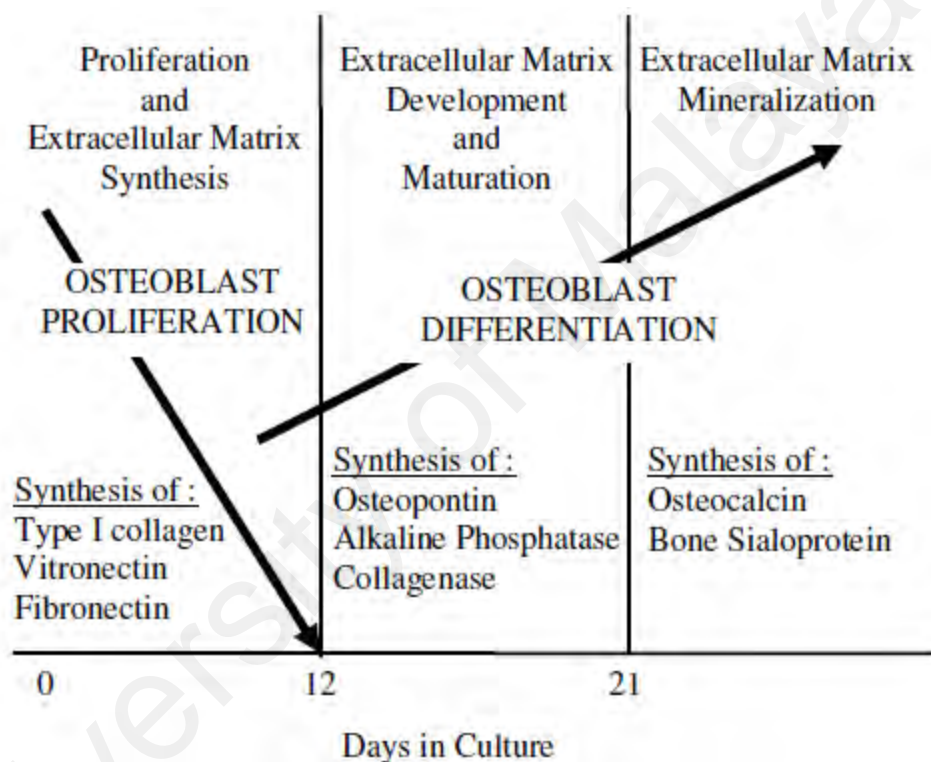


Figure 2.7: The time course of osteoblast function on a newly implanted biomaterial (Liu & Webster, 2007)

2.9 Summary

In summary, this chapter has provided a brief overview of the current available methods to synthesize hydroxyapatite ceramics and various processes and parameters that control its sinterability. Among of the parameters involved are powder chemical composition (Ca/P ratio of the starting powder), sintering temperature and heating rate, and also sintering technique and atmosphere. Besides that, the quest for naturally

derived hydroxyapatite has significantly increased not only because of their availability, lower cost and environmental friendly feature but also for their improved properties and performance as a bioceramic. Besides that, the continuous research attempts in producing biocompatible biomaterial from this natural organic waste have added a valuable aspect of its recovery. In addition, the interest in the synthesis of nanosized HA with a grain size less than 100 nm has increased. However, the precise control of crystal growth presents the utmost challenge. Therefore, synthesis of crystalline hydroxyapatite (HA) nanoparticles with expected microstructure is of primary importance because the process directly relates to the phase purity, morphology, and particle size of the final HA particles. These primary characteristics are widely documented to majorly affect the mechanical properties, bioactivity and biocompatibility of HA as a biomaterial.

CHAPTER 3: MATERIALS AND METHODS

3.1 Introduction

This chapter presented all the materials used and procedures involved throughout the work. The chemical and mechanical properties of the prepared materials were characterized and the in vitro biocompatibility test were detailed out.

3.2 Powder Preparation

In this work, phase pure HA powders were prepared using two different Ca sources that are from natural (waste eggshells) through solid state reaction (dry methods) and from commercially available chemicals through two different wet methods namely chemical precipitation and sol-gel methods.

3.2.1 Direct Conversion of Waste Eggshells as a Natural Source of Calcium

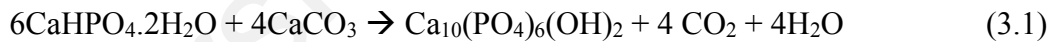
Precursor to HA Through Solid State Method

Calcium carbonate (CaCO_3) from waste eggshell was used as a source of calcium precursor to synthesize HA. This is done via calcinations of the eggshells and later subjected to sintering after appropriate processes to obtain pure HA. Waste eggshells were first cleaned and air-dried prior to the removal of the inner membrane layer. Subsequently, they were consistently crushed to a fine powder using a pestle and mortar. In order to establish an optimum calcinations temperature, various temperatures for calcination (600 °C, 650 °C, 700 °C, 750 °C and 800 °C) were investigated. Based on the phase purity of the CaCO_3 produced as well as the intensity of the inherent peaks of CaCO_3 shown on the XRD diffractograms, the optimum calcination temperature is selected. In this study, the optimum calcination temperature to obtain CaCO_3 is found to be 700 °C.

The calcined eggshell was then added to phosphorus precursor, calcium hydrogen phosphate dehydrate, $\text{CaHPO}_4 \cdot 2\text{H}_2\text{O}$ (DCPD, Nacalai Tesque, Japan) at a Ca/P ratio of 1.67 and this mixture is subjected to attrition milling (Akron Electric Inc., USA) with ethanol as a solvent at a speed of 400 rpm for 2 hours. The most significant effect is a modification of particle's surface charge, which depends on the nature of the solvent. The low dielectric constant and surface tension of alcohol induce a very low ionic strength of the solution and enhanced wettability of particles, which results in loosely bonded particles (Gross & Rodríguez-Lorenzo, 2004).

The obtained powder mixture was dried in the oven at 110 °C for overnight. The dried powder is sieved through the 212 μm mesh to obtain a fine powder, thus increase the number of crystallites in contact before formed into green compacts. The powder was put into a stainless steel mold and pressed uniaxially with an oil pressing machine (RMS Hydro, USA). The block was then preheat-treated at 800 °C for 5 hours to obtain a homogeneous composition.

The HA powder is obtained following the chemical reaction:



The heat-treated pellets were crushed and grind to break the particle agglomerates. In short, the HA derived from eggshell was referred to as HA-Es.

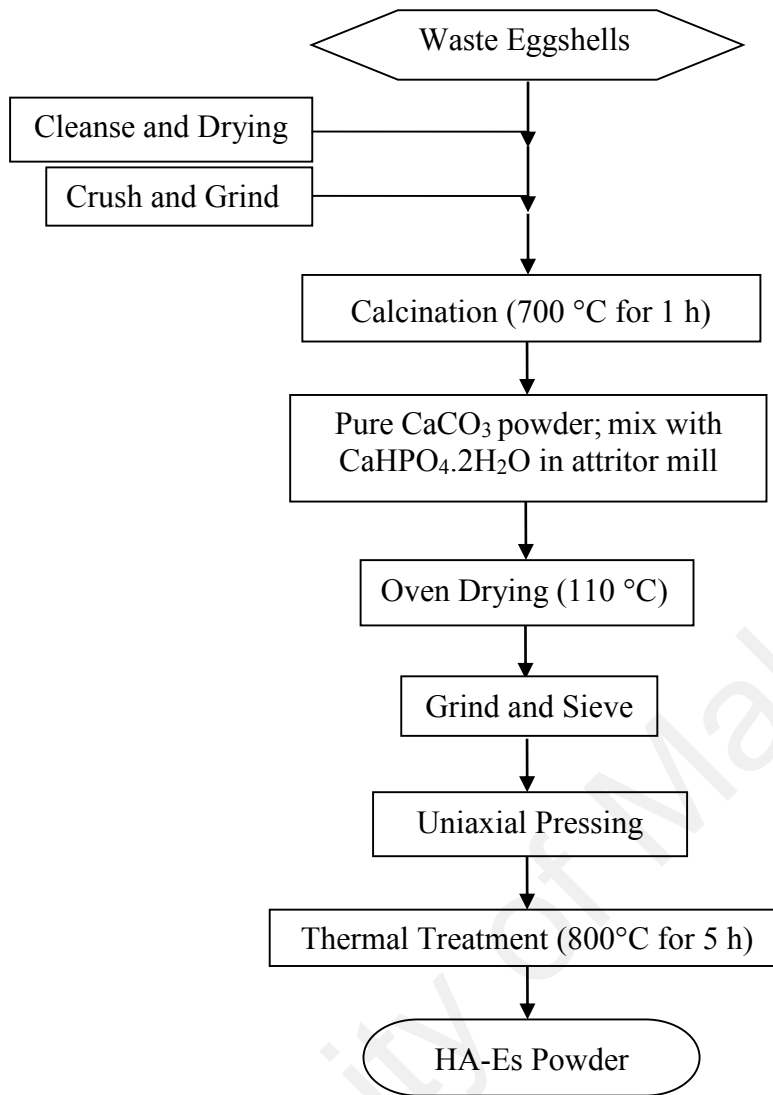


Figure 3.1: Flow chart of preparation of HA powder from waste eggshell via solid state reaction (HA-Es)

3.2.2 Preparation of HA Powder through Wet Chemical Precipitation

The HA powder was produced via a wet chemical precipitation method (Ramesh, 2004) comprising the precipitation from aqueous medium via a titration process by reacting calcium ion with phosphate ion based on a molar ratio of $\text{Ca/P} = 1.67$. The mixture was maintained at a pH of about 10-12 by the addition of small amounts of ammonium (NH_3) solution (25 % concentration). Calcium hydroxide, $\text{Ca}(\text{OH})_2$ (98 % purity, R&M Chemicals), and orthophosphoric acid, H_3PO_4 (85 % purity, Merck), were

used as Ca and P precursors, respectively with a molar ratio of 10:6 following the chemical reaction:



In general, the synthesis process involved the preparation of H_3PO_4 and $\text{Ca}(\text{OH})_2$ solution. To prepare the H_3PO_4 solution, the required amount of H_3PO_4 is diluted in distilled water, stir for 10 minutes and subsequently contained in a titration funnel. The pH of the prepared acid solution was about 1. A similar procedure was employed to prepare the $\text{Ca}(\text{OH})_2$ solution under stirring condition. The pH of the prepared $\text{Ca}(\text{OH})_2$ solution was about 12. The beaker containing the $\text{Ca}(\text{OH})_2$ solution was covered with a cling film to minimize contamination.

In a typical titration process, 0.6 mole of H_3PO_4 (400 mL) was added dropwise (9 drops to 10 drops per 10 s) into 1.0 mole of $\text{Ca}(\text{OH})_2$ solution (750 mL) under vigorous stirring. The titration process normally takes about 3 h. The pH of the mixture is monitored and maintained above 10.5 by adding ammonium (NH_3) solution (25 % concentration, J. T. Baker). Once titration is completed, the solution is continuously stirred for at least another 5 h to 6 h. The precipitate is allowed to settle overnight at room temperature before filtering and washing using distilled water. The filtered precipitate is dried in an oven at 60 °C for 24 h. The dried cake is then crushed and sieved to obtain well-defined HA powder, hereafter referred to as HA-Wp powder.

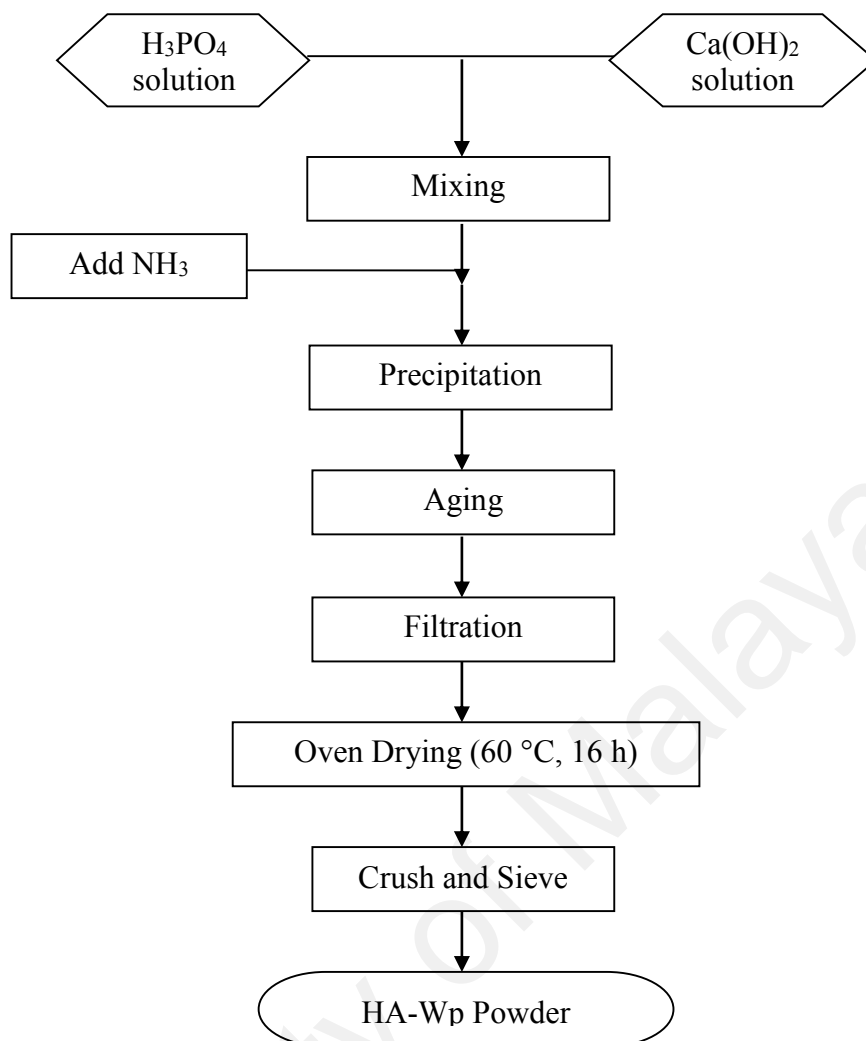


Figure 3.2: Flow chart of preparation of HA powder via wet chemical precipitation (HA-Wp)

3.2.3 Preparation of HA Powder through Sol-Gel Method

Sol-gel synthesis was employed based on the route which has been proposed by Sopyan et al. (2008) to produce HA by using $\text{Ca}(\text{NO}_3)_2 \cdot 4\text{H}_2\text{O}$ and *di*-ammonium hydrogen phosphate ($(\text{NH}_4)_2\text{HPO}_4$) as starting precursors. Ethylenedinitrilotetracetic acid (Titriplex II) is used as the chelating agent to prevent the immediate precipitate formation, and urea is used as a gelling agent. A 500 mL portion of ammonium solution (25 % solution, Merck) is used to alter the pH. Initially, 0.6 mole Titriplex II is dissolved in ammonia solution at 60 °C under vigorous stirring. An aqueous solution of 0.5 mole $\text{Ca}(\text{NO}_3)_2 \cdot 4\text{H}_2\text{O}$ and 0.3 mole $(\text{NH}_4)_2\text{HPO}_4$ were then added into the Titriplex

suspension, followed by adding 0.75 mole urea. The mixture is subsequently refluxed at 100 °C for 3 h to 5 h under stirring until a white gel is obtained. The white gel is allowed to settle overnight at room temperature before filtration and washing using distilled water. This gel is then dried at 500 °C for 3 h to ensure complete organic and inorganic substance removal. The HA obtained via this method is hereafter known as HA-Sg powder.

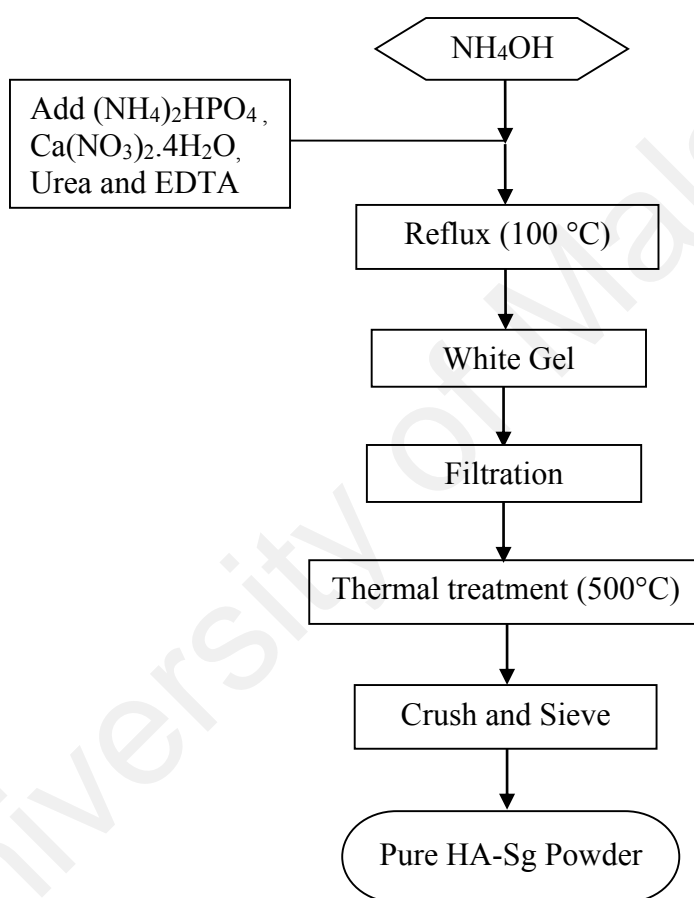


Figure 3.3: Flow chart of preparation of HA powder via sol-gel method (HA-Sg)

3.2.4 Calcination of HA Powder

In the present research, all the synthesized HA powders (HA-Es, HA-Wp and HA-Sg) were calcined in air, using a standard rapid heating furnace at five different temperatures i.e, 700 °C, 800 °C, 900 °C and 1000 °C. A furnace ramp rate of

10 °C/min (heating and cooling) and soaking time of 2 hours was used for each calcination profile.

3.3 Preparation of HA Green Compacts From Different Synthesis Methods

All the synthesized HA powders (HA-Es, HA-Wp and HA-Sg) was uniaxially compacted at 15 MPa (for HA-Es) and 2.5 MPa (for HA-Wp and HA-Sg) into circular disc samples. The green compacts were subsequently subjected to cold isostatic pressing at 200 MPa for 1 minute.

3.4 Sintering of HA Green Compacts

In this research, densification regime is carried out on HA green compacts at various temperature using conventional pressureless sintering and microwave sintering. Post sintering, evaluation on the mechanical properties of HA dense compacts from both sintering methods will be determined.

3.4.1 Conventional Pressureless Sintering (CS)

The consolidation of the particles by pressureless sintering was performed in air using conventional box furnace within a temperature range of 1000-1350 °C for 2 hours at a heating and cooling ramp rate of 5 °C/min. Sintered samples were then ground using silicon carbide (SiC) sand papers and polished to a 1 µm mirror finish using diamond paste as a polishing medium prior to evaluation.

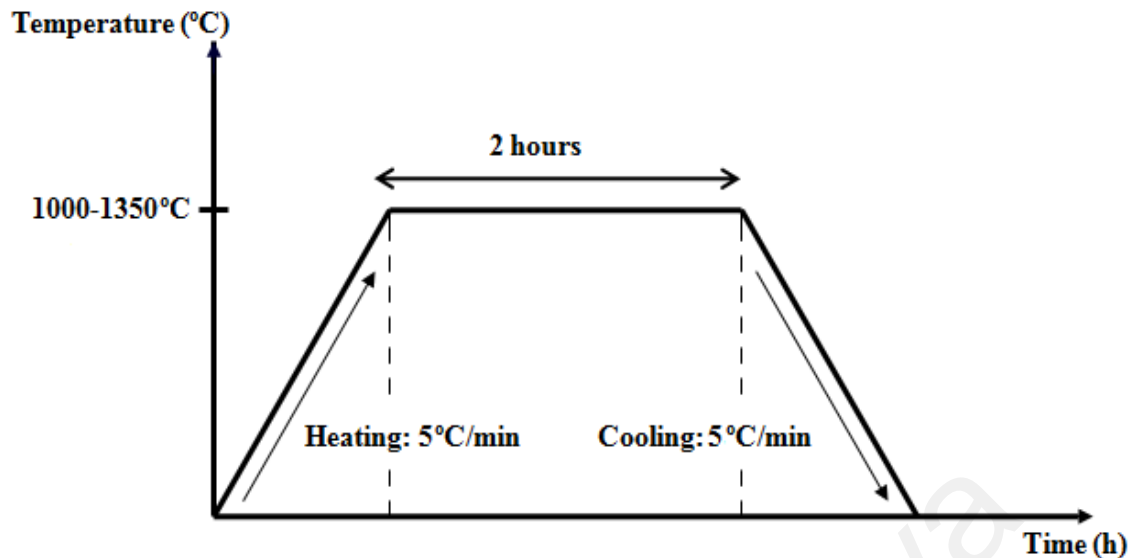


Figure 3.4: Pressureless sintering regime of synthesized HA green compacts

3.4.2 Microwave Sintering (MW)

The consolidation of the particles was performed using microwave sintering furnace (Shenzen BduVo, Delta, China) within a temperature range of 950-1250 °C for 15 minutes at a ramp rate of 30 °C/min (heating and cooling). The operating power of the microwave system was optimized through a number of trial runs and finally, it was set to an operation to avoid overheating and cracking of samples. Power was provided by a 6 kW magnetron which is controlled by a programmable process controller. The samples were placed in aluminosilicate crucible that utilizes silicon carbide as a susceptor medium. This is to enhance microwave heating through efficient coupling by facilitating hybrid heating at lower temperature range by minimizing the thermal gradients within the HA sample and subsequently providing the ability to heat the samples to a temperature beyond which they heat solely due to microwave radiation absorption (Curran et al., 2011).

Similarly, as in the conventional pressureless sintering, sintered samples were then ground using silicon carbide (SiC) sand papers and polished to a 1 μm mirror finish using diamond paste as a polishing medium prior to evaluation.

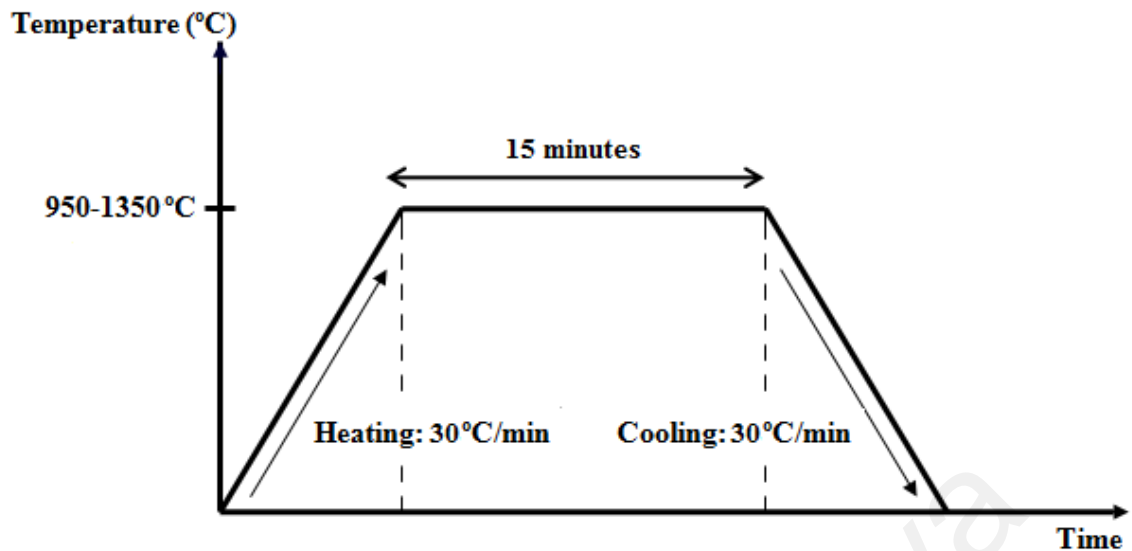


Figure 3.5: Microwave sintering regime of synthesized HA green compacts

3.5 Characterization of HA Powders and Compacts

All synthesized HA powders were characterized for their phase purity and stability using X-ray diffractometer, differential thermal analysis through TGDTA analyzer, surface area using BET analyzer, powder size and morphology using SEM and TEM. FTIR was used to characterize the functional groups in HA powder. Subsequently, the HA compacts were tested to determine the bulk density, microstructure evolution, mechanical properties along with in vitro bioactivity evaluation in phosphate buffered saline (PBS) solution and biocompatibility evaluation through cell study.

3.5.1 Phase Stability and Crystallite Size

X-ray diffraction (XRD) (PANalytical, Empyrean diffractometer, Netherlands) was used to determine the phases present in the powder as well as sintered samples. This analysis was carried out at room temperature, operated at 45 kV and 40 mA using Cu-K α as the radiation source. The X-ray step size was 0.026° with the scan angle (2θ) varying from 10° to 50°. In the present works, the crystalline phase present in the material was identified by comparing the prominent XRD peaks exhibited by the

material tested to that of standard reference JCPDS-ICCD (Joint Committee of Powder Diffraction Standard-International Centre for Diffraction Data) as shown in Table 3.1.

The crystallite size of the as-synthesized powders was calculated using the Scherrer's formula:

$$t = 0.9\lambda / \beta \cos\theta \quad (3.3)$$

where t is the average crystallite size, λ is the wavelength of the XRD radiation, β is the full width at half maximum (FWHM) value of the measured diffraction peak and θ is the diffraction angle of the investigated peak.

Table 3.1: JCPDS data reference

Material	Data Reference
Hydroxyapatite (HA)	PDF No. 74-566 for $\text{Ca}_{10}(\text{PO}_4)_6(\text{OH})_2$ PDF No. 9-432 for $\text{Ca}_5(\text{PO}_4)_6(\text{OH})_3$
α - TCP	PDF No. 9-348
β - TCP	PDF No. 9-169
TTCP	PDF No. 25-1137
CaO	PDF No. 37-1497

3.5.2 Differential Thermal Analysis

Differential thermal analysis (DTA) and thermogravimetric analysis (TG) were conducted on the as-synthesized HA-Wp and HA-Sg before drying and as-milled eggshell mixture in ambient air by using the TG/DTA instrument (Perkin Elmer, Pyris Diamond TG/DTA) with 5 °C/min heating rate from room temperature up to 1000 °C. This method was used to determine the phase stability and reaction temperatures of the produced HA powders.

3.5.3 Fourier Transform Infrared (FTIR)

Qualitative analysis of the molecular radicals was carried out via the attenuated total reflectance (ATR) method of the FTIR spectrometer (Perkin Elmer, Spectrum 100 Series). The powders were directly placed onto the holder and the possible structural variation and reactions in those samples were examined. The infrared spectrum with a resolution of 4 cm^{-1} and a scan number of 32 scans was adopted at a mid-infrared scan range 400 cm^{-1} to 4000 cm^{-1} .

3.5.4 Specific Surface Area

The Brunauer-Emmett-Teller (BET) method was used to measure the specific surface area of the powder. Nitrogen gas adsorption analysis was performed on an Autosorb-1 Analyzer by Quantachrome Instruments. Samples were outgassed at $150\text{ }^{\circ}\text{C}$ for 30 minutes under vacuum prior to testing.

3.5.5 Microstructural Examination

The morphology of the starting powder and the microstructural evolution of sintered samples under various sintering temperature were examined using a scanning electron microscope (SEM) (Phenom Pro X, Netherlands). For imaging of the as-synthesized HA nanopowder, carbon tape was placed on metal SEM mounts and the HA powders were sprinkled onto the mount with a spatula. Nanopowders were investigated under SEM at accelerating voltage of 15 kV at magnifications up to 40,000X.

To study the grain coarsening of sintered HA samples under various sintering temperatures and methods, the sintered dense samples were firstly polished to a reflective surface and thermally etched at temperature $50\text{ }^{\circ}\text{C}$ below the sintering temperature, using a ramp rate of $10\text{ }^{\circ}\text{C}/\text{min}$ and holding time of 30 minutes. This step is crucial to delineate the grain boundaries so that the grains can be better imaged in

SEM. In addition, the densities of the samples were measured before and after thermal etching and it was proven that thermal etching process did not affect the solid volume fraction of the samples. In order to remove contamination, the surface of the sample was cleaned in acetone and then placed onto an aluminum stub. The SEM function by focusing a small spot of electrons on a thick specimen and proceeds to scan across the specimen surface in a series of lines, using electrostatic or electromagnetic forces. Electrons emerging from the upper specimen surface are collected by an electron detector and used to produce an image on a monitor as a series of line.

The grain size of sintered HA was determined based on the linear intercept method from the SEM images and this method is accordance with ASTM E112-96 (ASTM, 2004). This technique requires measurements taken from polished sections, which a known test-line is drawn on an A4 size SEM micrograph of the selected polished section. Following this, the number of intercept between the test line and grain boundaries are counted. The test line should cover at least 50 grains and several lines are drawn and measured before the average value is taken.

The average grain size is then calculated according to the equation proposed by Mendelson (1969):

$$D = 1.56 \frac{C}{MN} \quad (3.4)$$

where,

D = average grain size.

C = total length of the test line.

M = the magnification of the SEM micrograph.

N = the number of grain boundary intercepts on the line.

Essentially, the end points of a test line are not intersections and not counted unless the end appeared to exactly touch a grain boundary, when a 0.5th intersection is scored.

A tangential intersection with a grain boundary is scored as a 1st intersection while for intersection coinciding with the junction of 3 grains is scored as a 1.5th intersection as shown in Figure 3.6.

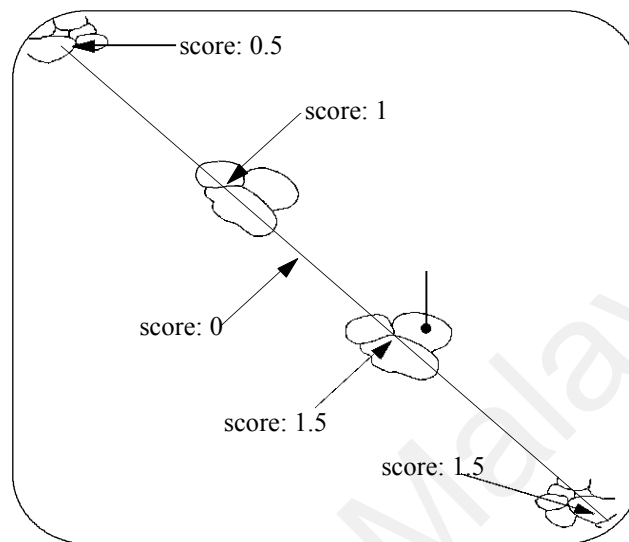


Figure 3.6: Diagram showing the score given for the type of intersections

3.5.6 Transmission Electron Microscopic Analysis

The morphology and particle size of synthesized HA powders at a significantly higher resolution were characterized using Transmission Electron Microscope (TEM) (JEOL, JEM-2100F, Japan) operating at accelerating voltages of 100-20 kV. For this observation, the HA powder suspension was prepared by mixing a very small amount of HA nanopowder with ethanol (95 %, Merck) solution followed by ultrasonication for 30 minutes. A drop of this suspension was applied onto a 200 mesh copper grid coated with a silicon monoxide film and left to dry completely prior to visualization via TEM.

3.5.7 Bulk Density Measurement

The bulk density of the sintered samples was measured after sintering at particular temperature and time using a water immersion technique which was based on the Archimedes method. The immersion medium used in the present research was distilled

water. A standard Mettler Toledo Balance AG204 densimeter was used and the samples were weighed initially while dry (in air) and then submerged into water until all surface bubbles had been removed. Consequently, the samples were then suspended in the distilled water and the suspended mass was measured. The bulk density of the sample was calculated by using the formula below:

$$\text{Bulk density, } \rho = \frac{W_1}{(W_1 - W_2)} \times \rho_w \quad (3.5)$$

where: ρ = Bulk density of the sample
 W_1 = Weight of sample in air
 W_2 = Weight of sample submerged in water
 ρ_w = Density of distilled water (the temperature effect on the water density was taken into consideration)

However, for green samples as well as low-density samples the bulk density was ascertained through the measurement of geometric dimensions and sample mass according to the following equations:

For disc samples:

$$\rho_g = \frac{m_g}{\left[\frac{\pi d^2 t}{4} \right]} \quad (3.6)$$

where m_g is the green mass, t is the disc thickness and d is the cylinder diameter. The relative density was calculated by taking the theoretical density of HA as 3.156 gcm^{-3} .

3.5.8 Vickers Microhardness Testing

Hardness is defined as the material's resistance to indentation (Slosarczyk & Bialoskorski, 1998) and it is closely related to the compressive strength, wear, corrosion

and machining performance of ceramics. In this work, Vickers indentation technique was used to determine the hardness of sintered HA sample.

For the Vickers microhardness test, the indentations were made using a pyramidal diamond indenter (HMV-2, Shimadzu, Japan). During the test, the indentation load was applied smoothly at varies loads (100 gf, 200 gf and 500 gf) for a loading time of 10 seconds and five indentations were made on each sample and the average value was taken. The physical quality of the indenter and the accuracy of the applied load must be controlled to obtain correct results. Literally, the Vickers impression appears to be square with the two diagonals having almost similar lengths (Figure 3.7 (a)). Once the load is removed, impression diagonals (Figure 3.7 (b)) are measured immediately with a Filar micrometer built in the attached microscope on the Vickers machine.

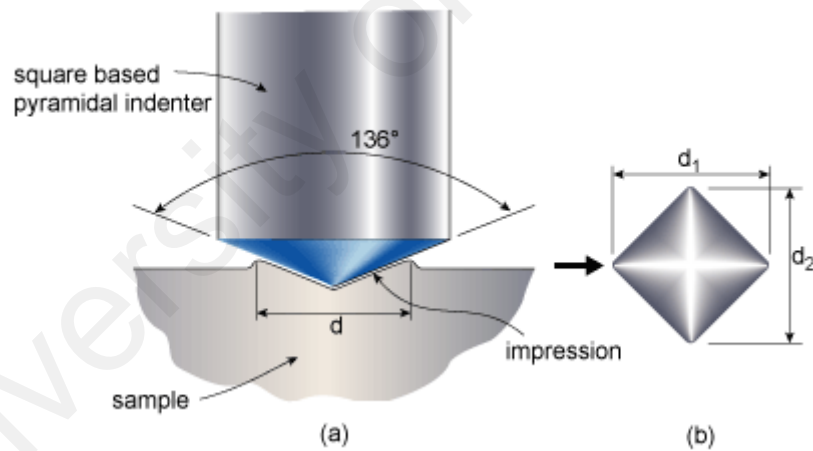


Figure 3.7: The Vickers Hardness Test: (a) Vickers indentation and (b) measurement of impression diagonals

The measurements are taken to the nearest 0.1 μm and thus, the average value, d , is obtained. Subsequently, the Vickers hardness (H_v) is calculated based on the surface area of the indent using equation:

$$H_v = \frac{1.854 P}{(D_{ave})^2} \quad (3.7)$$

where: P = Applied load (kgf).

$$D_{ave} = \frac{d_1 + d_2}{2} = \text{Mean of the measured indenter diagonals}$$

3.5.9 Indentation Fracture Toughness Measurements

The resistance of a material to crack propagation is defined as fracture toughness and is one measure of the strain-energy absorbing ability of brittle materials (Seghi et al., 1995). Indentation technique in evaluating the fracture toughness involves the direct measurement of radial crack length as a function of indentation load. The advantage of this method is the speed and ease of sample preparation and testing. Principally, it is the same as the microhardness measurement whereby the Vickers diamond indenter was driven into the specimen surface by a known load. When the indenter was removed, a characteristic pattern as in Figure 3.8 should be visible, comprising a central indentation with radial cracks emanating from the corners. Generally, there are 2 crack systems formed by the Vickers indenter; the Median or half-penny and the Palmqvist crack system (Kruzic et al., 2009). The crack system for HA has been established as Median-type (Niihara, et al., 1982). Thus, the fracture toughness (K_{Ic}) was determined from the equation (3.8) derived by Niihara (1982):

$$K_{Ic} = 0.203 \left[\frac{c}{a} \right]^{-1.5} (H_v) a^{0.5} \quad (3.8)$$

where: H_v = Vickers hardness

a = Half diagonal of the indent

c = The length of the surface trace of the half penny crack from the center of the indent as shown in Figure 3.8

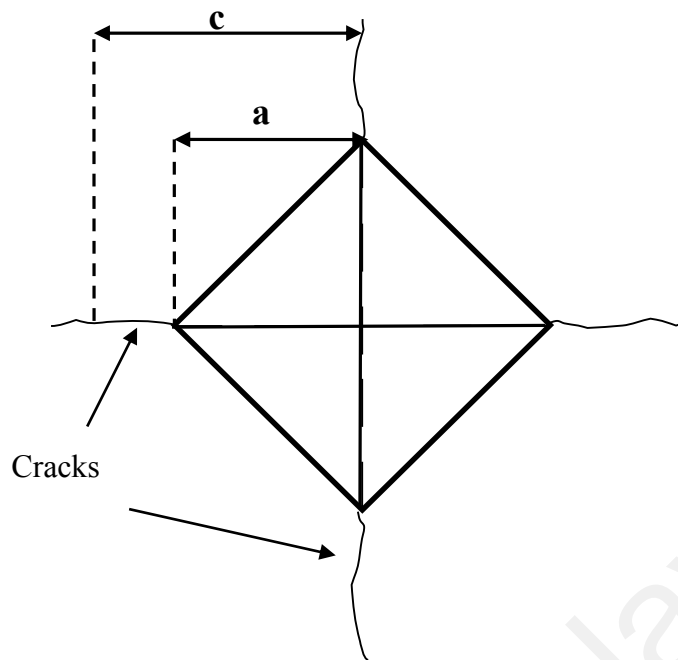


Figure 3.8: Vickers indentation showing cracks emanating from the four corner of the indent

3.6 In vitro Evaluation on the Bioactivity of Heat Treated HA-Es: Phosphate Buffered Saline (PBS)

The bioactivity evaluation was carried out by immersing the sintered disc samples in phosphate buffered saline (PBS) which imitate the in vitro environment as solute and ion concentration match to human blood plasma at 37 °C. PBS has been used biological research as it is non-toxic to most cells and being isotonic in nature (Asgary et al., 2009). The change of ion concentration and pH of the PBS was measured to evaluate the solubility of bioactive materials (Combes & Rey, 2002). In this work, PBS solution is prepared by using PBS buffer pouch (Sigma Aldrich, USA). This buffer pouch has been formulated to give a ready-to-use PBS solution upon dissolution in a specified quantity of distilled water. The PBS powder was first dissolved in one liter of distilled water which yields 0.01 M PBS solution which consists of 0.138 M NaCl and 0.0027 M KCl at pH 7.4.

The specimens used in this experiment were HA-Es powder compacts at 800 °C, 1200 °C and 1250 °C. 20 mL of PBS was first measured into a cylindrical plastic container before the assay could be carried out. Following this, the specimen was immersed in PBS solution for a certain period. The immersion duration was preset to 1, 3, 5, 7, 14 and 21 days. After a preset period, the specimen was removed from the PBS and gently washed with distilled water before dried in an oven at 37 °C for 1 day. Scanning electron microscope was used as a tool to confirm the apatite formation on the surface of the sample. The weight loss of the specimens was measured with two samples that remained in the PBS for each day. The samples were dried at 37 °C for two days (until their mass was stable) and weighed on a precision balance in order to calculate the percentage of weight loss (% wt loss) as shown in Equation 3.9.

$$\% \text{ wt}_{\text{loss}} = \frac{w_0 - w_i}{w_0} \quad (3.9)$$

w_i = Initial weight of the samples before immersion

w_0 = Weight of the samples after subjected to 2 days of oven drying

3.7 In vitro Evaluation on the Biocompatibility of Heat Treated HA-Es:

Cell Study

In the biocompatibility study of the HA-Es specimens, MC3T3-E1 osteoblast-like cell and rat bone marrow cell were used. The cell morphology, cell proliferation, cell differentiation and cell mineralization of the samples were investigated.

3.7.1 Sample Preparation

The cell study on the HA-Es samples was carried out on disc samples using a 20 mm diameter die. The as prepared HA-Es powders was pressed at 15 MPa and the green

compacts were subsequently subjected to cold isostatic pressing at 200 MPa for 1 minute. The biocompatibility was performed on the discs which have been heat treated at 800 °C, 1200 °C and 1250 °C for 2 hours. The specimens were sterilized at 120 °C for 4 hours before the cell seeding, following the placement in an aluminium foil covered crucible. In this experiment, the cells were grown in an incubator (AVO-200N, As One, Kyoto, Japan) at 37 °C with 5 % CO₂ at 100 % humidity.

3.7.2 MC3T3-E1 Osteoblast-like Cell

The MC3T3-E1 cells (Riken Biosources, Saitama, Japan) were cultured in polystyrene tissue dishes (Falcon, N.J USA) with a growth media of α -Modified Minimum Essential Medium (α -MEM; GIBCO, Invitrogen™, NY, USA) containing 10 % heat-inactivated fetal bovine serum (FBS; GIBCO, Invitrogen™, NY, USA), 1 % antibiotic Penicilin-streptomycin (GIBCO, Invitrogen™, NY, USA) at the laboratory of Department of Biomaterials, Faculty of Dental Science, Kyushu University, Japan.

The cells were allowed to multiply in an incubator at 37 °C with 5 % CO₂ at 100 % humidity. For seeding purpose, the passage 3 cells were used after it has reached the confluence and healthily adapt to the physiological environment. The cell was washed with phosphate buffered saline (PBS) and detached using 0.25 % trypsin-EDTA (Trypsin; GIBCO, Invitrogen™, NY, USA). Following this, the initial cell attachment, morphology and proliferation on the HA-Es samples (at different sintering temperature) were investigated.

3.7.3 Rat Bone Marrow Cell (RBMC) Isolation

The bone marrow cells were harvested from young (4 week-old rats) Sprague-Dawley (SD) rats at the laboratory of Department of Biomaterials, Faculty of Dental Science, Kyushu University, Japan. During the cells preparation, the femur and tibia of the rats were aseptically removed. After removal of epiphyses, bone marrow was flushed out from medullary cavity with α -MEM. After centrifugal at 12000 rpm for 5 minutes, the cells were collected and washed for three times. Bone marrow cells were cultured in a growth media with α -Modified Minimum Essential Medium (α -MEM; GIBCO, Invitrogen™, NY, USA) containing 15 % heat-inactivated fetal bovine serum (FBS: GIBCO, Invitrogen™, NY, USA), 1 % antibiotic Penicilin-streptomycin (GIBCO, Invitrogen™, NY, USA) and incubated at 37 °C with 5 % CO₂ in 100 % humidified atmosphere. For seeding purpose, the adherent cells were harvested and passaged using 0.25 % trypsin-EDTA (Trypsin; GIBCO, Invitrogen™, NY, USA) after it has reached the confluence.

An osteogenic medium consisting of growth medium plus 100 nM dexamethasone (Sigma), 10 mM β -glycerophosphate (Sigma) and 50 μ g/ml ascorbic acid (Wako Pure Chemical Industries Ltd., Japan) were used in the RBMC culturing with respect to the differentiation experiment. Following this, the cell attachment, morphology and proliferation on the HA-Es samples (at different sintering temperature) were investigated.

3.7.4 Cell Detachment and Cell Counting Prior to Seeding on the Sample

Counting of cells after trypsinization was conducted in order to measure the growth of cell populations. For that, any floating cells was removed by washing with PBS for two times. The cells adhered at the bottom were then harvested with 0.25 % Trypsin-EDTA. Afterward the growth medium (α -MEM+15 % FBS+1 % antibiotic) was added

to inactive Trypsin, the growth medium and Trypsin was mixing well by pipetting for 10 times and transferred to a 50 ml tube which was centrifuged at 12000 rpm for 3 minutes. The cells were counted on a hemacytometer (Burker-Turk counting chamber, ERMA Inc., Tokyo Japan) and seeded on the samples.

3.7.5 Cell Morphology

For cell morphologies evaluation, cells were loaded on the sample and incubated for preset period. The culture period was set for 4 hours, 1 day and 3 days in a 24-well plates. Cells were cultured on the samples at an initial seeding density of 1×10^4 cells/cm². After each predetermined period, the samples were gently rinsed with PBS before fixed with 3 % glutaraldehyde (SIGMA) in sodium phosphate buffer at 4 °C for 2 hours. The samples were dried in hexamethyldisilazane (HDMS, Wako Pure Chemical Industries Ltd., Japan). To ensure the complete removal of ethanol, this procedure was repeated for three times and followed by the sputtering of the samples with a thin gold film after the HDMS was completely evaporated. Then, the cell images on the HA-ES samples were visualized by SEM.

3.7.6 Cell Proliferation

Cell proliferation was examined using Cell Counting Kit-8 (CCK-8, Dojindo, Kumamoto, Japan) after 1, 3 and 5 days of culture according to the manufacturer's protocol. Due to its nonradioactive trait, CCK-8 allows sensitive colorimetric assays for the determination of the number of viable cells in cell proliferation. For this kit, tetrazolium salt (WST-8) is reduced by dehydrogenases in cells to give an orange-colored product (formazan), which is soluble in the tissue culture medium. The amount of the formazan dye generated by dehydrogenases in cells is directly proportional to the number of living cells (see Appendix C-4).

For cell proliferation, the samples with cells were washed with PBS for three times and cultured for 1 hour in an incubator with CCK-8 solution in growth solution (1:9). The resulting solution was then removed from the sample before being transferred to 96-well clear bottom plate. The absorbance at 450 nm was measured on a microplate reader (Tecan infinite M200, Austria GmbH, Grodig, Austria) and converted to cell number using a standard calibration curve obtained from the absorbance intensity of a known number of viable cells.

3.7.7 Cell Differentiation: Alkaline Phosphatase Activity

Alkaline phosphatase (ALP) is an enzyme produced by differentiating osteoblast and is responsible for the construction of bone matrix (Bernhardt et al., 2011). Proliferating osteoblasts show alkaline phosphatase (ALP) activity and this is greatly enhanced during in vitro bone formation. Therefore, ALP activity is important as it dictates and confirm the ability of the cells to carry out osteogenic functions and differentiate on an artificial material. ALP activity was evaluated by the quantitative measurement of p-nitrophenol formed at the absorbance of 405 nm due to p-nitrophenolate (Table 3.2) from the enzymatic hydrolysis of p-nitrophenylphosphate (pNPP).

In this research work, ALP activity was performed on the rat bone marrow cells after the cells were cultured on the sample for 7, 14 and 21 days. The alkaline phosphatase (ALP) activity was quantified using a Lab Assay ALP Kit (Wako Pure Chemical Industries Ltd., Japan) according to the manufacturer's instructions. Briefly, the medium was removed and the samples were washed with PBS. Then, 500 μ L of cell lysis buffer M (Wako Pure Chemical Industries Ltd., Japan) containing 20 mM Tris-HCl, 200 mM sodium chloride, 2.5 mM magnesium chloride, and 0.05% NP-40 substitute was added to each well and incubated at room temperature for 30 min. The resulting solution was transferred to 1ml centrifuge bottle. After centrifugation, 20 μ L of the cell lysate was

incubated with a buffer solution containing disodium *p*-nitrophenylphosphate at 37 °C for 15 min. The absorbance of the samples at 405 nm was measured using a microplate reader (TECAN). The protein concentration in the lysate was measured using the Bio-Rad Protein Assay (Bio-Rad Laboratories Inc., California, USA). The ALP activity was normalized to the total amount of cellular protein for each sample.

Table 3.2: Amount of working reagents used for ALP measurement

	Test	Blank	Standard
Working assay solution	100 µl	100 µl	100 µl
Sample	(sample) 20 µl	(distilled water) 20 µl	(dilution series) 20 µl
Shake for 1 minute by plate mixer and incubate for 15 min at 37 °C			
Stop solution	80 µl	80 µl	80 µl
Shake for 1 minute by plate mixer and measure the absorbance at 450 nm of wavelength using microplate reader			

3.7.8 Mineralization Assay

In the mineralization assay, the formation of mineralized nodules marked the osteoblast differentiation. The mineralized nodules is mainly composed of inorganic hydroxyapatite (HA) ($\text{Ca}_{10}(\text{PO}_4)_6(\text{OH})_2$) and organic components including type I collagen. In vitro mineralization by cultured osteoblasts is typically assessed using histochemical methods that includes Alizarin Red S. Alizarin Red S (ARS), an anthraquinone dye, has been widely used to evaluate calcium deposits in cell culture. The ARS staining is quite versatile because the dye can be extracted from the stained monolayer of cells and readily assayed

Firstly, the cells were seeded at an initial density of 4×10^4 cells/ml. After 14 days of culture, the specimens were washed twice with PBS. Calcium content of the supernatant was measured using a calcium C-test Wako kit (Wako Pure Chemical Industries Ltd., Japan) at an absorbance wavelength of 610 nm.

University of Malaya

CHAPTER 4: RESULTS AND DISCUSSION (PART 1)

4.1 Introduction

The results and discussion will be presented in two parts. This Chapter 4 (Part 1) presents the details of the experimental results and discussion of the powder characteristics of three different synthesized HA powders. The primary was HA-Es prepared by solid state reaction and subsequent heat treatment by using waste eggshells as Ca precursor followed by HA-Wp and HA-Sg which were prepared by wet chemical precipitation and sol-gel route, respectively, using commercially available precursor. Based on the comparison between the HA-Wp and HA-Sg powders, the powder that exhibited the overall best properties was selected for further studies.

4.2 Development and Characterization of Eggshell Based Hydroxyapatite (HA-Es) Based on A Solid State Reaction

The eggshell was first calcined to remove organic compounds in the inherent CaCO_3 in eggshell as it has high reactivity. Different calcination temperatures were used, e.g. 700 and 800 °C. These calcinations temperatures were chosen because the decomposition of CaCO_3 to CaO has taken place at 800 °C (Dasgupta et al., 2004; Siva Krishna et al., 2007; Ho et al., 2013). The XRD result of calcination of the eggshell is shown in Figure 4.1. Predominant peaks of inherent CaCO_3 (JCPDS: 00-086-2334) are observed in the structure of raw eggshells where the highest intensity peak is observed at a 2θ angle of 29.40° (Figure 4.1 (a)). Upon calcination of eggshells at 700 °C (Figure 4.1 (b)), the XRD analysis indicated that the inherent crystalline phase of pure CaCO_3 remained. However, after calcination at 800 °C (Figure 4.1 (c)) the presence of both CaCO_3 and CaO phases are observed. This indicates a partial decomposition of the CaCO_3 in eggshells to CaO has taken place. Moreover, Lee &

Oh (2003) reported that CaCO_3 has completely decomposed to CaO at $800\text{ }^\circ\text{C}$. Therefore, the calcination temperature of the crushed eggshells was chosen at $700\text{ }^\circ\text{C}$. Moreover, at this temperature, any organic residue is believed to be removed.

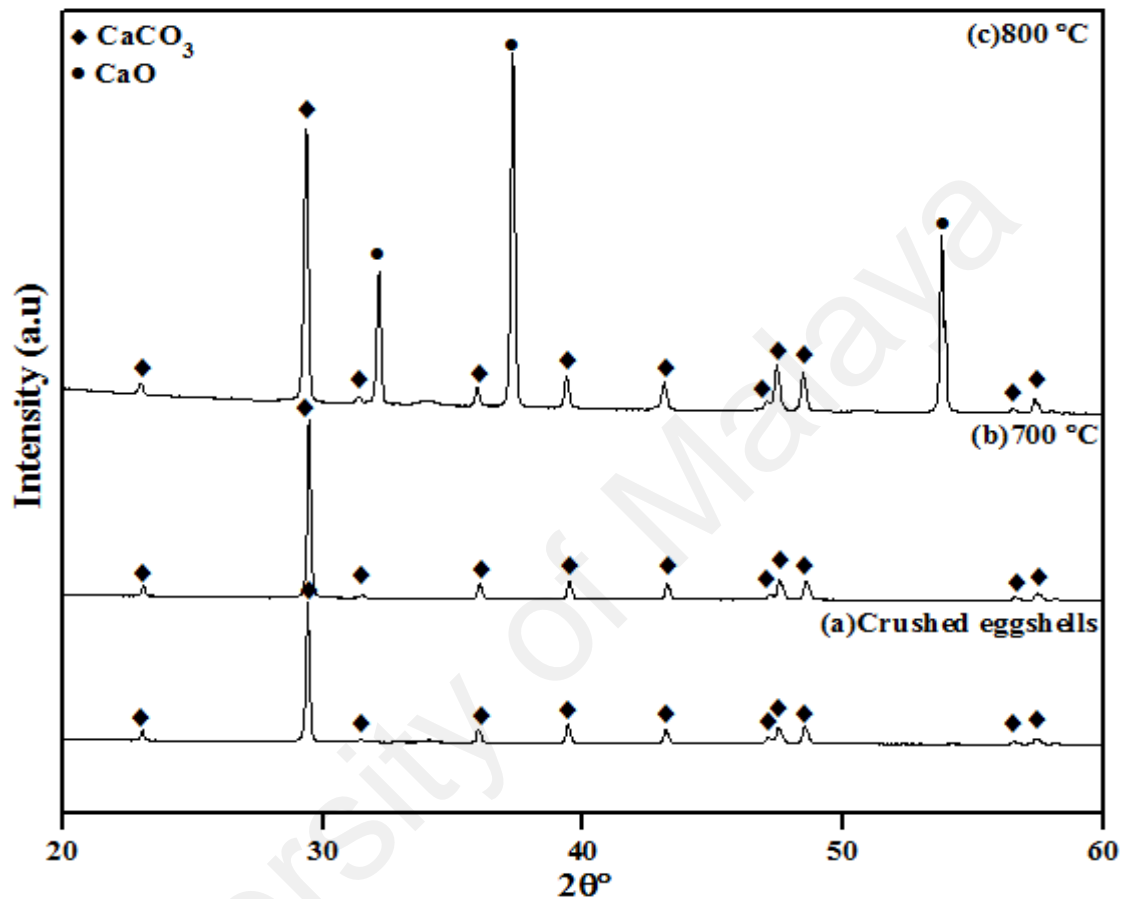


Figure 4.1: The XRD of crushed and heat treated eggshells

Upon mixing the calcined eggshell powder and $\text{CaHPO}_4 \cdot 2\text{H}_2\text{O}$ (DCPD) at 400 rpm for 2 hours, the powder mixture was subjected to thermal analysis to determine the temperature at which the chemical reaction of the HA formation has taken place. The TGA result of the mixture of calcined eggshell and DCPD is shown in Figure 4.2. The TGA curve shows about $\sim 2.68\%$ weight loss from room temperature to $200\text{ }^\circ\text{C}$, which was due to the evaporation of adsorbed water from the surface as well as pores (Yeong et al., 2001; Prabakaran & Rajeswari, 2009). Then the steady and continuous $\sim 6.31\%$ weight loss up to $\sim 500\text{ }^\circ\text{C}$ is ascribed to the loss of adsorbed and lattice water

(Siddhartan et al., 2009). The prominent weight loss of about ~13.28 % over the temperature range ~650 °C to 785 °C suggests that the partial reaction between CaCO_3 and $\text{CaHPO}_4 \cdot 2\text{H}_2\text{O}$ might take place, and so this weight loss could attribute to decarboxylation of CaCO_3 related to a release of carbon dioxide. Subsequently, the reaction of CaCO_3 and DCPD might be completed at about 800 °C and as such there were only insignificant weight changes (less than 1 % weight loss) up to 1000 °C. This indicates the high thermal stability of the synthesized HA-Es within that temperature range. Therefore, the heat treatment of mixture was chosen at an initial temperature of 800 °C.

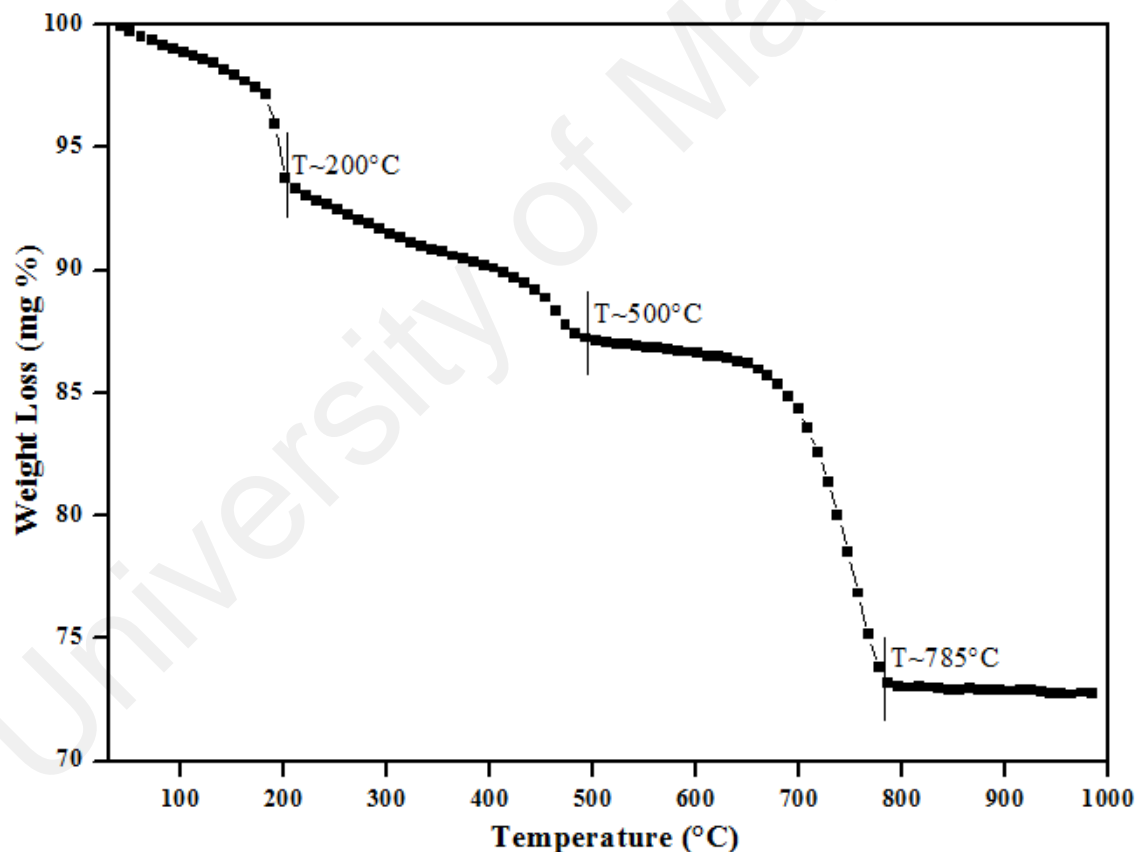


Figure 4.2: TGA analysis of eggshells powder and DCPD mixture after attrition milling

The earlier observation in TGA analysis is further supported by the XRD result of the calcined eggshell and DCPD mixture in an attempt to study the effect of calcination

at different temperatures, e.g. 700 °C, 800 °C, 900 °C and 1000 °C on HA-Es phase stability. The result shows that at 700 °C, the as-milled powder mixture has partially reacted and decomposed to biphasic calcium phosphate mixture (HA + β -TCP) with β -TCP being the dominant phase (Figure 4.3 (b)). As the calcinations increases to 800 °C, HA phase was found to be more thermodynamically stable with the absence of β -TCP peak as shown in Figure 4.3 (b). It was worth noting that the decomposition reaction has completed since it has transformed to phase pure HA as suggested in Equation 3.1 and described fully in Section 3.2.1. These results indicate that β -TCP was formed from the starting materials reaction meanwhile HA was then formed with an increase in heat treatment temperature. As the temperature increases to 900 °C (Figure 4.3 (c)) and 1000 °C (Figure 4.3 (d)), there was no decomposition to secondary phases detected. On the contrary, Wu et al. (2015) reported that heat treatment of HA derived from mixture of eggshell and DCPD, at 1000 °C with a ramp rate of 10 °C/min for 3 and 5 hours resulted in HA phase with traces of starting materials and β -TCP phase, respectively.

In this work, the XRD result in turn matched to the TGA result of insignificant weight changes observed starting from 800 °C up to 1000 °C (Figure 4.2). Raynaud et al. (2002) stated that decomposition of heat treated HA ceramic at 900 °C could be resulting from the non-stoichiometric composition of the starting HA powder. The only difference in XRD patterns of Figure 4.3 (c) – (e) is in the degree of HA crystallinity with sharper and more defined peaks. In addition, it was observed that the increase in heat treatment temperature resulted in an increase in the crystallite size since larger crystallites form favorably at a higher temperature (Ng et al., 2010). This, in turn, decreases the surface areas of the powders. The average crystallite size measured corresponding to the (211) and (112) planes is tabulated in Table 4.1.

Table 4.1: Crystallite size of calcined HA-Es powder at various temperatures

Temperature (° C)	Crystallite Size (nm)
800	56.11
900	69.52
1000	78.91

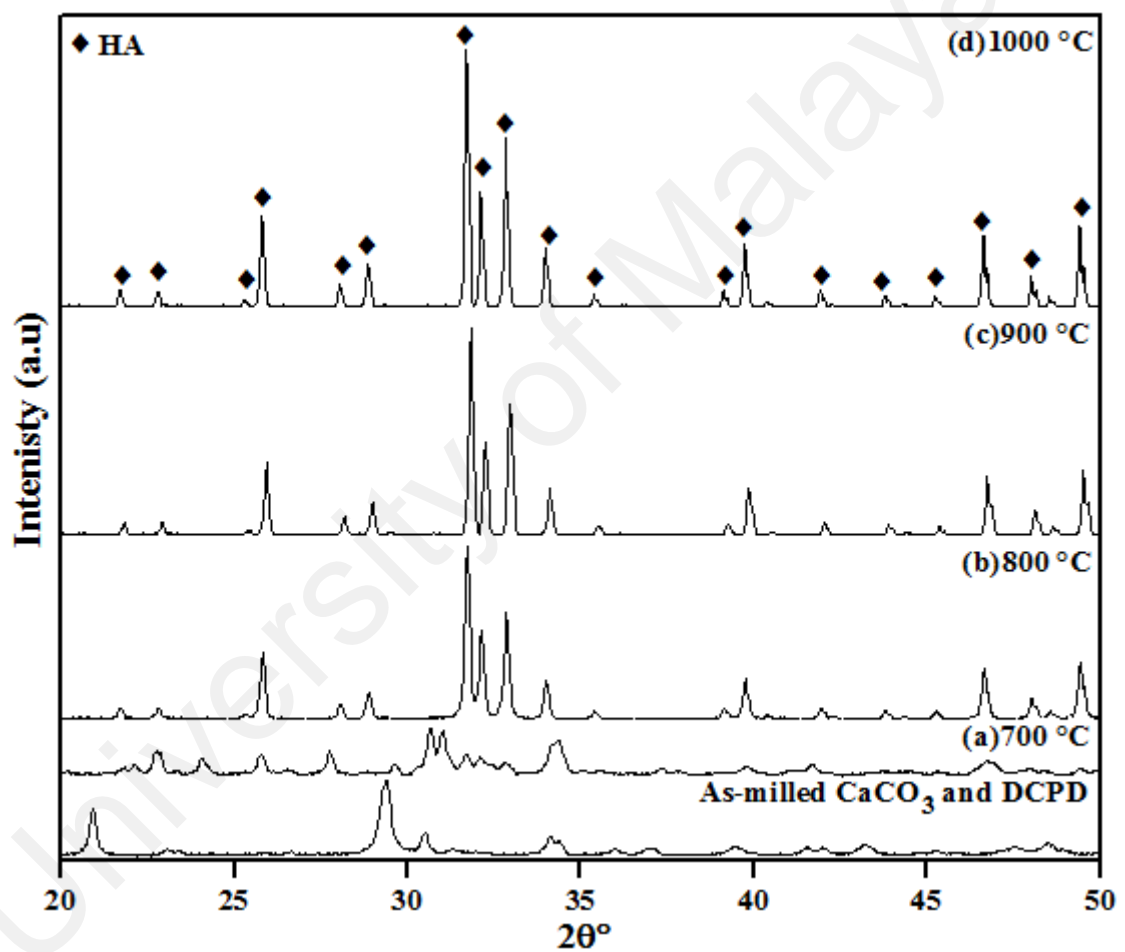


Figure 4.3: XRD patterns of as-milled and calcined at (a) 700 °C, (b) 800 °C, (c) 900 °C and (d) 1000 °C, powder mixture

The XRD pattern of the powder mixture after heat treatment at 800 °C for 5 hours is presented in Figure 4.4. Interestingly, all patterns matched with the JCPDS Card Number 09-0432 for hydroxyapatite. The highest intensity peak of (211) is observed at

a 2θ angle of 31.72° . This demonstrated that single phase HA was successfully derived from eggshell. This result is encouraging as there was no appearance of β -TCP and CaO phases as the calcination temperature increases above 650°C as reported by other work on solid state reaction (Guo et al., 2013). The average crystallite size of phase pure eggshell-derived HA (HA-Es) powder that corresponded to the (211) and (112) planes was found to be 54.60 nm whereas the specific surface area (SSA) of the HA-Es powder obtained from the BET measurement was $8.71\text{ m}^2/\text{g}$.

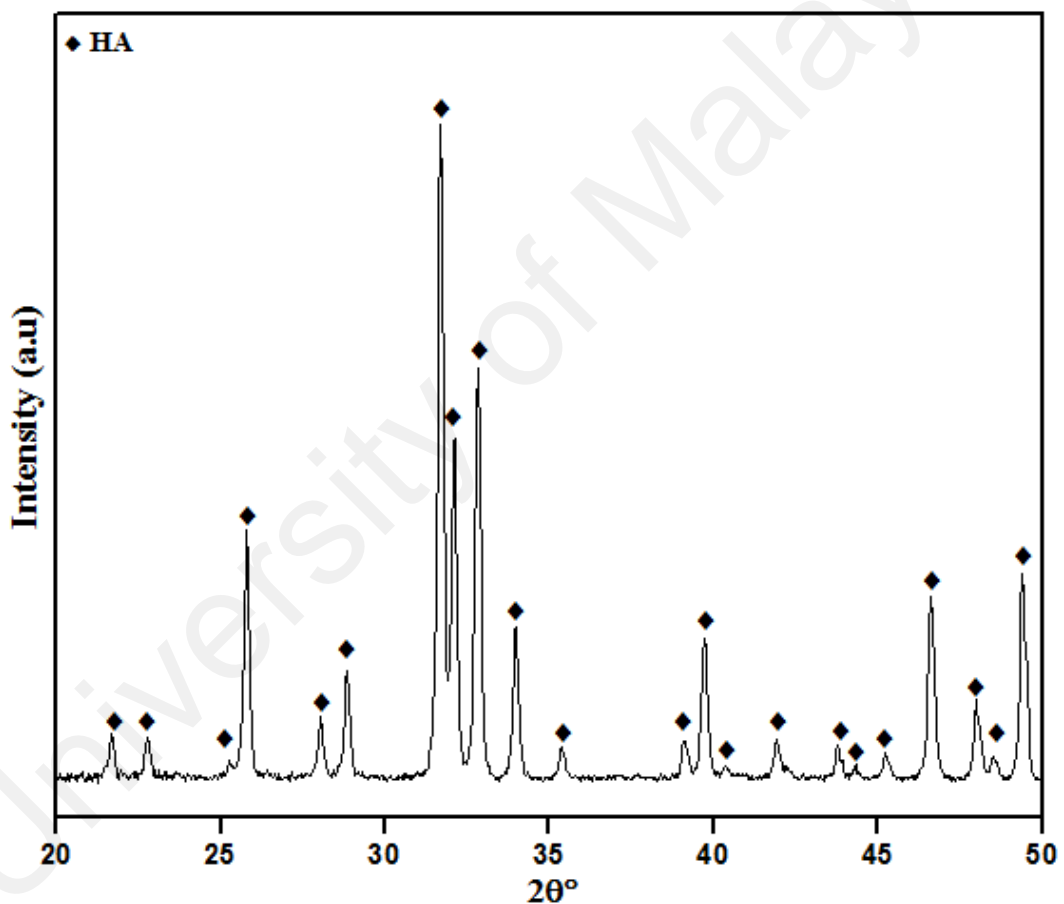


Figure 4.4: XRD patterns of HA-Es powder pre-heated at 800°C

In this work, the milling time employed was only 2 hours for the mixing purpose. Literally, the surface area of powders can be increased with the reduction of particle size by increasing the milling time (Wu et al., 2011). An increase in specific surface area of the powders generates more sites for adsorbing water to form hydroxyl groups of

single phase HA. Besides that, coarsening of HA crystallites reduced with lowest possible calcination temperature employed (400 - 900 °C), hence larger surface area of powders could be obtained (Patel et al., 2001). However, in this work 800 °C was found to be optimum calcination temperature to obtain single phase pure HA (Figure 4.3 (b)). Rhee et al. (2002) found that XRD peak of crystalline HA has broadened and SEM images of particle size have reduced with increasing milling time from 2 to 8 hours. However, the crystallite size of HA obtained in this is slightly smaller than a recent study that obtained the phase-pure HA-Es powder at 1200 °C with a crystallite size of 59.97 nm through solid state sintering method using 1 hour ball milling time for the powder mixing (Wu et al., 2015).

The FTIR spectrum of the HA-Es powder is shown in Figure 4.5. The characteristic peaks corresponding to PO_4^{3-} (ν_3 and ν_4) vibrations of HA are observed at 1038, 605 and 568 cm^{-1} . Besides that, another characteristic peak of PO_4^{3-} (ν_1 and ν_2) appeared at 1095, 962 and 475 cm^{-1} . A broad H_2O band observed at 3425 cm^{-1} and this is attributed to the ν_3 and ν_1 stretching modes of the H_2O molecules (Kumar et al., 2012). Besides that, a band observed at 3590 cm^{-1} indicates the characteristic of O-H stretching vibration of HA (Pramanik et al., 2007). Meanwhile, broad band at 1643 cm^{-1} observed in calcined HA-Es powder is attributed to the ν_2 bending mode of adsorbed H_2O (Koutsopoulos, 2002). Frequency band observed at 2365 cm^{-1} is a characteristic of free CO_2 (Kamalanathan et al., 2014). In addition, CO_3^{2-} vibration bands are clearly observed in the calcined powder at 1463 cm^{-1} , 1421 cm^{-1} (ν_3) and 875 cm^{-1} (ν_2). Similar bands were also observed in previous studies of HA-Es (Gergely et al., 2010; Kumar et al., 2012; Kamalanathan et al., 2014). In this study, the presence of these carbonate bands is caused by the adsorption of non-structural carbonate on the surface of HA-Es crystals (Boanini et al., 2010). In addition, the absence of surface OH band at

3644 cm^{-1} which represents the presence of CaO in calcium phosphate has collectively supported the preceding XRD results in Figure 4.4 (Gergely et al., 2010).

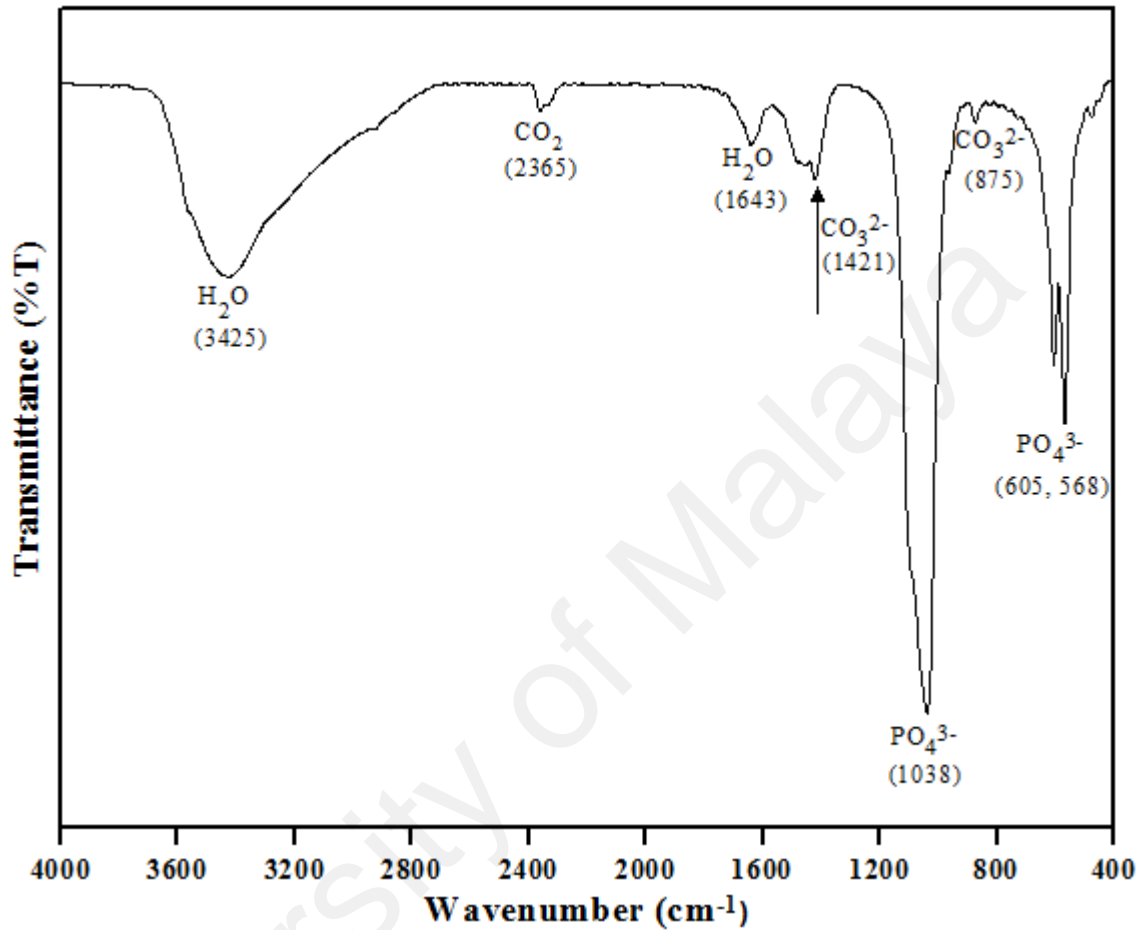


Figure 4.5: FTIR spectra of HA-Es powder pre-heated at 800 °C

Figure 4.6 shows the SEM microstructure of HA-Es powder after the heat treatment at 800 °C. Typical flower-like nanostructured HA was observed. The HA-Es microstructure composed of leaf-like flakes having the size of 100-200 nm in width. As mentioned, HA-Es has a low surface area of 8.71 m^2/g , hence there is less tendency to form large agglomerate due to the decreasing attraction between particles of Van der Waals interaction (Ferkel & Hellmig., 1999; Zanotto et al., 2011; Wu et al., 2015). In addition, the higher magnification of the particle surface that showed smooth surface of the powder particle was a typical characteristic of highly crystalline HA (Kalita et al.,

2007). Note that, calcination process which involved in the preparation process did not affect the particle sizes of HA powders (Patel et al., 2001). The similar flower-like microstructure of HA-Es has also been reported in a previous study whereby microwave irradiation conversion of eggshells was used (Kumar et al., 2012). On the other hand, spherical-like or rod-shaped HA-Es particles were observed in a study where the ball milling was used for the powder mixing instead of attrition (Wu et al., 2015).

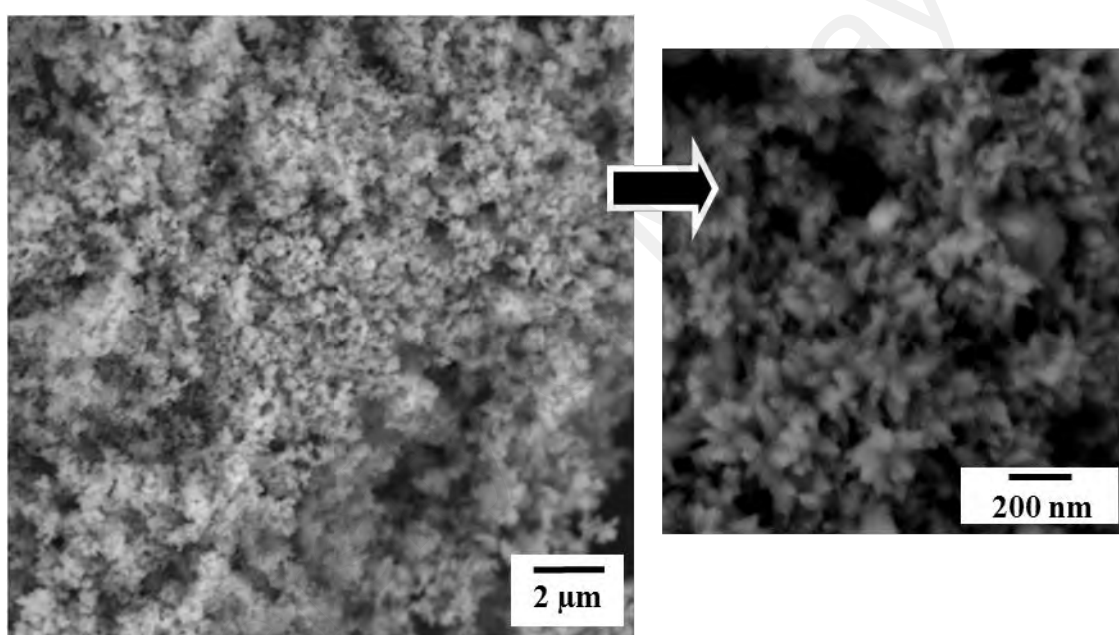


Figure 4.6: SEM of HA-Es powder pre-heated at 800 °C

It was reported that the flower-like HA act as effective carriers for drug delivery applications and bone substitutes (Wang & Shaw, 2009; Kumar & Girija, 2013). Therefore, by using attrition milling and preheat-treated at 800 °C for 5 hours, HA-Es consisted of the flower-like particle can be obtained and it can be understood that powder mixing method and heat treatment regime significantly affects the final powder morphology.

The elemental composition analysis result of the HA-Es powder by an EDS method are presented in Table 4.2. The EDS taken from individual agglomerated particles

revealed calcium and phosphorus as the primary constituents with ratio of Ca/P being 1.69 with some minor components such as C, O and Sr. The minor presence of Sr element in the nanocrystalline HA-Es powder was believed to be inherited from the biological origin of eggshells as the source of Ca precursor itself. A similar finding was also reported by Siddhartan et al. (2009). Besides that, it was reported that the basic crystallographic characteristics of HA were not affected by the presence of trace elements (Ho et al., 2013). But in return, the overall biological performance of the implant material could be improved.

Table 4.2: The elemental composition (wt %) of HA-Es.

Data are presented in mean \pm standard deviation

Element	Composition (wt. %)
Ca	15.1 \pm 0.4
P	8.9 \pm 0.5
Sr	0.3 \pm 3.2
C	42.6 \pm 1.1
O	32.9 \pm 0.8
Ca/P	1.69

4.3 Characterization of HA Powders Synthesized via Wet Chemical

Precipitation (HA-Wp) and Sol-Gel Method (HA-Sg) Using Commercial Chemicals as Ca-Precursor

The XRD patterns of the as-synthesized HA-Wp and HA-Sg after drying the powders from the two methods are presented in Figure 4.7. All patterns matched with the JCPDS Card Number 09-0432 for hydroxyapatite. Figure 4.7 also shows that both powders were purely crystalline HA phase. However, significant differences in degree of crystallinity (as indicated by the peak height) and peak width between HA-Wp and

HA-Sg powders were observed. The primary peaks of HA at (211), (112), and (300) from HA-Wp powder have broadened peaks. The broad diffraction peaks of HA-Wp indicated the powder is less crystalline which is a typical characteristic of HA prepared by wet precipitation method. In contrast, HA-Sg powder exhibited sharp reflections that represent the higher degree of crystallinity of the powder. As crystallization process is controlled by diffusion (Wu et al., 2015), the sharp peaks of the HA-Sg powder could be due to the higher temperature applied for the thermal treatment (500 °C) compared to that of HA-Wp powder drying (60 °C). Fathi et al. (2008) reported that the crystallinity and crystallite size of HA powder synthesized via the sol–gel method depended on calcination temperature, in which the degree of crystallinity increased with calcination temperature.

Broader peaks translate to a higher value of FWHM, which indicates smaller crystallite size (Li et al., 2008; Wu et al., 2013). In other words, HA obtained via the wet precipitation method had a smaller crystallite size compared to that HA obtained from sol–gel synthesis. This result was further confirmed by the crystallite size value obtained using the Scherrer's formula (Equation 3.3). The mean crystallite sizes for HA-Wp powder were 19.92 and 44.90 nm, taken at the (211) and (112) peaks of HA, respectively. In contrast, for the HA-Sg powder, the crystallite sizes that corresponded to the (211) and (112) planes were 51.23 and 59.84 nm, which are considerably larger than those of the HA-Wp powder.

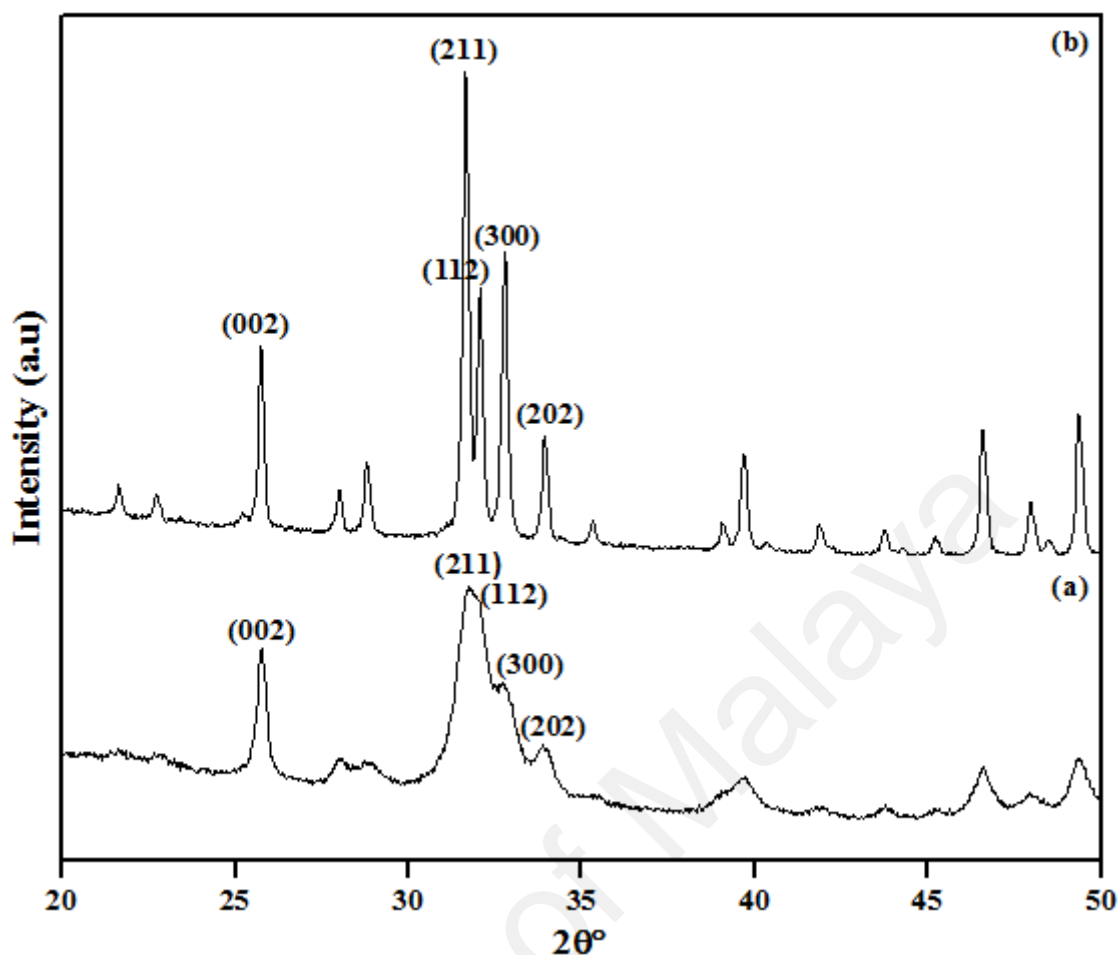


Figure 4.7: XRD patterns of as-synthesized HA powders obtained from:
 (a) wet chemical (HA-Wp) and (b) sol-gel (HA-Sg). All peaks corresponded to the HA phase

The smaller crystallite size of HA-Wp was also supported by the specific surface area results obtained from the BET measurement. The surface areas of HA-Wp and HA-Sg powders were 97.41 and 8.98 m²/g, respectively. Small surface area of HA-Sg can be associated with the favorable growth of crystallites due to higher synthesis temperature. In sol-gel synthesis, it involved reflux stage which took place at ~100 °C as described in Section 3.2.3. Meanwhile, synthesis of HA-Wp through chemical precipitation method was prepared at ~32 °C. As a result, the powder reactivity of HA-Wp could be significantly enhanced because of the smaller crystallite size, which consequently increases the specific surface area to volume ratio (Sooksaen, 2010). In

addition, the HA-Wp powder characteristic also more likely correlates to the properties of the bone mineral crystal, namely, low crystallinity with an extremely large surface area (Zhou & Lee, 2011; Khalid et al., 2013).

The effect of calcination at different temperatures of 800 °C, 900 °C and 1000 °C on HA phase stability was conducted on the as-synthesized HA-Wp and HA-Sg powders. According to Pattanayak et al. (2011), calcination at different temperatures (200 °C to 1000 °C) of HA powder synthesized via precipitation technique revealed that the crystalline HA phase was stable up to 600 °C prior to its transformation into crystalline TCP. A similar result was also obtained by Fathi et al. (2008) and Salimi et al. (2012) at a temperature of 600 °C in the thermal stability observation of HA synthesized via the sol-gel technique. Meanwhile, Sahu et al. (2012) found that HA powder obtained via sol-gel synthesis maintained its phase stability after calcination at 750 °C. Hence, in this work, the temperature range of 800 °C to 1000 °C was selected for calcining HA, taking into account that the possibility for HA decomposition to other phases, primarily β -TCP phase, can only be obtained after calcinations at $T > 700$ °C (Fathi et al., 2008; Champion, 2013).

The XRD patterns of the calcined HA are shown in Figure 4.8. Both powders maintained pure HA crystalline phase at 800 °C. HA-Wp powder decomposed to tricalcium phosphate (TCP) from 900 °C, as indicated in Figure 4.8 (b), in which β -TCP was presented along with HA phase. Moreover, the fraction of β -TCP phase increased upon calcinations at 1000 °C, as shown in Figure 4.8 (c). On the other hand, pure HA from sol-gel synthesis was stable at 900 °C (Figure 4.8 (e)) and started to decompose to TCP at 1000 °C, as shown in Figure 4.8 (f). In addition, it was observed that the increase in heat treatment temperature resulted in an increase in the crystallite size of the powders. This result is tabulated in Table 4.3.

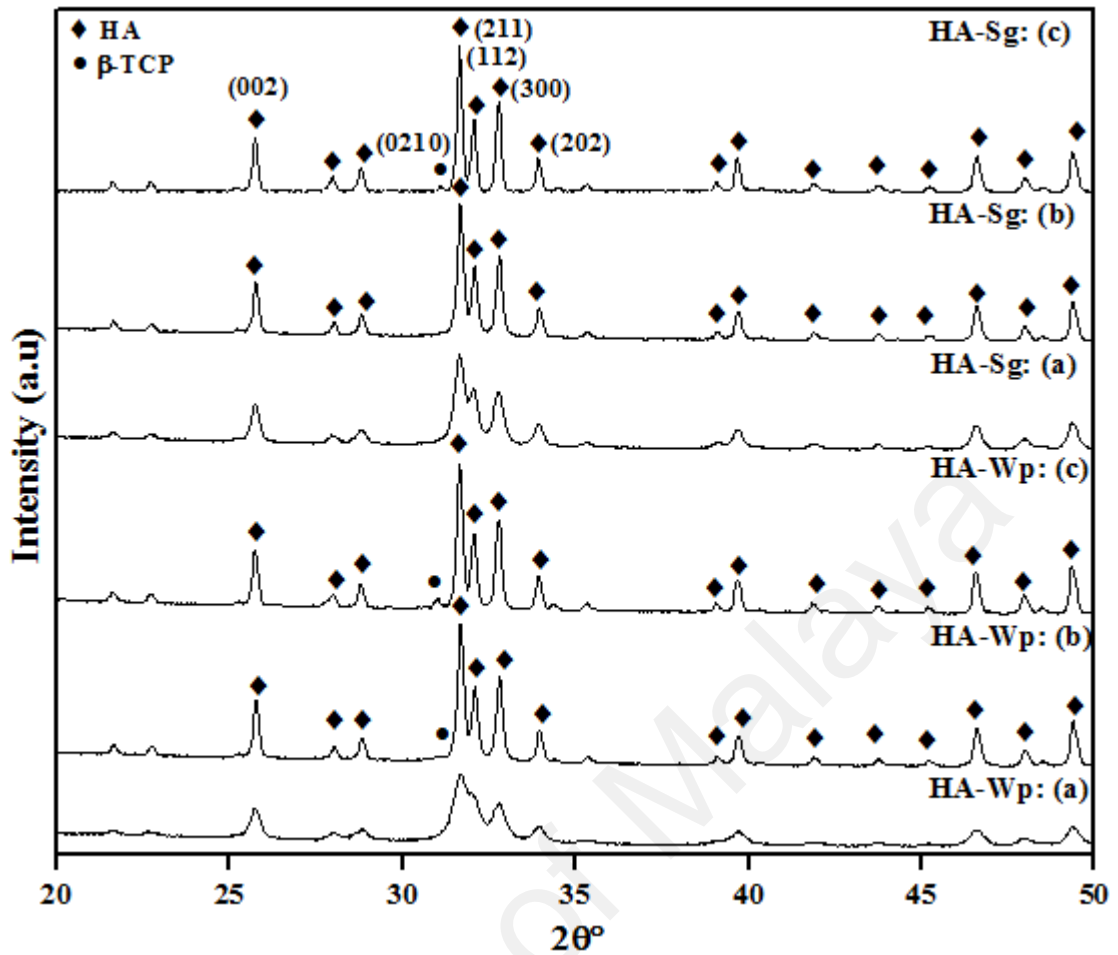


Figure 4.8: XRD patterns of calcined HA-Wp and HA-Sg powders at respective temperatures: (a) 800 °C, (b) 900 °C and (c) 1000 °C

The relative intensity ratio (RIR) of the HA:β-TCP was determined by using the XRD intensity (I) of planes reflection of (211) and (2 0 10) peaks of HA and β-TCP, respectively using the formula, $RIR = I_{\beta\text{-TCP}(0\ 2\ 10)} / (I_{\beta\text{-TCP}(0\ 2\ 10)} + I_{\text{HA}(211)})$ (Victoria & Gnanam, 2002; Zhang & Zhang, 2011). The result is shown in Table 4.4. It was found that the intensity ratio of β-TCP was extremely small for both calcined powders.

Table 4.3: Crystallite size of calcined HA-Wp and HA-Sg powders at various temperatures

Temperature (° C)	Crystallite Size (nm)	
	HA-Wp	HA-Sg
800	48.01	69.04
900	57.36	78.30
1000	65.23	85.20

Table 4.4: Relative intensity ratio of β -TCP presented in HA-Wp and HA-Sg powders upon calcination

Temperature (° C)	HA-Wp	HA-Sg
	β -TCP(%)	β -TCP(%)
800	0	0
900	2.30	0
1000	5.30	3.45

The decomposition of HA powders into β -TCP phosphate is a characteristic of Ca-deficient HA powders (Dorozkhin, 2010; Ergun et al., 2011; Mir et al., 2014). However, if the decomposition forms α -TCP as the secondary phase instead, this formation could not be attributed to non-stoichiometric HA. Instead, the formation could be due to the development of an intermediate phase, oxyapatite, which shows the gradual loss of the radical OH^- (dehydroxylation) when heated at atmospheric conditions. According to Fathi et al. (2008), pure HA powder derived from the sol-gel was only obtained after the powder was subjected to calcination at 600 °C, whereas Khalid et al. (2013) reported that sol-gel HA powder decomposed into β -TCP and CaO at 700 °C. However, in the present work, the characteristic of pure HA was achieved

by as-synthesized HA-Sg after thermal treatment at a comparatively low temperature of 500 °C (Figure 4.7) and its phase pure HA stability was maintained until 900 °C. Meanwhile, Sooksaen et al. (2010) indicated that HA powders calcined beyond 800 °C showed the presence of CaO when HA nanopowders were synthesized via a wet chemical process by using $\text{Ca}(\text{NO}_3)_2 \cdot 4\text{H}_2\text{O}$ and $(\text{NH}_4)_2\text{HPO}_4$ as Ca and P precursors. CaO is actually an impurity in most HAs derived via sol-gel, which is due to the decomposition of calcium nitrate that remains either partially reacted or unreacted in the gel during the sintering process (Fathi et al., 2008; Kusmanto et al., 2009; Khalid et al., 2013; Wu et al., 2013). However, in the present study, CaO was not detected by XRD for both HA-Wp and HA-Sg powders.

Figure 4.9 shows the FTIR spectra of the as-synthesized HA-Wp and HA-Sg powders. The FTIR spectra exhibited the typical characteristic bands of the calcium hydroxyapatite compound, namely, the existence of phosphate and hydroxyl groups. The characteristic bands of the phosphate group, PO_4^{3-} , can be seen at ~ 1086 , ~ 1025 , ~ 960 , ~ 595 , ~ 555 , and $\sim 465 \text{ cm}^{-1}$. In addition, the broad OH^- group band was detected at the range of 3200 cm^{-1} to 3600 cm^{-1} and at 630 cm^{-1} . The IR spectra also showed a broad and a bending mode corresponding to the carbonyl group, CO_3^{2-} , at 1300 cm^{-1} to 1600 cm^{-1} and at $\sim 875 \text{ cm}^{-1}$. This result may be due to the partial substitution of carbonate groups from the environment for OH^- and PO_4^{3-} in the lattice of synthetic hydroxyapatite (Kalita & Verma, 2010) and/or the adsorbed species remaining from aqueous precipitation (Landi et al., 2008). Landi et al. (2008) also reported that the substitution of carbonate ion enhance sinterability of HA ceramics and has no effect on the grain growth. However, the carbonate ions are expected to disappear from the apatite structure at a high temperature, i.e., during heat treatment, as reported previously in FTIR studies (Sopyan et al, 2011; Mir et al., 2014).

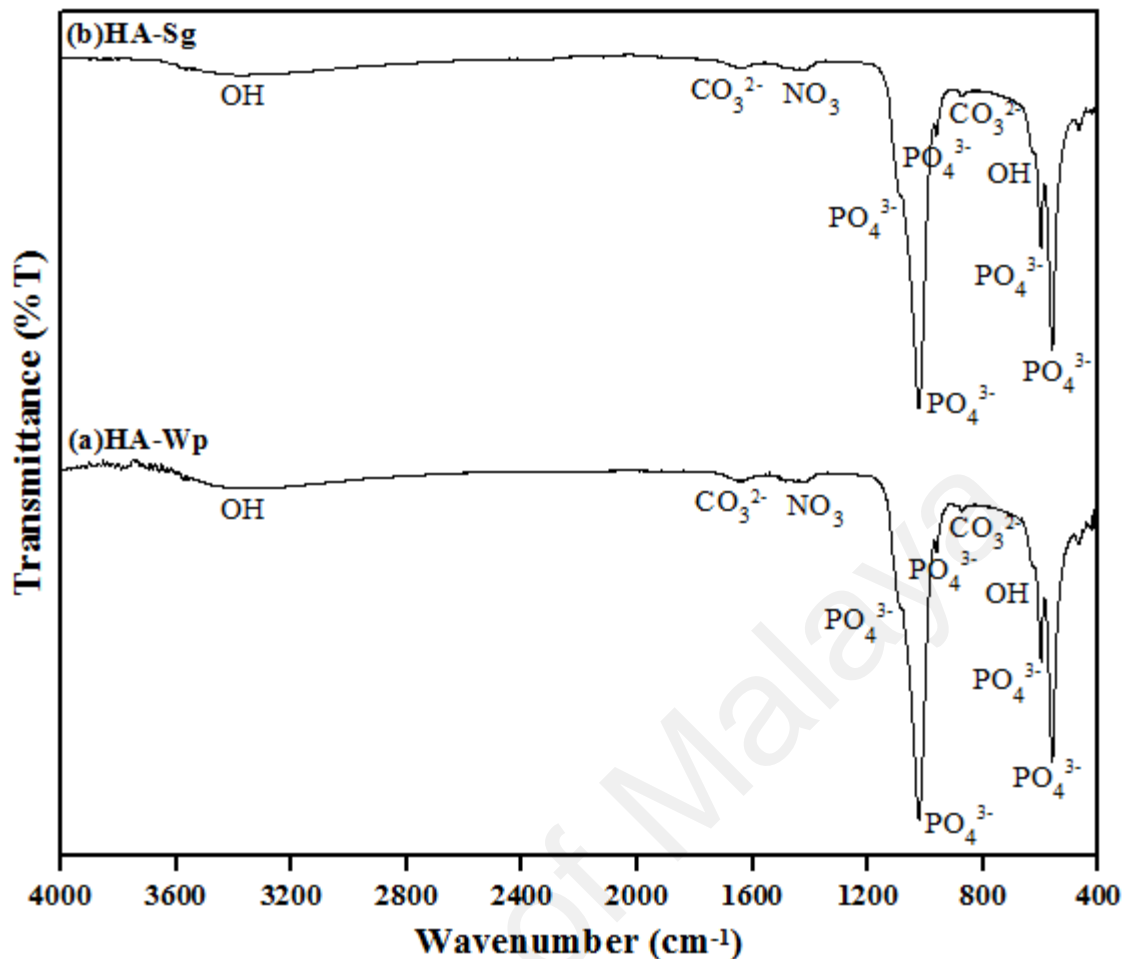
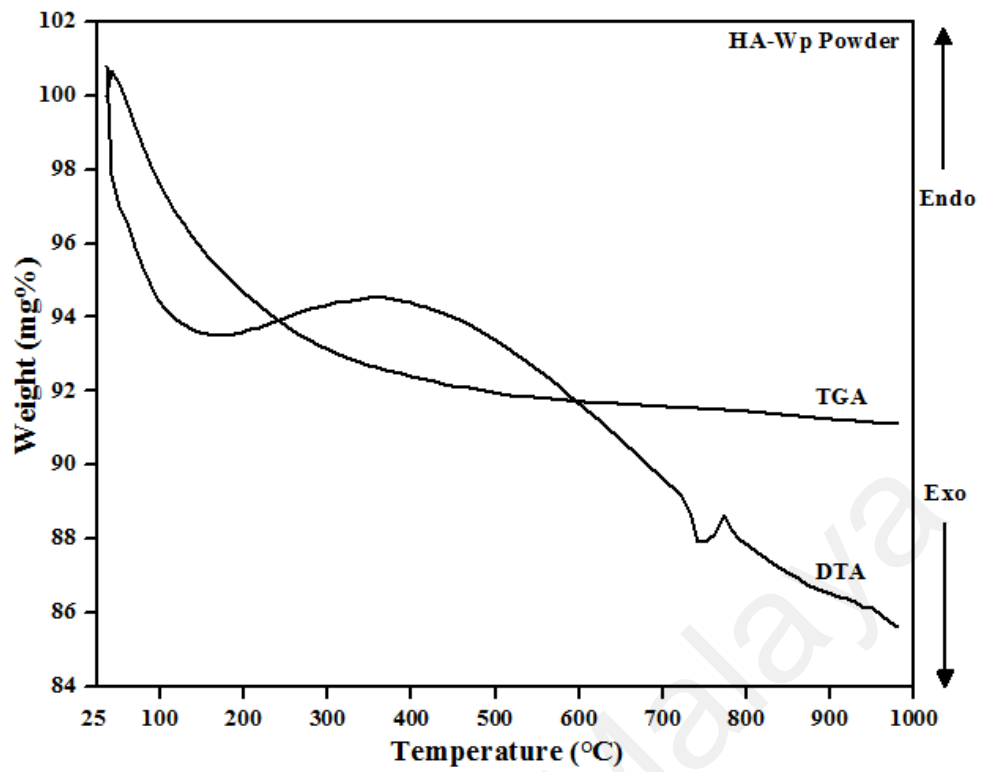
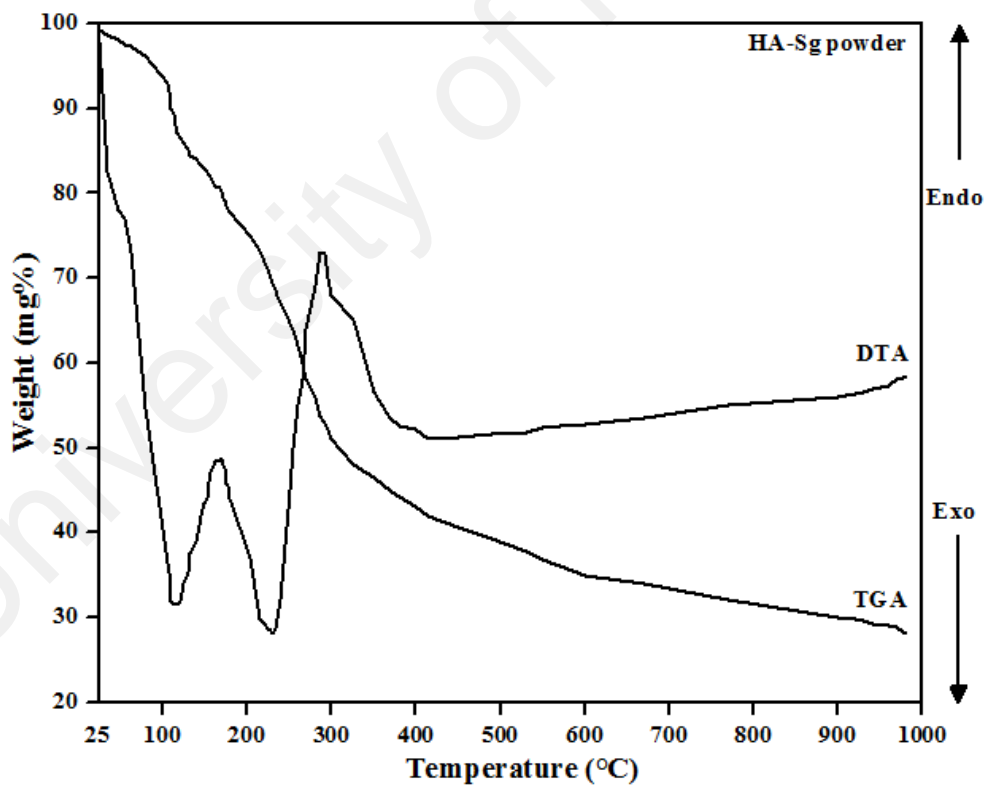


Figure 4.9: FTIR spectra of as-synthesized HA powders obtained from: (a) wet chemical precipitation (HA-Wp) and (b) sol-gel (HA-Sg) methods

The TG/DTA curves of the as-synthesized powders obtained via chemical precipitation and sol-gel synthesis is presented in Figure 4.10. Thermal analysis of the synthesized HA-Wp powder (Figure 4.10 (a)) shows a slight weight gain of $\sim 1\%$ as heating occurred. This result could be associated with the early carbonation process (Zhou & Lee, 2011). However, this process is believed to be disrupted by the desorption of water molecules, as depicted by the weight loss of about $\sim 5\%$ from $\sim 60\text{ }^{\circ}\text{C}$ to $\sim 195\text{ }^{\circ}\text{C}$. This phenomenon corresponds well with the endothermic peak in the DTA curve. Absorbed water was presented as a structured hydrated surface layer, which is a highly desirable condition for the enhancement of surface reactivity and maturation



(a)



(b)

Figure 4.10: TG/DTA analysis of as-synthesized HA powders from:

- (a) wet chemical precipitation (HA-Wp) and (b) sol-gel (HA-Sg before heat treatment) synthesis

process of HA powders (Morrissey et al., 2005). Subsequently, the exothermic reaction took place and continued until 845 °C. This continuous exothermic peak that corresponded with a total of ~6.7 % weight loss could be attributed to the crystallization process of the HA powder (Martinez-Castanon et al., 2012). Furthermore, the following exothermic peak starting from ~870 °C can be related to the initial dehydroxylation stage of HA decomposition. This phenomenon has also been reported by Martinez-Castanon et al. (2012), but the decomposition of Ca-deficient HA into β -TCP took place at a lower temperature of 813 °C. This decomposition confirmed that HA-Wp powder presents similar characteristics to Ca-deficient HA. Concurrently, a similar result was also observed from the XRD patterns in Figure 4.7 (b), in which the appearance of β -TCP for HA-Wp powder was detected at T = 900 °C after 2 h with 2.3 % fraction intensity of β -TCP.

Figure 4.10 (b) shows the TG/DTA curve for as-synthesized HA-Sg before drying via sol-gel synthesis. The first endothermic peak, which was accompanied by a weight loss of about ~10 % and occurred at ~110 °C, was due to the evaporation of water from the gel. Upon heating, a massive weight loss of ~45 % was observed within the temperature range of 120 °C and 380 °C. An exothermic peak at 160 °C, which corresponds to 16 % weight loss, is attributed to the decomposition and removal of ammonia, organic compounds, and urea. To date, no evidence regarding the possibility incorporation of ammonia ions into the apatite structure has been found in the literature. However, Morrissey et al. (2005) predicted that, with any chance of ammonia ion incorporation, the occurrence is expected to be at a low level because of their large size ($r_{\text{cationic}}=175$ pm), thereby rendering it negligible. At ~230 °C, the decomposition of nitrate and hydroxide occurred, as indicated by a weight loss of ~21 % corresponded to an endothermic peak in the DTA curve. This particular endothermic peak has been suggested as the onset of nitrate decomposition (Zakaria et al., 2013). At ~320 °C, an

exothermic peak was detected, which indicates the start of HA powder crystallization from its amorphous phase (Landi et al., 2008). Martinez-Castanon et al. (2012) have reported on the crystallization process of HA powder that occurs from 363 °C. This exothermic tendency continues up to 980 °C, thereby indicating the increase in crystallinity of HA powder. A similar phenomenon had also been reported elsewhere (Sopyan et al., 2011; Zhou & Lee, 2011). Referring to the XRD result of HA-Sg powder (Figure 4.8 (e)), a single pure HA phase was retained up to 900 °C, which slightly decomposed to β -TCP at 1000 °C for 2 hours. Thus, no definite exothermic peak reflecting this behavior was observed. In addition, the observation resulting from this analysis also clarified the reason for performing the heat treatment of sol-gel synthesized HA at 500 °C.

Figure 4.11 shows the FESEM microstructure of the as-synthesized calcium phosphate powders from wet precipitation, HA-Wp (Figure 4.11 (a)), and sol-gel synthesis, HA-Sg (Figure 4.11 (b)). Different morphologies can be observed. Both HA powders were built up from nanosized particles and showed high tendency to agglomerate. Juang & Hon (1996) and Ebrahimi-Kahrizsangi et al. (2010) stated that the high tendency of agglomeration was resulting from the increase of Van der Waals interactions due to the high surface energy of these nanoparticles. As observed in the SEM images, HA-Wp powders consisted of soft agglomerates of loosely packed smaller particles. The similar needle-like morphology of HA powder was also obtained by Martinez-Castanon (2012) through chemical precipitation while maintaining the pH reading and synthesis temperature at 7 and 60 °C, respectively.

On the contrary, HA-Sg powder appeared to be composed of hard agglomerates due to the necks formation between adjacent particles on HA-Sg powder as a result of the thermal treatment process (500 °C) carried out during the synthesis stage (Section 3.3.2). Stronger bonding between the HA-Sg particles are expected than the Van der

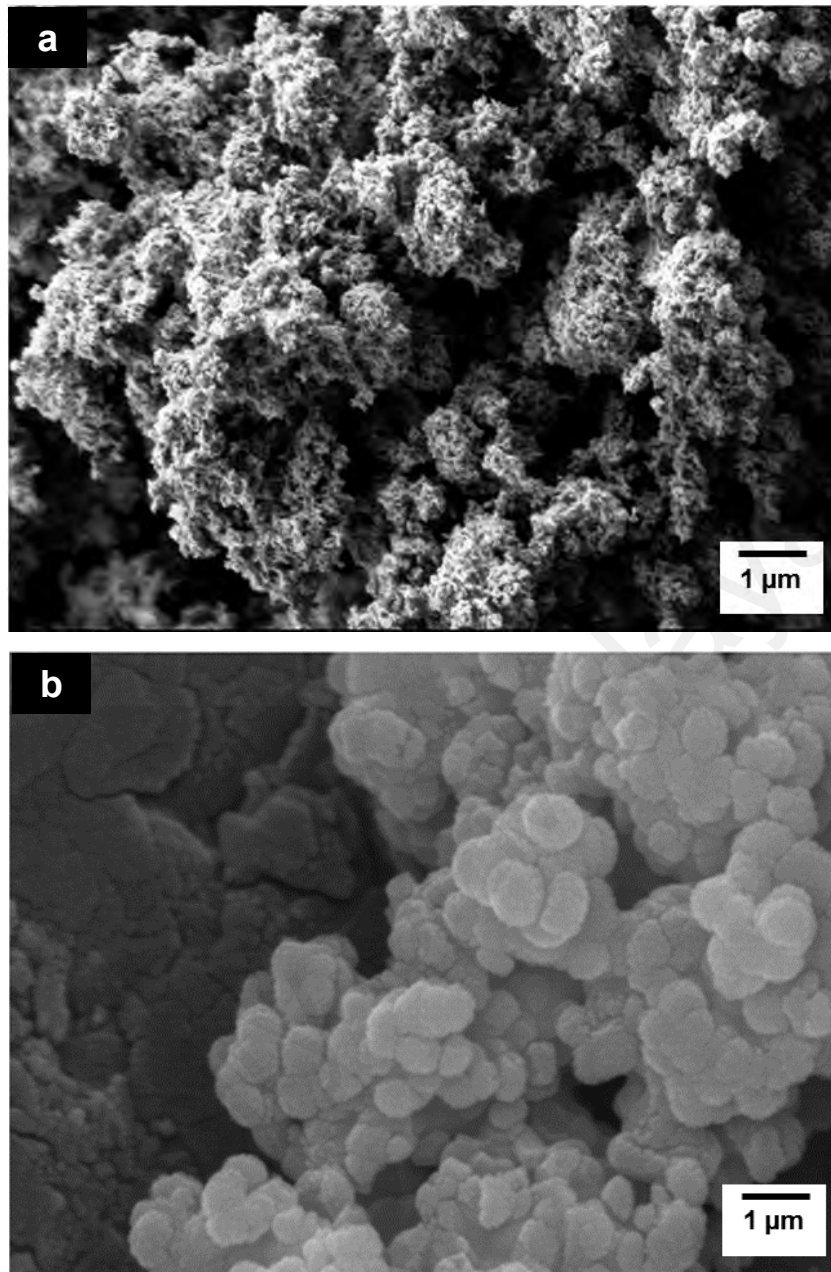


Figure 4.11: FESEM images of as-synthesized HA powders from:
(a) wet chemical precipitation (HA-Wp) and (b) sol-gel
(HA-Sg) synthesis

Waals interaction induced bonding of HA-Wp powder (Ferkel & Hellmig, 1999). Moreover, in sol-gel synthesis, dispersing all agglomerates even after rigorous stirring for hours is extremely difficult (Sahu et al., 2012). It was reported that HA starting powders with high crystallinity tend to form smaller agglomerates as they were built by larger particles (Landi et al., 2000). However, this was not observed for highly

crystalline as-synthesized HA-Sg powder in this work. Therefore, the hard agglomerate of HA-Sg powder is thought to be due to the formation of gel during the synthesis process.

HA-Wp particles were observed to be finer than those of the HA-Sg powder. Each crystallites cluster varied between ~60 nm to 100 nm and ~70 nm to 200 nm in diameter for HA-Wp and HA-Sg, respectively. Particle shape and size are known to significantly affect HA powder densification, sinterability, as well as its solubility upon implant. Nanosized HA possessed higher surface area and surface roughness (Sadat-Shojai et al., 2013), thereby resulting in better cell adhesion and bone regeneration. In addition, Zanotto et al. (2012) observed that the morphology change of HA nanoparticles is also related to their crystallinity. The needle-like shape HA nanoparticles with rough surface results in less crystalline HA, whereas the rod-like shape with a smooth surface for nanoparticles will yield a higher crystallinity (Zanotto et al., 2012). This observation can also indirectly explain the difference between HA-Wp and HA-Sg powder morphologies, as their HA crystallinity was observed to differ from one another (Figure 4.7). In other words, HA derived via sol-gel possessed higher crystallinity; thus, a smooth surface of globular-shaped nanoparticles was observed.

The EDS analyses of the HA-Wp and HA-Sg powders are presented in Table 4.5. The EDS on the individual agglomerated particles of HA-Wp and HA-Sg revealed calcium and phosphorus as the main constituents with a ratio of Ca/P being 1.63 and 1.77, respectively with two other components such as C and O.

Table 4.5: The elemental composition (wt %) of HA-Wp and HA-Sg samples. Data are presented in mean \pm standard deviation

Element	Composition (wt. %)	
	HA-Wp	HA-Sg
Ca	15.2 \pm 0.2	15.6 \pm 0.5
P	9.3 \pm 0.4	8.8 \pm 0.1
C&O	75.5	75.6
Ca/P	1.63	1.77

The TEM images (Figure 4.12) further revealed the internal microstructures of HA-Wp and HA-Sg powders. The HA-Wp powder is in the form of nanoscale needle-like shape particles (Figure 4.12 (a)), whereas the morphology of the HA-Sg powder consists of globular-shaped particles (Figure 4.12 (b)). The HA-Wp powder morphology was in nanocrystals of soft agglomerates, with individual average particle sizes ranging from \sim 11.74 nm to 50.72 nm in length and \sim 15 nm to 25 nm in width. On the other hand, the HA powder morphology from sol-gel synthesis (Figure 4.12 (b)) was highly agglomerated and confirms the presence of nanocrystals in spherical shape morphology with particle sizes from \sim 40.68 nm to \sim 82.87 nm in diameter.

The average size and morphology of both HA powders are summarized in Table 4.6. The agglomeration of the primary nanoparticles was predominant via sol-gel, thereby resulting in the formation of a cluster-like morphology. Furthermore, the calculated crystallite size based on XRD data also showed that the HA-Wp powder possessed a smaller average crystallites size (\sim 32.41 nm) compared with that derived via sol-gel HA (\sim 60.45 nm). The particle size trend obtained via the two synthesis methods is in accordance with the specific surface area results determined via the BET method. In the present study, the surface area of the powder via wet chemical synthesis (97.41 m²/g)

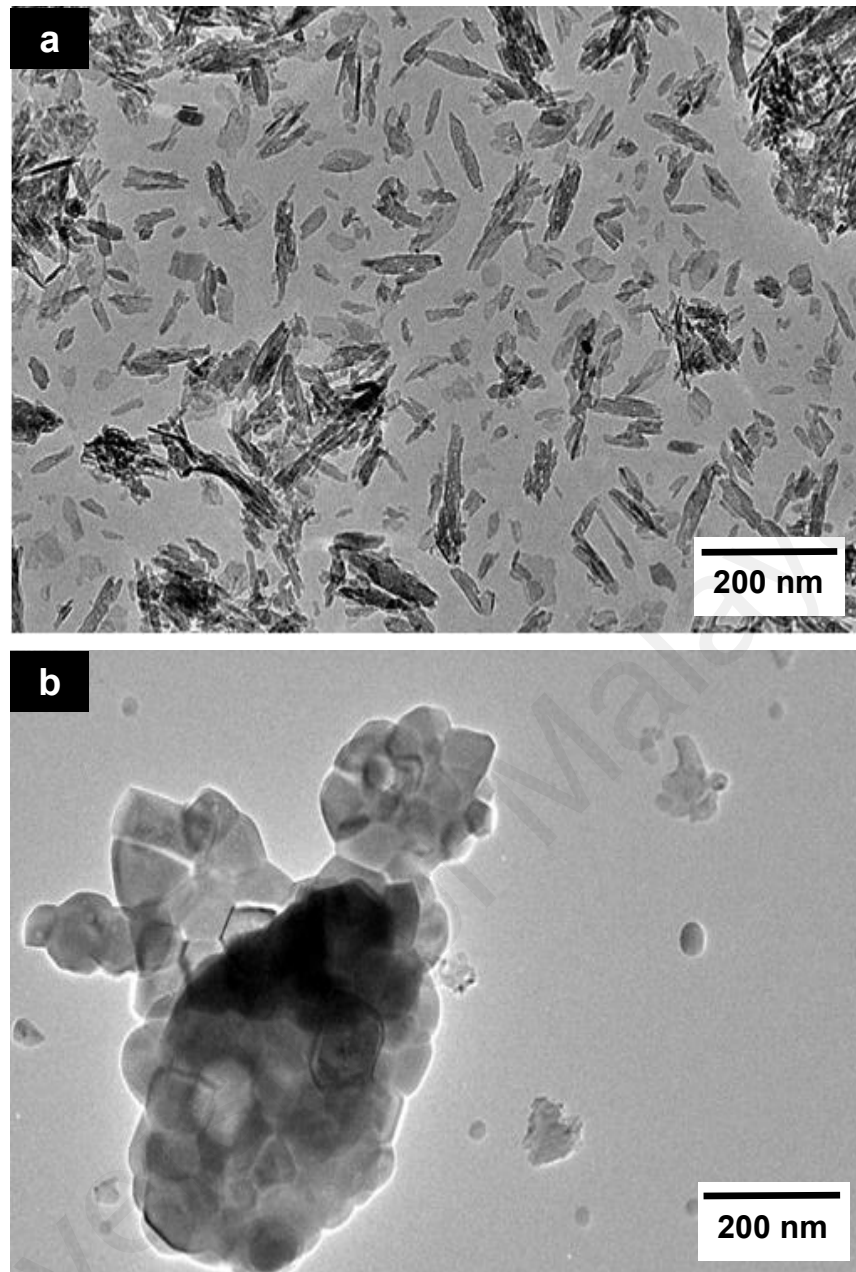


Figure 4.12: TEM images of synthesized nano-HA powder derived from: (a) wet chemical precipitation (HA-Wp) and (b) sol-gel (HA-Sg) method

showed a higher value compared with the powder obtained via sol-gel method (8.98 m²/g). The needle-like particle was found to be capable of enhancing sinterability and fracture toughness (Evis & Webster, 2011), whereas spherical-like particles were effective in drug delivery applications (Sahiner et al., 2012). Biological HA crystals

found in physiological human hard tissues are nanoscopic plat-like or rod-like crystals that are several nanometers in thickness and tens of nanometers in length (Sadat-Shojai et al., 2013). Hence, in this case, the microstructure of HA-Wp nanoparticles shows more similar characteristics to natural bone minerals than HA-Sg powder.

Table 4.6: Summary of the average size and morphology of wet chemical (HA-Wp) and sol-gel (HA-Sg) powders as observed by SEM and TEM

Sample	Average particle size (nm)	Average agglomerate size (nm)	Morphology
HA-Wp	~11 -51 (length) ~15-25 (diameter)	60-100nm	Needle-like particles
HA-Sg	~40- 83 (diameter)	70-200nm	Globular particles

CHAPTER 5: RESULTS AND DISCUSSION (PART 2)

5.1 Introduction

In Chapter 4, the properties of three different HA powders were investigated, that are HA synthesized via dry method (solid state reaction) and two HA powders derived from chemical precipitation methods (wet precipitation and sol-gel). In that chapter, the properties of synthesized HA powder using waste eggshell as Ca precursor through solid state reaction (HA-Es) was discussed followed by the discussion on the properties of HA powders synthesized via wet precipitation (HA-Wp) and sol-gel (HA-Sg) methods.

Meanwhile, in the present chapter, the sinterability of these powder compacts has been studied through pressureless conventional sintering and microwave sintering with respect to various sintering temperatures, in terms of HA phase stability via XRD analysis, linear shrinkage, microstructural evolution and grain size analysis via SEM. Then, the mechanical properties were evaluated in terms of bulk density, hardness and fracture toughness as a function of sintering temperature. The results obtained for HA-Es powder compacts are then compared to the properties of the chemical precipitation derived compacts.

It was noted that the HA powder prepared by wet chemical precipitation exhibited better properties than the sol-gel derived HA powder as discussed previously in Section 4.2. This preference was later supported by the properties of the sintered HA-Wp powder compacts. Therefore, towards the middle of this chapter, there is only discussion on the sintering behavior and the mechanical properties of HA-Es and HA-Wp powder since the synthesized HA-Sg powder has been shown to exhibit poor properties through its variation in phase stability and density upon conventional sintering.

Lastly, the final part of this chapter reported on the in vitro evaluation on the bioactivity of the heat treated HA-Es samples (800 °C , 1200 °C, 1250 °C) in phosphate

buffered saline (PBS) solution followed by their biocompatibility and biological cell studies (MC3T3-E1 osteoblast-like cell and rat bone marrow cells).

5.2 Consolidation of HA Powder through Conventional Pressureless Sintering

In the current work, all synthesized HA-Es, HA-Wp and HA-Sg powders were compacted into disc and rectangular bar samples and subsequently cold isostatically pressed (CIP) at 200 MPa prior to sintering. CIP was applied after uniaxial pressing to ensure intimate particle to particle contact in green compacts and obtain dense samples with limited grain growth (Chanda et al., 2009). The green densities of all HA powder compacts after CIP were found to be between 50 and 60 % of theoretical density ($\rho_{\text{HA}} = 3.156 \text{ g/cm}^3$) following CIP. The sintering was carried out in air atmosphere at different temperatures ranging from 1000 °C to 1350 °C with a heating ramp rate of 5 °C/min to the desired temperature and soaking time of 2 hours. All HA powder compacts did not show any cracking signs regardless the high sintering temperature employed.

5.2.1 HA Phase Stability

The diffraction patterns of the conventionally sintered HA-Es samples at varying temperatures, obtained for a 2θ range of 20°-50°, is presented in Figure 5.1. Peaks were identified using XRD pattern of pure HA (JCPDS: 00-009-0432). The results showed that the HA-Es phase stability was not disrupted when sintered from 1000 °C to 1250 °C. However, sintering at 1300 °C and 1350 °C resulted in decomposition of the HA phase to form small amounts of α -tricalcium phosphate (α -TCP, JCPDS: 00-009-0345) and tetracalcium phosphate (TTCP, JCPDS: 00-011-0232). This observation is simultaneously supported by the intensity of the (211) Miller lattice plane for HA at $2\theta \sim 31.77^\circ$, where the peak intensity was found to increase from 1000

to 1250 °C and decreased from 1300 to 1350 °C. In particular, the sintered HA-Es showed α -TCP phase without phase transformation to β -TCP. This could be associated with the conversion into β -TCP by departure from the stoichiometric Ca/P ratio (Lee & Oh, 2003). It was reported that formation of TCP during sintering of HA-Es indicates the Ca/P molar ratio could be below 1.67 (Krishna et al. 2007). This is supported by the EDS analysis of the sintered HA-Es sample at 1300 °C which resulted in lower than stoichiometric Ca/P ratio that of 1.55.

In a work by Ho et al. (2013) on sintering of HA prepared by heat treatment the eggshell powder and DCPD mixture, it was revealed that β -TCP was the main phase after sintering at 1100 °C for 1 hour. A small quantity of HA and diffraction pattern of the starting materials were also detected. As the sintering time was increased to 3 hours, the main phase detected was HA with a small fraction of β -TCP. Only when the sintering time was increased to 5 hours, pure HA was obtained at 1100 °C. Similar finding was also reported by Wu et al. (2015) where sintering of HA derived from eggshell at 1100 °C for 1 hour resulted in the appearance of unreacted starting materials and β -TCP in the samples. Only when the sintering temperature raised to 1200 °C, these peaks of starting precursors completely disappeared as they have been incorporated into the HA and β -TCP lattice. These findings were totally contrary to this work, where phase pure HA has been obtained at the temperature of 1000 °C for 2 hours sintering time. The difference in the results reported in the literature and the present work could be attributed to the purity of the starting powders and milling parameters. For example, using ethanol as milling medium could contribute to the formation of secondary phases upon sintering due to insufficient H₂O present in the medium to suppress decomposition activity in the HA structure (Yeong et al., 2001).

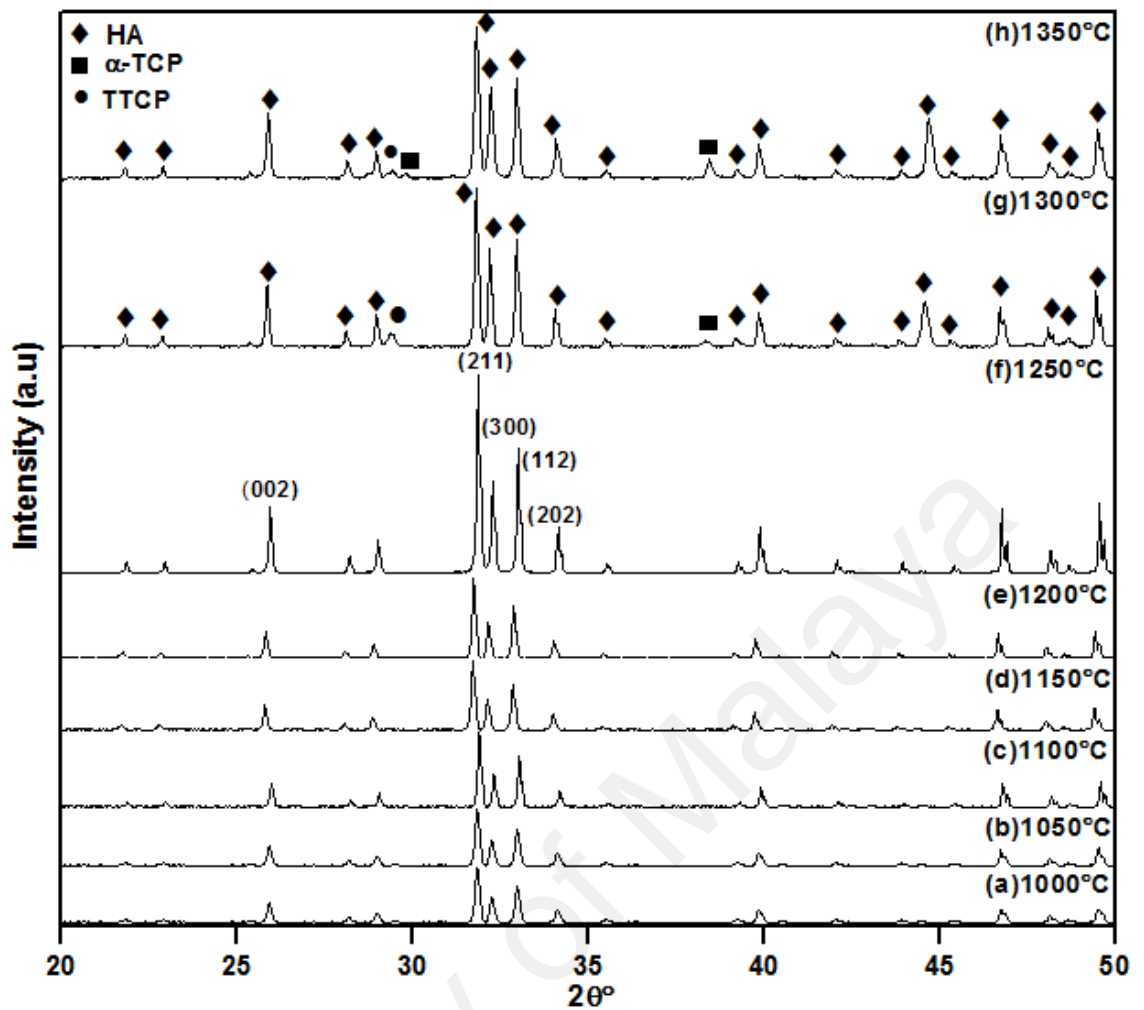


Figure 5.1: XRD patterns of HA-Es samples sintered at various temperatures

In addition, HA powders derived from eggshell have been reported to degrade at high temperatures with the appearance of CaO (Gergely et al., 2010). As a consolation, the present of CaO was not detected in this high temperature sintered HA-Es samples as reported in the literature, particularly for HA sintered at 1350 °C (Kamalanathan et al., 2014). In this work, although the intention is to produce pure HA from eggshell powders, the presences of a small amount of α -TCP and TTCP at 1300 °C and above may not be detrimental since these phases have good biocompatibility and higher solubility than HA whilst CaO is toxic to the biological cells.

The XRD traces of conventionally sintered HA-Wp and HA-Sg compacts with respect to sintering temperature are presented in Figure 5.2 and Figure 5.3, respectively.

XRD spectrum of HA-Wp compacts revealed the presence of only HA phase. There was no formation of secondary phases such as TCP, TTCP and CaO detected throughout the sintering regime employed and this result revealed that the high sintering temperature had a negligible effect on the phase stability of sintered HA-Wp. A similar result was also reported by Tan et al. (2008) in the study of HA powder synthesized using the same technique as HA-Wp but sintered at a lower sintering ramp rate of 2 °C/min. Nevertheless, another work by Mostafa (2005) on similar synthesis method reported that their HA was partially transformed into β -TCP upon sintering at 1100 °C. On another note, Muralithran and Ramesh (2000) reported that synthetic HA prepared via wet chemical precipitation started to decompose at 1400 °C but the sign of melting of HA compacts was observed at 1450 °C. Note that the difference between the present sintering regime and those reported in the literature is that the sintering was carried out at the ramp rate of 5 °C/min instead of 2 °C/min. The higher ramp rate employed in this work as applied to the synthesized HA-Wp powder compacts has successfully maintained HA phase stability throughout the sintering regime. It is unclear at this stage the effect of ramp rate employed during the sintering on the phase stability of HA. Additional work would be required to understand this phenomenon.

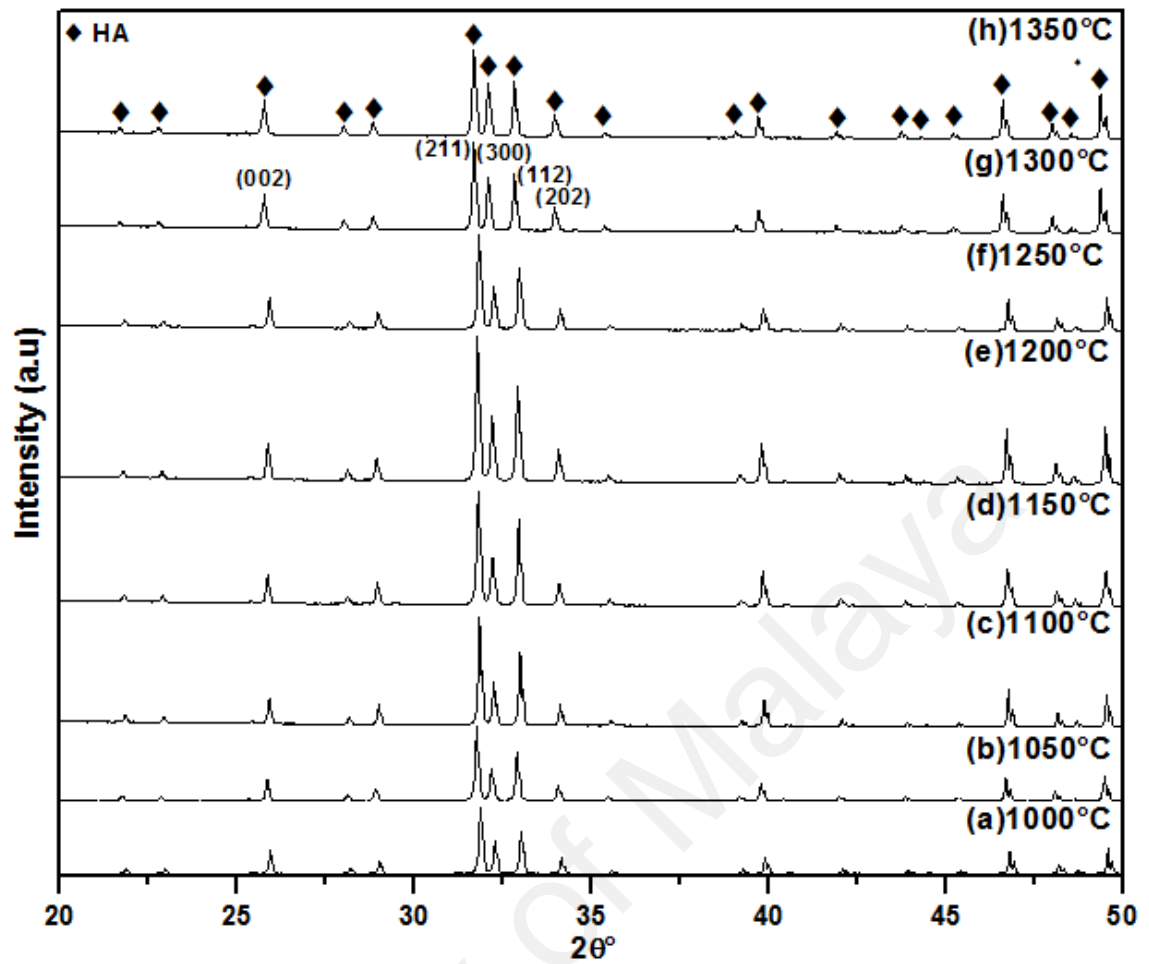


Figure 5.2: XRD patterns of HA-Wp samples sintered at various temperatures.

All the peaks corresponded to that of stoichiometric HA

As for HA-Sg, the XRD traces revealed that there were no secondary phases present in the HA lattice as the sintering temperature increases to 1250 °C. The decomposition of HA to the secondary phase corresponding to CaO (JCPDS: 00-048-1467) was observed at a sintering temperature of 1300 °C onwards (Figure 5.3 (g) – (h)). This finding is expected since CaO is regarded as an impurity in most sol-gel derived HA as unreacted $\text{Ca}(\text{NO}_3)_2$ decomposed to CaO during heat treatment typically above 800 °C (Hsieh et al., 2001; Kuriakose & Kalkura, 2004; Fathi et al., 2008; Sooksaen et al., 2010). It was also reported that CaO forms during sintering if the Ca/P molar ratio of the HA exceeds the value of 1.67 (Slosarczyk et al., 1996; Suchanek & Yoshimura, 1998, Krishna, 2007). In this work, the Ca/P ratio was found to be above 1.67 which

was indicated by the presence of CaO at the sintering temperature of 1300 °C and as supported by the Ca/P ratio of HA-Sg starting powder at 1.77 (Table 4.5). Nonetheless, the presence of CaO is not favored in HA phase as it is detrimental to the mechanical properties. Fanovich & Lopez (1998) found that the existence of CaO in HA would decrease the strength due to the stresses developed in the matrix as a result of a change in volume associated with the formation of Ca(OH)_2 which subsequently transforms into CaCO_3 . This finding has also helped to support the conclusion that the HA-Wp powder has better phase stability and purity than HA-Sg powder as has been discussed in Section 4.2

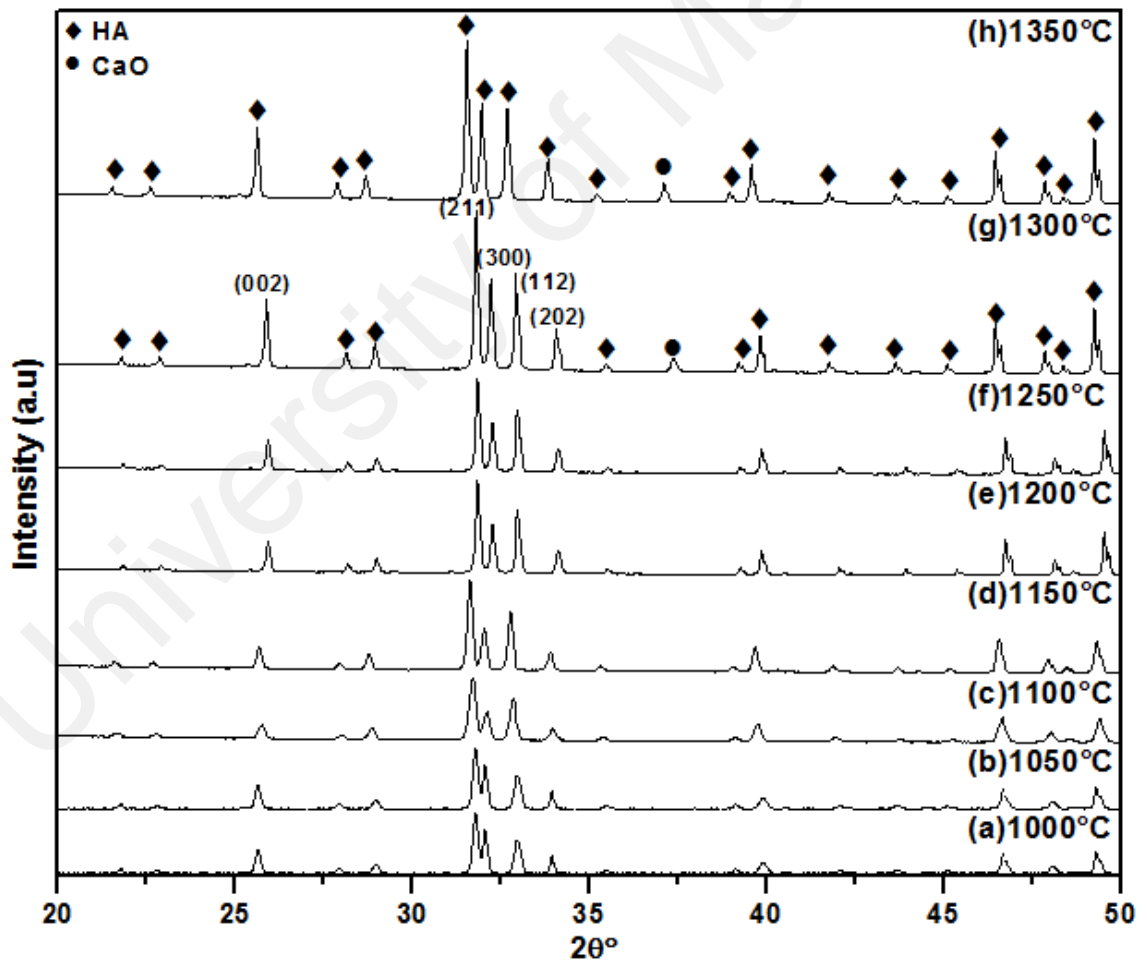


Figure 5.3: XRD patterns of HA-Sg samples sintered at various temperatures

5.2.2 Linear Shrinkage

Figure 5.4 shows the linear shrinkage with respect to the sintering temperature of the conventionally sintered HA-Es samples. The linear shrinkage of all types of HA compacts was calculated based on their length measurement of the cold isostatically pressed bar samples. There was no sign of cracking observed in any of the HA-Es samples. The result indicates that the HA-Es shows an almost linear increase in shrinkage with sintering temperature. It is known that prior calcination treatment on HA powder delays the initiation of sintering. Juang & Hon (1996) reported that for calcination at 800 °C and above, the shrinkage rate decreases, therefore, higher temperature is necessary to reach the final stage of sintering. Meanwhile, for non-calcined and calcined at 700 °C samples, it was reported that the sintering start to begin at a lower temperature and higher temperature is needed for pore diminishing in the final sintering stage, hence, there is a tendency for grain growth to take place simultaneously (Juang & Hon, 1996).

As described in Section 3.2.1, the HA-Wp powder did not undergo any heat treatment process after the synthesis stage. Hence, larger linear shrinkage was expected for non-calcined HA-Wp powder compacts as the shrinkage was related to both the loss of volatile species especially water and densification on sintering as depicted in Figure 5.5. In this current work, HA-Es powder was calcined at 800 °C during the preparation of the powder, hence, it is expected for the HA-Es to exhibit lower linear shrinkage than conventionally sintered HA-Wp samples due to the densification on sintering. For example, HA-Wp recorded shrinkage of approximately 17.3 % at 1050 °C, whereas the HA-Es required a higher temperature of about 1350 °C to achieve that similar shrinkage value. For HA-Wp, the increase in linear shrinkage (up to 22.7 %) was observed followed by minor changes in the linear shrinkage as the sintering temperature increased

beyond 1100 °C. This result is in agreement with the findings of Gibson et al. (2001) where final linear shrinkage of ~24 % was achieved by synthetic HA derived from wet chemical precipitation of $\text{Ca}(\text{OH})_2$ and H_3PO_4 . However, this result is contrary to the linear shrinkage values reported by Tan et al. (2008) corresponding the sintering behavior of stoichiometric HA powder derived from wet chemical precipitation method using similar starting materials. These authors found that the final linear shrinkage value was between 34-35 %. The difference in the sintering behavior could be attributed to the different physical characteristics of the HA-Wp powder used in this study.

Meanwhile, for HA-Sg, the increase in linear shrinkage was found to be the lowest among these HA powder compacts with final linear shrinkage values of about ~14.7 % as depicted in Figure 5.5. Note that its linear shrinkage has only started to take place at a sintering temperature of 1100 °C. Juang & Hon (1996) reported that calcination at 1000 °C is not suitable for HA powders as the powder particles become coarse agglomerate hence total shrinkage is reduced and the densification is inhibited. A similar finding of decreased total shrinkage was also observed in this study for HA-Sg compacts although the starting HA-Sg powder has been heat treated at a much lower temperature of 500 °C. This is because the starting powder of HA-Sg powder has the biggest agglomerate size (~70-200 nm) as reported in Section 4.2. Therefore, higher temperature is needed for HA-Sg sintering to obtain a similar level of densification as the other samples.

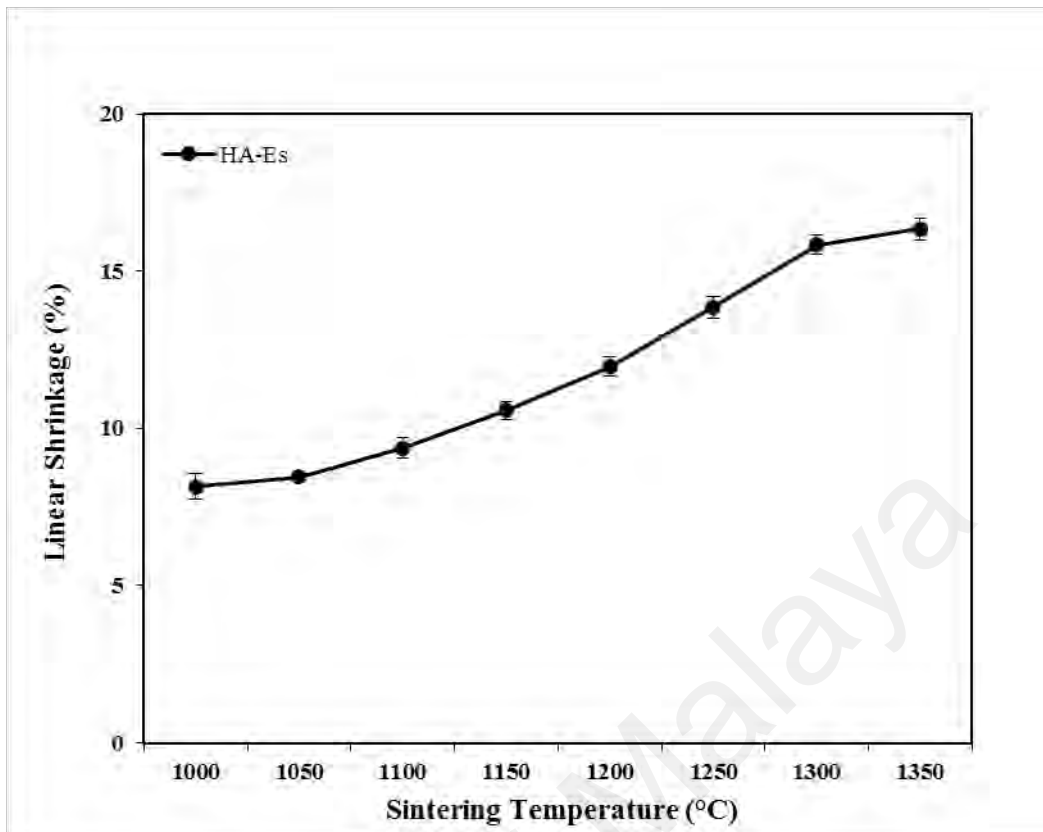


Figure 5.4: Linear shrinkage of HA-Es samples at various sintering temperatures

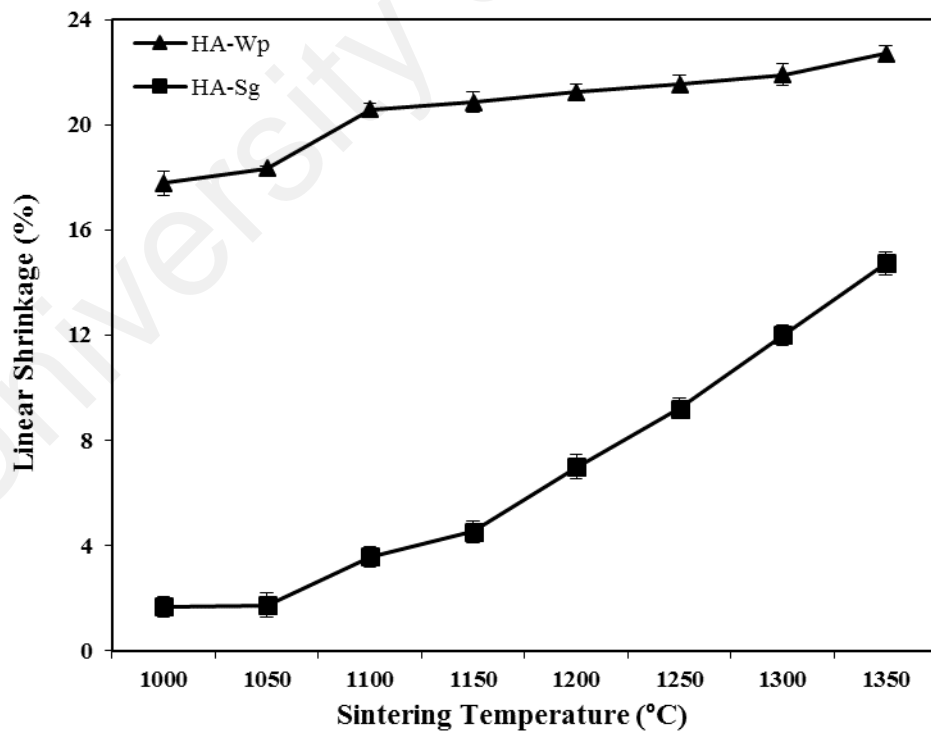


Figure 5.5: Linear shrinkage of HA-Wp and HA-Sg samples at various sintering temperatures

5.2.3 Bulk Density Analysis

The densification curve for HA-Es as a function of sintering temperatures is shown in Figure 5.6. In general, the bulk density increases with increasing sintering temperature up to 1350°C. The relative density increased from 85.9 % at 1000 °C to a maximum of 99.3 % at 1350°C. The increase in density is due to the fact that pore elimination occurs during densification, where this is achieved via the diffusion of matter through the grain boundaries of the particles, or the particle volume itself (Ramesh et al., 2008; Champion, 2013).

Initially, the small increase in density before the stage of onset of densification corresponds to the first stage of sintering where necking is formed between the powder particles from 1000-1050 °C. Meanwhile, the second stage of sintering corresponds to the removal of most of the porosity and the onset of densification. As mentioned in Section 5.2.2 on its linear shrinkage, the final stage of sintering took place at a slightly higher temperature and this is supported by its sharp increase in its relative density (onset of densification) at 1200 °C and 1250 °C. Sintering above this temperature range resulted in a small increase in density as it has reached the final stage of sintering as only small levels of porosity removed and grain growth begins. In addition, the results indicated that the amount of secondary phases detected by XRD in the samples sintered at 1300 °C and 1350 °C must be small since the relative density for these samples were generally high, in the range of 98–99 %.

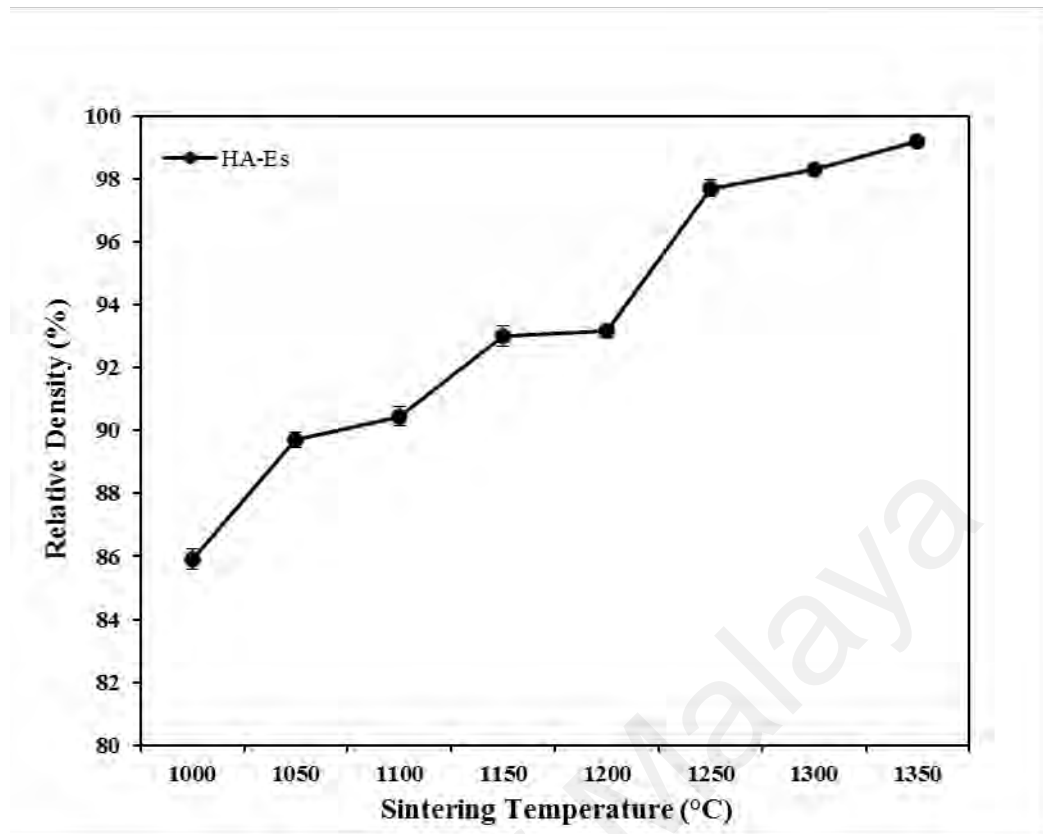


Figure 5.6: The variation in relative density of conventional sintered HA-Es as a function of sintering temperature

Meanwhile, HA-Wp exhibits a steady increase in density is observed with an increase in sintering temperature up to 1250 °C as shown in Figure 5.7. Relative density increases from 89.9 % at 1000 °C to a maximum of 99.1 % at 1250 °C. The onset of densification has taken place between 1050 °C and 1100 °C. As sintering begins and shrinkage stops at a lower temperature, a higher temperature is needed for pore diminishing in the final sintering stage hence grain growth has also taken place simultaneously, between 1200 °C and 1250 °C. Maximum densification of 99.1 % was achieved at 1250 °C. Beyond this point, it is believed that consolidation no longer contributed to an increase in density but promoted grain growth. This is clearly shown in the slight decrease in relative density for HA-Wp at 1300 °C and 1350 °C to about ~98.3 %.

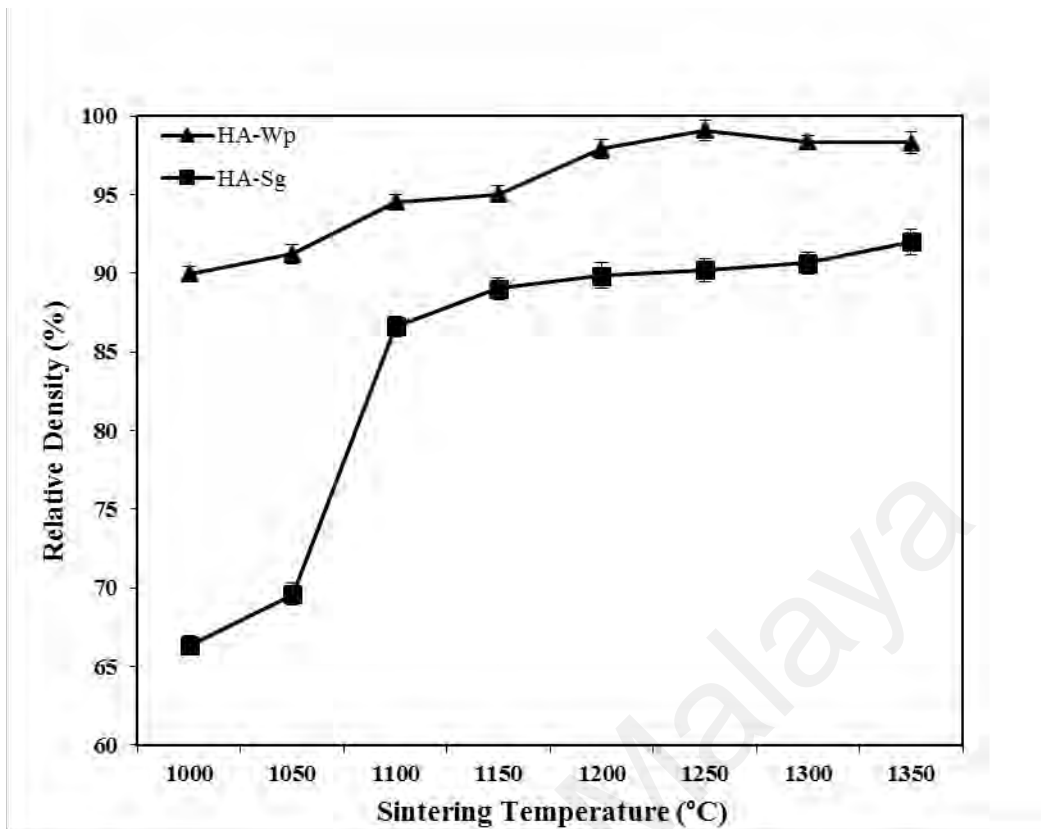


Figure 5.7: The variation in relative density of conventional sintered HA-Wp and HA-Sg as a function of sintering temperature

For HA-Sg samples, it seems that densification does not occur at 1000°C. This is clearly shown in Figure 5.8, that sintering of HA-Sg at 1000 °C results in a sample with a low relative density of 66.3 %. This could probably due to the small green densities of the samples (~50 %) during the preparation stage. A similar pattern was also observed at 1050 °C as the densification only increases to 69.6 %. This was supported by the almost no definite changes in its linear shrinkage at this temperature range as shown Figure 5.5. The onset densification had only started to take place at 1100 °C to 86.6 %. Densification occurred at 1250°C as a reduction in pore volume and shrinkage is observed, resulting in a relative density of 90.2%. As the sintering temperature increased, so does the relative density but highest relative density achieved is only 92.0 % at 1350 °C. However, as in Figure 5.3 (f) – (g), the decomposition of HA to CaO has taken place between the temperature range of 1300-1350 °C. Considering these

facts, HA-Sg powder synthesized by a sol-gel method in this present study is not suitable for the application as a bone substitute material. Moreover, the results of phase stability, linear shrinkage and relative density and the prior powder characterization in Chapter 4 shows that HA-Wp powder compacts have proven to offer better properties than HA-Sg. Hence, the HA-Wp powder was chosen as the preferred synthesized HA powder which was prepared via a wet method for further sinterability study.

In general, the densification behavior of HA-Wp was superior to that of HA-Es. For HA-Wp, the highest relative density of 99.1 % could be attained when sintered at 1250 °C, whereas for HA-Es the similar density was attained at a sintering temperature of 1350 °C. This could be attributed to its large driving force for densification due to the higher surface area of the powder (97.41 m²/g) as compared to 8.71 m²/g for the HA-Es powder. Actually, the lower surface area is expected as HA-Es powder was subjected to thermal treatment of 800 °C during the HA powder preparation. On the contrary, the delay in sintering for HA-Es has reduced its driving force for grain growth as has been observed in HA-Wp samples. Moreover, the difference in the powder morphology between HA-Es and HA-Wp powders that are of petal-like flakes and needle-like morphology, respectively, has also contributed to the difference packing density in the green state hence the different sintering behavior (Wang & Shaw, 2007).

5.2.4 Microstructural Evolution and Grain Size Analysis

SEM images of HA-Es compacts that were sintered at various temperatures are presented in Figure 5.8. It was observed that at 1000 °C necking formation between the grains has taken place, followed by solid bridges formation at 1050 °C. These phenomena correspond to the first stage of sintering. The second stage of sintering persists until 1200 °C as it was found that samples sintered at 1200 °C exhibited a more

densely packed microstructure with less amount of porosity than those sintered below 1200 °C. This densely packed grain microstructure of sintered HA-Es with increasing sintering temperature corresponds well to the gradual increase in relative density of sintered HA-Es with increasing sintering temperature as shown in Figure 5.6. Further increase in sintering temperature in the final stage of sintering was accompanied by a slight grain coarsening particularly at 1250 °C. Note that, the average grain size was still in submicron range of $0.95\pm 0.02\ \mu\text{m}$ as shown in Figure 5.10. For HA-Es compacts, the smallest average grain size of $0.58\pm 0.02\ \mu\text{m}$ is attained at 1100 °C, whereas the largest average grain size of $5.76\pm 0.01\ \mu\text{m}$ is obtained at 1350 °C. At 1150 °C and 1200 °C, HA-Es had an average grain size of $0.66\pm 0.02\ \mu\text{m}$ and $0.75\pm 0.02\ \mu\text{m}$, respectively. Sintering beyond 1250 °C resulted in a rapid grain growth i.e. the HA grain size increased from $0.95\pm 0.02\ \mu\text{m}$ (at 1250 °C) to $3.36\pm 0.02\ \mu\text{m}$ (at 1300 °C) and finally to $5.76\pm 0.01\ \mu\text{m}$ (at 1350 °C). However, the rate of the exaggerated grain growth was not as high when compared to that reported in the literature where the grain size of HA increased from approximately 2 to 8 μm when the sintering temperature was increased by 50 °C, from 1200 °C to 1250 °C (Ramesh et al. 2013).

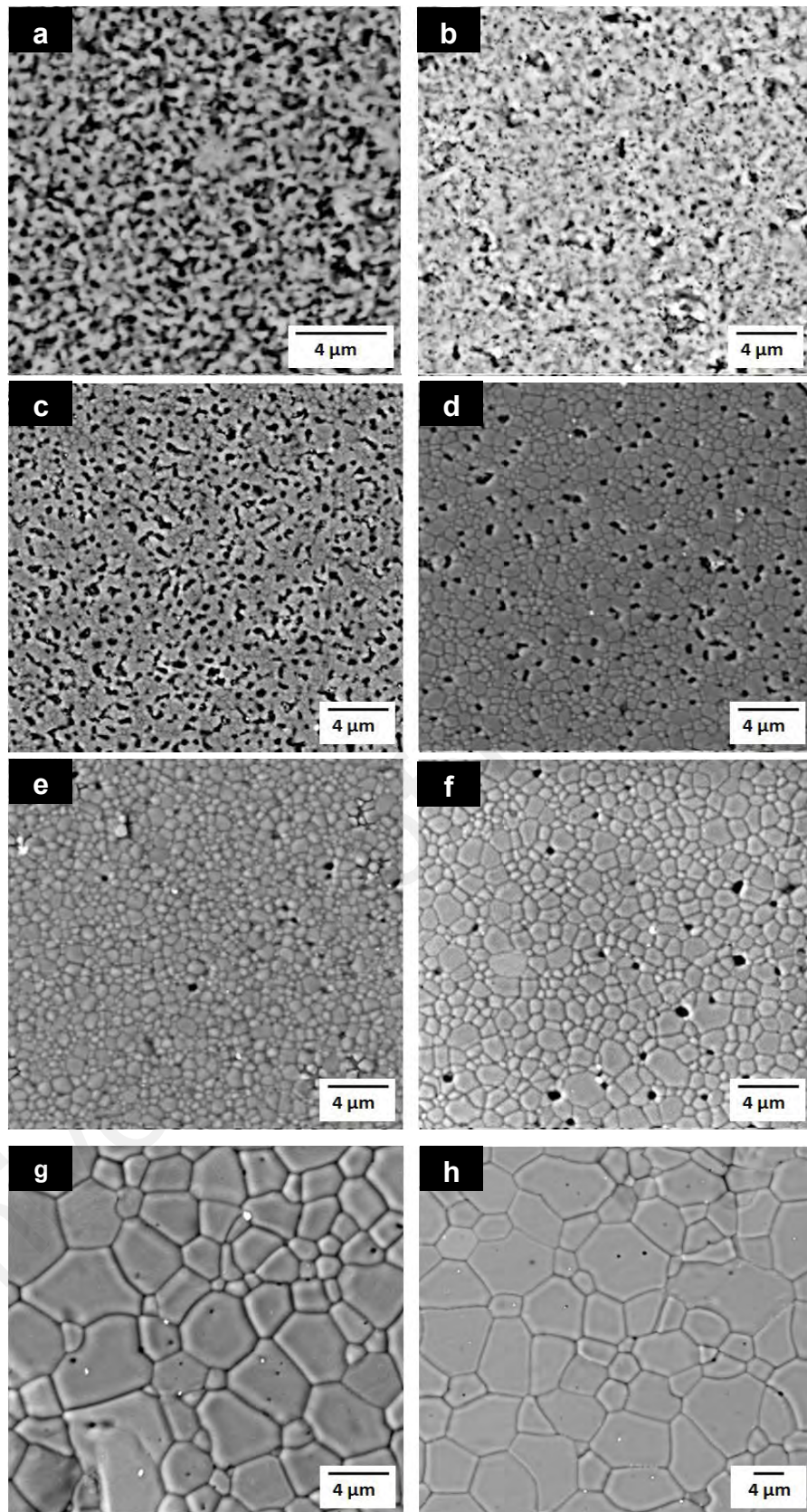


Figure 5.8: Microstructural evolution of HA-Es sintered at (a) 1000 °C, (b) 1050 °C, (c) 1100 °C, (d) 1150 °C, (e) 1200 °C, (f) 1250 °C, (g) 1300 °C and (h) 1350 °C

Figure 5.9 presents the microstructural evolution of sintered HA-Wp samples at various temperature. For HA-Wp, when the sintering temperature increased from 1000-1350 °C, the samples exhibited a more densely packed grain microstructure that corresponds to the densification of HA-Wp. In Figure 5.9 (a), it can be seen that the micrograph consists of a fused grains with interconnected porosity as the neck formations between the agglomerated particles had taken place. This indicates the first stage of sintering. The similar result was also observed for HA-Es sintered but at a higher temperature, 1050 °C. Beyond this temperature, the grains were nearly equal in shape with a large number of intergranular pores. The average grain size was measured to be $0.45\pm 0.05\ \mu\text{m}$ as depicted in Figure 5.10. At 1100 °C, the grain size slightly increased to $0.69\pm 0.08\ \mu\text{m}$ with reduced numbers of intergranular pores. Consecutively, at 1150 °C and 1200 °C, the more uniform microstructure can be observed. It can be seen that their grains are more delineate and their average grain sizes have increased to $0.93\pm 0.09\ \mu\text{m}$ and $1.62\pm 0.09\ \mu\text{m}$ at 1150 °C and 1200 °C, respectively. With further increase in sintering temperature from 1250 °C to 1350 °C, the grain size increased rapidly from $4.31\pm 0.07\ \mu\text{m}$ to $8.62\pm 0.07\ \mu\text{m}$. Similar result was reported in a work by Ramesh et al. (2013), where the grain size of HA-Wp increased from 2 to 8 μm when samples were sintered from 1200 °C to 1250 °C.

Note that, HA-Wp exhibited larger grain sizes at all sintering temperature than the conventionally sintered HA-Es. This could be related to the synthesized HA-Wp powder that has a higher sinterability resulting from its smaller particle size and larger powder surface area hence more reactive particles and higher packing density. According to Herring Law of sintering, sintering rate was inversely proportional to the square of the powder particle size (Kothapalli, et al. 2004). In addition, this results is in line with the expectation that higher sintering temperature is needed for HA-Es in order to maximize densification due to small powder surface area as compared to HA-Wp.

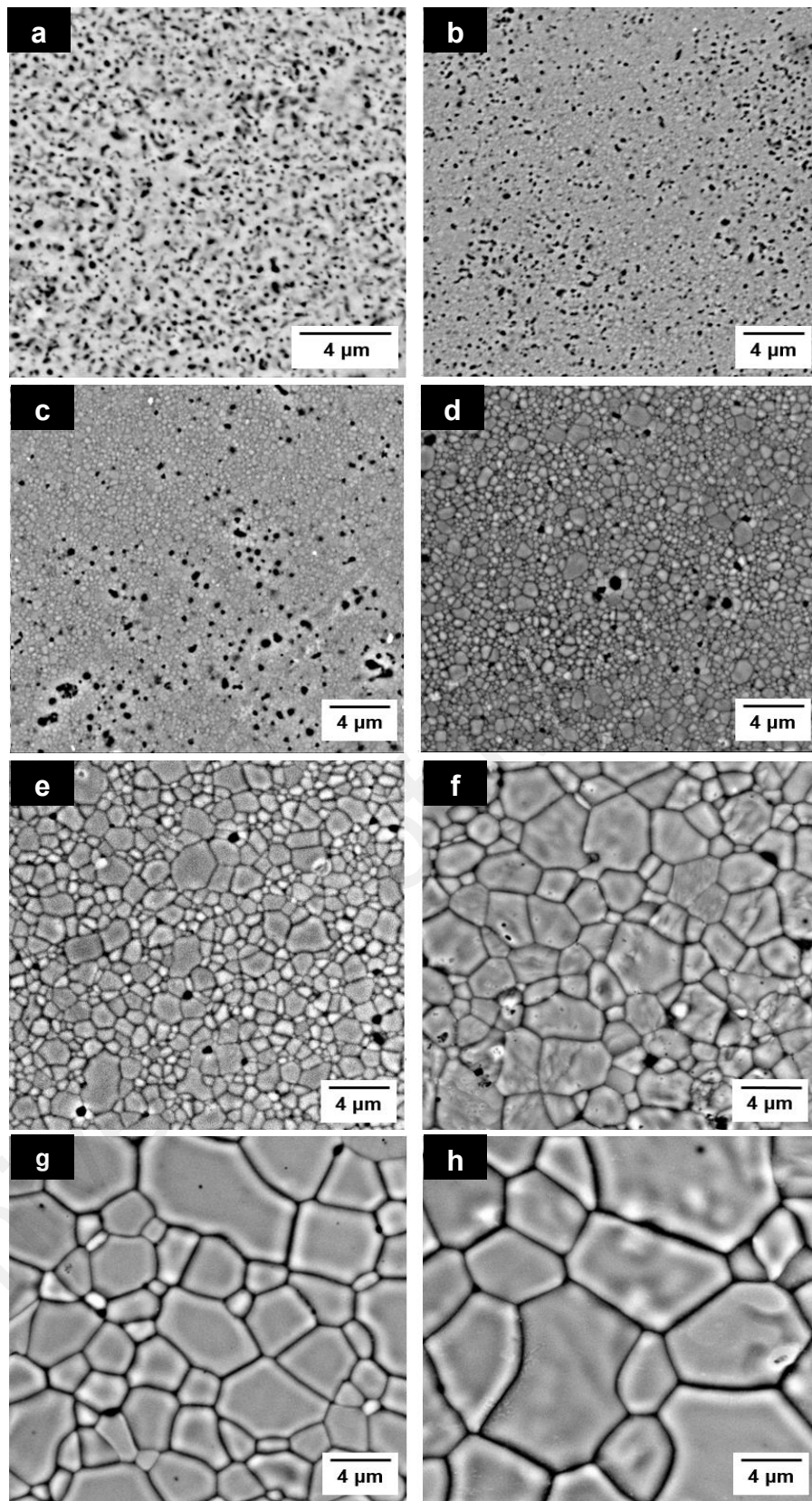


Figure 5.9: Microstructural evolution of HA-Wp sintered at (a)1000 °C, (b)1050 °C, (c)1100 °C, (d)1150 °C, (e)1200 °C, (f)1250°C, (g)1300°C and (h)1350°C

Hence, less probability of a rapid grain growth observed for these HA-Es powder compacts in conventional sintering below 1250 °C. Beyond this sintering temperature, rapid grain growth of HA-Es has been observed along with the decomposition of HA to biphasic mixture although the relative density at this temperature was very high, in the range of 98–99 %. Moreover, accelerated grain growth at high sintering temperature is a typical result for conventional pressureless sintering due to the uncontrollable presence of moisture in the sintering atmosphere which has been reported to inhibit densification of HA and accelerate grain growth (Suchanek & Yoshimura, 1998).

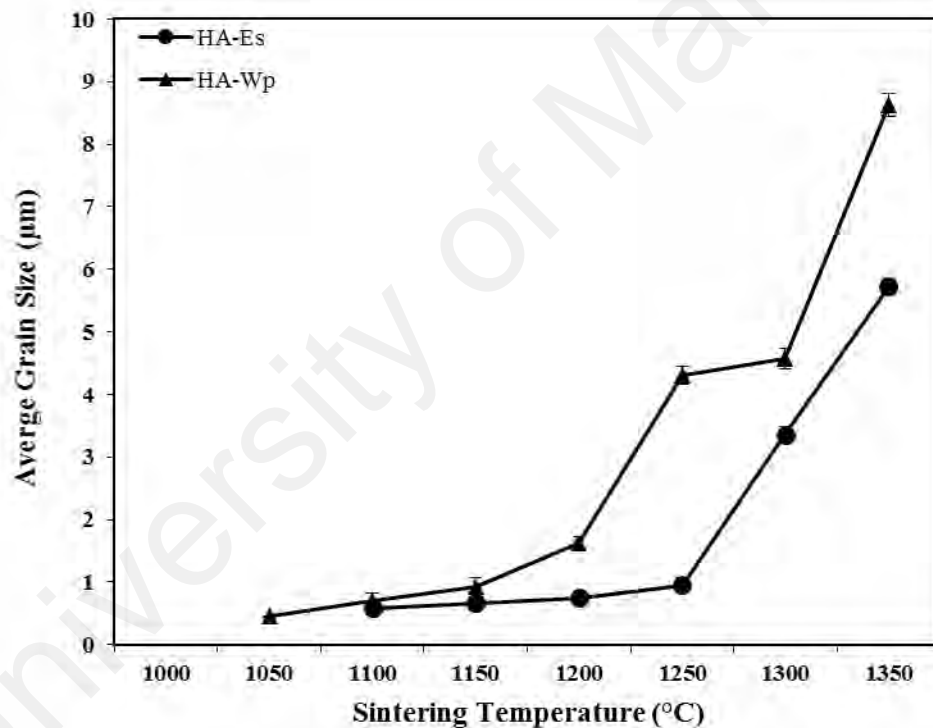


Figure 5.10: Average grain size variation of HA-Es and HA-Wp sintered at various temperatures

5.2.5 Vickers Hardness Analysis

The effect of sintering temperature on the Vickers hardness of HA-Es and HA-Wp is shown in Figure 5.11. The hardness of HA-Es increased from a low value of 2.75 ± 0.08 GPa at 1000 °C to 3.04 ± 0.04 GPa at 1100 °C then up to a maximum of

5.62±0.05 GPa at sintering temperature of 1250 °C. Beyond 1250 °C, the hardness decreased from 5.56±0.05 GPa to 4.26±0.09 GPa at 1350 °C. The rapid increase in hardness up to 1250 °C could be attributed to the increase in relative density as shown in Figure 5.10. It is well documented that the hardness of HA increased with increasing relative density (Wang & Shaw, 2009). However, in the present study, the aforementioned observation is partially true. As can be noted, the hardness decreased as the sintering temperature increased from 1250 to 1350 °C despite showing an increased in relative density from about 98 % to 99.3 %, respectively (Figure 5.6). It is believed that the slight decreased in the Vickers hardness of HA-Es is associated with the decomposition of HA phase at these temperatures as depicted by the XRD traces shown in Figure 5.1. This observation was also collectively supported by similar findings in other works (Koutsopoulos, 2002; Aminzare et al., 2013). Interestingly, the hardness values of the HA-Es sample sintered at 1300 °C and 1350 °C which decomposed to α -TCP and TTCP were 5.56 and 4.26 GPa, respectively. The relatively high value retained by the sintered samples could be explained by the theory reported by Slosarczyk and Bialoskorski (1998). In this case, the formation of surface compression due to the phase transitional to TCP could possibly maintain the strength of the material.

Similar trend as of HA-Es was also observed in the hardness of HA-Wp whereas Vickers hardness increases from a low value of 3.14 GPa at 1000 °C up to a maximum of 4.80 GPa at sintering temperature of 1200 °C and beyond 1200 °C, the hardness decreases from 4.71 GPa to 4.44 GPa at 1350 °C. It can be noted that basically, HA-Wp displayed superior hardness as compared to HA-Es samples. However, as the sintering temperature reaches 1200 °C the trend was disrupted as the hardness for HA-Wp started to decrease beyond that temperature. In contrast, the hardness of HA-Es continuously increases when the sintering temperature was raised to 1250 °C.

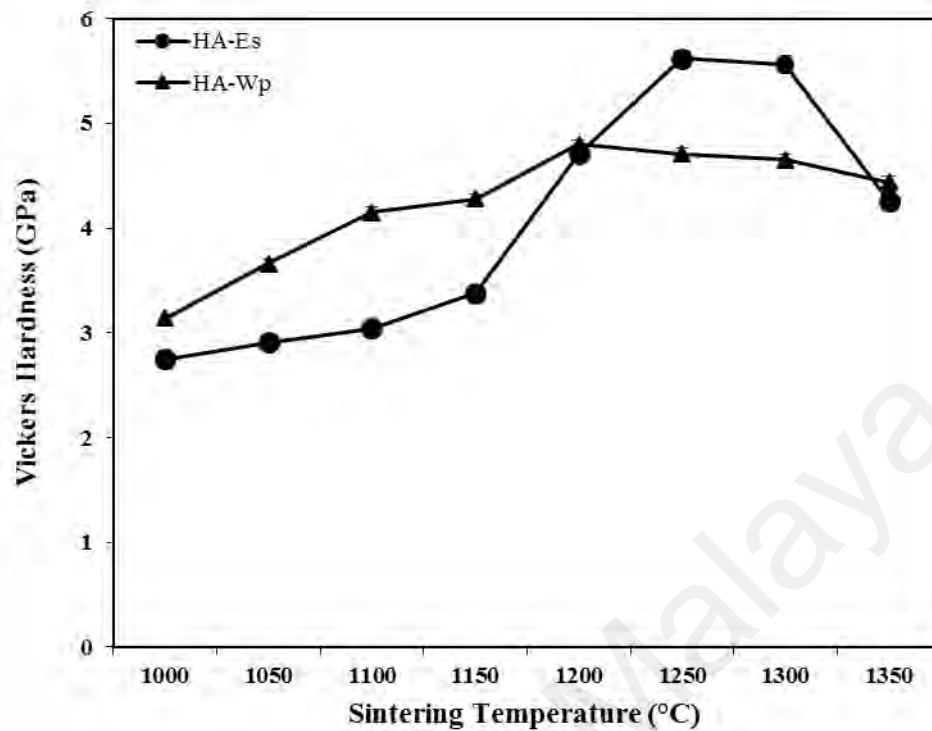


Figure 5.11: The variation in Vickers hardness of conventional sintered HA-Es and HA-Wp as a function of sintering temperature

With this, the linear increment of hardness up to 1200 °C could also be attributed to the increased in relative density as shown in Figure 5.7. In contrast, the hardness decreased beyond this temperature despite still having a high relative density of ~98%. However, there was no decomposition of HA-Wp sintered samples detected at all sintering temperature (Figure 5.2). Since the decline of hardness value at a temperature higher than 1200 °C was not due to the thermal decomposition (Figure 5.2) nor can be related to the bulk density, the microstructure of the sintered samples could be the primary factor that governs the hardness of HA-Wp at high temperatures. A general observation can be drawn from the finding is that the hardness of HA ceramic was strongly influenced by the sintered density.

5.2.6 Fracture Toughness

The fracture toughness variation with respect to sintering temperature for HA-Es is shown in Figure 5.12. The fracture toughness of HA-Es sintered samples at 1000 °C and 1050°C are not available as there was no formation of corner cracks after Vickers indentation is made on their polished sample. Note that, at this temperature range (1000 -1050 °C), the density of the HA-Es sample was below 90 % and the SEM images (Figure 5.8) showed the porosity on the surface of the samples. Therefore data to evaluate fracture toughness could not be obtained. The fracture toughness was observed to fluctuate from a low value of 1.26 MPam^{1/2} at 1100 °C to the highest value of 1.51 MPam^{1/2} at 1250 °C. Sintering beyond 1250 °C resulted in a decline in the fracture toughness to 1.45 MPam^{1/2} at 1300 °C and 1.22 MPam^{1/2} at 1350 °C. This decreased in the fracture toughness from 1250 °C to 1350 °C is in tandem with the increased in the average grain size of the HA, from 0.95 µm to 5.76 µm (Figure 5.10), respectively and in part to the decomposition of the HA phase to TCP and TTCP (Figure 5.1).

As for HA-Wp, in general, the fracture toughness variation exhibited a very similar trend with the variation in Vickers hardness (Figure 5.11), i.e. the fracture toughness value increases with sintering temperature up to 1250 °C and then decreased linearly as the temperature increases. In this study, at a low temperature of 1050 °C, low fracture toughness value (0.76 MPam^{1/2}) was recorded which could be attributed to the weak grain boundaries of the HA matrix at low temperature (Champion, 2013). The fracture toughness then increases to a value of 0.90 MPam^{1/2} at 1100 °C up to a maximum of 1.29 MPam^{1/2} at a sintering temperature of 1200 °C. Beyond 1200 °C, it decreases from 1.21 MPam^{1/2} at 1250 °C to 0.71 MPam^{1/2} at 1350 °C.

It is reported in previous research that the decline in mechanical properties such as hardness and fracture toughness of HA were expected at higher temperatures above 1200 °C mainly due to HA decomposition to TCP and CaO (Buys et al, 1995). The

volume changes associated with the formation of these new secondary phases creates internal strain within the HA matrix. This was not the case in this work since HA decomposition was not detected for all the HA-Wp sintered up to 1350 °C. This rapid drop of fracture toughness could be correlated to the abnormal grain growth after specific sintering temperature as shown in Figure 5.9. These large grains are believed to provide an easy path or crack propagation and hence resulting in lower fracture toughness (Ramesh et al., 2011).

It is observed that Vickers hardness is governed by relative density meanwhile fracture toughness is largely governed by grain size. The reduction in grain size translates to an increase in K_{Ic} , as a smaller grain size promotes inter-granular fracture (Veljovic et al., 2009). Note that synthesis of nanostructured HA is a critical feature in the enhancement of fracture toughness.

In the present work, the high toughness recorded for HA-Es ($1.51 \text{ MPam}^{1/2}$) while retaining its phase stability at 1250 °C is very encouraging as many researchers reported a much lower fracture toughness value (below $1.0 \text{ MPam}^{1/2}$) for their HA compacts (Buys et al., 1995; Slosarczyk & Bialoskorski, 1998; Yeong et al., 2001; Rhee, 2002; Wang & Shaw, 2009; Song et al., 2011; Lin et al., 2012). In addition, the maximum toughness values recorded of HA-Wp ($1.29 \text{ MPam}^{1/2}$) was also slightly higher than the reported average value. It is understood that the presence of needle-like crystals in HA-Wp (as in Figure 4.6 (a)) could have contributed to the enhancement in the fracture toughness (Fujishiro et al., 1993).

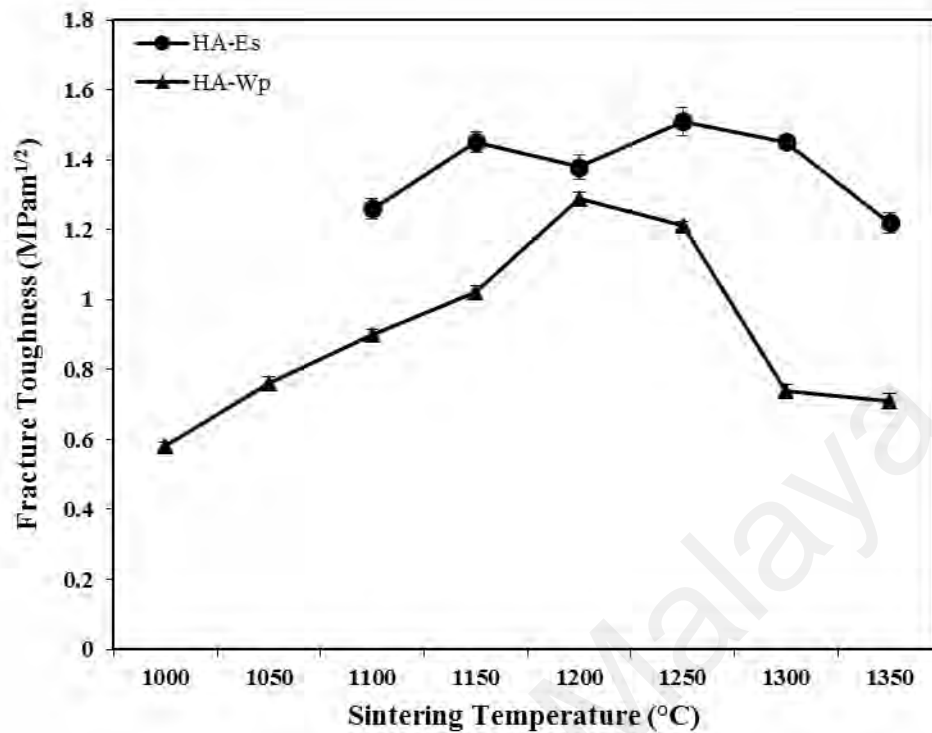


Figure 5.12: The variation in fracture toughness of conventional sintered HA-Es and HA-Wp as a function of sintering temperature

5.3 Consolidation of HA Powder through Microwave Sintering

In this section, the effect of rapid sintering by microwave heating on the densification and mechanical properties of nanocrystalline HA bioceramic powder prepared via solid-state reaction and wet chemical precipitation are discussed. The synthesized nano-sized HA-Es and HA-Wp powders were compacted into a disc and rectangular bar samples and subsequently cold isostatically pressed (CIP) at 200 MPa prior to microwave sintering to obtain HA powder compacts with a green density within the range of 52 % to 60 %. After through a number of trial runs, the operating power of the microwave system was optimized. The sintering was carried out in a microwave sintering furnace at different temperatures ranging from 950 °C to 1250 °C with a heating ramp rate of 30 °C/min to the desired temperature and dwell time of 15 minutes and subsequently left to furnace cool. The microwave sintered HA compacts are then termed as HA-Es(M) and

HA-Wp(M), respectively. After sintering, the general observation was that HA-Es(M) and HA-Wp(M) samples did not show any cracking sign regardless the high heating rate that was employed during microwave sintering.

5.3.1 HA Phase Stability

The XRD phase analysis of the HA-Es(M) compacts sintered at varying temperatures is presented in Figure 5.13. The XRD traces indicate that the phase stability of HA-Es powder compacts was not disrupted by microwave sintering up to 1200 °C as all major peaks of pure HA (JCPDS: 00-009-0432) was detected. However, sintering at 1250 °C resulted in decomposition of the HA phase to form small amounts of β -TCP (JCPDS: 00-009-0169) and α -TCP (JCPDS: 00-009-0348). Generally, high temperature sintering of HA can lead to the partial thermal decomposition of HA into TCP and/or TTCP (Ramesh et al., 2008). This observation is simultaneously supported by the intensity of the (211) lattice plane at $2\theta \sim 31.77^\circ$, which was increasing from 950 °C to 1200 °C but decreasing at 1250 °C. Similarly, such decomposition to β -TCP and CaO at 1250 °C has also been reported in the sinterability study of eggshell derived HA powder through microwave sintering (Krishna et al., 2007). However, the presence of CaO phase was not detected throughout this microwave sintering regime which is similar to the behavior of HA-Es samples sintered through conventional sintering (Figure 5.1). This finding has somehow highlighted the advantage of the eggshell derived HA through solid state reaction. Indirectly, this indicates that the HA-Es powder synthesized in this present work has better phase stability and compared to the reported literature.

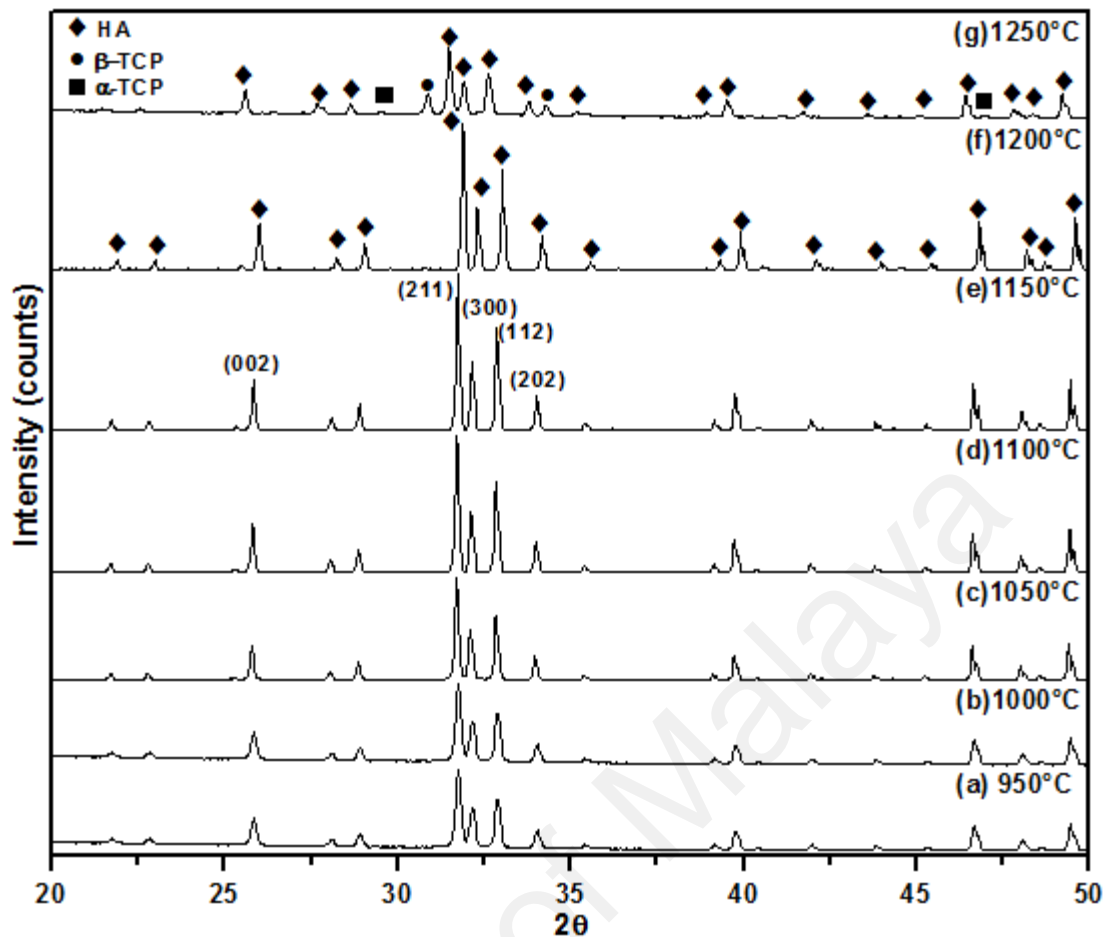


Figure 5.13: XRD patterns of HA-Es(M) samples microwave-sintered at various temperatures

Meanwhile, XRD traces of the HA-Wp(M) samples revealed the presence of only HA phase from 950 °C to 1100 °C as typically shown in Figure 5.14. The formation of secondary phases such as β -TCP and α -TCP were detected from 1150 °C and 1200 °C, respectively. A similar decomposition was also observed for the sample of HA-Es(M) at the similar sintering temperature. However, as the sintering temperature reaches 1250 °C, there is a substantial increase in the intensity of the main β -TCP peak (0 2 10) alongside the other β -TCP peaks, until it exhibits similar intensity of the HA main peak corresponding to the (211) lattice plane. This, in turn, occurs with a reduction in the intensity of the main HA peaks. This observation indicated that the degradation of HA-Wp(M) to TCP is greater than

reported for conventionally sintered HA-Es and HA-Es(M). However, the presence of calcium oxide (CaO) phase was not detected at all sintering temperature. These results indicated that the microwave sintering has disrupted the phase stability of HA synthesized via wet chemical precipitation which is in contrast to the findings in a research reported in the literature where phase stability of HA was maintained throughout the microwave sintering regime (Ramesh et al., 2007a; 2011).

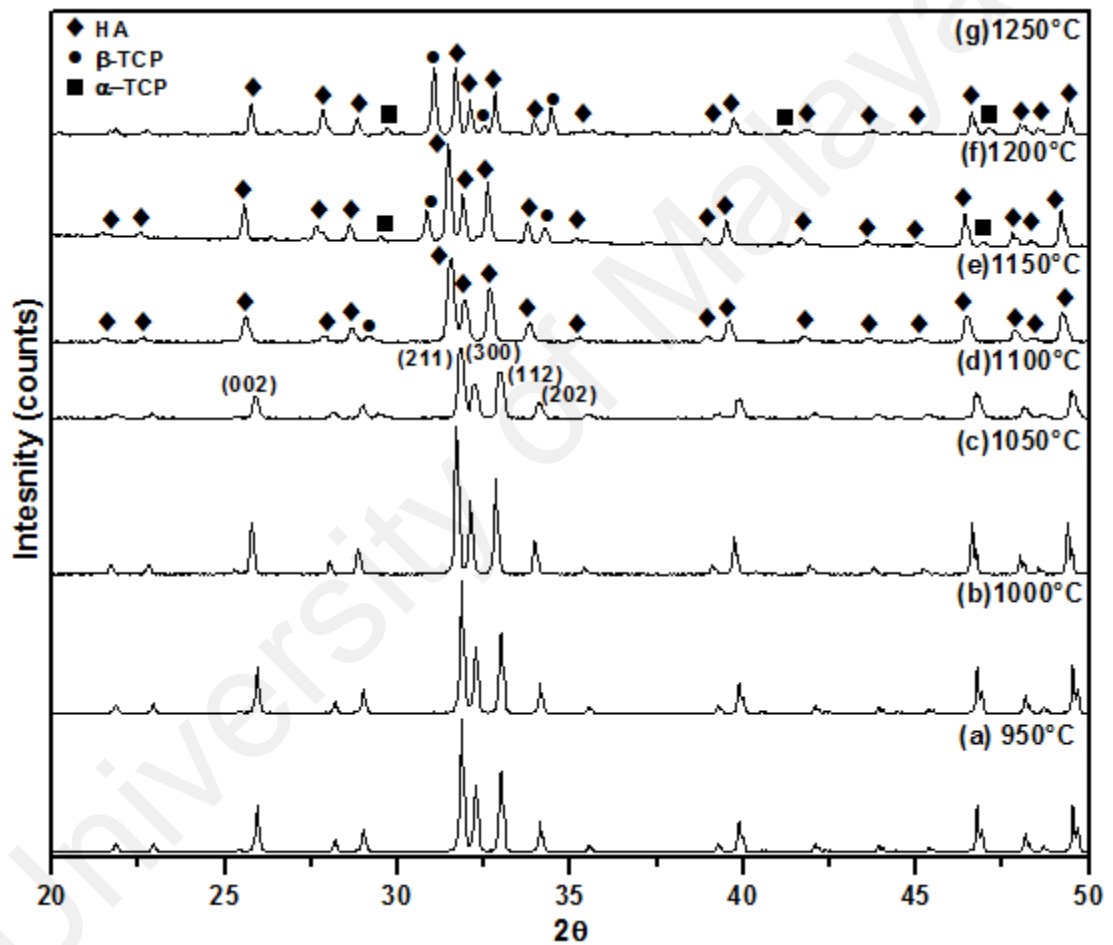


Figure 5.14: XRD patterns of HA-Wp(M) samples microwave-sintered at various temperatures

Wang et al. (1998) claimed that thermal decomposition takes place through two stages that are dehydroxylation and decomposition, and this occurrence could be observed by comparing the XRD peaks position of the sintered material to the standard

JCPDS data for stoichiometric HA (Ramesh et al., 2008). This hypothesis has been supported by Gu et al. (2002). In Figure 5.13, it can be visually seen that the peak shifting of HA-Es(M) are not visible at the three main lattice planes of HA; (211) at 31.77°, (300) at 32.90° and (112) at 32.20°; from 950 °C to 1200 °C, except at 1250 °C. The peak shifting for HA-Es(M) was found to vary between 0.04° - 0.07°. This observation is in line with the hypothesis claimed in the aforementioned reported literature. As for HA-Wp(M), the peak shifting of the lattice planes can be obviously seen in Figure 5.14 and the peak shifting was found to vary between 0.05° - 0.11°.

It was also reported only shorter incubation period (sintering time) is needed at a high sintering temperature in order to avoid dissociation of HA (Van Landuyt et al., 1995). For example, OH dissociation occurred at 1300 °C after sintering for 8 hours meanwhile sintering at 1450 °C, the phase structure can be maintained up to 3 hours only. This belief has also been verified and confirmed in a reported microwave sinterability study on stoichiometric synthesized HA (Ramesh et al., 2008) where no HA decomposition was detected at all sintering temperatures up to 1350 °C for 30 to 35 minutes. Hence, in this work, the initial expectation was that the application of rapid microwave sintering with very short sintering time would be advantageous as for suppressing the dissociation of HA and impeding the HA phase decomposition. However, the end results obtained is totally opposite to the expectation as HA-Wp(M) was found to lose its OH group gradually from as low as 1100 °C.

5.3.2 Linear Shrinkage

The linear shrinkage based on the length measurement of the bar samples for HA-Es(M) with respect to sintering temperature is shown in Figure 5.15. As discussed in Section 5.2.2 on the linear shrinkage of pressureless sintered HA-Es and HA-Wp compacts, a similar observation was also found for their microwave sintered samples whereas HA-Es(M) showing lower linear shrinkage than HA-Wp(M) due to the different physical characteristics of the starting HA powders. In general, the results indicate that the HA-Es(M) exhibits a gradual increase in linear shrinkage from 1.0 % to 16.2 %, meanwhile, HA-Wp(M) experienced higher linear shrinkage of 18.5 % to 20.5 %. However, sintering at temperatures below 1150 °C had a minor effect on the linear shrinkage of HA-Wp(M) as depicted in Figure 5.15.

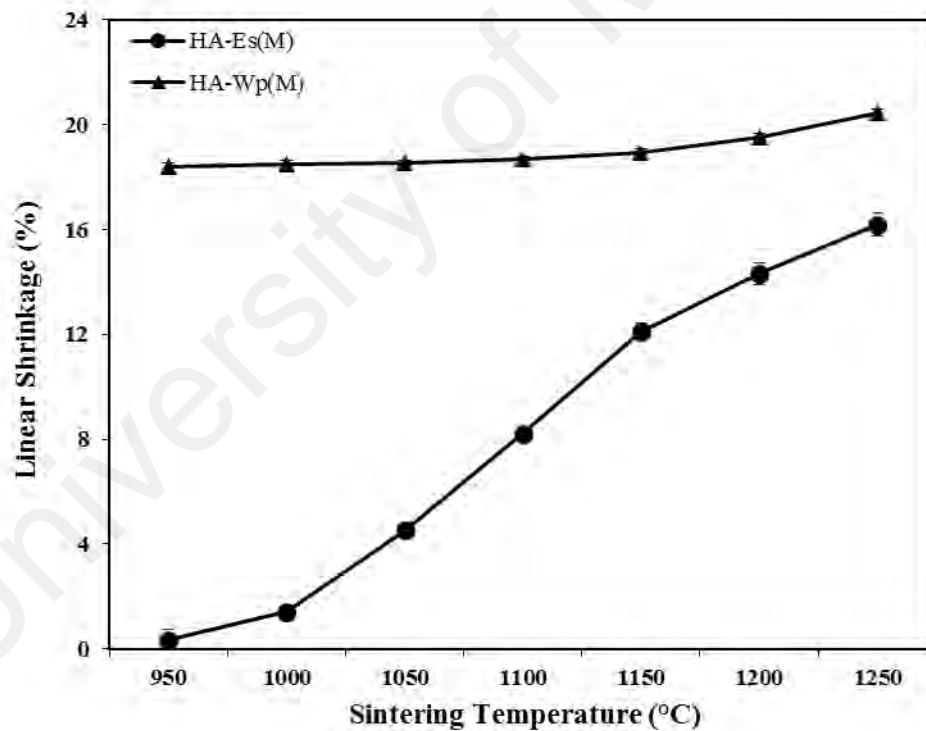


Figure 5.15: Linear shrinkage of HA-Es(M) and HA-Wp(M) samples microwave-sintered at various sintering temperatures

5.3.3 Microstructural Evolution and Grain Size Analysis

The microstructural evolution of the HA-Es(M) sintered at various temperatures is presented in Figure 5.16. In Figure 5.16(a), it can be seen that the micrograph consists of a fine mixture of petal-like flakes structure of the HA-Es agglomerates which are still intact with slightly deformed agglomerates. Roughly it can be seen that there was no bonding formed between the flowers like agglomerates at the low microwave sintering temperature of 950 °C. However, the HA-Es agglomerates have fused and bond with adjacent particles with increased interconnected porosity due to surface diffusion at a sintering temperature of 1000 °C. This finding is similar to the observation on porous HA bioceramics obtained via microwave sintering by Veljovic et al. (2009). At 1050 °C, the neck formations between the agglomerated particles had taken place and at this stage, the microstructure was characterized by spherical and shapeless inter-agglomerate pores. As the sintering temperature increased to 1100 °C, the small particulate phase was widely found across the surface of the grain boundaries and within the grains, as reported by Chanda et al. (2009). Therefore, stronger bonds between the agglomerates were formed. The average grain size was measured to be 0.75 ± 0.05 μm . Meanwhile at 1150 °C, HA-Es(M) exhibits more uniform microstructure, fewer intergranular pores and accompanied by grain coarsening with a slight increase in average grain size to 0.85 ± 0.04 μm . At 1200 °C, grain growth has started as the average grain size has tremendously increased by a factor of 2.4 to 2.08 ± 0.04 μm . Note that, at 1250 °C, phase decomposition to TCP has taken place and beyond this point, the greater portion of HA-Es(M) had been transformed to β -TCP and α -TCP as seen in Figure 5.13. The grain size was found to increase by a factor of 1.1 to 2.28 ± 0.06 μm when the temperature increased by 50 °C from 1200 °C.

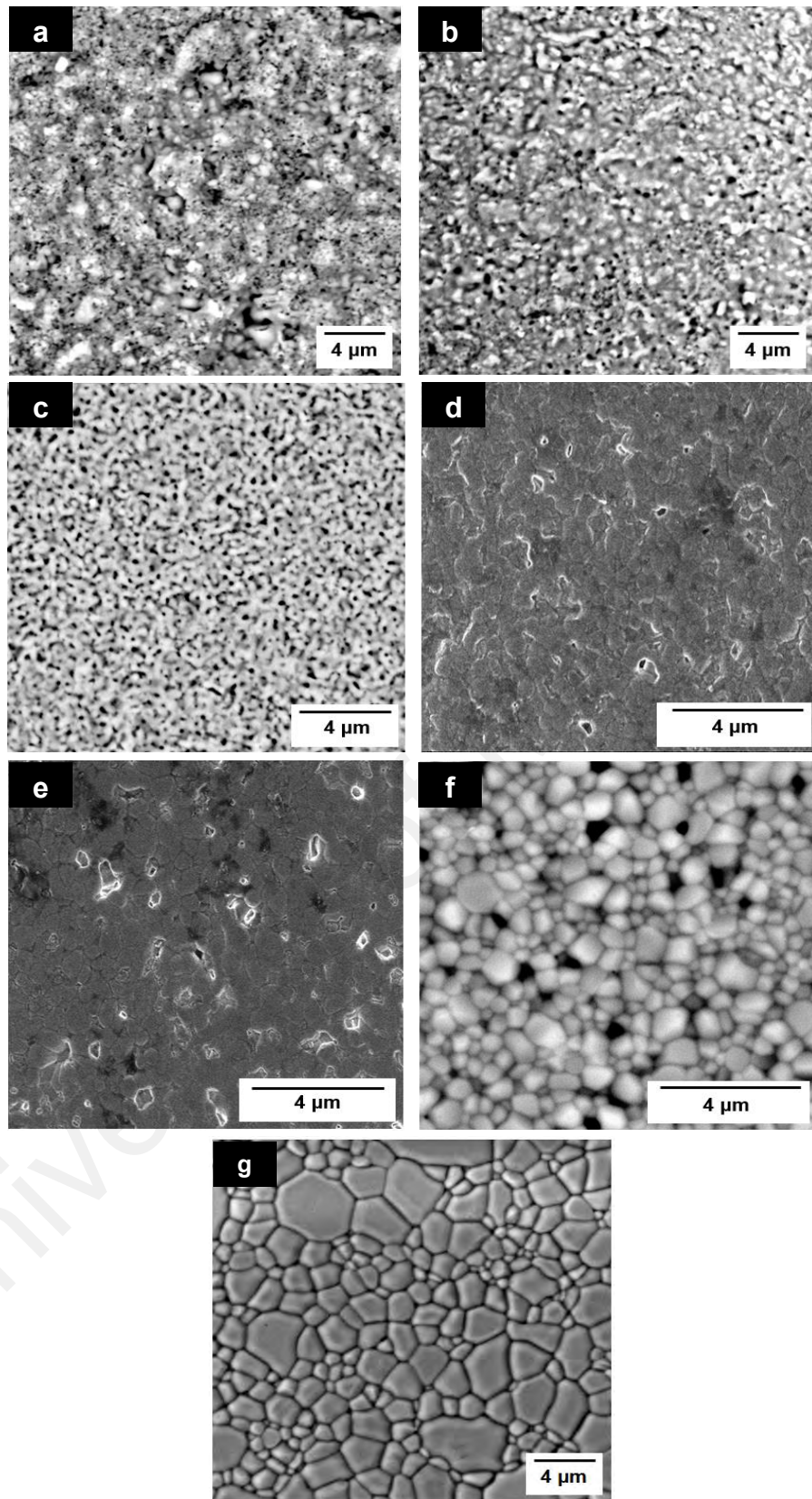


Figure 5.16: Microstructural evolution of HA-Es(M) samples microwave-sintered at (a)950 °C, (b)1000 °C, (c)1050 °C, (d)1100 °C, (e)1150 °C, (f)1200 °C and (g)1250 °C

Meanwhile, as for HA-Wp(M) compacts, the SEM micrographs exhibits less dense and fine grain microstructure at 950 °C and 1000 °C. At 950 °C, nano-sized grains were formed at the surface of the agglomerates. The necking formation which indicates the first stage of sintering was observed to have started at 1000 °C as shown in Figure 5.17 (b). The image appears to consist of grains that were attached together with interconnected porosity, as also seen for HA-Es at 1000 °C. Beyond this temperature that is of 1050 °C, the grains were equal in shape with a number of intergranular pores. The average grain size was measured to be 0.63 ± 0.03 μm as depicted in Figure 5.18. At 1100 °C, the grain size slightly increased to 0.85 ± 0.05 μm with reduced numbers of intergranular pores. Consecutively, at 1150 °C and 1200 °C, a more uniform microstructure can be observed. It can be seen that their grains are more delineate and their average grain sizes have increased to 0.96 ± 0.05 μm and 1.29 ± 0.03 μm at 1150 °C and 1200 °C, respectively. Note that, for sintering of HA-Wp(M) compacts, the decomposition of HA to β -TCP has started to take place at 1150 °C. With further increase in sintering temperature to 1250 °C, the grain size increase rapidly by a factor of 2 and measured to be 2.58 ± 0.05 μm . A similar result was reported by Ramesh et al. (2008), where the grain size of microwave sintered HA-Wp compacts increased by a factor of 2.4 from 0.86 μm to 2.08 μm when the temperature increased from 1200 °C to 1300 °C.

At 1200 °C, HA-Wp(M) exhibited larger grain sizes than the microwave sintered HA-Es. This could be related to the synthesized HA-Wp powder that has a higher sinter activity resulting from its larger surface area. However, as the temperature reaches 1250 °C, the grain growth for HA-Wp(M) compacts was found to increase higher than the HA-Es(M). This could be related to the larger domination of crystalline TCP in the HA phase (Figure 5.14) compared to 1250 °C sintered HA-Es(M). In addition, this result is in line with the lower linear

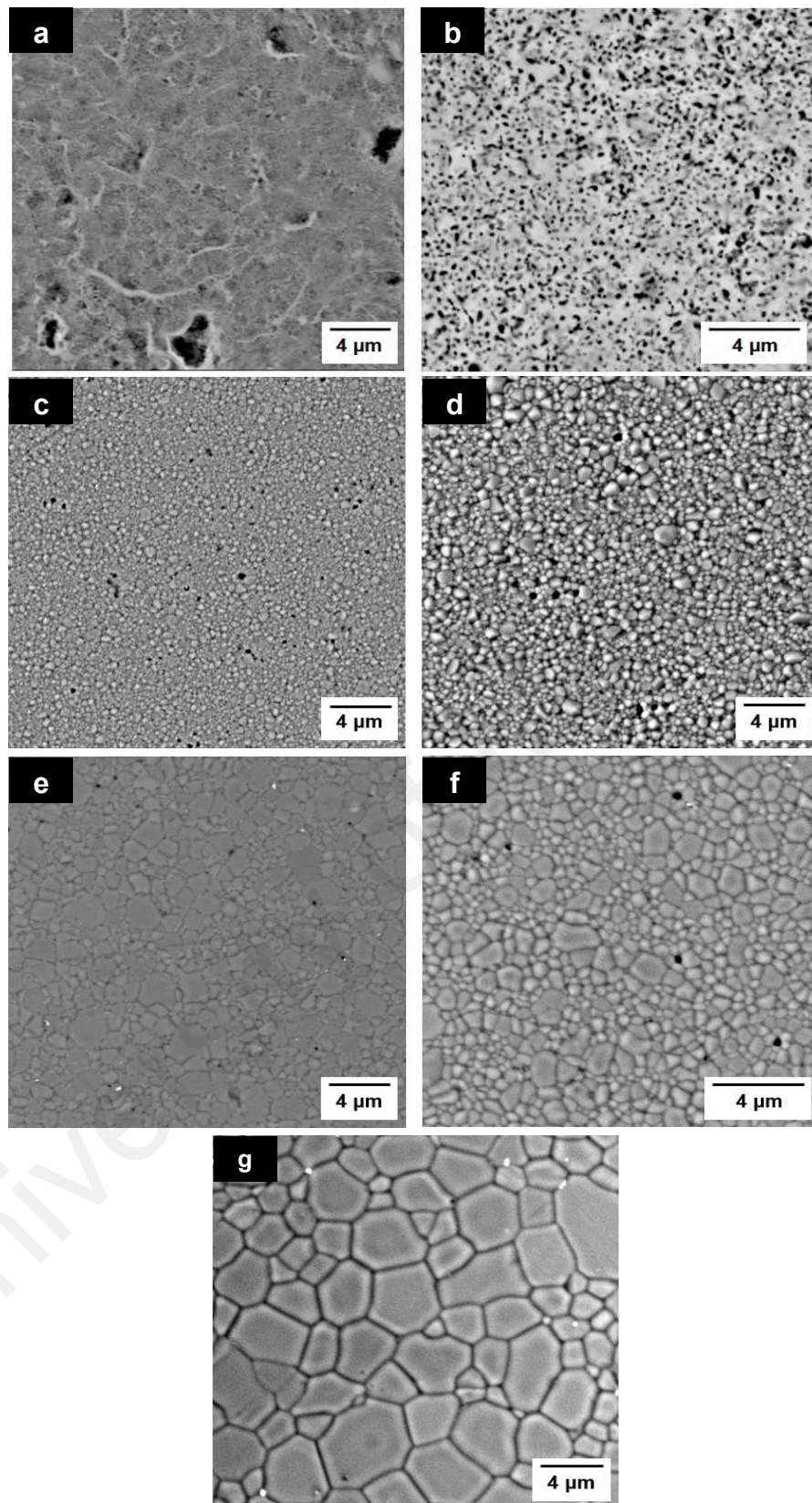


Figure 5.17: Microstructural evolution of HA-Wp(M) samples microwave-sintered at (a) 950 °C, (b) 1000 °C, (c) 1050 °C, (d) 1100 °C, (e) 1150 °C, (f) 1200 °C and (g) 1250 °C

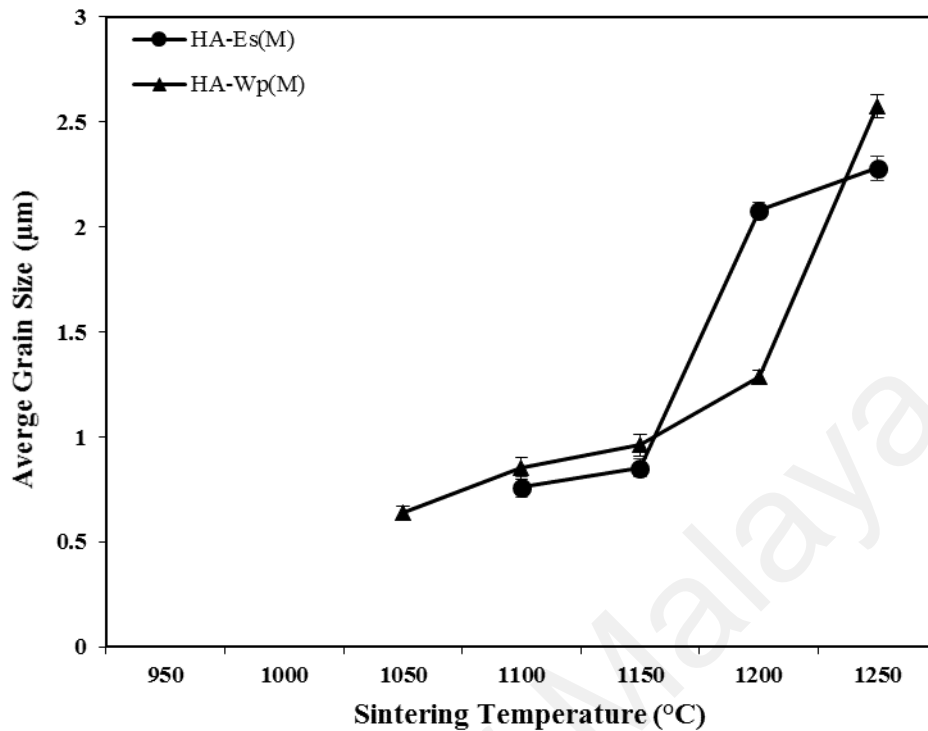


Figure 5.18: Average grain size variation of HA-Es(M) and HA-Wp(M) samples microwave-sintered at various temperatures

shrinkage result obtained for HA-Es(M) sintered compacts (Figure 5.15), which indicates that higher sintering temperature is needed for maximum densification. This is because the synthesized HA-Es powder was calcined prior compaction, hence less probability of a rapid grain growth as the sintering rate was reduced due to larger powder particle size (Kothapalli et al., 2004).

On top of all, these results indicate that microwave sintering regime employed did not promote extensive grain growth. This is proven by the nanostructure (less than 1 µm) exhibited by their SEM images even when sintered at 1150 °C as shown in Figure 5.16(e) and 5.17(e). In addition, the lower grain growth exhibited by HA-Es(M) and HA-Wp(M) could also reflect the lower densification achieved in these samples. Thus, it is believed that the grain boundary diffusion through the densification mechanism

does not reach a densification level which is conducive to grain growth (Curran et al., 2011).

5.3.4 Bulk Density Analysis

The effect of microwave sintering on the densification of HA as a function of sintering temperatures is shown in Figure 5.19. The steady increase in both bulk density variation corresponds well with a densely packed microstructure of both sintered HA-Es and HA-Wp with increasing sintering temperature as shown in the SEM images in Figures 5.16 and 5.17, respectively. This trend is similar to the observation for conventional sintered HA-Es and HA-Wp compacts (Section 5.2.4). The onset of densification for HA-Es(M) and HA-Wp(M), which is showed by the sharp increase in the sintered density has taken place between 1050 °C to 1100 °C.

The HA-Es(M) ceramic exhibited a lower value of 92.4 % at 950 °C to 92.8 % when sintered at 1000 °C. The relative density increased from 93.1 % at 1050 °C to above 95 % of theoretical density value when sintered at 1150 °C. The HA-Es compacts achieved the maximum value of 97.1 % when sintered at 1250 °C. As for HA-Wp(M), 94.8 % of theoretical density was achieved at 950 °C and increased to 95.4 % when the temperature increased to 1000 °C. The onset of densification was presented by the increase from the value of 95.8 % to 97.0 % when sintered between the range of 1050 °C and 1100 °C. HA-Wp(M) powder compacts achieved a maximum value of 98.4 % when sintered at 1250 °C and this observation was similar to the findings that have been reported in the literature (Vijayan & Varma, 2002; Yang et al., 2002; Ramesh et al., 2007a; Declan et al., 2011).

However, the maximum value of relative density achieved by both HA-Es(M) and HA-Wp(M) compacts at 1250 °C corresponded to the density of biphasic mixture phase (HA and TCP) as both HA have decomposed to secondary phases at 1250 °C and

1100 °C, respectively. This apparent increase, in this case, might be due to the allotropic transformation of HA to β -TCP which has a lower theoretical density of 3.07 g/cm³ (Raynaud et al., 2002; Krishna et al., 2007). In addition, Krishna et al. (2007) reported on the microwave sinterability study of synthesized HA with a needle-like structure that HA with such structure have better compactness and densification than flake-like morphology. Nonetheless, the bulk density variation of the HA-Wp(M) was higher than the HA-Es(M) at all sintering temperature. In fact, the lower grain growth exhibited by HA-Es(M) samples as in Figure 5.18 reflects the lower densification level obtained by the samples. This was also supported by the linear shrinkage result obtained for HA-Es(M) sintered compacts (Figure 5.15) as higher sintering temperature is necessary for maximum densification.

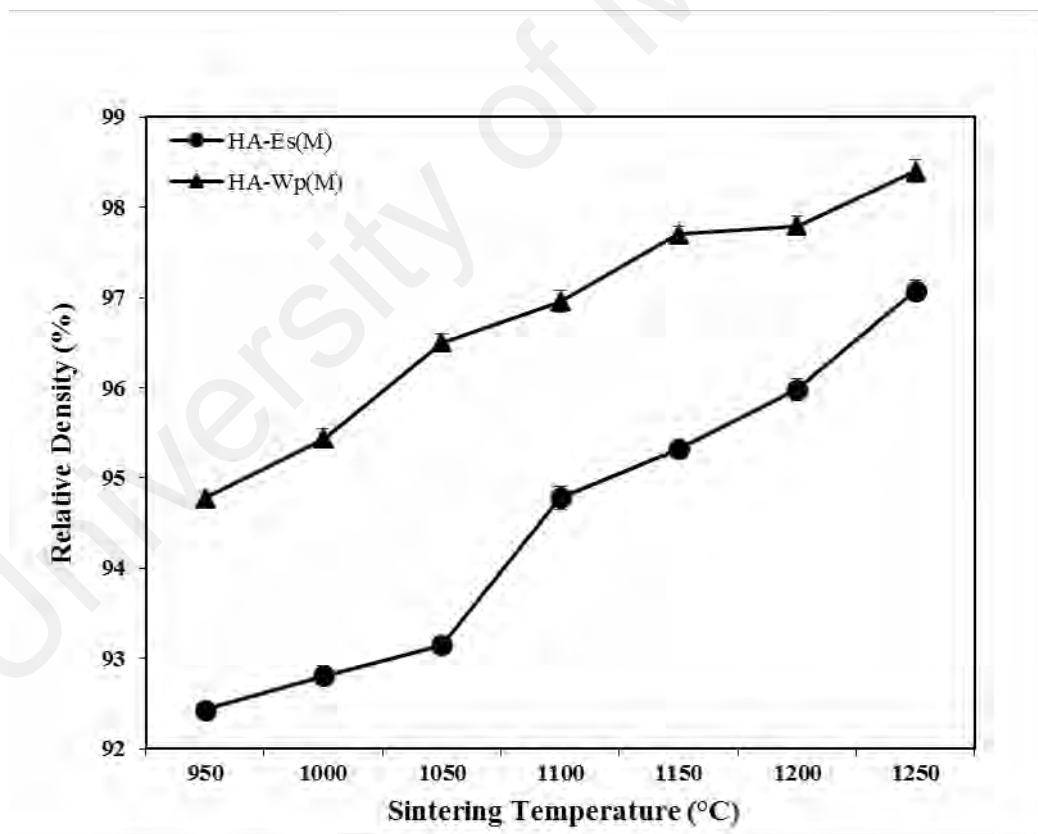


Figure 5.19: The variation in relative density of microwave-sintered HA-Es(M) and HA-Wp(M) as a function of sintering temperature

5.3.5 Vickers Hardness Analysis

The hardness values of both HA pellets with sintering temperature is shown in Figure 5.20. In general, the hardness for HA-Es(M) and HA-Wp(M) increases with sintering temperature up to 1200 °C and then decreases as the sintering temperature increases to 1250 °C. The lowest hardness value of 0.48 ± 0.06 GPa and 0.93 ± 0.05 GPa were measured for HA-Es(M) compacts sintered at 950 °C and 1000 °C, correspondingly. The sintered HA-Es(M) exhibits a remarkable increase in hardness from 1.06 ± 0.03 GPa at 1050 °C to 3.43 ± 0.04 GPa at 1150 °C and then gradually attain a maximum value of 3.65 ± 0.07 GPa at 1200 °C. Note that, when the sintering temperature reaches 1250 °C, the hardness value decreases to 3.41 ± 0.09 GPa. It should be noted that the hardness corresponds to that of β -TCP as HA-Es(M) has decomposed to the biphasic mixture at this temperature.

As for HA-Wp(M) powder compacts, the maximum hardness values of 3.82 ± 0.09 GPa was achieved at 1100 °C. It was found that the hardness increases linearly from 3.17 ± 0.08 GPa to 3.58 ± 0.11 GPa at the temperature range from 950 °C to 1050 °C. Beyond 1100 °C, the hardness has greatly decreased to 3.53 ± 0.11 GPa and 3.22 ± 0.10 GPa at 1150 °C and 1250 °C, respectively, despite both having a high relative density of ~ 98.4 %. Such observation was directly related to the decomposition of HA to very minor amount β -TCP starting from 1100 °C as shown in its XRD pattern (Figure 5.14(d)). The most intensive transformation from HA to β -TCP phase occurred at 1250 °C. The similar observation was also noted for HA-Es(M) sintered at 1250 °C with a relative density of 97.1 %. These results could be associated with the high expansion due to the transformation (HA to TCP) that could have induced residual stresses within the densified material and hence resulting in lower hardness (Veljovic et al., 2010). Besides that, the SEM micrographs of HA-Es(M) and HA-Wp(M) showed the increase in grain size by a factor of 1.1 and 2 at 1250 °C, respectively, hence the reduction in

hardness. Therefore, this lower hardness value can be correlated to the presences of TCP phase.

Besides that, it is noteworthy that the hardness value of HA-Es(M) is lower than HA-Wp(M) at sintering temperature below than 1200 °C. Besides that this could also be related to the porosity as shown in the SEM micrographs in Figure 5.18. A similar observation has been discussed earlier in the bulk density result whereas lower grain growth by HA-Es(M) samples (Figure 5.18) indicate the lower level densification obtained by the samples.

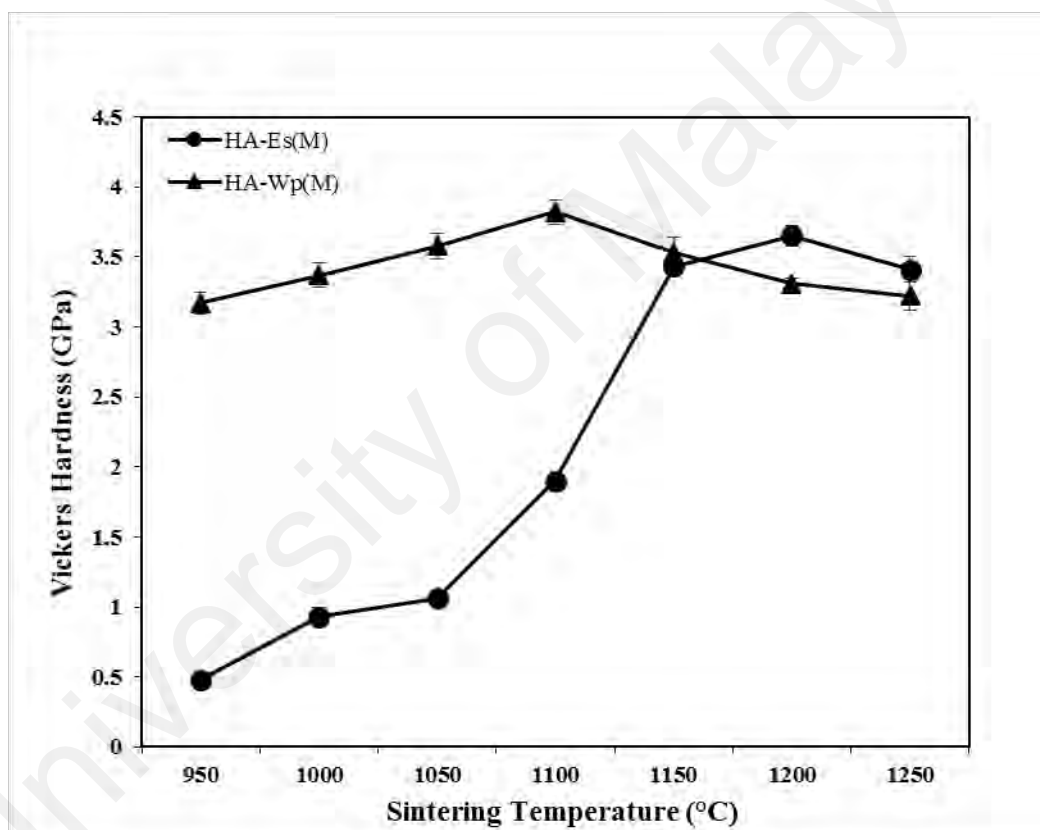


Figure 5.20: The variation in Vickers hardness of microwave sintered HA-Es(M) and HA-Wp(M) as a function of sintering temperature

5.3.6 Fracture Toughness Analysis

Figure 5.21 presented the fracture toughness of the sintered ceramics as a function of the sintering temperature. In general, the fracture toughness of the HA-Es(M) was found to increase with increasing sintering temperature. However, the microwave sintered

HA-Es samples at 950 °C and 1000°C did not result in the formation of corner cracks after Vickers indentation is made on their polished sample, and therefore data to evaluate fracture toughness could not be obtained for these samples. This could be due to the porosity on the surface of the samples as depicted in Figure 5.16(a) and (b). In addition, the HA-Es(M) ceramics at this particular temperature can be categorized as brittle since cracks are not formed in soft materials (Chona, 2002).

The fracture toughness was found to vary between $0.74 \pm 0.04 \text{ MPam}^{1/2}$ at 1050 °C to a maximum of $1.05 \pm 0.02 \text{ MPam}^{1/2}$ at 1200 °C. A similar trend as in Vickers hardness result was observed whereby the fracture toughness (K_{Ic}) decreases to $0.86 \pm 0.02 \text{ MPam}^{1/2}$ with further increase in the temperature to 1250 °C. This behaviour was due to the decomposition of HA to TCP phase and supported by the increase in grain size ($2.30 \mu\text{m}$) at this particular temperature.

Meanwhile, the trend of fracture toughness for HA-Wp(M) was also found to be very similar to its hardness result, where the fracture toughness increases with sintering temperature. Following this, the value peaked at a certain temperature before decreases with subsequent increase sintering temperature. The K_{Ic} varies from $0.67 \pm 0.02 \text{ MPam}^{1/2}$ at 1050 °C to a maximum of $0.86 \pm 0.02 \text{ MPam}^{1/2}$ at 1100 °C. Beyond that temperature, the fracture toughness decreases up to 1250 °C, i.e. from a maximum of $0.86 \pm 0.02 \text{ MPam}^{1/2}$ at 1100 °C to a minimum of $0.57 \pm 0.03 \text{ MPam}^{1/2}$ at 1250 °C. The decrement is in line with the hardness result and recorded grain growth with an increase in sintering temperature.

To date, maximum K_{Ic} for HA which subjected to microwave sintering reported in the literature was found to be $1.45 \text{ MPam}^{1/2}$ at 1050 °C (Ramesh et al., 2008), whilst the average K_{Ic} for sintered HA that collectively reported in the literature varied between 0.96 and $1.06 \text{ MPam}^{1/2}$ (Ramesh et al., 2007a; Wang & Shaw, 2009). However, the maximum K_{Ic} values at 1300 °C for HA-Wp(M) was found to be slightly below than the

average values reported at 1300 °C in the literature. Moreover, none has reported on fracture toughness of the eggshell derived HA powder, particularly synthesized via solid-state reaction. Therefore, the slightly high K_{Ic} than the reported average value obtained for HA-Es(M) in this work was encouraging. Nevertheless, it is believed that the improvement in fracture toughness could be attributed to both the improved characteristics and sinterability of the synthesized HA-Es powder. Hence, limited grain growth during microwave sintering was observed.

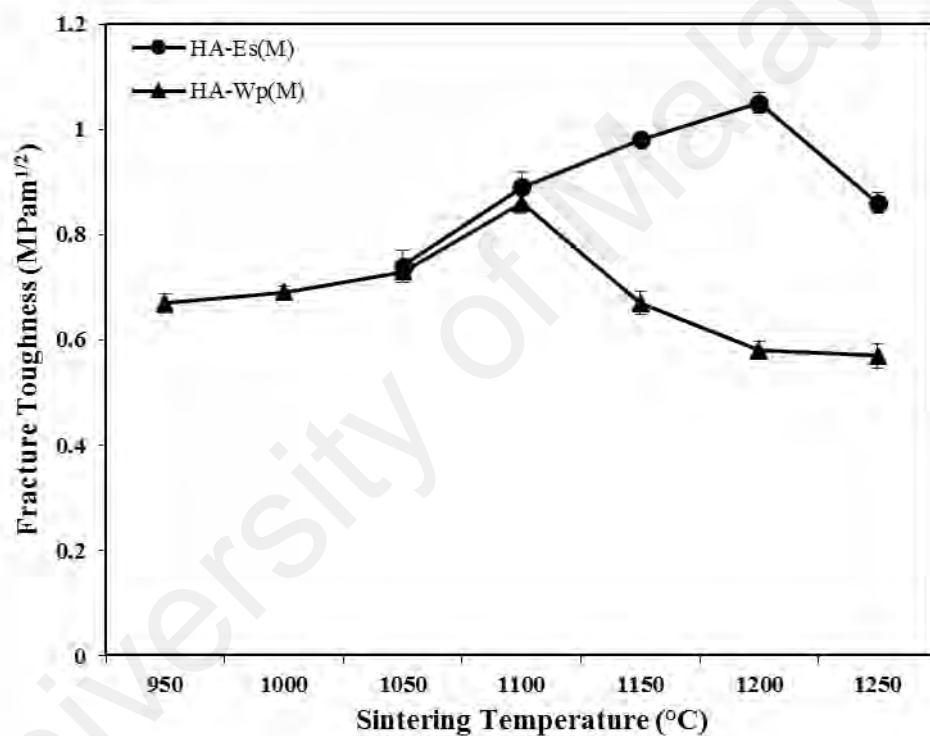


Figure 5.21: The variation in fracture toughness of microwave sintered HA-Es(M) and HA-Wp(M) as a function of sintering temperature

As previously mentioned, the trend of fracture toughness of both HA sintered samples correlated well with the variation in Vickers hardness (Figure 5.20) as both showing exactly the same trend line. Figure 5.22 and Figure 5.23 show the influence of sintering temperature as reflected by the relative density on the Vickers hardness and fracture toughness, respectively, of both HA sintered by microwave sintering. It was

found that the hardness of both HA-Es(M) and HA-Wp(M) compacts increased with a relative density (sintering temperature). The hardness peaked at 3.65 ± 0.07 GPa (1200 °C) and 3.82 ± 0.09 GPa (1100 °C), respectively and then decreased beyond the temperature at which maximum hardness was attained, although the densities of both sintered samples were still high above 96.0 %.

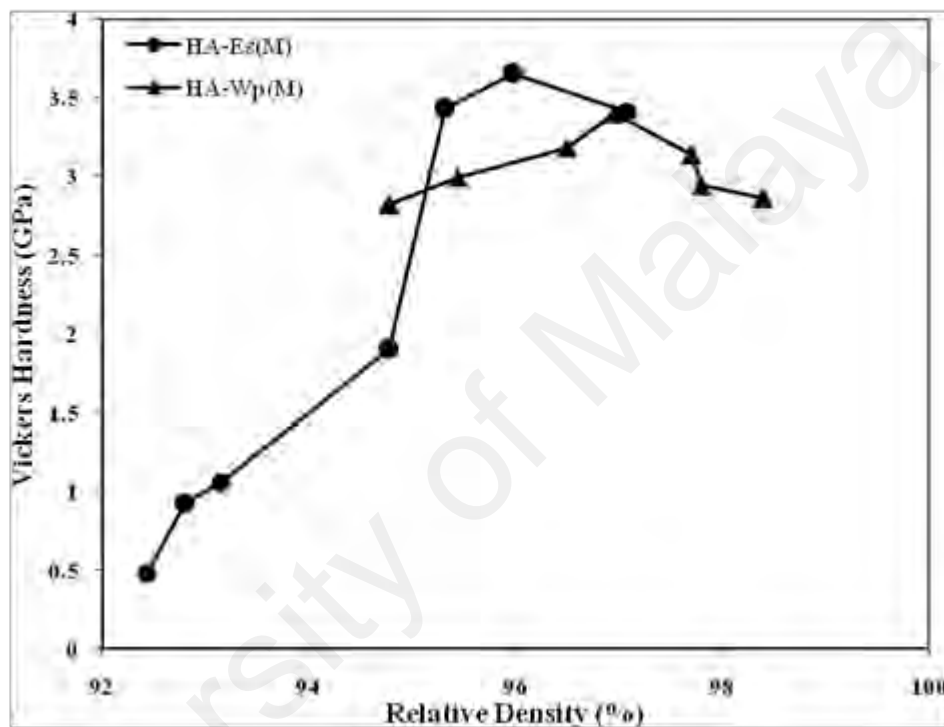


Figure 5.22: The effect of relative density on the Vickers hardness of sintered HA

A similar trend was also observed in the fracture toughness for both HA-Es and HA-Wp powder compacts, where the toughness peaked at 1.05 ± 0.02 MPam^{1/2} and 0.86 ± 0.02 MPam^{1/2} before decreased with further increase in sintering temperature. With this, the increase in relative density has clearly influenced the improvement in hardness and toughness of HA-Es(M) and HA-Wp(M) at 1200 °C and 1100 °C as shown in Figure 5.23. However, the decrease beyond the maximum value attained could not be due to the effect of bulk density.

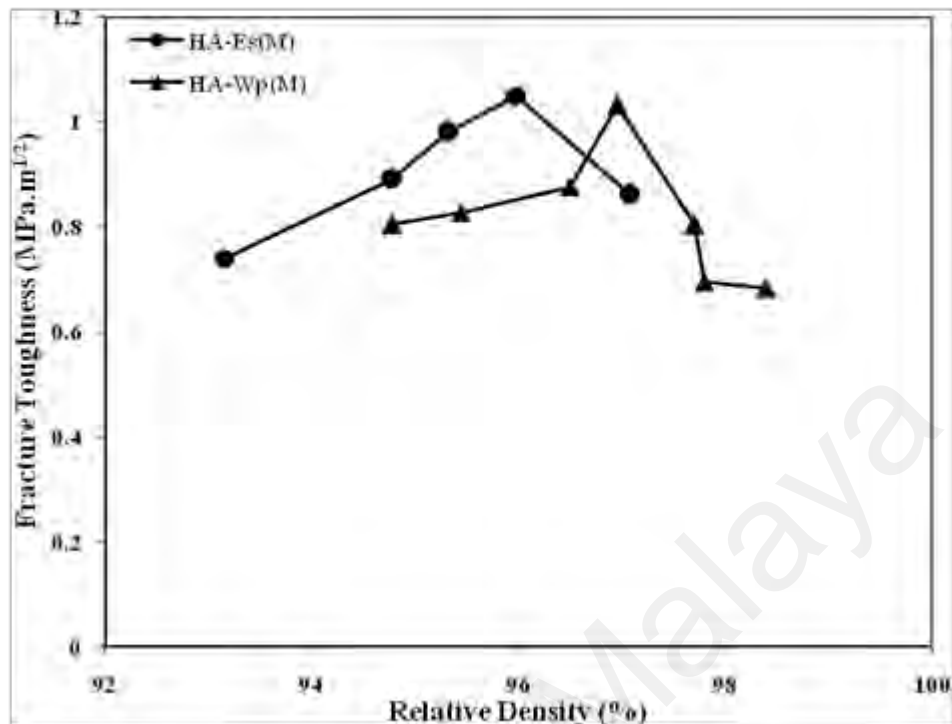


Figure 5.23: The effect of relative density on the fracture toughness of sintered HA

Despite the HA decomposition to TCP exhibited by these powder compacts (Figure 5.13 and 5.14), the decreased in hardness and toughness could be associated with a grain size effect as shown in Figure 5.24 and 5.25. It was observed that these properties increased with grain size before reaching a maximum value at a critical grain size limit (d_c) after which both properties started to decrease with increasing grain size resulting from sintering at a higher temperature.

It was found that below the critical grain size limit (d_c), the hardness and toughness are governed by bulk density. Meanwhile above the critical limit, grain growth acts as the controlling parameter. In this work, the d_c for the HA-Es(M) and HA-Wp(M) are $\sim 2.08 \mu\text{m}$ and $\sim 0.85 \mu\text{m}$, respectively. Therefore, above this critical grain size limit, the mechanical properties (hardness and fracture toughness) seems to depreciate despite exhibiting high bulk density. The finding is somehow conformed to the general consent that dehydroxylation does not contribute to the declined in mechanical properties when

sintered at high temperatures. This observation is in agreement with the findings reported in the literature (Ramesh et al., 2008, Kamalanathan et al., 2014). From the results presented for the microwave sinterability study, it was found that HA-Es prepared using eggshell as Ca precursor by solid state reaction exhibited overall better sintered properties when compared to HA-Wp ceramic prepared by the wet precipitation method. Therefore based on this study, the HA-Es was selected for subsequent investigation.

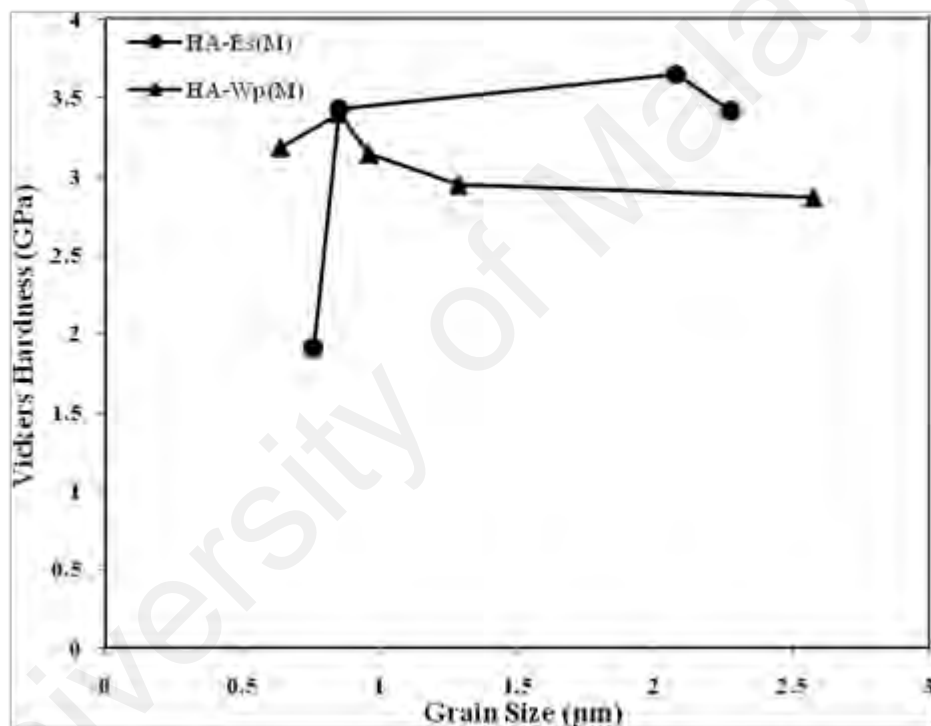


Figure 5.24: Vickers hardness dependence on the grain size of HA in microwave sintering

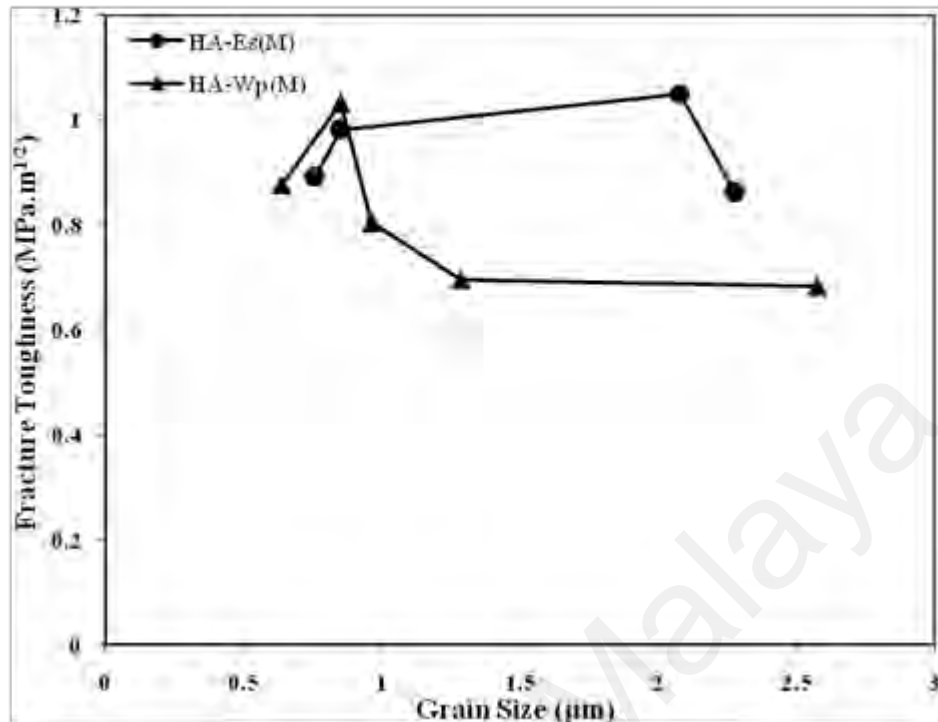


Figure 5.25: Fracture toughness dependence on the grain size of hydroxyapatite

5.4 Conventional Pressureless Sintering Versus Microwave Sintering

This section is to compare the sinterability of HA-Es(C) via the conventional method and HA-Es(M) by microwave technique in order to choose the best type of sintered HA-Es ceramics for further study on its biocompatibility. The comparison was made based on the grain size and mechanical properties of the sintered HA compacts. Besides these, the phase stability of the HA-Es samples was also taken into consideration.

Figure 5.26 shows the XRD traces of HA-Es(C) and HA-Es(M) at temperatures ranging between 1100 °C and 1250 °C. For HA-Es(C), no secondary phases were present in the HA lattice within this temperature range. Phase stability of HA-Es(C) was disrupted at 1300 °C (as shown in Figure 5.1) due to decomposition of HA to TTCP and α -TCP. Meanwhile for HA-Es(M), the phase stability of HA was disrupted at a lower temperature of 1250 °C. Having that, HA-Es(C) has proven to have slightly better phase stability in conventional sintering.

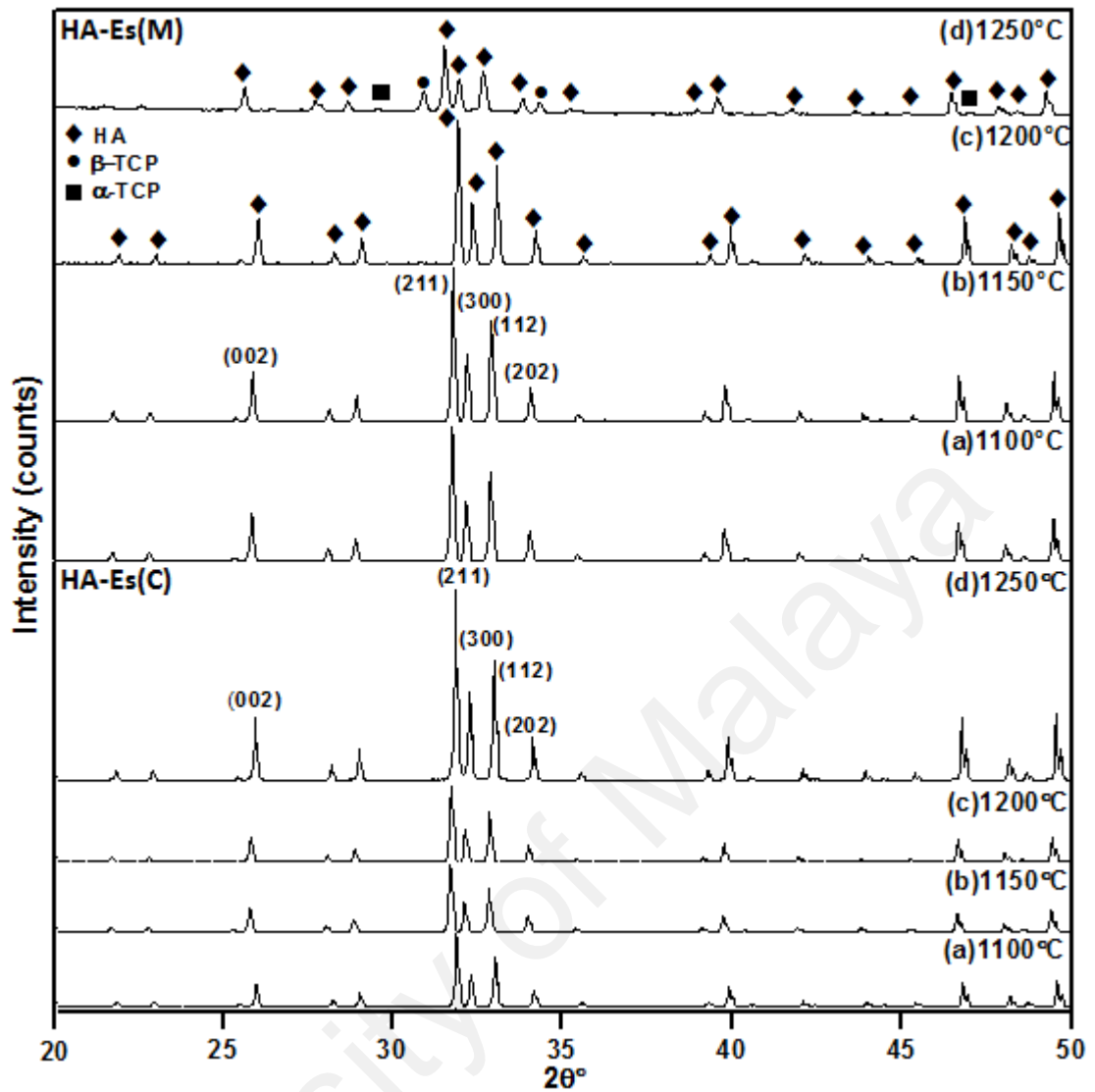


Figure 5.26: Comparison of XRD patterns between conventional and microwave sintered HA-Es at various temperatures

The effects of sintering methods on the densification of HA-Es compacts is shown in Figure 5.27. The bulk density variation of HA-Es samples sintered by both methods was found to increase with increasing sintering temperature but at different rates. A similar observation was also observed for the grain size (Figure 5.28), hardness (Figure 5.29) and fracture toughness (Figure 5.30) variation with sintering temperature. The bulk density of HA-Es(M) was found to be higher than HA-Es(C) throughout the sintering regime employed. The maximum density value recorded for HA-Es(C) was 99.2 % at 1350 °C, whilst for HA-Es(M), the maximum bulk density was 97.1 % at 1250 °C. Note

that, HA-Es(C) and HA-Es(M) have decomposed to secondary phases beyond 1300 °C and 1200 °C, respectively. This result has found to be comparable with that reported for microwave sintered eggshell derived HA at 1250 °C with reported value at 98 % of HA theoretical density although the phase decomposition to biphasic mixture has taken place (Veljovic,et al., 2010). Based on the results, the effectiveness of microwave sintering can be noted as higher density value of HA-Es(M) was achieved at all temperatures. Moreover, this rapid sintering (30 °C/min) indicates shorter sintering time than conventional sintering (5 °C/min). For example, sintering of HA to 1200 °C via microwave took about 96 minutes in comparison to 588 minutes taken by the conventional sintering method. This advantage is presented in Table 5.1 which compares the total sintering time taken to achieve the respective densities with respect to sintering temperature.

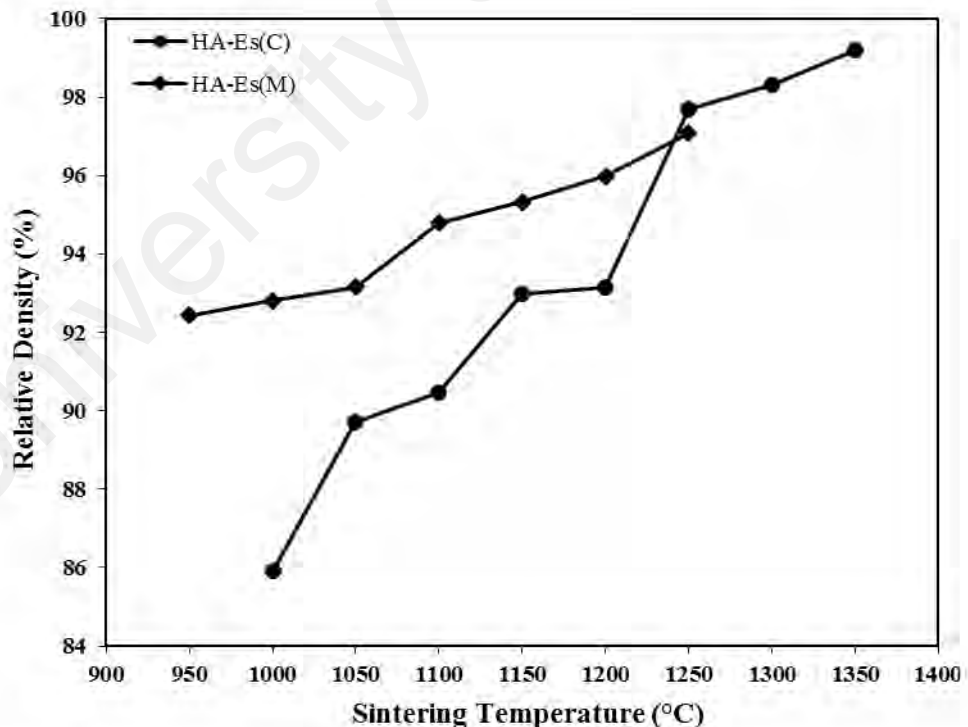


Figure 5.27: Relative density of HA-Es sintered at various temperatures by the conventional and microwave methods

Table 5.1: Total sintering time for two different sintering methods

SINTERING TEMPERATURE (°C)	CONVENTIONAL SINTERING		MICROWAVE SINTERING	
	Time Taken (min)	Relative Density (%)	Time Taken (min)	Relative Density (%)
1000	508	85.92	80.3	92.81
1050	528	89.7	83.7	93.15
1100	548	90.45	87.0	94.78
1150	568	92.99	90.3	95.32
1200	588	93.15	93.7	95.978
1250	608	97.7	97	97.078

In terms of the average grain size with sintering temperature for both methods, it can be seen from Figure 5.28 that HA-Es(C) exhibited finer grain size than HA-Es(M) at all sintering regime. Note that, the grain growth of HA-Es(C) has only started to take place at 1300 °C. The smallest average grain size of $0.58 \pm 0.02 \mu\text{m}$ was attained at 1100 °C. At the sintering temperature of 1150 °C and 1200 °C, HA-Es(C) had an average grain size of $0.66 \pm 0.02 \mu\text{m}$ and $0.75 \pm 0.02 \mu\text{m}$, respectively. Sintering beyond 1250 °C resulted in a rapid grain growth from nanometer range to micron size, i.e. the HA grain size increased from $0.95 \pm 0.02 \mu\text{m}$ (at 1250 °C) to $3.36 \pm 0.02 \mu\text{m}$ (at 1300 °C) and finally to $5.76 \pm 0.01 \mu\text{m}$ at 1350 °C.

As discussed earlier for Figure 5.24, the critical grain size limit (d_c) of HA-Es(M) is $\sim 2.08 \mu\text{m}$ which was achieved at 1200 °C. Hence, sintering at temperature higher than 1200 °C, the mechanical properties of HA-Es(M) would be expected to deteriorate despite the further increased in its bulk density with sintering temperature. This phenomenon was confirmed by the result obtained in the variation of Vickers hardness and fracture toughness of the HA-Es(M) samples, where the hardness and toughness decreased beyond 1250 °C after the maximum values peaked at 1200 °C as shown in Figure 5.29 and Figure 5.30.

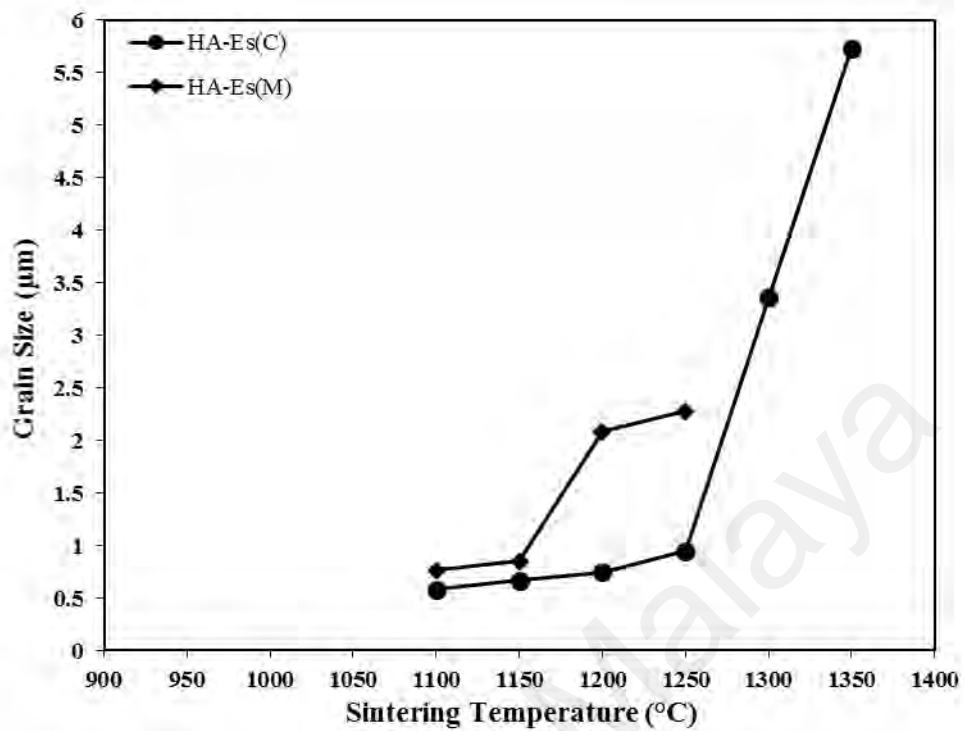


Figure 5.28: Average grain size of HA-Es sintered at various temperatures by the conventional and microwave methods

Figure 5.29 depicts that hardness of HA-Es increase with sintering temperature regardless the sintering method but at different rates. For example, the maximum hardness obtained for HA-Es(C) was 5.56 GPa at 1250 °C. Meanwhile, the highest hardness for HA-Es(M) was found to be 3.65 GPa at 1200 °C and both powders still retained the HA phase stability at that particular temperature. This has indirectly tarnished the ability to attain comparable hardness in shorter sintering time in microwave sintering.

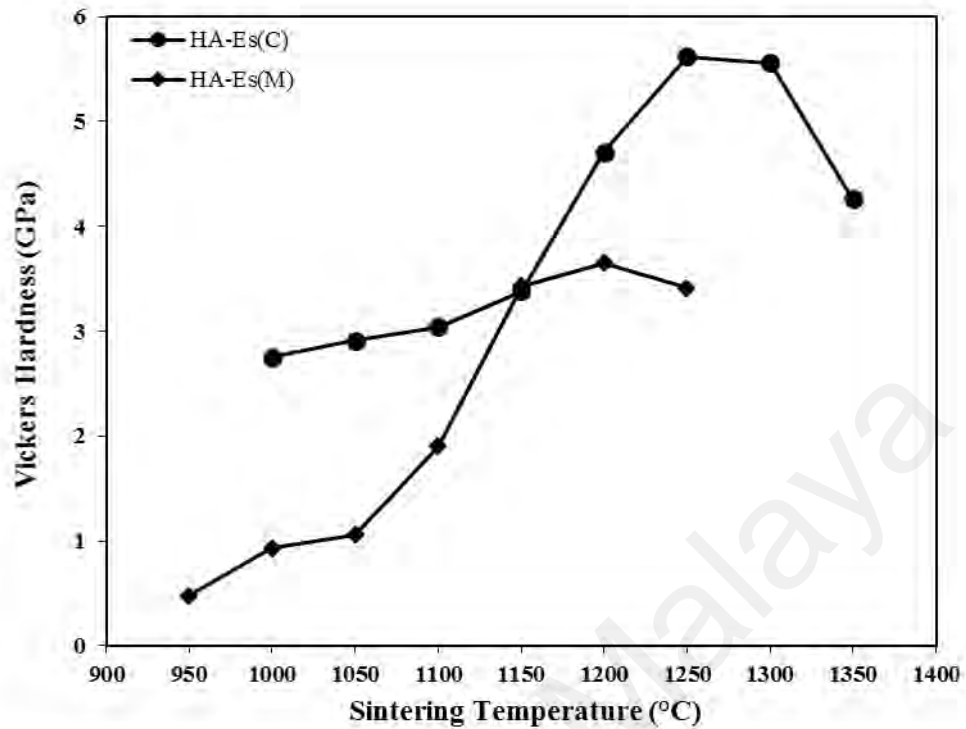


Figure 5.29: Vickers hardness of HA-Es sintered at various temperatures by the conventional and microwave methods

A similar observation to the trend of Vickers hardness was also observed in the fracture toughness (Figure 5.30) where maximum fracture toughness for HA-Es(C) and HA-Es(M) was reported to be $1.51 \text{ MPam}^{1/2}$ and $1.05 \text{ MPam}^{1/2}$ at $1250 \text{ }^\circ\text{C}$ and $1200 \text{ }^\circ\text{C}$, respectively. Note that, the higher fracture toughness achieved by HA-Es(C) ($1.51 \text{ MPam}^{1/2}$) while retaining its phase stability at $1250 \text{ }^\circ\text{C}$ and average grain size of $0.95 \pm 0.02 \text{ }\mu\text{m}$ are very encouraging. The unusual behavior exhibited by this eggshell derived HA could be linked to the enhancement in crack resistance associated with the intergranular fracture mechanism (cracks through the grain boundaries) which is promoted by the nanoscale grain size (Wang & Shaw, 2007; 2009). However, at this stage, the exact mechanism is still unclear and further study would be required to elucidate the phenomenon.

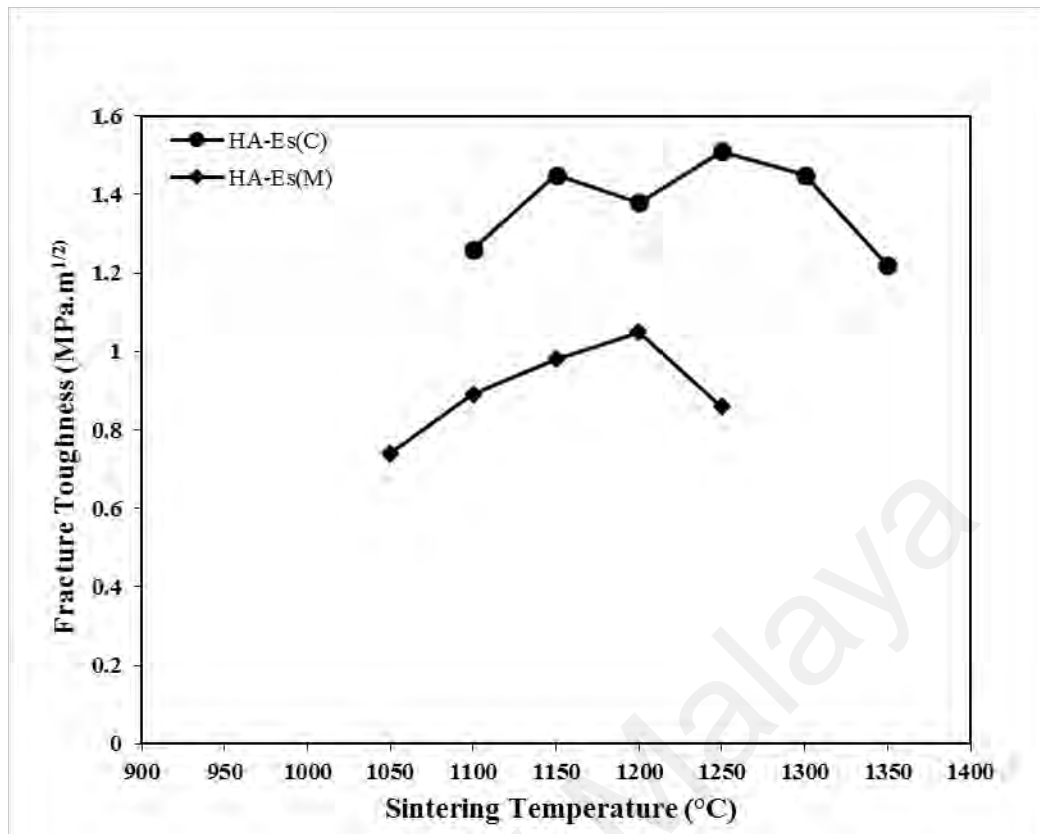


Figure 5.30: Fracture toughness of HA-Es sintered at various temperatures by the conventional and microwave methods

Based on the literature survey, the highest fracture toughness of 1.52 MPam^{1/2} was reported for hot pressed sintered HA at 1000 °C in an argon atmosphere for 1 hour, with translucent nanostructure and average grain size of 50 nm. Besides that, collective studies on spark plasma sintered HA has consistently resulted in higher toughness (1.0 – 1.25 MPam^{1/2}) than conventional sintering with the same grain size. Thus, these literature findings have collectively supported the belief that the fracture toughness of conventionally sintered HA-Es having submicron meter range grain size (~950 nm) is comparable with that of HA attained from spark plasma sintering and hot pressing.

In addition, the nanostructured HA-Es was produced from using natural waste eggshells as a direct Ca precursor through a simple solid state sintering at 1250 °C. Therefore, taking into consideration the combination of the improved powder and mechanical properties, it is suggested that a valuable HA-Es body with a low degree of

porosity with the potential for clinical implant has successfully being produced at a temperature of 1250 °C via conventional sintering.

5.5 Biocompatibility of Eggshell Derived Hydroxyapatite

Sintered hydroxyapatite have been documented to have biocompatibility and tissue integration (Hench, 1991; Kokubo et al., 1992; Kim et al., 2005). However, it was reported that the ability of bone integration decreases with increasing sintering temperature (Kim et al., 2005). It has been shown that eggshell-derived hydroxyapatite (HA-Es) is a promising bone graft substitute material as it showed good biocompatibility (Kumar & Girija, 2013; Kattimani et al., 2014; Demirel et al., 2016). Kattimani et al. (2014) reported that eggshell derived HA used as a filler in the osseous regeneration in maxillary cystic bone defect led to the complete bone formation by the end of week 8. In their study, the eggshell derived HA have been proven to enhance the bone regeneration as it facilitates bone adsorption and calcium release, which stimulates osteoblast differentiation and bone formation.

As previously stated, the pure HA-Es compacts were successfully synthesized after heat treatment at 800 °C while the HA-Es sintered at 1250 °C showed the optimum properties in terms of mechanical properties. Noted that, sintered HA at different sintering temperatures has different apatite-forming abilities and tissue responses. Therefore, the HA-Es compacts at 800 °C, 1200 °C and 1250 °C were chosen for the biocompatibility and biological cell studies. The heat treatment temperature was stated in parenthesis. For example, the HA-Es sample after heat-treated at 800 °C was stated as HA-Es(800).

5.5.1 In vitro Biodegradation Studies

The biodegradation test was conducted using Phosphate Buffered Saline (PBS) (Sigma Aldrich, USA). One packet of the PBS crystals, when diluted, makes up to 1 liter of 0.01M PBS with pH 7.4 at 25 °C. The HA-Es compacts were separately immersed in 20 ml PBS solution for up to 21 days at 37 °C. The degree of degradation was estimated by measuring the changes of pH in PBS solution and weight of the samples before and after the immersion.

Figure 5.31 shows the typical SEM images of the heat-treated HA-Es samples before and after immersion in PBS (for 21 days). The apatite formation was reported to involve the dissolution of ions from the surface of the material with time until it reaches the supersaturation of the biological fluid (Gomes et al., 2011). In addition, the dissolution in this process depends on the crystallinity and grain size of the sample. After immersion in PBS, the SEM images revealed the formation of apatite layer with aggregated spherical apatite on the surface of all samples. Sintered HA formed a bone-like apatite layer on its surface and subsequently bonds to the living bone by this apatite layer.

These results are in agreement with the previous report of in vitro study via SBF on eggshell derived HA (Kumar & Girija, 2013). However, it is difficult to observe the apatite layer on HA-Es(800) due to its porous structure and small particle size.

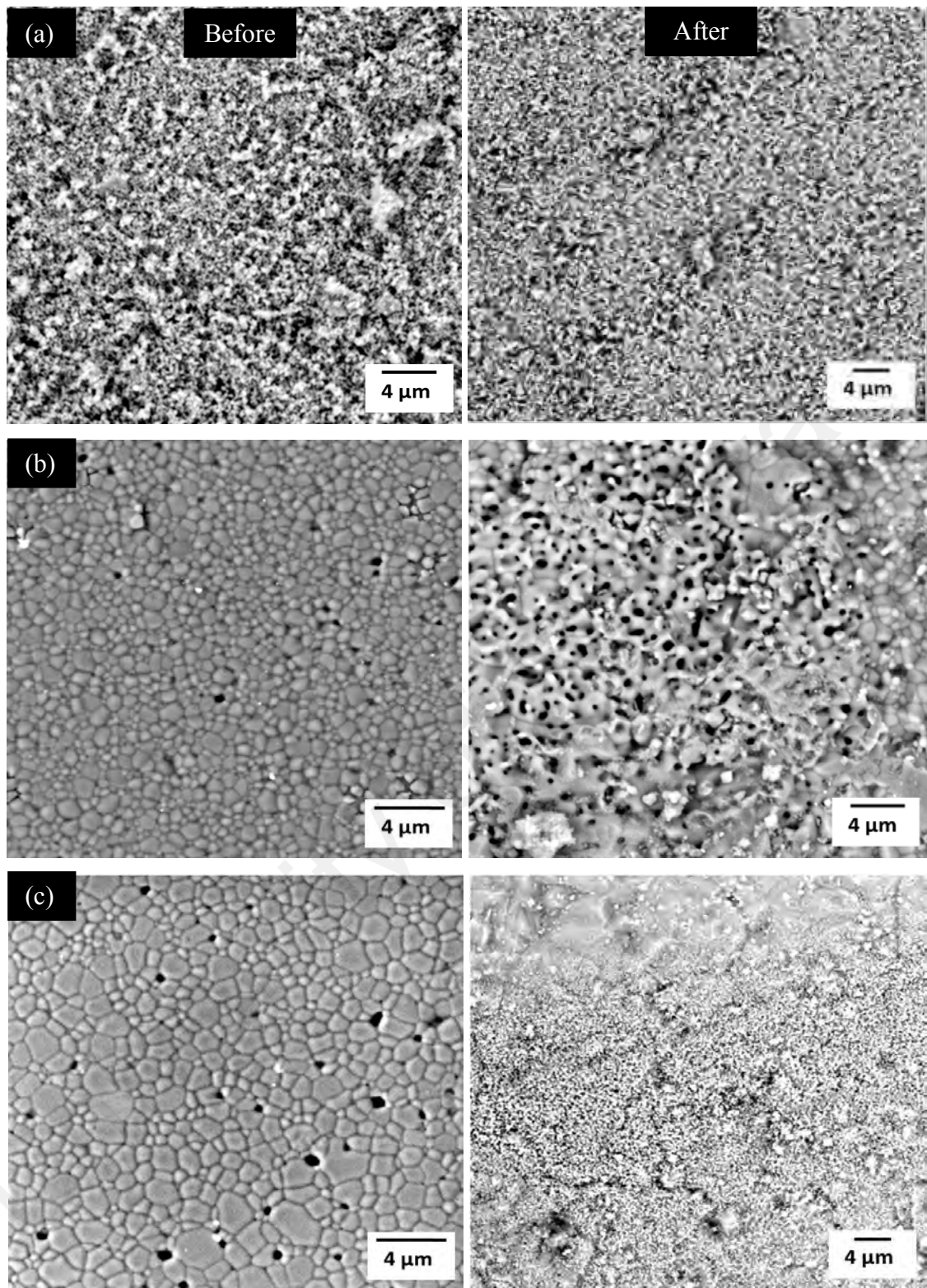


Figure 5.31: Typical SEM micrographs of the eggshell derived HA compacts before and after immersion in PBS: (a) HA-Es(800), (b) HA-Es(1200) and (c) HA-Es(1250)

Figure 5.32 summarized the changes of pH value versus immersion duration. When HA-Es samples were immersed in PBS, a similar pattern of fluctuation in pH was recorded for all the samples, where higher pH values than the standard pH of PBS (pH 7.4) were recorded. It was reported that dissolution of Ca ions contributes to the increase in pH value with immersion time. Kheradmandfard et al. (2012) reported that the increase in pH was resulted from the ionic exchange between H^+ within the PBS solution and Ca^{2+} in the HA compacts. Hence., more Ca dissolution, the higher PBS pH value. In addition, the increase in pH of the solution accommodates the nucleation of apatite (Pan et al., 2010) and the release of Ca from HA indicated the solubility of these materials (Boanini et al., 2010; Bang et al., 2015).

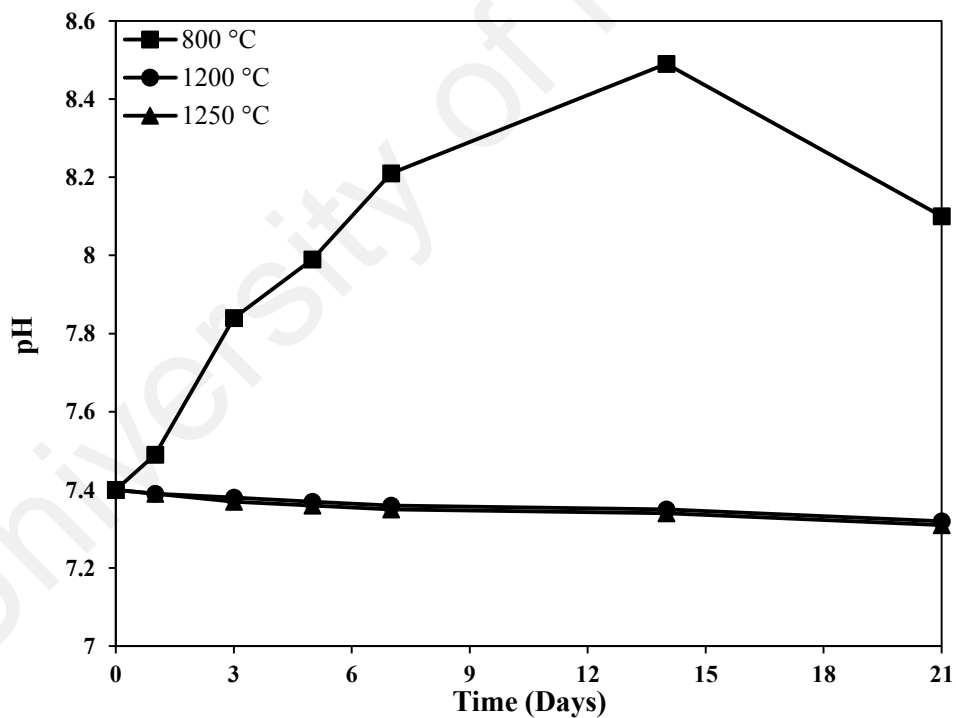


Figure 5.32: The changes of PBS solution pH with respect to the number of immersion days of HA-Es sample

In this work, HA-Es(800) showed higher pH values and it can be suggested that it dissolves faster than those of other HA-Es samples. However, the loose compact of the

HA-Es(800) might as well contribute to this dissolution. Furthermore, it was difficult to observe the formation of apatite layer on its surface due the porous structure of the sintered HA-Es(800) samples itself (as shown in Figure 3.31).

Figure 5.33 shows the mass loss (in mg) of HA-Es compacts studied when immersed in PBS for 21 days. In general, the HA-Es(800) showed the higher tendency of degradation, with the mass loss of ~ 0.48 mg/g after immersion in PBS for 21 days. Meanwhile, HA-Es(1200) showed about ~ 0.13 mg/g after 21 days of immersion. The similar trend was also observed for HA-Es(1250) after 21 days of immersion in PBS, in which ~ 0.12 mg/g mass loss was recorded. There was a significant mass loss recorded from day 15 of the immersion. Based on these results, it can be concluded that the HA-Es exhibited a low dissolution rate before day 15 of immersion and beyond this high dissolution was recorded for all samples.

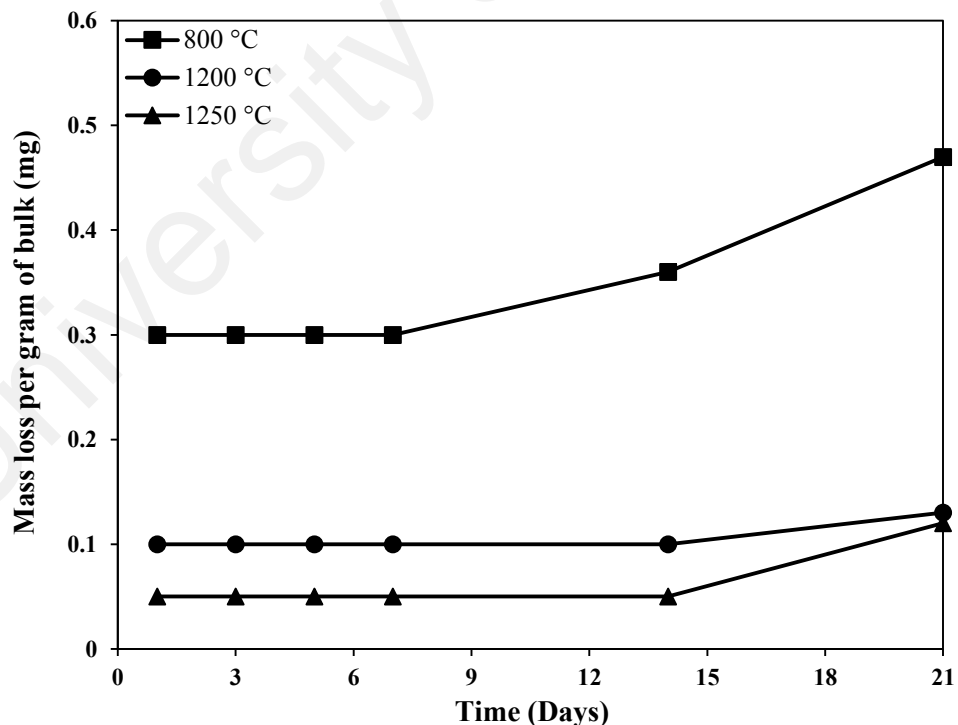


Figure 5.33: Mass loss (in milligrams) of as-prepared and sintered HA-Es samples with respect to immersion periods in PBS solution

5.5.2 Cell study in vitro: MC3T3-E1 Osteoblast-like Cell

Cell study were carried out on the surface of HA-Es discs (as-prepared at 800 °C, 1200 °C and 1250 °C) with the diameter of ~15 mm and thickness of ~3 mm by performing cell attachment and proliferation. These two characteristics are the prerequisites for osteointegration in bone graft substitution.

5.5.2.1 Cell morphology and adherence

The ability of the MC3T3-E1 osteoblast-like cell to attach on the surface of the eggshell derived HA samples is very crucial since it will dictate the further cell functions such as migration, proliferation and differentiation (Milovac et al., 2014). Cells grow in number once they were attached to a surface and then progressively cover the entire surface before initiating differentiation (Nie et al, 2013; Bang et al., 2015).

The morphological features of the MC3T3-E1 cell on the surface of the HA-Es after 4 hours, 1 day and 3 days of culture at different magnifications are shown in Figure 5.34 and Figure 5.35. The biocompatibility nature of the eggshell derived HA in this study was confirmed by the SEM images which showing the presence of osteoblast cells attached on these surfaces.

Generally, cells attached well on all surface specimens whilst the largest number of cells were found attached to HA-Es(1250). After 4 hours of incubation, the attached cells showed the elongated polygonal shape. On day 1 and day 3, it can be observed that the density of osteoblast cells increase along with the flattening of the polygonal shape.

Concurrently, the filopodial extension from the cell edges was also observed as the cells attached and spread. Subsequently, the cells grew and formed an intimate contact with the surface of specimens before continue to proliferate on all surfaces. After day 3, the cells formed a layer to cover the surface in order to induce the extracellular matrix development (Balamurugan et al. 2008; Magallanes-Perdomo et al., 2010). This finding

has supported the results on biocompatibility obtained by previous works on eggshell derived HA via microwave irradiation (Kattimani et al, 2014) and sol-gel method (Demirel et al., 2016).

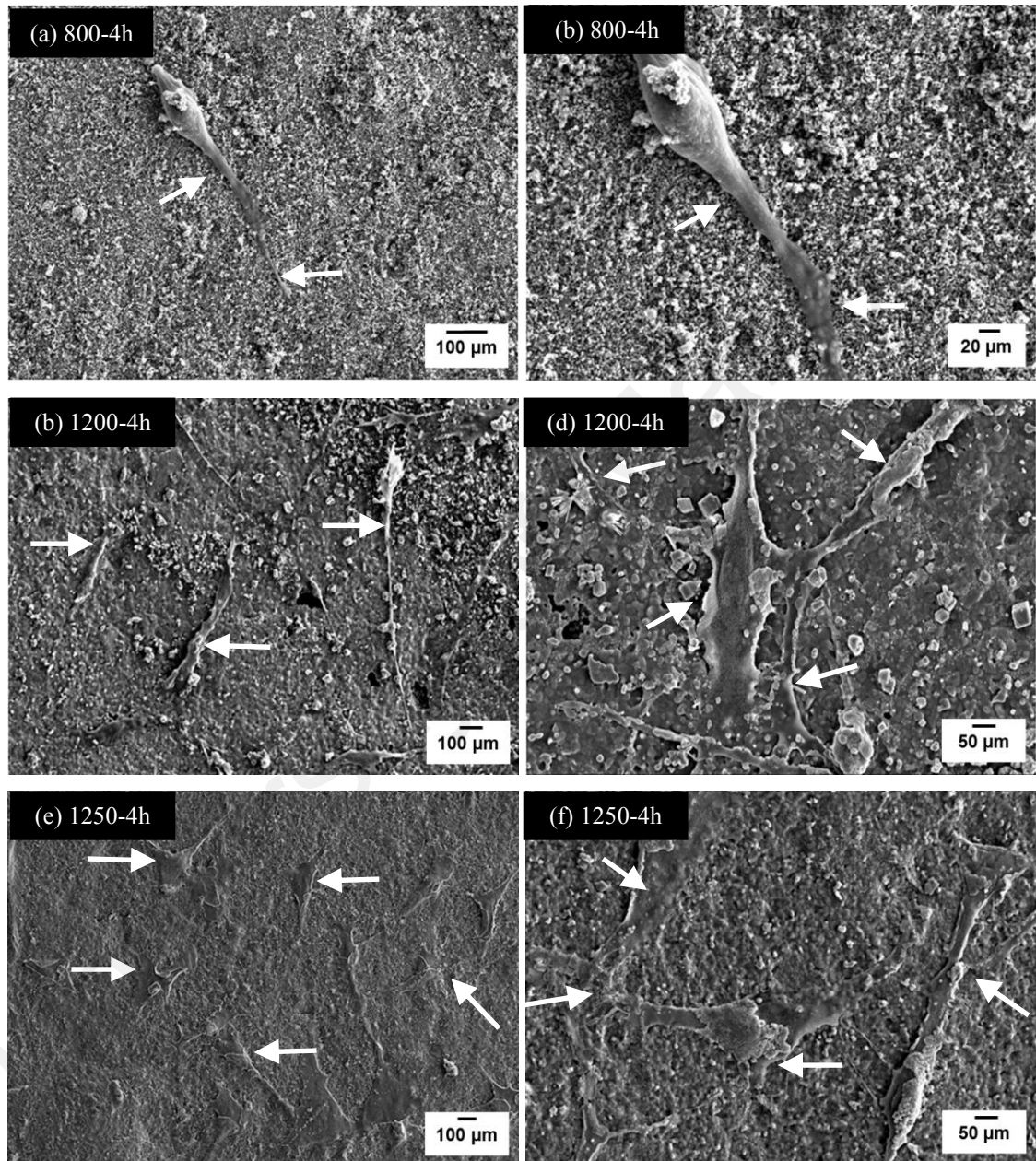


Figure 5.34: Cell morphology on the surface of HA-Es samples after 4 hours of incubation at different magnification. The white arrows indicate the adhered cell

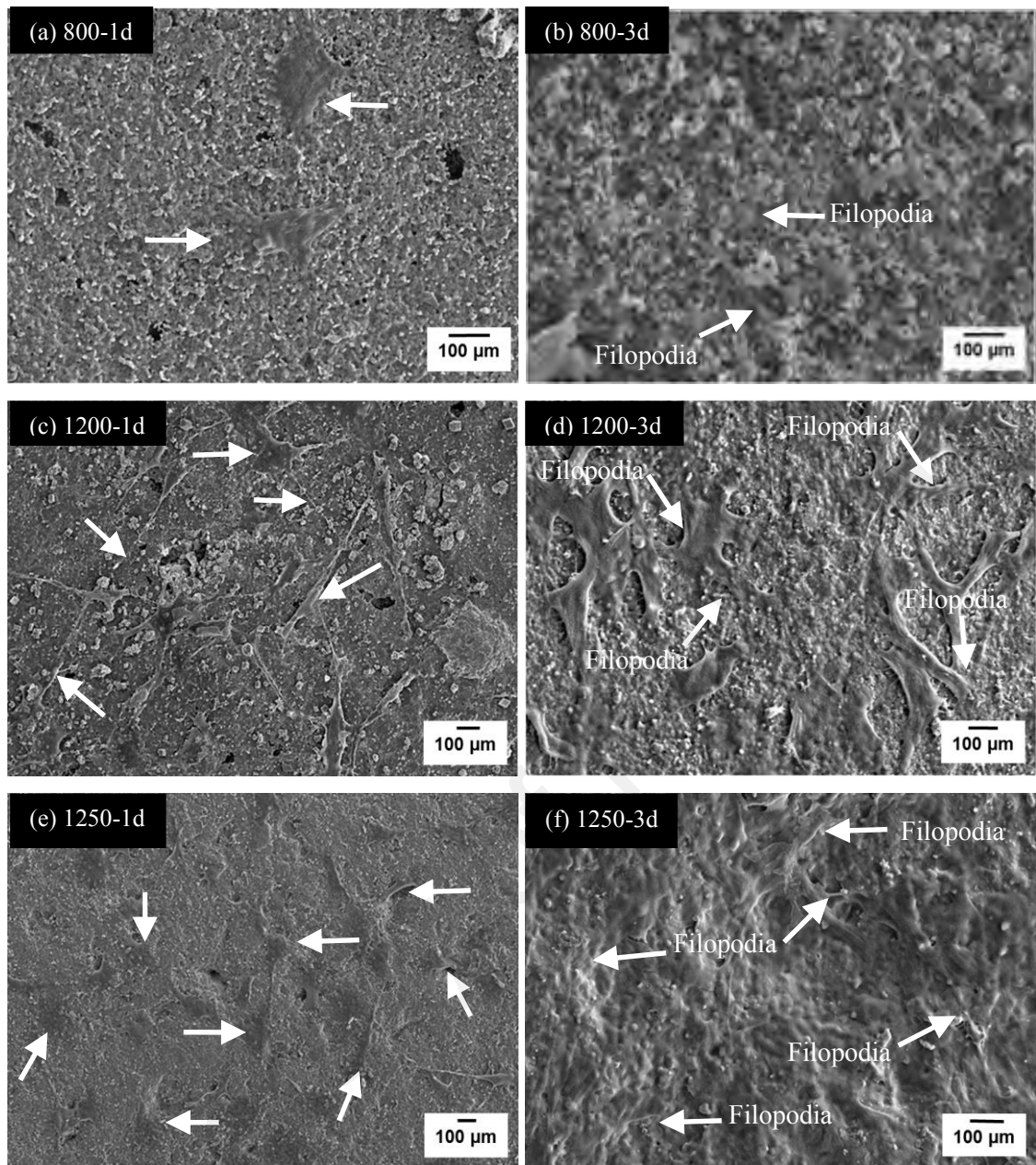


Figure 5.35: SEM images of osteoblast cell attachment on the surface of HA-Es samples at different sintering conditions. The white arrows indicate the adhered cell

5.5.2.2 Cell proliferation

The numbers of living cells on samples after seeding was examined using the Cell Counting Kit-8 (CCK-8) kit for 1, 3 and 5 days culture time. Figure 5.36 shows the number of proliferated cells in the average of three samples with the standard deviation. Generally, an active cells proliferation is denoted by the increased cells number over the

culture time. It was found that the proliferation of HA-Es(800) and HA-Es(1200) was fairly similar after 1 and 3 days of culture. As for HA-Es(800), the loose compaction of the HA-Es particles as shown in Figure 5.31(a) could have inhibited the osteoblast cell-like growth at the beginning of the culture (Bang et al., 2015). Therefore, the proliferation process could not be observed on the samples even up to 5 days of culture. Meanwhile, the number of cells on HA-Es(1200) have only significantly increased after 5 days of culture as presented in Figure 5.36. However, for HA-Es(1250) the proliferation rate increases with culture period accordingly. This indicates that the cells proliferated well on HA-Es(1250) specimens.

Itala et al. (2010) reported that roughened surfaces enhanced the initial cells attachment. This observation is true for the case of HA-Es(1200). However, roughened surface did not have an effect on the proliferation rate or morphology. Although its SEM images showing rougher surface, it did not affect the cells proliferation rate. In addition, Quarles et al. (1992) reported that MC3T3-E1 cells were difficult to differentiate into adipocytes in the presence of resveratrol. Meanwhile, bone marrow cell can differentiate into osteoblasts and adipocytes in high density. This might as well have influenced the above result. Hence, the in vitro study was also conducted using rat bone marrow cell (RBMC) to evaluate the cell proliferation and differentiation on this sintered eggshell derived HA samples.

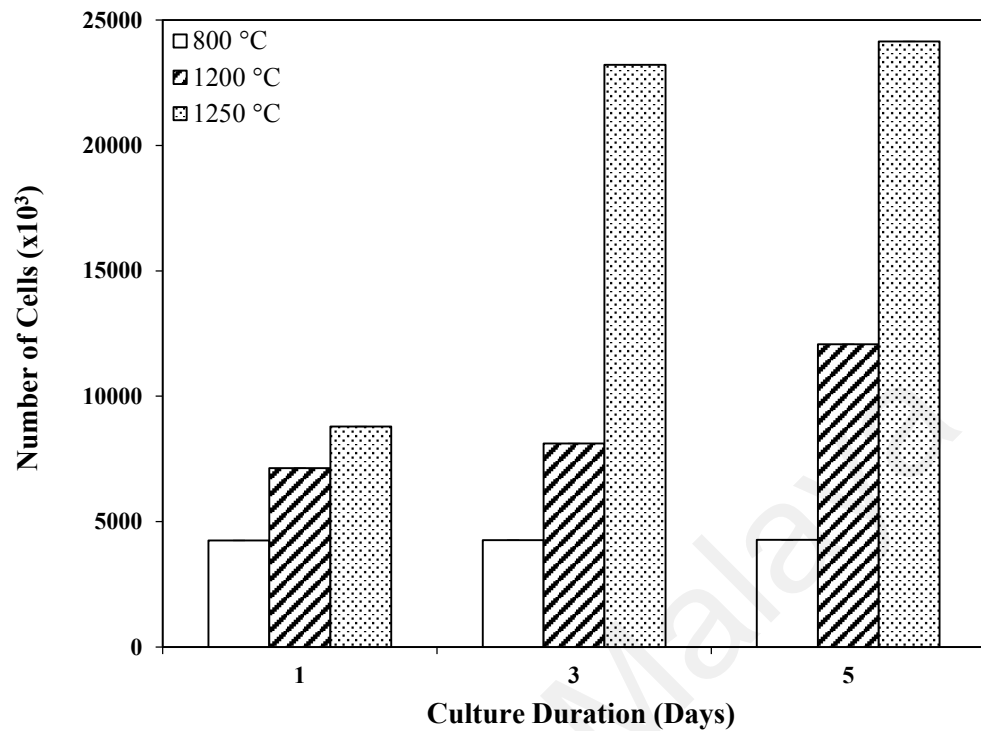


Figure 5.36: MC3T3-E1 cell proliferation on the different HA-Es samples

5.5.3 Cell Study In vitro: Rat Bone Marrow Cells (RBMC)

Similarly, the in vitro studies were carried out on the surface of HA-Es compacts at 800 °C, 1200 °C and 1250 °C.

5.5.3.1 Cell morphology and adherence

Figure 5.37 represents the morphologies of rat osteoblast cells after 4 hours cultured on sintered HA-Es samples. From the SEM observation, it can be clearly seen that the cells attached well on all surface specimens but more cells were attached on the HA-Es(1250 °C) (Figure 5.37 (c)) than those of the other HA-Es samples. Besides that, the cells on HA-Es(1200) and HA-Es(1250) exhibited lamellipodia extensions with cell flattening and increase number of filopodia at the edge of the cells with increased sintering temperature of the HA-Es samples. In addition, it can be clearly observed that the elongated cell strongly adhered onto the surface HA-Es(1250) sample.

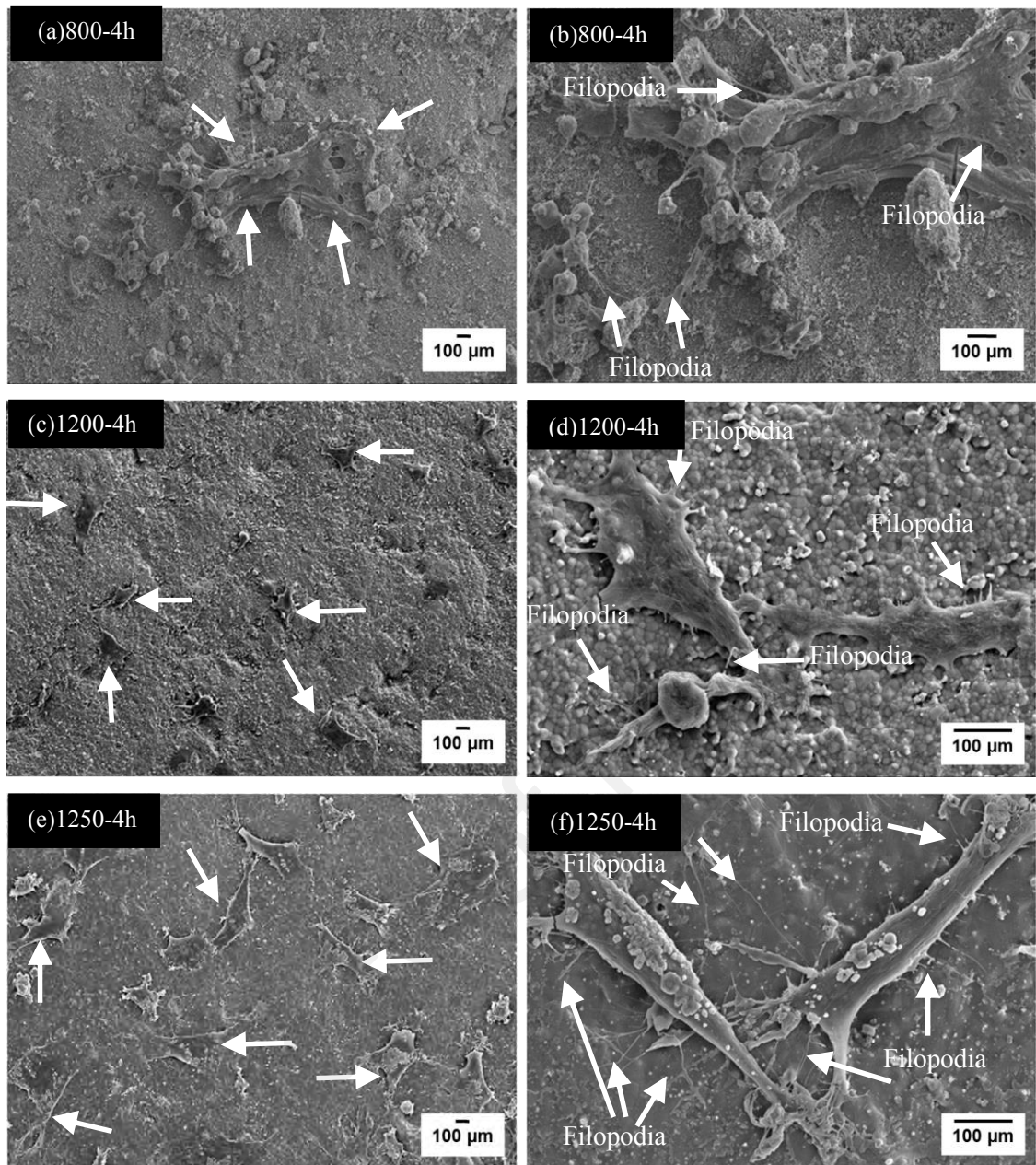


Figure 5.37: SEM images of bone marrow cell morphology on HA-Es samples after 4 hours of culture at different magnification. The white arrows indicate the adhered cell

It has been collectively reported that surface properties (roughness, topography, etc.) and chemistry of the implant influence cell-material interface and therefore the different rate and quality of new tissue formation (Hutmacher, 2000; Deligianni et al., 2001; Nalla et al., 2005, Bang et al., 2015). In this work, the HA-Es(1250) sample has proven

to provide a preferable surface for the cells to attach and migrate, which was probably due its high density structure topography.

5.5.3.2 Cell proliferation

In this work, cell proliferation was evaluated using the CCK-8 kit for 1, 3 and 5 day culture time. The numbers of living cells with time on the HA-Es surfaces is depicted in Figure 5.38. The increasing number of cells with incubation period indicates active proliferation on the samples.

After day 1, it was found that cells on each HA-Es samples have proliferated at a different rate. The number of cells was greatly increased with increase in sintering temperature of the specimens following this order: HA-Es(800) < HA-Es(1200) < HA-Es(1250). At day 3, rat bone marrow cells on the HA-Es(1250) proliferated at approximately two times higher rate than the HA-Es(1200) sample. It was reported that the difference in this activity is more likely to be caused by topography (Li et al., 2009).

After day 5, the cell proliferation for all samples continuously increases, following the similar order after day 1. This trend signified that the cells proliferated well on all sintered HA-Es specimens. In this work, HA-Es(1250) specimen have shown the highest number of proliferated cells at each culture day.

Bang et al. (2014) concluded that the rough specimen surface is appropriate for good initial cell attachment while the smooth surface is for cell proliferation. Hence, HA-Es(1250) was expected to have the smoothest surface than the other samples and this can be virtually seen from the SEM images in Figure 5.37 (c) itself. Besides that, small grain size would be beneficial for cell proliferation (Roohani-Esfahani et al., 2011). This is due to the increase in grain boundary at the surface. In this study, the conventionally sintered HA-Es(1250) exhibited nanoscale average grain size of $0.95\pm 0.02\ \mu\text{m}$ as depicted in Figure 5.10. Hence, the combination of nanoscale average

grain size and smooth surface and of the HA-Es(1250) was expected to have contributed to the cell proliferation behavior on its surface.

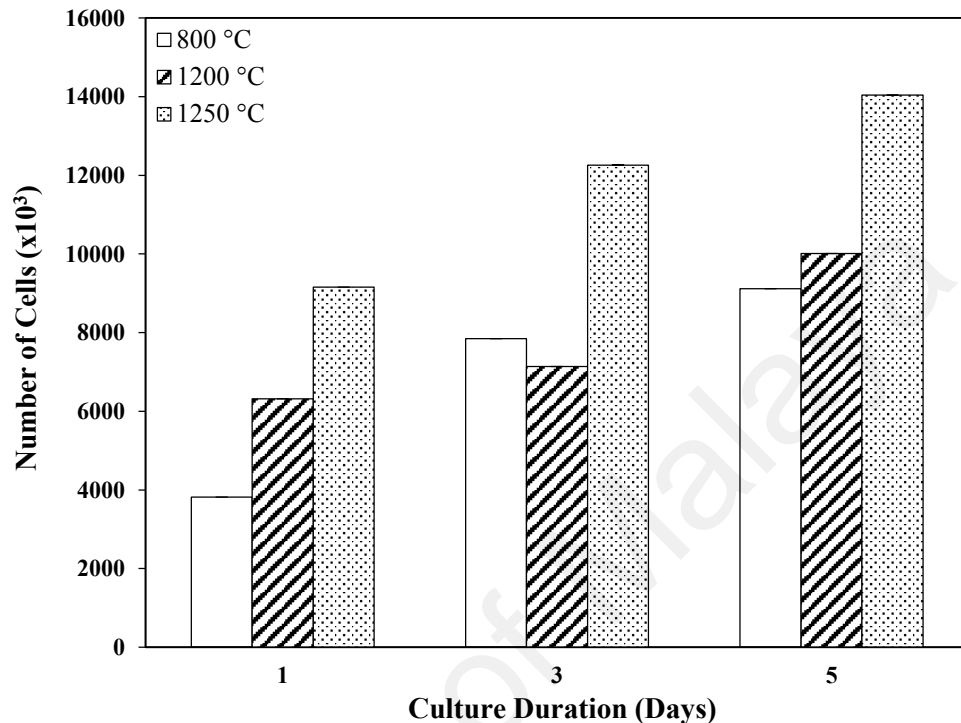


Figure 5.38: RBMC cell proliferation on the different HA-Es samples

Bernhardt et al. (2011) claimed that a cell response regulation could be increased by scaffold with increased hydrophilic property as it could keep the cells on its surface for a longer contact period. As eggshell derived HA is known to have hydrophilic property (Kattimani et al., 2014), hence the cells can adhere and proliferate better on the eggshell derived HA surface. In addition, the other elements inherent in eggshells such as carbonate and Mg could induce a better guide signal for the cells to adhere and migrate (Hing et al., 2005; Landi et al. 2010). For example, Hesaraki et al. (2014) reported that carbonated HA showed better cellular response than sintered HA due to the extension of Ca^{2+} at a higher level that facilitates the potential of membrane ionic exchange. Hence, based on these studies, the eggshell derived HA in this work could have high Ca^{2+}

concentration that induces better dissolution and chemical surface interaction (Bang et al, 2015) and therefore a better interaction with the cells.

5.5.3.3 Cell differentiation

The cells differentiation activity on as-prepared HA-Es (800) and sintered HA-Es (1200) and HA-Es(1250) samples are shown in Figure 5.39. ALP activity is an important marker of osteoblast protein (Hong et al., 2010). It is highly noted at the early state of bone maturation (Kim et al., 2004). The increase in its activity is associated with number of cells that have differentiated into the osteoblast phenotype. In this study, the results indicated that cells on all HA-Es specimens increase continuously in activity with an increase in incubation period from 7 to 14 days, where cells grown on sintered eggshell derived HA at 1250 °C shows highest enzyme activity according to the following order; HA-Es(1250C) > HA-Es(1200) > HA-Es(800). The similar pattern was also observed in the cells proliferation (Figure 5.38).

This finding is contrary to the findings by Landi et al. (2004) which claimed the reverse relationship between proliferation and ALP activity; ALP activity is lowered as the cells induced to proliferate. However, this result is in agreement with the findings by Nalla et al. (2005) and Bernhardt et al. (2011), which stated that ALP activity was associated with the number of adherent cells. In other words, as the number of viable cells increased, higher cells adhesion and proliferation were observed on the HA-Es(1250) and thus resulting in high ALP activity.

However, the HA-Es specimens showed a tendency to decrease in its ALP activity after 21 days. Brown et al. (2003) claimed that such phenomenon is attributed to the late stage of culture. It was further stated that at this stage, the osteoblast cells has advancing to the maturation and subsequent production of mineralized matrix. This result recommends that these cells are able to carry out osteogenic functions and differentiate

on all the samples as reported in other previous works (Kattimani et al, 2014; Bang et al., 2015; Mehtap & Bunyamin, 2016).

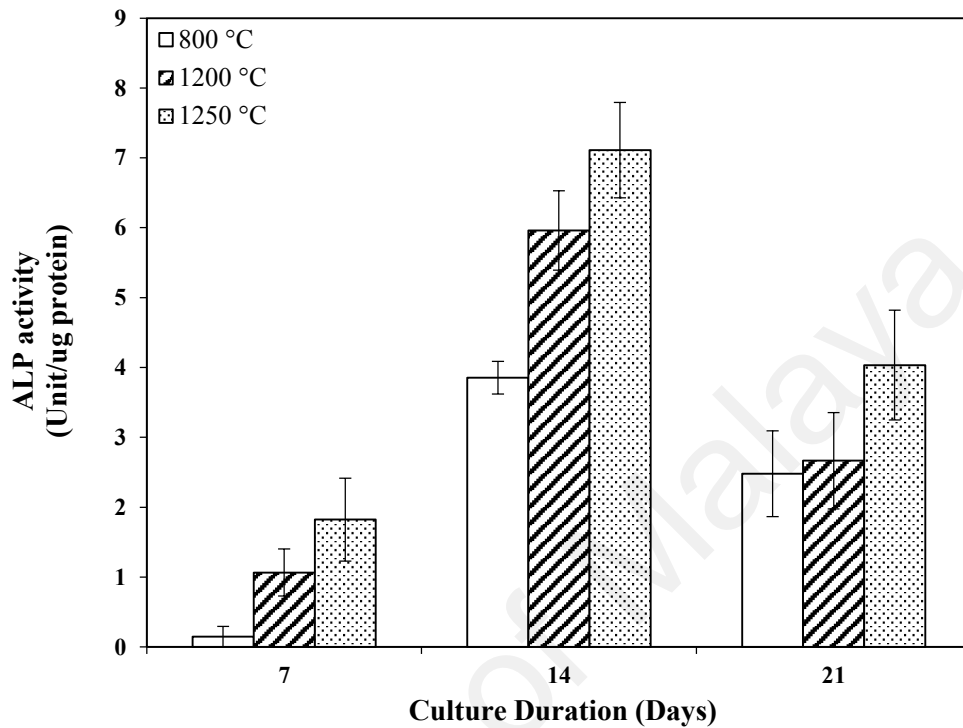


Figure 5.39: ALP activity of RBMC on different HA-Es samples

5.5.2.4 Cell mineralization: Alizarin red S staining

The images of Alizarin red S staining result of HA-Es samples after 14 and 21 days is shown in Figure 5.40. It was found that the area of mineralized nodules detected on HA-Es(800) was the smallest. Meanwhile, HA-Es(1250) surfaces were largely covered by the mineralized nodules than that on the HA-Es(1200) surfaces. As reported elsewhere, the earliest and most efficient calcium deposition was expected to be on HA-Es(1250) due to the largest areas of mineralized nodules after 14 days. This is proven by the area of mineralized nodules after 21 days. Generally, it can be concluded that these HA-Es specimens provide an excellent surface for cell maturation.

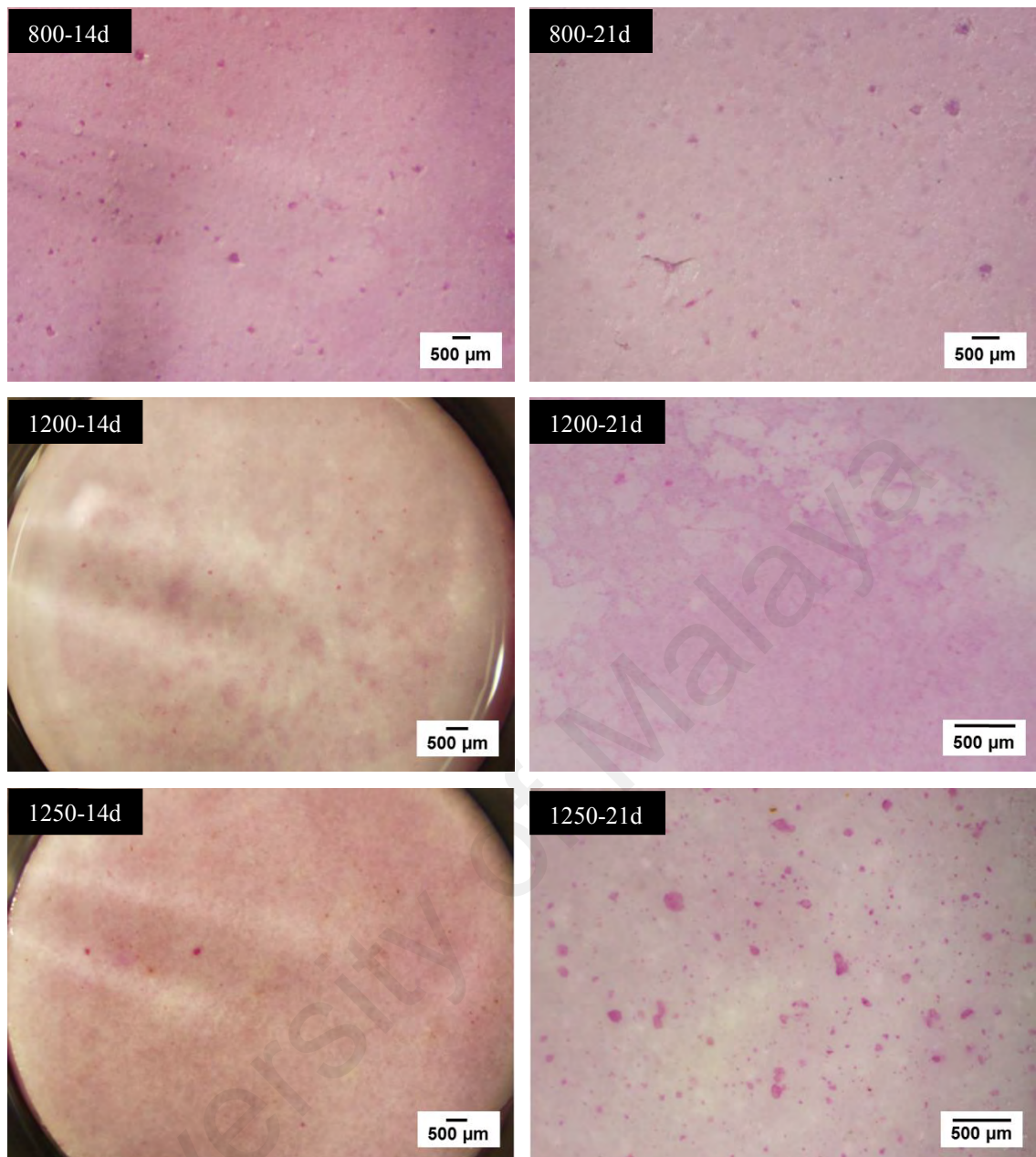


Figure 5.40: Bone nodule formation on HA-Es at:

(a) 800 °C, (b) 1200 °C and (c) 1250 °C

Figure 5.41 shows the calcium concentration synthesized by the cells on the HA-Es sample after 14 and 21 days of culture. It was observed that the result is parallel to the finding in bone nodule observation as depicted in Figure 5.40, in which more calcium present on the HA-Es(1250) samples when compared to the other HA-Es samples (See Appendix C-6). This indicates that HA-Es(1250) has provided the best surface for the cells to function accordingly.

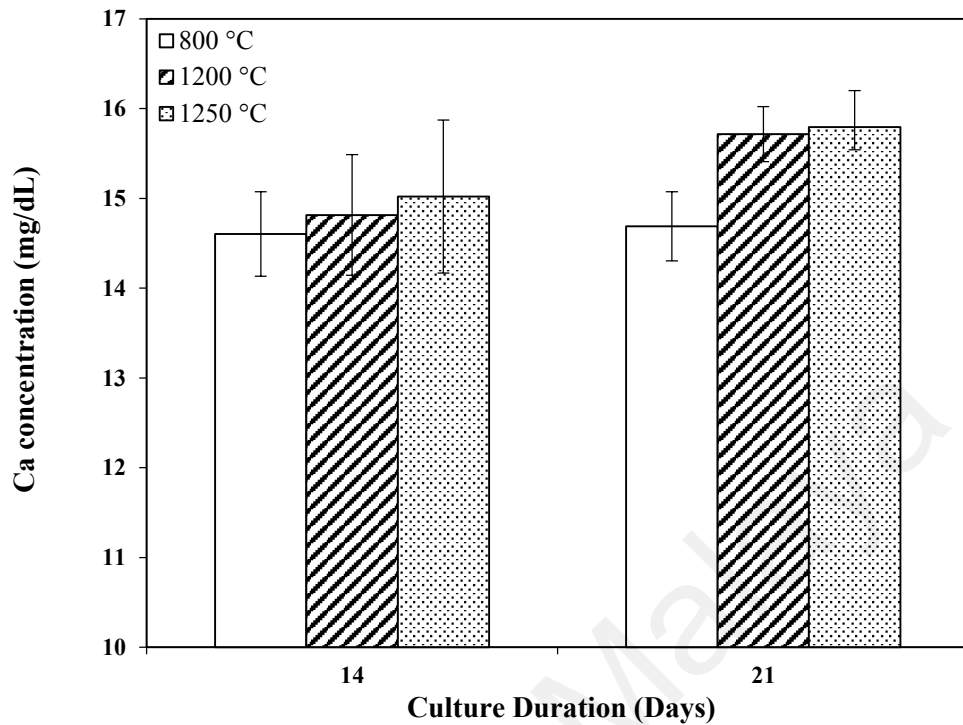


Figure 5.41: Calcium quantification detected on HA-Es samples after 14 and 21 days of culture

It can be deduced that both the mechanical properties and the efficiency of HA in cell response are grain size dependent activities (Wu et al, 2015). Smaller grain size will induce an increase in grain boundary at the surface and therefore facilitates the cells to proliferate (Roohani-Esfahani et al., 2011). In addition, the bioactivity of HA decreases with increasing sintering temperature (Kokubo et al., 2003) as the grain size normally increased with sintering temperature. Although the similar trend of increasing grain size with sintering temperature was observed in this study, however, the advantage of preserving submicron meter grain size even at a higher sintering temperature of 1250 °C might contribute to its best bioactivity result of HA-Es at this temperature, as compared to the lower sintering temperature specimens viz. HA-Es(800) and HA-Es(1200). Hence, in this study, the rate formation of biologically active bone-like apatite on its surface is a reflectance on the effect of HA grain size, regardless of the sintering

temperature. Moreover, the smoother surface topography of HA-Es(1250) (Figure 5.37 (c)) has also played its role in enhancing the proliferation rate.

Based on both in vitro dissolution study and cell culture investigations, it can be concluded that the sintered eggshell derived HA showed excellent biological performance. HA-Es(1250) was found to have the best cell responses. Besides that, the good indicators of cell response is collectively represented by the adhesion, proliferation, differentiation and mineralization processes of the HA ceramics. Moreover, the similar attributes is expected when the biomaterial is used in vivo (Matesanz et al., 2014; Bang et al., 2015). This finding has somehow complemented its overall best properties in mechanical properties evaluation (Section 5.4) as well.

University of Malaya

CHAPTER 6: CONCLUSIONS AND FUTURE WORK

6.1 Conclusion

In the present work, phase pure hydroxyapatite using waste eggshell as calcium precursor was successfully produced through solid state reaction (HA-Es). Hydroxyapatite (HA) powders were also synthesized using wet chemical synthesis route that is wet precipitation (HA-Wp) and sol-gel synthesis (HA-Sg). The sinterability of the synthesized HA powders was investigated through conventional pressureless sintering (1000-1350 °C) and microwave sintering (950-1250 °C).

The phase stability and mechanical properties of HA-Es for each sintering method were deliberated and compared to the properties of HA-Wp and HA-Sg, respectively. The in vitro biodegradation and cell culture of HA-Es using MC3T3-E1 osteoblast-like cell and rat bone marrow cells have also been studied to evaluate the biocompatibility and biological performance of the bioceramic.

The conclusions from this research are as follows:

1. Nanostructured HA was successfully produced from using waste eggshells as a direct source of calcium precursor through a simple solid state sintering method. Phase pure highly crystalline HA-Es powder was obtained after pre-heat treatment of calcined eggshell and DCPD at 800 °C with typical flower-like morphology, comprising of petal-like flakes having an average size of 100–200 nm in width. The crystallite size calculated using XRD data was found to be ~54.6 nm whereas the BET specific surface area of the HA-Es powder was 8.71 m²/g. The small surface area was expected due to the calcination employed during the powder preparation which could result in hard agglomerates of particles.

2. Both wet chemical synthesis route, namely chemical precipitation and sol-gel methods present the ability to produce single-phase nanoparticle HA powders with different morphologies and particle sizes. Upon calcination, the HA-Wp powder decomposed into β -TCP at 900 °C, whereas HA-Sg started to dissociate to the secondary phase of β -TCP at 1000 °C. However, the fraction of β -TCP phase in both powders was relatively small with maximum values of 5.30 % and 3.45 % at 1000 °C for the HA-Wp and HA-Sg powders, respectively. Both powders were believed to behave as Ca deficient apatite, which presents better bioresorbable properties than stoichiometric HA. In terms of powder morphologies and particle sizes, the HA-Wp powder presented a smaller crystallite size and a considerably higher BET surface area of 97.4 m²/g compared with that of the HA-Sg powder at 8.98 m²/g. The micrograph of the HA-Wp sample showed soft agglomerates of needle-like particles (average of ~31.2 nm), whereas hard agglomerates of globular-shaped particles (average of ~61.8 nm) were observed in the HA-Sg powder. HA powder prepared via wet-chemical synthesis with a poor crystalline structure, a smaller size of needle-like nanoparticles, as well as a large surface area, is expected to present greater reactivity than HA-Sg powder for bone substitute material because HA-Wp exhibits more similar characteristics to natural bone mineral crystals.
3. Sintering of these HA powders through conventional pressureless sintering (1000-1250 °C) revealed that the decomposition of HA-Es to α -TCP and TTCP has taken place beyond 1250 °C. There was no secondary phases detected in the HA-Wp at all sintering temperatures meanwhile HA-Sg decomposed to the secondary phase of CaO at 1300 °C.

4. For HA-Wp, the maximum relative density of 99.1 % at 1250 °C was only attained by HA-Es at 1350 °C. A lower grain growth was observed for HA-Es compared to HA-Wp at all sintering temperature due to its lower shrinkage rate which was resulted from the heat treatment process carried out on the HA-Es powder during the synthesis stage.
5. Both Vickers hardness and fracture toughness are largely governed by grain size. The average grain size of the HA-Es was below 1 μm for sintering up to 1250 °C, however sintering beyond this temperature resulted in phase decomposition along with a rapid grain growth, hence, a concomitant decreased in the Vickers hardness as well as fracture toughness. Meanwhile for HA-Wp, the hardness and fracture toughness started to decline with increasing temperature beyond 1200 °C accompanied by rapid grain growth.
6. Sintering of HA-Es at 1250 °C gave better HA properties with 97.7 % relative density, high hardness and fracture toughness of 5.62 GPa and 1.51 MPam^{1/2}, respectively while limiting its grain size to 0.95 μm. Meanwhile for HA-Wp, sintering at 1200 °C resulted in a sintered body having a relative density of 96.9 %, hardness of 3.82 GPa and fracture toughness of 1.29 MPam^{1/2} with a grain size of 1.62 μm.
7. The high toughness recorded for HA-Es of 1.51 MPam^{1/2} while retaining its phase stability at 1250 °C with submicron meter range grain size (~0.950 μm) obtained from conventional sintering was very encouraging since such high toughness is normally reported for HA sintered using sophisticated techniques such as hot pressing and spark plasma sintering.

8. Sintering of the HA powders through microwave sintering (950-1250 °C) revealed that the decomposition of HA-Es(M) to β -TCP and α -TCP has taken place beyond 1200 °C. Decomposition of HA-Wp(M) to β -TCP and α -TCP phases were detected at 1150 °C and 1200 °C, respectively.
9. The maximum HA-Es(M) relative density of 97.1 % at 1250 °C was attained by HA-Wp(M) at 1100 °C. HA-Es(M) exhibited lower densification level due to porosity on the samples surface hence lower linear shrinkage. Domination of crystalline TCP in the HA-Wp(M) at 1250 °C resulted in exaggerated grain growth from 0.85 μm to 2.58 μm .
10. The hardness and fracture toughness of the HA-Es(M) and HA-Wp(M) samples was initially influenced by the increase in relative density with sintering temperature until they reached a maximum value at a critical grain size limit (d_c) of 2.08 μm and 0.85 μm at 1200 °C and 1100 °C, respectively. Above this critical limit, grain growth acts as the controlling parameter. The properties then decreased with increasing grain size despite exhibiting high bulk density.
11. Microwave sintering of HA-Es at 1200 °C gave collective properties with 96.0 % relative density, high hardness and fracture toughness of 3.65 GPa and 1.05 MPam^{1/2}, respectively but with slight grain growth to 2.08 μm . Meanwhile for HA-Wp, sintering at 1100 °C resulted in HA with a relative density of 96.9 %, high hardness 3.82 GPa but low fracture toughness of 0.86 MPam^{1/2} while limiting its grain growth to 0.85 μm . HA-Es(M) exhibited the maximum K_{Ic} value of 1.05 MPam^{1/2} at 1200 °C while retaining its HA phase stability.

12. Conventional pressureless sintering is the worthwhile technique for producing dense calcium phosphate ceramics with a fine microstructure. Eggshell derived HA exhibited better phase stability, grain size and, improved mechanical properties (hardness and fracture toughness) via conventional sintering than microwave sintering despite the effectiveness of microwave sintering in saving time and energy.
13. With respect to the combination of the improved powder and mechanical properties, a valuable HA-Es body that has the potential for clinical implant has successfully been produced at the temperature of 1250 °C via conventional pressureless sintering.
14. Both the mechanical properties and the efficiency of HA in cell response are grain size dependent. Smaller grain size provides larger grain boundary area and therefore facilitates cells proliferation. In vitro dissolution study in phosphate buffer saline (PBS) and cell culture results confirmed that sintered eggshell derived HA exhibited good apatite-forming ability in PBS and results in good biological performance of both MC3T3-E1 osteoblast-like cell and rat bone marrow cell culture. HA-Es sintered at 1250 °C showed the best cell response and biological performance.
15. The adhesion, proliferation, differentiation and mineralization processes of the HA-Es ceramics are the good indicators of the cell response that could be expected when a biomaterial is used in vivo.

6.2 Recommendation for Future Work

Throughout the studies, there were some unexplained observations noted which necessitate further investigation. The current study has also given some ideas, which could be exploited to enhance the sinterability of eggshell derived HA, particularly its fracture toughness for clinical applications. Following are some suggestions for further work:

1. In the preparation of eggshell derived HA powder, additional study on the synthesis parameters could be carried out such as the effect of different milling duration, calcination temperature and sintering ramp rate and time on the phase stability and microstructure (morphology and size) of the prepared HA. The concentrations of Ca and P in the synthesized HA powder and the dissolution of Ca ion in PBS solution can be measured using finer measurement method of Inductively Coupled Plasma (ICP) spectroscopy. For a better understanding of the dehydroxylation phenomenon, Raman spectroscopy could be used for the intended analysis.
2. In optimization of mechanical properties of HA, the influence of other sintering additives could also be explored. For example, silicate and carbonate substitution have been reported to be beneficial on the sintering of synthesized HA particularly in increasing the specific surface areas and promoting better bioactivity of the sintered body. This tailored design of materials would be valuable to explore other potentials in eggshell derived HA as a candidate for the development of drug delivery carriers or bioprobes.
3. As mentioned in Section 5.4, the toughness value of HA-Es obtained from conventional sintering at 1250 °C is comparable with the HA sintered using

spark plasma sintering and hot pressing in other studies. Hence, it will be interesting to completely compare the mechanical properties of the present sintered HA-Es powder with that such advanced processing techniques.

4. Although phosphate buffered saline (PBS) solution was used to evaluate the biocompatibility of the HA-Es, an extension to this project such as exposure in simulated body fluid (SBF) and photoluminescence characterization should also be carried out to confirm further the degree of its biological response and gain a better understanding as well. In addition, the wettability (contact angle between liquid-vapor interface and a solid surface) test can be carried out to measure the energy density on the surface of the liquid as it is one of very important factors for HA surface.
5. In this work, although the eggshell derived HA (HA-Es) is reported to have good biocompatibility and in vitro material properties to support cell attachment, proliferation and differentiation in rat bone marrow cells, in vitro toxicity analysis and histological investigation are necessary to confirm its nature of bone regeneration.

REFERENCES

- Abdulrahman, I., Tijani, H. I., Mohammed, B. A., Saidu, H., Yusuf, H., Jibrin, M. N., & Mohammed, S. (2014). From Garbage to Biomaterials: An Overview on Egg Shell Based Hydroxyapatite. *Journal of Materials*, 2014, 1-6.
- Agrawal, D. K. (1998). Microwave processing of ceramics. *Current Opinion in Solid State and Materials Science*, 3(5), 480-485.
- Ajdukovic, Z., Ignjatovic, N., Petrovic, D., & Uskokovic, D. (2007). Substitution of osteoporotic alveolar bone by biphasic calcium phosphate/poly-DL-lactide-co-glycolide biomaterials. *Journal of biomaterials applications*, 21(3), 317-328.
- Akram, M., Ahmed, R., Shakir, I., Ibrahim, W. A. W., & Hussain, R. (2014). Extracting hydroxyapatite and its precursors from natural resources. *Journal of Materials Science*, 49(4), 1461-1475.
- Alexandra, B. & Raul, B. (2011). Border between sol-gel and wet precipitation in calcium phosphates synthesis. In E. M. Rachel (Eds.), *The Sol-Gel Process: Uniformity, Polymers and Applications* (pp. 747-756). New York: Nova Science Publishers Inc.
- Aminzare, M., Eskandari, A., Baroonian, M. H., Berenov, A., Razavi Hesabi, Z., Taheri, M., & Sadrnezhaad, S. K. (2013). Hydroxyapatite nanocomposites: Synthesis, sintering and mechanical properties. *Ceramics International*, 39(3), 2197-2206.
- Anselme, K. (2000). Osteoblast adhesion on biomaterials. *Biomaterials*, 21(7), 667-681.
- Asgary, S., Eghbal, M. J., Parirokh, M., & Ghoddusi, J. (2009). Effect of two storage solutions on surface topography of two root-end fillings. *Australian Endodontic Journal*, 35(3)
- Bahrololoom, M. E., Javidi, M., Javadpour, S., & Ma, J. (2009). Characterisation of natural hydroxyapatite extracted from bovine cortical bone ash. *J. Ceram. Process. Res*, 10, 129-138.
- Banerjee, A., Bandyopadhyay, A., & Bose, S. (2007). Hydroxyapatite nanopowders: Synthesis, densification and cell-materials interaction. *Materials Science and Engineering C*, 27(4), 729-735.

- Bang, L. T., Long, B. D., & Othman, R. (2014). Carbonate hydroxyapatite and silicon-substituted carbonate hydroxyapatite: synthesis, mechanical properties, and solubility evaluations. *The Scientific World Journal*, 2014.
- Bang, L. T., Ramesh, S., Purbolaksono, J., Ching, Y. C., Long, B. D., Chandran, H., & Othman, R. (2015). Effects of silicate and carbonate substitution on the properties of hydroxyapatite prepared by aqueous co-precipitation method. *Materials & Design*, 87, 788-796.
- Barakat, N. A. M., Khil, M. S., Omran, A. M., Sheikh, F. A., & Kim, H. Y. (2009). Extraction of pure natural hydroxyapatite from the bovine bones bio waste by three different methods. *Journal of Materials Processing Technology*, 209(7), 3408–3415.
- Barralet, J. E., Lilley, K. J., Grover, L. M., Farrar, D. F., Ansell, C., & Gbureck, U. (2004). Cements from nanocrystalline hydroxyapatite. *Journal of Materials Science: Materials in Medicine*, 15(4), 407-411.
- Ben-Nissan, B. (2004). Biomimetics and Bioceramics. *Learning from Nature How to Design New Implantable Biomaterials*, 89–103.
- Bernhardt, A., Lode, A., Peters, F., & Gelinsky, M. (2013). Comparative evaluation of different calcium phosphate-based bone graft granules—an in vitro study with osteoblast-like cells. *Clinical oral implants research*, 24(4), 441-449.
- Best, S. M., Porter, A. E., Thian, E. S., & Huang, J. (2008). Bioceramics: Past, present and for the future. *Journal of the European Ceramic Society*, 28(7), 1319–1327.
- Boanini, E., Gazzano, M., & Bigi, A. (2010). Ionic substitutions in calcium phosphates synthesized at low temperature. *Acta Biomaterialia*, 6(6), 1882–1894.
- Bose, S., Dasgupta, S., Tarafder, S., & Bandyopadhyay, A. (2010). Microwave-processed nanocrystalline hydroxyapatite: Simultaneous enhancement of mechanical and biological properties. *Acta Biomaterialia*, 6(9), 3782–3790.
- Boutinguiza, M., Pou, J., Comesana, R., Lusquinos, F., De Carlos, A., & Leon, B. (2012). Biological hydroxyapatite obtained from fish bones. *Materials Science and Engineering C*, 32(3), 478–486.
- Brendel, T., Engel, A., & Rüssel, C. (1992). Hydroxyapatite coatings by a polymeric route. *Journal of Materials Science: Materials in Medicine*, 3(3), 175-179.

- Buys, A. J., Sorrell, C. C., Brandwood, A. B. A. U. O. N. S. W., & Milthorpe, B. K. (1995). Hydroxyapatite sintering characteristics: correlation with powder morphology by high-resolution microscopy. *Journal of Materials Science Letters*, 14(10), 744-747.
- Carter, C. B., & Norton, M. G. (2007). *Ceramic materials: science and engineering*. Springer Science & Business Media.
- Champion, E. (2013). Sintering of calcium phosphate bioceramics. *Acta Biomaterialia*, 9(4), 5855–5875.
- Chanda, A., Dasgupta, S., Bose, S., & Bandyopadhyay, A. (2009). Microwave sintering of calcium phosphate ceramics. *Materials Science and Engineering C*, 29(4), 1144–1149.
- Chaudhry, H. N., Hughes, B. R., & Ghani, S. A. (2012). A review of heat pipe systems for heat recovery and renewable energy applications. *Renewable and Sustainable Energy Reviews*, 16(4), 2249-2259.
- Chona, R. (Ed.). (2002). *Fatigue and fracture mechanics: 32nd volume* (Vol. 1406). ASTM International.
- Combes, C., & Rey, C. (2002). Adsorption of proteins and calcium phosphate materials bioactivity. *Biomaterials*, 23(13), 2817–2823.
- Correia, R. N., Magalhaes, M. C. F., Marques, P. A. A. P., & Senos, A. M. R. (1996). Wet synthesis and characterization of modified hydroxyapatite powders. *Journal of Materials Science: Materials in Medicine*, 7(8), 501-505.
- Crockett, J. C., Rogers, M. J., Coxon, F. P., Hocking, L. J., & Helfrich, M. H. (2011). Bone remodelling at a glance. *Journal of Cell Science*, 124, 991–998.
- Curran, D. J., Fleming, T. J., Towler, M. R., & Hampshire, S. (2011). Mechanical parameters of strontium doped hydroxyapatite sintered using microwave and conventional methods. *Journal of the Mechanical Behavior of Biomedical Materials*, 4(8), 2063–2073.
- Das, S., Mukhopadhyay, A. K., Datta, S., & Basu, D. (2008). Prospects of microwave processing: An overview. *Bulletin of Materials Science*, 31(7), 943–956.

- Dasgupta, P., Singh, A., Adak, S., & Purohit, K. M. (2004). Synthesis and characterization of hydroxyapatite produced from eggshell. *International Symposium of Research Students on Materials Science and Engineering*, 1–6.
- Dee, K. C., Puleo, D. A., & Bizios, R. (2003). *An introduction to tissue-biomaterial interactions*. New Jersey: John Wiley & Sons.
- Deville, S., Saiz, E., & Tomsia, A. P. (2006). Freeze casting of hydroxyapatite scaffolds for bone tissue engineering. *Biomaterials*, 27(32), 5480-5489.
- Dorozhkin, S. V. (2009). Calcium orthophosphates in nature, biology and medicine. *Materials*, 2(2), 399–498
- Dorozhkin, S. V. (2010). Bioceramics of calcium orthophosphates. *Biomaterials*, 31(7), 1465–1485.
- Dorozhkin, S. V. (2010). Nanosized and nanocrystalline calcium orthophosphates. *Acta Biomaterialia*, 6(3), 715–734.
- Driessens, F. C. M., Boltong, M. G., De Maeyer, E. A. P., Wenz, R., Nies, B., & Planell, J. A. (2002). The Ca/P range of nanoapatitic calcium phosphate cements. *Biomaterials*, 23(19), 4011–4017.
- Ebrahimi-Kahrizsangi, R., Nasiri-Tabrizi, B., & Chami, A. (2010). Synthesis and characterization of fluorapatite-titania (FAp-TiO₂) nanocomposite via mechanochemical process. *Solid State Sciences*, 12(9), 1645–1651.
- Ergun, C., Evis, Z., Webster, T. J., & Sahin, F. C. (2011). Synthesis and microstructural characterization of nano-size calcium phosphates with different stoichiometry. *Ceramics International*, 37(3), 971–977.
- Eshtiagh-Hosseini, H., Housaindokht, M. R., & Chahkandi, M. (2007). Effects of parameters of sol–gel process on the phase evolution of sol–gel-derived hydroxyapatite. *Materials Chemistry and Physics*, 106(2), 310-316.
- Evis, Z., & Webster, T. J. (2011). Nanosize hydroxyapatite: doping with various ions. *Advances in Applied Ceramics*, 110(5), 311–321.
- Fang, Z. Z., & Wang, H. (2008). Densification and grain growth during sintering of nanosized particles. *International Materials Reviews*, 53(6), 326-352.

- Fanovich, M. A., & Porto-Lopez J. M. (1998). Influence of temperature and additives on the microstructure and sintering behaviour of hydroxyapatites with different Ca/P ratios. *Journal of Materials Science: Materials in Medicine*, 9(1), 53-60.
- Fathi, M. H., Hanifi, A., & Mortazavi, V. (2008). Preparation and bioactivity evaluation of bone-like hydroxyapatite nanopowder. *Journal of Materials Processing Technology*, 202(1-3), 536–542.
- Feng, W., Mu-Sen, L., Yu-Peng, L., & Yong-Xin, Q. (2005). A simple sol-gel technique for preparing hydroxyapatite nanopowders. *Materials Letters*, 59(8-9), 916–919.
- Ferkel, H., & Hellmig, R. J. (1999). Effect of nanopowder deagglomeration on the densities of nanocrystalline ceramic green bodies and their sintering behaviour. *Nanostructured Materials*, 11(5), 617-622.
- Fujishiro, Y., Yabuki, H., & Kawamura, K. (1993). Preparation of needle-like hydroxyapatite by homogeneous precipitation under hydrothermal conditions. *Journal of Chemical Technology and Biotechnology*, 57(4), 349–53.
- Fulmer, M. T., Ison, I. C., Hankermayer, C. R., Constantz, B. R., & Ross, J. (2002). Measurements of the solubilities and dissolution rates of several hydroxyapatites. *Biomaterials*, 23(3), 751–755.
- Gergely, G., Weber, F., Lukacs, I., Illes, L., Toth, A. L., Horvath, Z. E., ... Balazsi, C. (2010). Nano-hydroxyapatite preparation from biogenic raw materials. *Central European Journal of Chemistry*, 8(2), 375–381.
- Gibson, I. R., Best, S. M., & Bonfield, W. (2002). Effect of silicon substitution on the sintering and microstructure of hydroxyapatite. *Journal of the American Ceramic Society*, 85(11), 2771-2777.
- Gibson, I. R., Ke, S., Best, S. M., & Bonfield, W. (2001). Effect of powder characteristics on the sinterability of hydroxyapatite powders. *Journal of Materials Science: Materials in Medicine*, 12, 163–171.
- Gibson, I. R., Rehman, I., Best, S. M., & Bonfield, W. (2000). Characterization of the transformation from calcium-deficient apatite to β -tricalcium phosphate. *Journal of Materials Science: Materials in Medicine*, 11(12), 799-804.

- Goller, G., Oktar, F. N., Agathopoulos, S., Tulyaganov, D. U., Ferreira, J. M. F., Kayali, E. S., & Peker, I. (2006). Effect of sintering temperature on mechanical and microstructural properties of bovine hydroxyapatite (BHA). *Journal of Sol-Gel Science and Technology*, 37(2), 111–115.
- Goloshchapov, D. L., Kashkarov, V. M., Rumyantseva, N. A., Seredin, P. V., Lenshin, A. S., Agapov, B. L., & Domashevskaya, E. P. (2013). Synthesis of nanocrystalline hydroxyapatite by precipitation using hen's eggshell. *Ceramics International*, 39(4), 4539–4549.
- Gross, K. A., & Rodríguez-Lorenzo, L. M. (2004). Sintered hydroxyfluorapatites. Part I: Sintering ability of precipitated solid solution powders. *Biomaterials*, 25(7-8), 1375–1384.
- Grossin, D., Rollin-Martinet, S., Estournès, C., Rossignol, F., Champion, E., Combes, C., ... & Drouet, C. (2010). Biomimetic apatite sintered at very low temperature by spark plasma sintering: physico-chemistry and microstructure aspects. *Acta Biomaterialia*, 6(2), 577-585.
- Gu, Y. W., Khor, K. A., & Cheang, P. (2004). Bone-like apatite layer formation on hydroxyapatite prepared by spark plasma sintering (SPS). *Biomaterials*, 25(18), 4127-4134.
- Gu, Y. W., Loh, N. H., Khor, K. A., Tor, S. B., & Cheang, P. (2002). Spark plasma sintering of hydroxyapatite powders. *Biomaterials*, 23(1), 37-43.
- Guo, X., Yan, H., Zhao, S., Li, Z., Li, Y., & Liang, X. (2013). Effect of calcining temperature on particle size of hydroxyapatite synthesized by solid-state reaction at room temperature. *Advanced Powder Technology*, 24(6), 1034–1038.
- Habib, F., Alam, S., Zahra, N., Irfan, M., & Iqbal, W. (2012). Synthesis route and characterization of hydroxyapatite powder prepared from waste egg shells. *Journal of the Chemical Society of Pakistan*, 34(3).
- Haddow, D. B., James, P. F., & Van Noort, R. (1996). Characterization of sol-gel surfaces for biomedical applications. *Journal of Materials Science: Materials in Medicine*, 7(5), 255-260.
- Han, Y., Xu, K., Montay, G., Fu, T., & Lu, J. (2002). Evaluation of nanostructured carbonated hydroxyapatite coatings formed by a hybrid process of plasma spraying and hydrothermal synthesis. *Journal of biomedical materials research*, 60(4), 511-516.

- Harabi, A., Belamri, D., Karboua, N., & Mezahi, F. Z. (2011). Sintering of bioceramics using a modified domestic microwave oven : Natural hydroxyapatite sintering. *Journal of Thermal Analysis and Calorimetry*, 104(1), 383–388.
- He, H., Bleby, T. M., Veneklaas, E. J., Lambers, H., & Kuo, J. (2012). Precipitation of calcium, magnesium, strontium and barium in tissues of four Acacia species (leguminosae: Mimosoideae). *PLoS ONE*, 7(7), 1–12.
- Hench, L. L. (1991). Bioceramics: From Concept to Clinic. *Journal of the American Ceramic Society*, 74(7), 1487–1510.
- Hench, L. L. (1998). Biomaterials: A forecast for the future. *Biomaterials*, 19(16), 1419–1423.
- Hench, L. L. (2000). (ii) The challenge of orthopaedic materials. *Current orthopaedics*, 14(1), 7-15.
- Hench, L. L., & Thompson, I. (2010). Twenty-first century challenges for biomaterials. *Journal of the Royal Society Interface*, 7(Suppl 4), S379-S391.
- Hing, K. A., Best, S. M., & Bonfield, W. (1999). Characterization of porous hydroxyapatite. *Journal of Materials Science: Materials in Medicine*, 10(3), 135-145.
- Ho, W. F., Hsu, H. C., Hsu, S. K., Hung, C. W., & Wu, S. C. (2013). Calcium phosphate bioceramics synthesized from eggshell powders through a solid state reaction. *Ceramics International*, 39(6), 6467–6473.
- Hoepfner, T. P., & Case, E. D. (2003). The influence of the microstructure on the hardness of sintered hydroxyapatite. *Ceramics International*, 29(6), 699-706.
- Hong, Y., Fan, H., Li, B., Guo, B., Liu, M., & Zhang, X. (2010). Fabrication, biological effects, and medical applications of calcium phosphate nanoceramics. *Materials Science and Engineering R: Reports*, 70(3-6), 225–242.
- Hsieh, M. F., Perng, L. H., Chin, T. S., & Perng, H. G. (2001). Phase purity of sol-gel derived hydroxyapatite ceramic. *Biomaterials*, 22, 2601 – 2607.
- Huang, Y. C., Hsiao, P. C., & Chai, H. J. (2011). Hydroxyapatite extracted from fish scale: Effects on MG63 osteoblast-like cells. *Ceramics International*, 37(6), 1825–1831.

- Huber, F. X., Belyaev, O., Hillmeier, J., Kock, H. J., Huber, C., Meeder, P. J., & Berger, I. (2006). First histological observations on the incorporation of a novel nanocrystalline hydroxyapatite paste OSTIM® in human cancellous bone. *BMC Musculoskeletal Disorders*, 7(1), 1.
- Ignatius, A. A., Betz, O., Augat, P., & Claes, L. E. (2001). In vivo investigations on composites made of resorbable ceramics and poly (lactide) used as bone graft substitutes. *Journal of Biomedical Materials Research*, 58(6), 701-709.
- Ishikawa, K., Matsuya, S., Miyamoto, Y., & Kawate, K. (2003). 9.05-Bioceramics. *Comprehensive Structural Integrity*, Pergamon, Oxford, 169-214.
- Janackovic, D., Petrovic-Prelevic, I., Kostic-Gvozdenovic, L., Petrovic, R., Jokanovic, V., & Uskokovic, D. P. (2001). Influence of Synthesis Parameters on the Particle Sizes of Nanostructured Calcium-Hydroxyapatite. In *Key Engineering Materials* (Vol. 192, pp. 203-206). Trans Tech Publications.
- Jaramillo, C. D., Rivera, J. A., Echavarría, A., O'byrne, J., Congote, D., & Restrepo, L. F. (2010). Osteoconductive and osseointegration properties of a commercial hydroxyapatite compared to a synthetic product. *Revista Colombiana de Ciencias Pecuarías*, 23(4), 471-483.
- Jarcho, M, O'Connor, J. R., & Paris, D. A. (1977). Ceramic hydroxylapatite as a plaque growth and drug screening substrate. *Journal of Dental Research*, 56(2), 151-156.
- Jillavenkatesa, A., Hoelzer, D. T., & Condrate Sr, R. A. (1999). An electron microscopy study of the formation of hydroxyapatite through sol-gel processing. *Journal of Materials Science*, 34(19), 4821-4830.
- Juang, H. Y., & Hon, M. H. (1996). Effect of calcination on sintering of hydroxyapatite. *Biomaterials*, 17(21), 2059–2064.
- Juhasz, J. A., & Best, S. M. (2012). Bioactive ceramics: Processing, structures and properties. *Journal of Materials Science*, 47(2), 610–624.
- Kalita, S. J., & Verma, S. (2010). Nanocrystalline hydroxyapatite bioceramic using microwave radiation: Synthesis and characterization. *Materials Science and Engineering C*, 30(2), 295–303.
- Kalita, S. J., Bhardwaj, A. & Bhatt, H. A. (2007). Nanocrystalline calcium phosphate ceramics in biomedical engineering, *Materials Science and Engineering C*, 27, 441–449.

- Kamalanathan, P., Ramesh, S., Bang, L. T., Niakan, A., Tan, C. Y., Purbolaksono, J., ... Teng, W. D. (2014). Synthesis and sintering of hydroxyapatite derived from eggshells as a calcium precursor. *Ceramics International*, 40(PB), 16349–16359.
- Kang, S. J. L. (2004). *Sintering: densification, grain growth and microstructure*. Butterworth-Heinemann.
- Khalid, M., Mujahid, M., Amin, S., Rawat, R. S., Nusair, A., & Deen, G. R. (2013). Effect of surfactant and heat treatment on morphology, surface area and crystallinity in hydroxyapatite nanocrystals. *Ceramics International*, 39, 39–50.
- Khalil, K. A. (2012). *Advanced sintering of nano-ceramic materials*. INTECH Open Access Publisher.
- Khalil, K. A., Kim, S. W., Dharmaraj, N., Kim, K. W., & Kim, H. Y. (2007). Novel mechanism to improve toughness of the hydroxyapatite bioceramics using high-frequency induction heat sintering. *Journal of materials processing technology*, 187, 417-420.
- Kim, B. S., & Mooney, D. J. (1998). Development of biocompatible synthetic extracellular matrices for tissue engineering. *Trends in Biotechnology*, 16(5), 224-230.
- Kim, B. S., Baez, C. E., & Atala, A. (2000). Biomaterials for tissue engineering. *World Journal of Urology*, 18(1), 2-9.
- Kim, B. S., Yang, S. S., & Lee, J. (2014). A polycaprolactone/cuttlefish bone-derived hydroxyapatite composite porous scaffold for bone tissue engineering. *Journal of Biomedical Materials Research - Part B Applied Biomaterials*, 102(5), 943–951.
- Kim, H. M., Himeno, T., Kokubo, T., & Nakamura, T. (2005). Process and kinetics of bonelike apatite formation on sintered hydroxyapatite in a simulated body fluid. *Biomaterials*, 26(21), 4366–4373.
- Kim, H. W., Georgiou, G., Knowles, J. C., Koh, Y. H., & Kim, H. E. (2004). Calcium phosphates and glass composite coatings on zirconia for enhanced biocompatibility. *Biomaterials*, 25(18), 4203–4213.
- Kim, J., Lim, D., Kim, Y. H., Young-Hag, K., Lee, M. H., Han, I., ... & Park, J. C. (2011). A comparative study of the physical and mechanical properties of porous hydroxyapatite scaffolds fabricated by solid freeform fabrication and polymer

replication method. *International Journal of Precision Engineering and Manufacturing*, 12(4), 695-701.

Kokubo, T., & Takadama, H. (2006). How useful is SBF in predicting in vivo bone bioactivity? *Biomaterials*, 27(15), 2907–2915.

Kokubo, T., Kim, H. M., & Kawashita, M. (2003). Novel bioactive materials with different mechanical properties. *Biomaterials*, 24(13), 2161–2175

Kothapalli, C., Wei, M., Vasiliev, A., & Shaw, M. T. (2004). Influence of temperature and concentration on the sintering behavior and mechanical properties of hydroxyapatite. *Acta Materialia*, 52(19), 5655–5663.

Koutsopoulos, S. (2002). Synthesis and characterization of hydroxyapatite crystals: A review study on the analytical methods. *Journal of Biomedical Material Research*, 62, 600-612.

Krishna, D. S. R., Siddharthan, A., Seshadri, S. K., & Kumar, T. S. (2007). A novel route for synthesis of nanocrystalline hydroxyapatite from eggshell waste. *Journal of Materials Science: Materials in Medicine*, 18(9), 1735-1743.

Kruzic, J. J., Kim, D. K., Koester, K. J., & Ritchie, R. O. (2009). Indentation techniques for evaluating the fracture toughness of biomaterials and hard tissues. *Journal of the Mechanical Behavior of Biomedical Materials*, 2(4), 384-395.

Kumar, G. S., & Girija, E. K. (2013). Flower-like hydroxyapatite nanostructure obtained from eggshell: A candidate for biomedical applications. *Ceramics International*, 39(7), 8293–8299.

Kumar, G. S., Thamizhavel, A., & Girija, E. K. (2012). Microwave conversion of eggshells into flower-like hydroxyapatite nanostructure for biomedical applications. *Materials Letters*, 76, 198–200.

Kuriakose, T. A., Kalkura, S. N., Palanichamy, M., Arivuoli, D., Dierks, K., Bocelli, G., & Betzel, C. (2004). Synthesis of stoichiometric nano crystalline hydroxyapatite by ethanol-based sol–gel technique at low temperature. *Journal of Crystal Growth*, 263(1), 517-523.

Kusmanto, F., Walker, G., Gan, Q., Walsh, P., Buchanan, F., Dickson, G., ... Dring, M. (2008). Development of composite tissue scaffolds containing naturally sourced microporous hydroxyapatite. *Chemical Engineering Journal*, 139(2), 398–407.

- Kweh, S. W. K., Khor, K. A., & Cheang, P. (1999). Production and characterization of hydroxyapatite (HA) powders. *Journal of Materials Processing Technology*, 89-90, 373–377.
- Landi, E., Celotti, G., Logroscino, G., & Tampieri, A. (2003). Carbonated hydroxyapatite as bone substitute. *Journal of the European Ceramic Society*, 23(15), 2931-2937.
- Landi, E., Logroscino, G., Proietti, L., Tampieri, A., Sandri, M., & Sprio, S. (2008). Biomimetic Mg substituted hydroxyapatite: from synthesis to in vivo behavior. *Journal of Materials Science: Materials in Medicine*, 19, 239–247
- Landi, E., Tampieri, A., Celotti, G., & Sprio, S. (2000). Densification behaviour and mechanisms of synthetic hydroxyapatites. *Journal of the European Ceramic Society*, 20(14-15), 2377–2387.
- Landi, E., Uggeri, J., Sprio, S., Tampieri, A., & Guizzardi, S. (2010). Human osteoblast behavior on as-synthesized SiO₄ and B-CO₃ co-substituted apatite. *Journal of Biomedical Materials Research Part A*, 94(1), 59-70.
- Lau, M., Lau, K., Ku, H., Bahattacharyya, D., & Yao, Y. (2012). Measurements of Heat Treatment Effects on Bovine Cortical Bones by Nanoindentation and Compression Testing. *Journal of Biomaterials and Nanobiotechnology*, 03(01), 105–113.
- Layrolle, P., Ito, A., & Tateishi, T. (1998). Sol-Gel Synthesis of Amorphous Calcium Phosphate and Sintering into Microporous Hydroxyapatite Bioceramics. *Journal of the American Ceramic Society*, 81(6), 1421-1428.
- Lee, S. J., & Oh, S. H. (2003). Fabrication of calcium phosphate bioceramics by using eggshell and phosphoric acid. *Materials Letters*, 57(29), 4570–4574.
- LeGeros, R. Z. (1990). Calcium phosphates in oral biology and medicine. *Monographs in oral science*, 15, 1-201.
- LeGeros, R. Z., & LeGeros, J. P. (1993). Dense hydroxyapatite. *Advanced series in ceramics*, 1, 139-180.
- Li, B., Chen, X., Guo, B., Wang, X., Fan, H., & Zhang, X. (2009). Fabrication and cellular biocompatibility of porous carbonated biphasic calcium phosphate ceramics with a nanostructure. *Acta Biomaterialia*, 5(1), 134–143.

- Li, S., Izui, H., & Okano, M. (2008). Densification, microstructure, and behavior of hydroxyapatite ceramics sintered by using spark plasma sintering. *Journal of Engineering Materials and Technology*, 130(3), 0310121-0310127.
- Li, S. T., Park, J. B., & Bronzino, J. D. (2003). Biomaterials: Principles and Applications. Eds. JB Park, JOS Bronzino.—Boca Raton (Florida, USA): SRC Press LLC, 115-139.
- Li, X., An, Y. H., Wu, Y. D., Song, Y. C., Chao, Y. J., & Chien, C. H. (2007). Microindentation test for assessing the mechanical properties of cartilaginous tissues. *Journal of Biomedical Materials Research Part B: Applied Biomaterials*, 80(1), 25-31.
- Liu, C., Xia, Z., & Czernuszka, J. T. (2007). Design and development of three dimensional scaffolds for tissue engineering. *Chemical Engineering Research and Design*, 85, 1051-1064.
- Liu, D., Yang, Q., Troczynski, T., & Tseng, W. J. (2002). Structural evolution of sol-gel derived hydroxyapatite. *Biomaterials*, 23, 1679–1687.
- Liu, H., & Webster, T. J. (2007). Bioinspired nanocomposites for orthopedic applications. *Nanotechnology for the Regeneration of Hard and Soft Tissues*, 8.
- Liu, Y., & Shen, Z. (2012). Dehydroxylation of hydroxyapatite in dense bulk ceramics sintered by spark plasma sintering. *Journal of the European Ceramic Society*, 32(11), 2691-2696.
- Lu, X., Wang, Y. bo, Wang, J. xin, Qu, S. xin, Weng, J., Xin, R. long, & Leng, Y. (2006). Calcium phosphate crystal growth under controlled environment through urea hydrolysis. *Journal of Crystal Growth*, 297(2), 396–402.
- Lukic, M. J., Skapin, S. D., Markovic, S., & Uskokovic, D. (2012). Processing route to fully dense nanostructured HAp bioceramics: From powder synthesis to sintering. *Journal of the American Ceramic Society*, 95(11), 3394–3402.
- Martinez-Castanon, G. A., Loyola-Rodriguez, J. P., Zavala-Alonso, N. V., Hernandez-Martinez, S. E., Nino-Martinez, N., Ortega-Zarzosa, G., & Ruiz, F. (2012). Preparation and characterization of nanostructured powders of hydroxyapatite. *Superficies Y Vacio*, 25(2), 101–105.

- Mazaheri, M., Haghhighatzadeh, M., Zahedi, A. M., & Sadrnezhad, S. K. (2009). Effect of a novel sintering process on mechanical properties of hydroxyapatite ceramics. *Journal of Alloys and Compounds*, 471(1-2), 180–184.
- Milovac, D., Gallego-Ferrer, G., Ivankovic, M., & Ivankovic, H. (2014). PCL-coated hydroxyapatite scaffold derived from cuttlefish bone: In vitro cell culture studies. *Materials Science and Engineering C*, 42, 264–272.
- Mir, M., Siddiqi, S. A., Hussain, T., Chaudhry, A. A., Rehman, I. U., Khan, A. S., & Abbas, G. (2014). Synthesis and characterization of calcium deficient apatite granules for drug eluting bone graft applications. *Ceramics International*, 40(7), 10719-10725.
- Mondal, S., Mahata, S., Kundu, S., & Mondal, B. (2010). Processing of natural resourced hydroxyapatite ceramics from fish scale. *Advances in Applied Ceramics*, 109(4), 234.
- Monmaturapoj, N. (2008). Nano-size Hydroxyapatite Powders Preparation by Wet-Chemical Precipitation Route Particle sizes and density were analyzed by. *Journal of Materials, Materials and Minerals*, 18(1), 15–20.
- Morrissey, R., Rodriguez-Lorenzo, L. M., & Gross, K. A. (2005). Influence of ferrous iron incorporation on the structure of hydroxyapatite. *Journal of Materials Science: Materials in Medicine*, 16, 387–392.
- Mostafa, N. Y. (2005). Characterization, thermal stability and sintering of hydroxyapatite powders prepared by different routes. *Materials Chemistry and Physics*, 94(2-3), 333–341.
- Muralithran, G., & Ramesh, S. (2000). The effects of sintering temperature on the properties of hydroxyapatite. *Ceramics International*, 26, 221–230.
- Nakamura, T., Imai, Y., Matsumoto, T., Sato, S., Takeuchi, K., Igarashi, K., ... & Nishina, H. (2007). Estrogen prevents bone loss via estrogen receptor α and induction of Fas ligand in osteoclasts. *Cell*, 130(5), 811-823.
- Nakano, T., Umakoshi, Y., & Tokumura, A. (2002). Variation in crystallinity of hydroxyapatite and the related calcium phosphates by mechanical grinding and subsequent heat treatment. *Metallurgical and Materials Transactions A*, 33(3), 521-528.

- Nayak, A. K. (2010). Hydroxyapatite synthesis methodologies: An overview. *International Journal of ChemTech Research*, 2(2), 903–907.
- Ng, S., Guo, J., Ma, J., & Loo, S. C. J. (2010). Synthesis of high surface area mesostructured calcium phosphate particles. *Acta Biomaterialia*, 6(9), 3772–3781.
- Niihara, K., Morena, R., & Hasselman, D. P. H. (1982). Evaluation of K_{Ic} of brittle solids by the indentation method with low crack-to-indent ratios. *Journal of Materials Science Letters*, 1(1), 13-16.
- Orlovskii, V. P., Komlev, V. S., & Barinov, S. M. (2002). Hydroxyapatite and hydroxyapatite-based ceramics. *Inorganic Materials*, 38(10), 973–984.
- Ozawa, M., & Suzuki, S. (2002). Microstructural Development of Natural Hydroxyapatite Originated from Fish-Bone Waste through Heat Treatment. *Journal of the American Ceramic Society*, 17(188335), 2000–2002.
- Palin, E., Liu, H., & Webster, T. J. (2005). Mimicking the nanofeatures of bone increases bone-forming cell adhesion and proliferation. *Nanotechnology*, 16(9), 1828.
- Pan, H., Zhao, X., Darvell, B. W., & Lu, W. W. (2010). Apatite-formation ability - Predictor of “bioactivity”? *Acta Biomaterialia*, 6(11), 4181–4188.
- Park, J., & Lakes, R. S. (2007). *Biomaterials: an introduction*. Springer Science & Business Media.
- Patel, N., Gibson, I. R., Ke, S., Best, S. M., & Bonfield, W. (2001). Calcining influence on the powder properties of hydroxyapatite. *Journal of Materials Science: Materials in Medicine*, 12(2), 181–188.
- Pattanayak, D. K., Dash, R., Prasad, R. C., Rao, B. T., & Rama Mohan, T. R. (2007). Synthesis and sintered properties evaluation of calcium phosphate ceramics. *Materials Science and Engineering C*, 27(4), 684–690.
- Pattanayak, D. K., Divya, P., Upadhyay, S., Prasad, R. C., Rao, B. T., & Mohan, T. R. (2005). Synthesis and evaluation of hydroxyapatite ceramics. *Trends of Biomaterials and Artificial Organs*, 18, 87-92.

- Pattanayak, D. K., Rao, B. T., & Mohan, T. R. R. (2011). Calcium phosphate bioceramics and bioceramic composites. *Journal of Sol-Gel Science and Technology*, 59(3), 432–447.
- Paul, W., & Sharma, C. P. (2006). Nanoceramic matrices: biomedical applications. *American Journal of Biochemistry and Biotechnology*, 2(2), 41-48.
- Paz, A., Guadarrama, D., López, M., González, J. E., Brizuela, N., & Aragón, J. (2012). A Comparative Study of Hydroxyapatite Nanoparticles Synthesized By Different Routes. *Quim. Nova*, 35(9), 1724–1727.
- Piccirillo, C., Pintado, M. M., & Castro, P. M. (2013). Hydroxyapatite and calcium phosphates from marine sources: extraction and characterization. *Marine Biomaterials (Characterization, Isolation and Applications)*, 29-44.
- Piccirillo, C., Silva, M. F., Pullar, R. C., Braga Da Cruz, I., Jorge, R., Pintado, M. M. E., & Castro, P. M. L. (2013). Extraction and characterisation of apatite- and tricalcium phosphate-based materials from cod fish bones. *Materials Science and Engineering C*, 33(1), 103–110.
- Pietak, A. M., Reid, J. W., Stott, M. J., & Sayer, M. (2007). Silicon substitution in the calcium phosphate bioceramics. *Biomaterials*, 28(28), 4023-4032.
- Prabakaran, K., Balamurugan, A., & Rajeswari, S. (2005). Development of calcium phosphate based apatite from hen's eggshell. *Bulletin of Materials Science*, 28(2), 115–119.
- Pramanik, S., Agarwal, A. K., Rai, K. N., & Garg, A. (2007). Development of high strength hydroxyapatite by solid-state-sintering process. *Ceramics International*, 33(3), 419–426.
- Prokopiev, O., & Sevostianov, I. (2006). Dependence of the mechanical properties of sintered hydroxyapatite on the sintering temperature. *Materials Science and Engineering A*, 431(1-2), 218–227.
- Ramay, H. R., & Zhang, M. (2003). Preparation of porous hydroxyapatite scaffolds by combination of the gel-casting and polymer sponge methods. *Biomaterials*, 24(19), 3293-3302.
- Ramesh, S. (2001). Grain Size-Properties Correlation in Polycrystalline Hydroxyapatite Bioceramic, *Malaysia Journal of Chemistry*, 3(1), 35-40.

- Ramesh, S. (2004). A method for manufacturing hydroxyapatite bioceramic. *Malaysia Patent*.
- Ramesh, S., Aw, K. L., Tolouei, R., Amiriyani, M., Tan, C. Y., Hamdi, M., ... Teng, W. D. (2013). Sintering properties of hydroxyapatite powders prepared using different methods. *Ceramics International*, 39(1), 111–119.
- Ramesh, S., Natasha, A. N., Tan, C. Y., Bang, L. T., Niakan, A., & Purbolaksono, J. (2015). Characteristics and properties of hydroxyapatite derived by sol – gel and wet chemical precipitation methods. *Ceramics International*, 41(9), 10434–10441.
- Ramesh, S., Tan, C. Y., Bhaduri, S. B., & Teng, W. D. (2007a). Rapid densification of nanocrystalline hydroxyapatite for biomedical applications. *Ceramics International*, 33(7), 1363–1367.
- Ramesh, S., Tan, C. Y., Bhaduri, S. B., Teng, W. D., & Sopyan, I. (2008). Densification behaviour of nanocrystalline hydroxyapatite bioceramics. *Journal of Materials Processing Technology*, 206(1-3), 221–230.
- Ramesh, S., Tan, C. Y., Sopyan, I., Hamdi, M., & Teng, W. D. (2007b). Consolidation of nanocrystalline hydroxyapatite powder. *Science and Technology of Advanced Materials*, 8(1-2), 124–130.
- Ramesh, S., Tolouei, R., Hamdi, M., Purbolaksono, J., Y Tan, C., Amiriyani, M., & D Teng, W. (2011). Sintering Behavior of Nanocrystalline Hydroxyapatite Produced by Wet Chemical Method. *Current Nanoscience*, 7(6), 845–849.
- Rao, R. R., Roopa, H. N., & Kannan, T. S. (1997). Solid state synthesis and thermal stability of HAP and HAP- β -TCP composite ceramic powders. *Journal of Materials Science: Materials in Medicine*, 8(8), 511-518.
- Rapacz-Kmita, A., Paluszkiwicz, C., Slosarczyk, A., & Paszkiewicz, Z. (2005). FTIR and XRD investigations on the thermal stability of hydroxyapatite during hot pressing and pressureless sintering processes. *Journal of Molecular Structure*, 744-747(SPEC. ISS.), 653–656.
- Ratner, B. D., Hoffman, A. S., Schoen, F. J., & Lemons, J. E. (2004). *Biomaterials science: an introduction to materials in medicine*. United States: Academic Press.
- Raynaud, S., Champion, E., Bernache-Assollant, D., & Thomas, P. (2002). Calcium phosphate apatites with variable Ca/P atomic ratio I. Synthesis, characterisation and thermal stability of powders. *Biomaterials*, 23(4), 1065–1072.

- Rhee, S. H. (2002). Synthesis of hydroxyapatite via mechanochemical treatment. *Biomaterials*, 23(4), 1147–1152.
- Rodriguez-Lorenzo, L. M., Vallet-Regi, M., & Ferreira, J. M. F. (2001). Fabrication of hydroxyapatite bodies by uniaxial pressing from a precipitated powder. *Biomaterials*, 22(6), 583–588.
- Ruksudjarit, A., Pengpat, K., Rujijanagul, G., & Tunkasiri, T. (2008). Synthesis and characterization of nanocrystalline hydroxyapatite from natural bovine bone. *Current Applied Physics*, 8(3-4), 270–272.
- Ruppel, M. E., Miller, L. M., & Burr, D. B. (2008). The effect of the microscopic and nanoscale structure on bone fragility. *Osteoporosis International*, 19(9), 1251–1265.
- Ryu, H. S., Youn, H. J., Hong, K. S., Chang, B. S., Lee, C. K., & Chung, S. S. (2002). An improvement in sintering property of β -tricalcium phosphate by addition of calcium pyrophosphate. *Biomaterials*, 23(3), 909–914.
- Sadat-Shojai, M., Khorasani, M. T., Dinpanah-Khoshdargi, E., & Jamshidi, A. (2013). Synthesis methods for nanosized hydroxyapatite with diverse structures. *Acta Biomaterialia*, 9(8), 7591–7621.
- Saeri, M. R., Afshar, A., Ghorbani, M., Ehsani, N., & Sorrell, C. C. (2003). The wet precipitation process of hydroxyapatite. *Materials Letters*, 57(24-25), 4064–4069.
- Sahiner, N., Silan, C., Sagbas, S., Ilgin, P., Butun, S., Erdugan, H., & Ayyala, R. S. (2012). Porous and modified HA particles as potential drug delivery systems. *Microporous Mesoporous Materials*, 155(1), 124–130.
- Sahu, S., Mehra, D., & Agarwal, R. (2012). Characterization and Thermal Analysis of Hydroxyapatite Bioceramic Powder Synthesized by Sol-Gel Technique. *International Journal of Applied Science and Technology*, 3(2), 281–289.
- Salimi, M. N., Bridson, R. H., Grover, L. M., & Leeke, G. A. (2012). Effect of processing conditions on the formation of hydroxyapatite nanoparticles. *Powder Technology*, 218, 109–118.
- Sanosh, K. P., Chu, M. C., Balakrishnan, A., Kim, T. N., & Cho, S. J. (2010). Sol-gel synthesis of pure nano sized β -tricalcium phosphate crystalline powders. *Current Applied Physics*, 10(1), 68–71.

- Sanosh, K. P., Chu, M. C., Balakrishnan, A., Kim, T. N., & Cho, S. J. (2010). Pressureless sintering of nanocrystalline hydroxyapatite at different temperatures. *Metals and Materials International*, 16(4), 605-611.
- Santos, M. H., Oliveira, M. De, Souza, L. P. D. F., Mansur, H. S., & Vasconcelos, W. L. (2004). Synthesis control and characterization of hydroxyapatite prepared by wet precipitation process. *Materials Research*, 7(4), 625-630.
- Sarig, S., & Kahana, F. (2002). Rapid Formation of Nanocrystalline Apatite. *Journal of Crystal Growth*, 237-23(1), 55-59.
- Seema, K., Uma, B., & Suchita, K. (2012). Transformations in sol-gel synthesized nanoscale hydroxyapatite calcined under different temperatures and time conditions. *Journal of Materials Engineering and Performance*, 21(8), 1737-1743.
- Seghi, R. R., Denry, I. L., & Rosenstiel, S. F. (1995). Relative fracture toughness and hardness of new dental ceramics. *The Journal of Prosthetic Dentistry*, 74(2), 145-150.
- Shaltout, A. A., Allam, M. A., & Moharram, M. A. (2011). FTIR spectroscopic, thermal and XRD characterization of hydroxyapatite from new natural sources. *Spectrochimica Acta - Part A: Molecular and Biomolecular Spectroscopy*, 83(1), 56-60.
- Siddharthan, A., Kumar, T. S. S., & Seshadri, S. K. (2009). Synthesis and characterization of nanocrystalline apatites from eggshells at different Ca/P ratios. *Biomedical Materials (Bristol, England)*, 4(4), 045010-045018.
- Silva, C. C., Pinheiro, A. G., Miranda, M. A. R., Góes, J. C., & Sombra, A. S. B. (2003). Structural properties of hydroxyapatite obtained by mechanosynthesis. *Solid State Sciences*, 5(4), 553-558.
- Sinha, A., Ingle, A., Munim, K. R., Vaidya, S. N., Sharma, B. P., & Bhisey, A. N. (2001). Development of calcium phosphate based bioceramics. *Bulletin of Materials Science*, 24(6), 653-657.
- Slosarczyk, A., & Bialoskorski, J. (1998). Hardness and fracture toughness of dense calcium-phosphate-based materials. *Journal of Materials Science: Materials in Medicine*, 9, 103-108.

- Slosarczyk, A., & Piekarczyk, J. (1999). Ceramic materials on the basis of hydroxyapatite and tricalcium phosphate. *Ceramics International*, 25(6), 561–565.
- Slosarczyk, A., Stobierska, E., Paszkiewicz, Z., & Gawlicki, M. (1996). Calcium phosphate materials prepared from precipitates with various calcium:phosphorus molar ratios. *Journal of American Ceramic Society*, 79, 2539–44.
- Song, J., Liu, Y., Zhang, Y., & Jiao, L. (2011). Mechanical properties of hydroxyapatite ceramics sintered from powders with different morphologies. *Materials Science and Engineering A*, 528(16-17), 5421–5427.
- Sooksaen, P., Jumpanoi, N., Suttiphan, P., & Kimchaiyong, E. (2010). Crystallization of Nano-Sized Hydroxyapatite via Wet Chemical Process under Strong Alkaline Conditions. *Science Journal Ubonratchathani University*, 1(1), 20–27.
- Sopyan, I., Ramesh, S., Nawawi, N. A., Tampieri, A., & Sprio, S. (2011). Effects of manganese doping on properties of sol–gel derived biphasic calcium phosphate ceramics. *Ceramics International*, 37(8), 3703–3715.
- Sopyan, I., Toibah, A. R., & Natasha, A. N. (2008). Nanosized bioceramic hydroxyapatite powders via sol-gel method. *International Journal of Mechanical and Materials Engineering*, 3, 133–138.
- Stojanovic, B. D., Simoes, A. Z., Paiva-Santos, C. O., Jovalekic, C., Mitic, V. V., & Varela, J. A. (2005). Mechanochemical synthesis of barium titanate. *Journal of the European Ceramic Society*, 25(12), 1985–1989.
- Studart, A. R., Gonzenbach, U. T., Tervoort, E., & Gauckler, L. J. (2006). Processing routes to macroporous ceramics: A review. *Journal of the American Ceramic Society*, 89(6), 1771–1789.
- Suchanek, W., & Yoshimura, M. (1998). Processing and properties of hydroxyapatite-based biomaterials for use as hard tissue replacement implants. *Journal of Materials Research*, 13(01), 94–117.
- Suchanek, W. L., Shuk, P., Byrappa, K., Riman, R. E., TenHuisen, K. S., & Janas, V. F. (2002). Mechanochemical–hydrothermal synthesis of carbonated apatite powders at room temperature. *Biomaterials*, 23, 699–710.
- Suzuki, O. (2010). Octacalcium phosphate: Osteoconductivity and crystal chemistry. *Acta Biomaterialia*, 6(9), 3379–3387.

- Tadic, D., & Epple, M. (2003). Mechanically stable implants of synthetic bone mineral by cold isostatic pressing. *Biomaterials*, 24(25), 4565–4571.
- Tadic, D., & Epple, M. (2004). A thorough physicochemical characterisation of 14 calcium phosphate-based bone substitution materials in comparison to natural bone. *Biomaterials*, 25(6), 987–994.
- Tadic, D., Beckmann, F., Schwarz, K., & Epple, M. (2004). A novel method to produce hydroxyapatite objects with interconnecting porosity that avoids sintering. *Biomaterials*, 25(16), 3335–3340.
- Takahashi, H., Yashima, M., Kakihana, M., & Yoshimura, M. (1995). Synthesis of stoichiometric hydroxyapatite by a Gel route from the aqueous solution of citric and phosphonoacetic acids. *European Journal of Solid State and Inorganic Chemistry*, 32(7-8), 829-835.
- Tampieri, A., Sprio, S., Ruffini, A., Celotti, G., Lesci, I. G., & Roveri, N. (2009). From wood to bone: multi-step process to convert wood hierarchical structures into biomimetic hydroxyapatite scaffolds for bone tissue engineering. *Journal of Materials Chemistry*, 19(28), 4973.
- Tan, C. Y., Ramesh, S., Aw, K. L., Yeo, W. H., Hamdi, M., & Sopyan, I. (2008). Effect of powder calcination on the sintering of hydroxyapatite. *The Medical Journal of Malaysia*, 63 (21), 87–88.
- Tan, N., Kou, Z., Ding, Y., Leng, Y., Liu, C., & He, D. (2011). Novel substantial reductions in sintering temperatures for preparation of transparent hydroxyapatite bioceramics under ultrahigh pressure. *Scripta Materialia*, 65(9), 819–822.
- Tang, C. Y., Uskokovic, P. S., Tsui, C. P., Veljovic, D., Petrovic, R., & Janackovic, D. (2009). Influence of microstructure and phase composition on the nanoindentation characterization of bioceramic materials based on hydroxyapatite. *Ceramics International*, 35(6), 2171–2178.
- Taş, A. (2001). Molten salt synthesis of calcium hydroxyapatite whiskers. *Journal of the American Ceramic Society*, 84(2), 295–300.
- Thangamani, N., Chinnakali, K., & Gnanam, F. D. (2002). The effect of powder processing on densification, microstructure and mechanical properties of hydroxyapatite. *Ceramics International*, 28(4), 355–362.

- Thein-Han, W. W., & Misra, R. D. K. (2009). Biomimetic chitosan–nanohydroxyapatite composite scaffolds for bone tissue engineering. *Acta Biomaterialia*, 5(4), 1182-1197.
- Thomas, V., Dean, D. R., & Vohra, Y. K. (2006). Nanostructured biomaterials for regenerative medicine. *Current Nanoscience*, 2(3), 155-177.
- Tripathi, G., & Basu, B. (2012). A porous hydroxyapatite scaffold for bone tissue engineering: Physico-mechanical and biological evaluations. *Ceramics International*, 38(1), 341–349.
- Trommer, R. M., Santos, L. A., & Bergmann, C. P. (2007). Alternative technique for hydroxyapatite coatings. *Surface and Coatings Technology*, 201(24), 9587-9593.
- Vallet-Regí, M., & González-Calbet, J. M. (2004). Calcium phosphates as substitution of bone tissues. *Progress in Solid State Chemistry*, 32(1), 1-31.
- Van Landuyt, P., Li, F., Keustermans, J. P., Streydio, J. M., Delanny, F., & Munting, E. (1995). The influence of high sintering temperature on the mechanical properties of hydroxyapatite. *Journal of Materials Science: Materials in Medicine*, 6, 8–13.
- Varma, H., Vijayan, S. P., & Babu, S. S. (2002). Transparent Hydroxyapatite Ceramics through Gelcasting and Low-Temperature Sintering. *Journal of the American Ceramic Society*, 85(2), 493-495.
- Veljovic, D., Jokic, B., Petrovic, R., Palcevskis, E., Dindune, A., Mihailescu, I. N., & Janackovic, D. (2009). Processing of dense nanostructured HAP ceramics by sintering and hot pressing. *Ceramics International*, 35(4), 1407–1413.
- Veljovic, Dj., Zalite, I., Palcevskis, E., Smiciklas, I., Petrovic, R., & Janackovic, Dj. (2010). Microwave sintering of fine grained HAP and HAP/TCP bioceramics. *Ceramics International*, 36(2), 595–603.
- Verdelis, K., Lukashova, L., Wright, J. T., Mendelsohn, R., Peterson, M. G. E., Doty, S., & Boskey, A. L. (2007). Maturation changes in dentin mineral properties. *Bone*, 40(5), 1399-1407.
- Victoria, E. C., & Gnanam, F. D. (2002). Synthesis and Characterisation of Biphasic Calcium Phosphate. *Trends Biomaterials and Artificial Organs*, 16(1), 12–14.

- Vijayalakshmi Natarajan, U., & Rajeswari, S. (2008). Influence of calcium precursors on the morphology and crystallinity of sol-gel-derived hydroxyapatite nanoparticles. *Journal of Crystal Growth*, 310(21), 4601–4611.
- Vijayan, S., & Varma, H. (2002). Microwave sintering of nanosized hydroxyapatite powder compacts. *Materials Letters*, 56(5), 827–831.
- Walsh, P. J., Buchanan, F. J., Dring, M., Maggs, C., Bell, S., & Walker, G. M. (2008). Low-pressure synthesis and characterisation of hydroxyapatite derived from mineralise red algae. *Chemical Engineering Journal*, 137(1), 173–179.
- Wang, J., & Shaw, L. L. (2009). Nanocrystalline hydroxyapatite with simultaneous enhancements in hardness and toughness. *Biomaterials*, 30(34), 6565–6572.
- Wang, J., & Shaw, L. L. (2010). Grain-size dependence of the hardness of submicrometer and nanometer hydroxyapatite. *Journal of the American Ceramic Society*, 93(3), 601–604.
- Wang, M. (2007). Materials selection and scaffold fabrication for tissue engineering in orthopaedics. *Advanced Bioimaging Technologies in Assessment of the Quality of Bone and Scaffold Materials: Techniques and Applications*, 259–288.
- Wang, M., Hench, L. L., & Bonfield, W. (1998). Bioglass/high density poly-ethylene composite for soft tissue applications: preparation and evaluation. *Journal of Biomedical Material Research*, 42, 577–586.
- Wang, P. E., & Chaki, T. K. (1993). Sintering behaviour and mechanical properties of hydroxyapatite and dicalcium phosphate. *Journal of Materials Science: Materials in Medicine*, 4(2), 150–158.
- Webster, T. J. (2001). Nanophase ceramics: the future orthopedic and dental implant material. *Advances in Chemical Engineering*, 27, 125–166.
- Webster, T. J., Ergun, C., Doremus, R. H., Siegel, R. W., & Bizios, R. (2000). Specific proteins mediate enhanced osteoblast adhesion on nanophase ceramics. *Journal of Biomedical Materials Research*, 51(3), 475–483.
- Wu, S. C., Hsu, H. C., Hsu, S. K., Chang, Y. C., & Ho, W. F. (2015). Effects of heat treatment on the synthesis of hydroxyapatite from eggshell powders. *Ceramics International*, 1–7.

- Wu, S. C., Hsu, H. C., Wu, Y. N., & Ho, W. F. (2011). Hydroxyapatite synthesized from oyster shell powders by ball milling and heat treatment. *Materials Characterization*, 62(12), 1180–1187.
- Wu, S. C., Tsou, H. K., Hsu, H. C., Hsu, S. K., Liou, S. P., & Ho, W. F. (2013). A hydrothermal synthesis of eggshell and fruit waste extract to produce nanosized hydroxyapatite. *Ceramics International*, 39(7), 8183–8188.
- Xu, Y., Wang, D., Yang, L., & Tang, H. (2001). Hydrothermal conversion of coral into hydroxyapatite. *Materials Characterization*, 47(2), 83–87.
- Yang, Y., Ong, J. L., & Tian, J. (2002). Rapid sintering of hydroxyapatite by microwave processing. *Journal of Materials Science Letters*, 21(1), 67–69.
- Ye, W., & Wang, X. X. (2007). Ribbon-like and rod-like hydroxyapatite crystals deposited on titanium surface with electrochemical method. *Materials Letters*, 61(19), 4062–4065.
- Yeong, K. C. B., Wang, J., & Ng, S. C. (2001). Mechanochemical synthesis of nanocrystalline hydroxyapatite from CaO and CaHPO₄. *Biomaterials*, 22(20), 2705–2712.
- Yen, F. L., Shih, W. J., Hon, M. H., Chen, H. T., Hung, I. M., Ko, H. H., & Wang, M. C. (2012). Understanding the biocompatibility of sintered calcium phosphate with ratio of [Ca]/[P] = 1.50. *Journal of Nanomaterials*, 1–8.
- Yuan, H., & de Groot, K. (2004). Calcium phosphate biomaterials: an overview. In *Learning from Nature How to Design New Implantable Biomaterials: From Biomineralization Fundamentals to Biomimetic Materials and Processing Routes* (pp. 37–57). Springer Netherlands.
- Zakaria, S. M., Sharif Zein, S. H., Othman, M. R., Yang, F., & Jansen, J. A. (2013). Nanophase hydroxyapatite as a biomaterial in advanced hard tissue engineering: a review. *Tissue Engineering Part B: Reviews*, 19(5), 431–441.
- Zanotto, A., Saladino, M. L., Martino, D. C., & Caponetti, E. (2012). Influence of Temperature on Calcium Hydroxyapatite Nanopowders. *Advances in Nanoparticles*, 01(03), 21–28.
- Zhang, H., & Zhang, M. (2011). Characterization and thermal behavior of calcium deficient hydroxyapatite whiskers with various Ca/P ratios. *Materials Chemistry and Physics*, 126 (3), 642–648.

Zhang, X., & Vecchio, K. S. (2006). Creation of dense hydroxyapatite (synthetic bone) by hydrothermal conversion of seashells. *Materials Science and Engineering C*, 26(8), 1445–1450.

Zhou, H., & Lee, J. (2011). Nanoscale hydroxyapatite particles for bone tissue engineering. *Acta Biomaterialia*, 7(7), 2769–2781.

University of Malaya

LIST OF PUBLICATIONS AND PAPERS PRESENTED

1. **Nawawi, N. A.**, Singh, R., Hamdi, M., Young, T. C., Purbolaksono, J., & Toulouei, R. (2014). Synthesis and Properties of Biphasic Calcium Phosphate Prepared by Different Methods. *Advanced Materials Research*, 970. 20-25.
2. Ramesh, S., **Natasha, A. N.**, Tan, C. Y., Bang, L. T., Niakan, A., Purbolaksono, J., Chandran, H., Ching, C. Y., Ramesh, S. & Teng, W. D. (2015). Characteristics and properties of hydroxyapatite derived by sol-gel and wet chemical precipitation methods. *Ceramics International*, 41(9), 10434-10441.
3. Ramesh, S., **Natasha, A. N.**, Tan, C. Y., Bang, L. T., Ching, C. Y., & Chandran, H. (2016). Direct conversion of eggshell to hydroxyapatite ceramic by a sintering method. *Ceramics International*, 42(6), 7824-7829.

LIST OF CONFERENCE ATTENDED

1. **ICoSEM 2013**, 1st International Conference on the Science and Engineering of Materials, 13-14 November 2013, Kuala Lumpur, Malaysia.
2. **AUN/SEED-NET 2014**, Regional Conference on Materials Engineering, in conjunction with 3rd UM-JWRI International Seminar, 11-12 November 2014, Kuala Lumpur, Malaysia.

APPENDIX A

A-1: Calculation for the synthesis of eggshell derived hydroxyapatite through solid-state reaction (HA-Es)

The calcium-to-phosphorous molar (Ca/P) ratio is 1.67

Stoichiometric Equation:



Molar mass of $\text{CaHPO}_4 \cdot 2\text{H}_2\text{O}$ = 170.07 (g/mol)

Molar mass of CaCO_3 = 100.09 (g/mol)

Note that, the amount of $\text{CaHPO}_4 \cdot 2\text{H}_2\text{O}$ used = 10.25 g

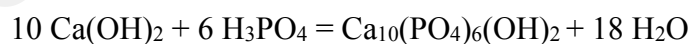
Hence, the amount of CaCO_3 is:

$$m_{\text{CaCO}_3} = 10.25(\text{g}) \times \frac{4 \times 100.09(\text{g/mol})}{6 \times 170.07(\text{g/mol})} = 4.02(\text{g})$$

A-2: Calculation for the synthesis of Hydroxyapatite through wet chemical precipitation (HA-Wp)

The calcium-to-phosphorous molar (Ca/P) ratio is 1.67

Stoichiometric Equation:



1 mol $\text{Ca}(\text{OH})_2 \implies 6/10 \text{H}_3\text{PO}_4 = 0.6 \text{H}_3\text{PO}_4$

Molar mass of $\text{Ca}(\text{OH})_2$ = 74.08 (g/mol)

Molar mass of H_3PO_4 = 98 (g/mol)

We know that acid is 85 % pure, therefore the amount of H_3PO_4 is:

$$\ast 0.6 \text{ mol H}_3\text{PO}_4 = (0.6)(98 \text{ g/mol})(100) / 85 = 69.176 \text{ g}$$

APPENDIX B



Figure B-1: Attritor Mill (Akron Electric Inc., USA) used to mixing calcined eggshell and calcium hydrogenphosphate dehydrate powder



Figure B-2: Box Furnace used to perform conventional pressureless sintering



Figure B-3: Microwave Furnace (Shenzen BduVo, Delta, China)
used to run microwave sintering



Figure B-4: Preparation of sample for sintering regime

APPENDIX C

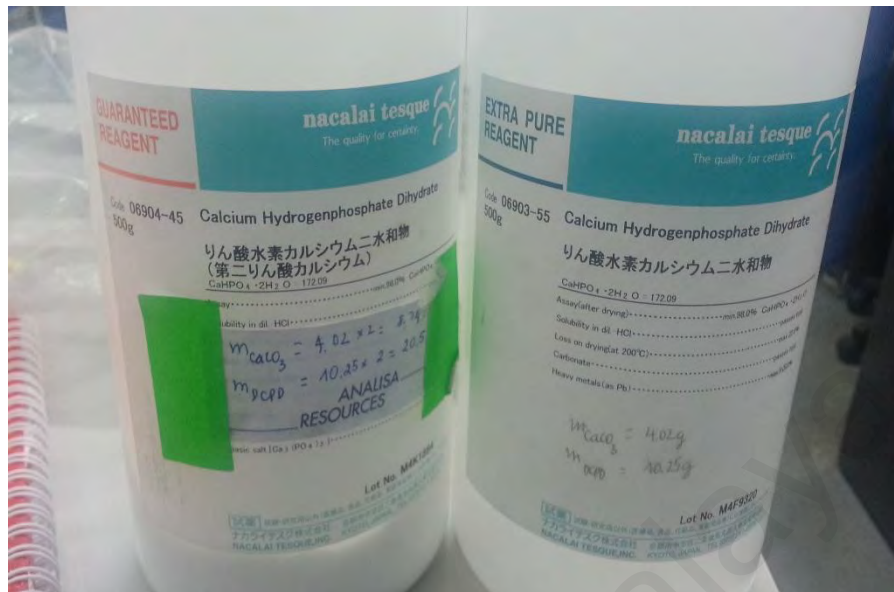


Figure C-1: Calcium Hydrogenphosphate Dihydrate (DCPD, Nacalai Tesque, Japan) as the source of phosphorus in the solid state sintering

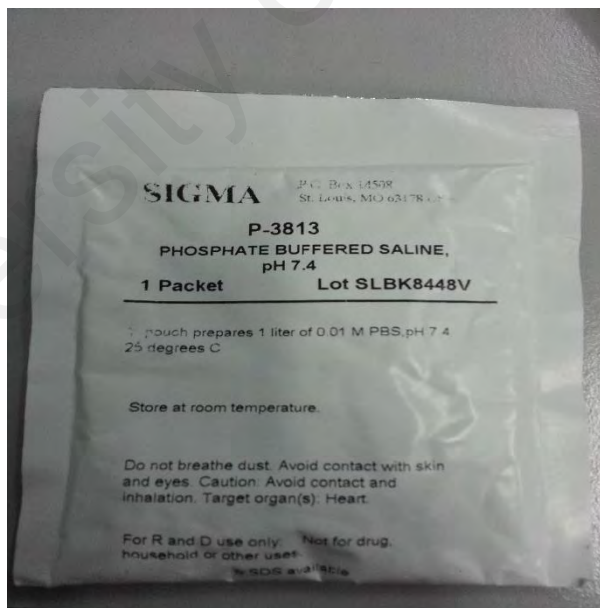


Figure C-2: Phosphate Buffer Saline (PBS) buffer pouch (Sigma Aldrich, USA) used for in vitro biodegradation study



Figure C-3: Surface of HA-Es(1250) compact after 21 days of PBS immersion

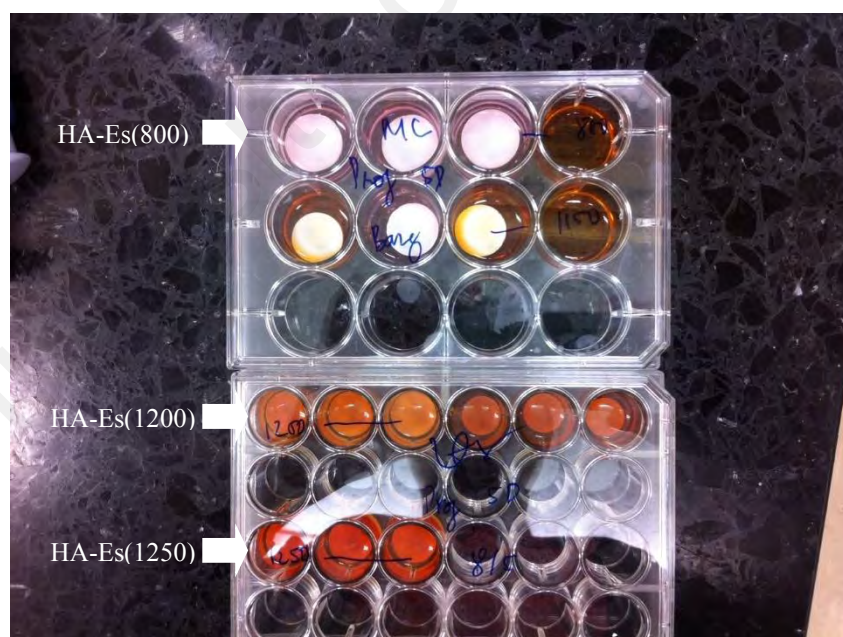


Figure C-4: Rat bone marrow cell proliferation on different HA-Es samples after 5 days. The amount of the formazan dye (orange-colored product) generated by dehydrogenases in cells is directly proportional to the number of living cells



Figure C-5: Bio-Rad Protein Assay (Bio-Rad Laboratories Inc., USA) for cell differentiation purpose



Figure C-6: Calcium quantification of HA-Es(800)-Sp1, HA-Es(1200)-Sp2 and HA-Es(1250)-Sp3 as compared to the standard solution 10,5, 0.5 and blank after 21 days. Literally, the bluer the solution, the higher is Ca concentration